Computational Modelling of Ingestion through Turbine Rim-Seals

Lalwani, Yogesh

Award date:
2014

Awarding institution:
University of Bath

UNIVERSITY OF BATH

Computational Modelling of Ingestion through Turbine Rim-Seals

Yogesh Lalwani

A thesis submitted for the degree of Doctor of Philosophy

University of Bath

Department of Mechanical Engineering

March 2014

ABSTRACT

Hot gas ingestion through rim-seals (also commonly known as ingress) and into the wheel-space between rotating and stationary discs is a key concern and an important factor the engine designer should take into account when designing the turbine stage of an engine. The flow past the stationary vanes and rotating blades in the turbine annulus creates an unsteady 3D variation of pressure radially outwards the rim-seal. Ingress and egress occur through those parts of the seal clearance where the external pressure is higher and lower, respectively, than that in the wheel-space.

Most computational studies of ingress have been conducted using unsteady flow. This report describes a computational study carried out to better understand ingress using a steady-state model which has the advantage of being faster and which requires significantly less computational resources. The ingested flow within a turbine stage was obtained by modelling the annulus alongside the wheel-space in a multi-domain simulation. Previous studies have shown that when modelling ingress via a steady model and using the blades in a fixed, or frozen position, an uncertainty arises as to where to position the blades relative to the vanes and how many positions are required to properly capture the ingested flow effect. In the present study, a non-bladed, 3D, steady CFD model was employed to eliminate the uncertainty and complexity of fixing the rotor blade at a given position, whilst also reducing the mesh size for the rotor domain.

The simulations were carried out using the commercial CFD code, ANSYS CFX. Initially the code was used to calculate the flow structure of an axisymmetric rotor-stator system with no ingress, validating the fluid dynamics within the wheel-space against experimental data in terms of axial distributions of radial and tangential velocity. The CFD model was extended to include the annulus with only the stationary vane and excluding the rotating blade, in which the non-axisymmetric pressure variation in the annulus was seen to cause ingress. The pressure distribution in the annulus was analysed for different rotational Reynolds number computations, differing sealing flows and varying ratios of axial Reynolds number to rotational Reynolds number; in all the

cases showed good agreement with experimentally measured data at the University of Bath.

The axial-clearance seal was the main seal used to verify the non-bladed CFD method, which was extensively validated against experimental data. Validation was performed between the computed results and the measured data within the wheel-space in terms of radial distributions of core swirl ratio, and the sealing effectiveness and static pressures on the stator wall. The computations showed very good agreement with experiments for swirl ratio and pressure, while the sealing effectiveness showed reasonable agreement with experiments.

The non-bladed CFD method was also used to perform computations for radial-clearance and double-clearance seals. Engine representative seals, known as double-clearance seals were also computed, where an outer wheel-space is created by the inner seal, which is seen to act as a damping chamber which holds and contains most of the ingested fluid, hence improving the sealing effectiveness and reducing the swirl within the inner wheel-space. The computed results for all the seals show a good prediction of the flow structure (swirl ratio) within the wheel-space, and reasonable agreement with experiments for the sealing effectiveness.

In parallel with the computational programme, experiments were performed in the research facility which models hot-gas ingestion into the wheel-space of an axial turbine stage. The performance (i.e. sealing effectiveness) of three different radial-clearance seals was measured via CO_2 gas concentration measurements. The radial-clearance seals are differentiated as follows: a baseline radial seal, a radial seal with a decreased axial overlap, and a radial seal with a tighter radial clearance. A non-dimensional sealing parameter, which combines the different effects of rotating flows inside the wheel-space into a single parameter, Φ_o is used for the presentation of the data. The measurements show that increasing the axial overlap and decreasing the radial clearance increases the effectiveness of the radial-clearance seal.

The non-bladed CFD model is a useful 3D tool for a turbine design engineer. The lack of experimental facilities and/ or data would make this 3D model an indispensable CFD tool for quantitatively predicting the flow structure within the wheel-space, and qualitatively predicting the sealing effectiveness for any given rim-seal geometry.

ACKNOWLEDGEMENTS

I would like to thank my supervisors, Dr. M. Wilson and Prof. G. D. Lock for their continuous guidance and support. Prof. J. M. Owen is also thanked for always being there to offer advice and direction. My gratitude is extended to Dr. C. M. Sangan, Dr. O. J. Pounteney and J. A. Scobie for their collaboration in providing experimental results for validation. Finally, R. Teuber is thanked for his assistance at the preliminary stage of my research.

NOMENCLATURE

a	Inner radius of disc
A	Area
b	Radius of seal
c	Concentration
$C_{d,e}, C_{d,i}$	Discharge coefficients for egress, ingress
C_p	Pressure coefficient ($= (p - \bar{p})/(1/2\,\rho\Omega^2 b^2)$)
$C_{p,max}$	Pressure coefficient ($= \Delta p/(1/2\,\rho \mathrm{W}^2)$)
C_w	Non-dimensional flow rate ($= m/\mu b$)
$C_{w,e}, C_{w,i}$	Values of C_w for egress, ingress
$C_{w,o}$	Non-dimensional sealing flow rate ($= m_o/\mu b$)
$C_{w,min}$	Minimum value of $C_{w,o}$ to prevent ingress
G	Gap ratio ($= s/b$)
G_c	Seal-clearance ratio ($= s_c/b$)
k	Turbulence kinetic energy
K	Empirical constant
$\dot{m}$	Mass flow rate
M	Mach number
p	Static pressure
$\bar{p}$	Average static pressure along one vane pitch
p'	Modified pressure ($= p + \frac{2}{3}\rho k + \frac{2}{3}\mu_{eff}\frac{\partial U_k}{\partial x_k}$)
P_k	Turbulence production rate due to viscous forces
r, ϕ, z	Radial, circumferential and axial coordinates
Re_ϕ	Rotational Reynolds number ($= \rho\Omega b^2/\mu$)

Re_w	Mainstream flow axial Reynolds number ($= \rho \mathrm{W} b/\mu$)
s	Axial space between rotor and stator
s_c	Seal clearance
S_M	Sum of body forces
u_τ	Friction velocity ($= \sqrt{\tau_w/\rho}$)
u^+	Near wall velocity
U	Bulk mean velocity of sealing flow ($= \dot{m}_o/2\pi\rho b s_c$)
V_r, V_ϕ, V_z	Radial, tangential and axial components of velocity
W	Axial velocity in annulus
x	Non-dimensional radial location ($= r/b$)
y	Distance normal to the wall
y^+	Non-dimensional wall distance ($= \rho y u_\tau/\mu$)
Z	Axial distance from the stator
β	Swirl ratio ($= V_\phi/\Omega r$); blade angle
β_o	Blade angle at design
$\beta\phi$	Numerical advection correction
Γ_c	Ratio of discharge coefficients ($= C_{d,i}/C_{d,e}$)
ΔC_p	Non-dimensional pressure difference ($= \Delta p/(1/2\,\rho\Omega^2 b^2)$)
Δp	Peak-to-trough pressure difference ($= p_{2,max} - p_{2,min}$)
ε	Sealing effectiveness; turbulence eddy dissipation
ε_c	Concentration effectiveness
Φ	Non-dimensional sealing parameter ($= C_w/2\pi G_c Re_\phi$)
Φ_i	Value of Φ when $\mathrm{C}_w = C_{w,i}$
Φ_i^*	Value of Φ_i when $\Phi_o = 0$

Φ_{min}	Value of Φ when $C_w = C_{w,min}$
Φ_o	Value of Φ when $C_w = C_{w,o}$
θ	Angular coordinate, non-dimensional vane pitch
λ_T	Turbulent flow parameter ($= C_{w,o} Re_{\phi}^{-0.8}$)
μ	Dynamic viscosity
μ_{eff}	Effective viscosity accounting for turbulence
μ_t	Turbulence viscosity
ρ	Density
σ	Standard deviation
τ_ω	Wall shear stress
ω	Turbulence frequency
Ω	Angular velocity of rotating disc

TURBULENCE MODEL CONSTANTS

$C_\mu, C_{\varepsilon 1}, C_{\varepsilon 2}, \sigma_k, \sigma_\varepsilon$	$k-\varepsilon$ model constants
$\alpha, \beta, \beta', \sigma_k, \sigma_\omega$	$k-\omega$ model constants
α_1, S, F_1, F_2	SST model constants
$P_{kb}, P_{\varepsilon b}, P_{\omega b}$	Influence of buoyancy forces

SUBSCRIPTS

a	Annulus
e	Egress
i	Ingress
o	Superposed flow or sealing flow
ip	Evaluation at an integration point
up	Value at the upwind node
1,2	Locations in wheel-space and annulus, respectively

TABLE OF CONTENTS

TABLE OF FIGURES

1 INTRODUCTION

1.1 HISTORY OF THE GAS TURBINE

Newton's third law of motion states that 'for every force acting on a body, there is an equal and opposite reaction'. The jet engine was born on this principle, whereby forcing either a liquid or gaseous fluid in one direction, creates an equal and opposite reaction that drives the engine, commonly known as the force of power.

The first ever machine known in human history that utilises Newton's third law of motion, is known as 'Hero's Engine' or an aeolipile, depicted in Figure 1.1. It was produced as a toy in Greece around 120 BC; it is effectively a reaction steam turbine which uses the momentum of the steam released from a number of jets, to create an equal and opposite reaction to the jets themselves, causing the engine to revolve.

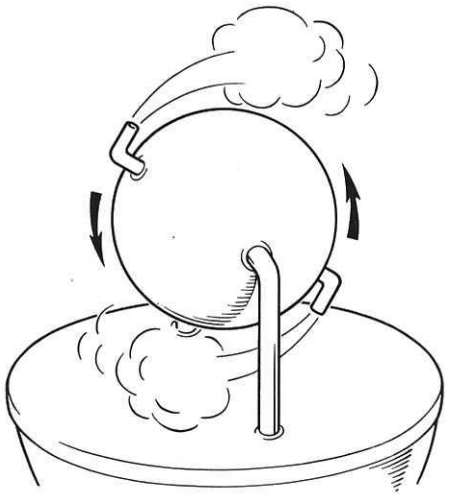

Figure 1.1 Hero's engine or aeolipile [1]

Around 1500 AD, Leonardo da Vinci designed a hot air driven axial turbine in the exhaust duct of a fireplace, effectively to be used to turn a roasting spit. In 1791, a British patent for the first true gas turbine was given to John Barber, which included most of the elements present in modern day gas turbines, however it was never built. In America, George Baily Brayton invented the Brayton cycle in 1872, where this thermodynamic cycle would later be the foundation for Whittle's engine. In the same year, a gas turbine engine was built by Franz Stolze, however the engine required external power to run.

In 1903, the first gas turbine that was able to produce more power (11 hp) than required to run its own components was built by a Norwegian, Aegidius Elling. In 1908, Hanz Holzworth built a gas turbine with a valve-controlled combustion chamber in Germany. Frank Whittle patented his design for a centrifugal gas turbine for jet propulsion in 1930, which had its first successful use in April 1937.

Brown Boveri is the pioneer for the successful construction of the first gas turbine to be expressly operated for power generation in the 1930s. In 1939 he built the first simple cycle gas turbine power plant explicitly for power generation, with a power output of 4 MW and a thermal efficiency of 17% [2], which was commissioned in a Swiss emergency power station in Neuchatel.

Gas turbines are heat engines, and like all heat engines, fuel is burnt to convert energy into something useful. For gas turbines, that 'something useful' is a fast moving jet of air which propels an aircraft forward, or powers a turbine which drives a load for an electrical generator, a compressor for a gas pipeline, a ship's propeller, or even a water jet.

Figure 1.2 shows the pressure, temperature and velocity variations through a typical single-spool axial flow turbo-jet engine. In the compressor section, the pressure and temperature increase as a result of work being done on the air. In the combustor, the temperature of the gas is further increased by burning fuel. In the turbine section, energy is extracted from the hot gas by an expansion process, which results in a decrease of temperature and pressure. This extracted energy is converted to shaft power to turn the compressor. In the aviation sector, gas turbines further expand the hot gas stream in the nozzle, to produce a high exit kinetic energy for thrust purposes. However, in the power generation sector, gas turbines do not require thrust, thus all the energy in the hot gas is extracted (after accounting for the compressor) to power an electrical generator.

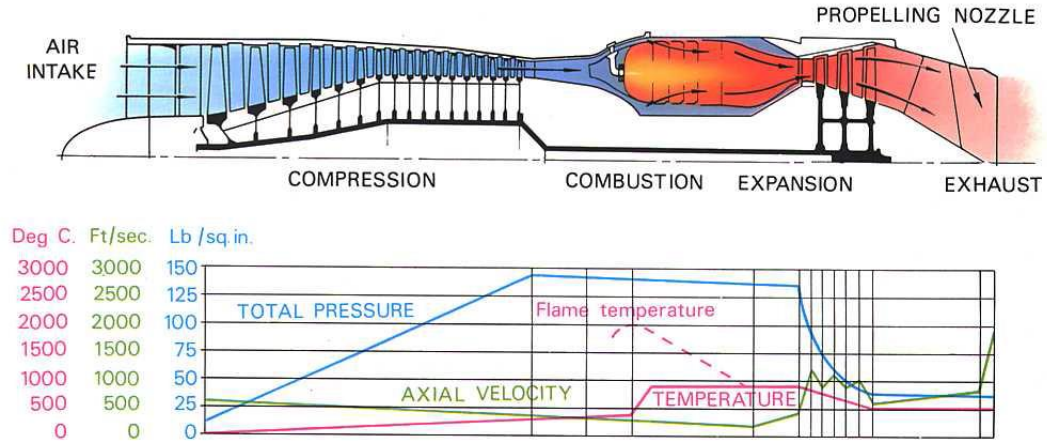

Figure 1.2 Variation of temperature, pressure and velocity through simple turbojet [3]

1.1.1 Gas Turbine Advantages

Previous studies [4] suggest that the core of a gas turbine can be about 20 times more powerful than a same-sized piston engine. This is because gas turbines have large, open flow paths with a continuous cycle, which can intake much more air than an equally-sized piston engine over the same interval time. Even if, assuming that only a third of the air passing through a gas turbine is used for combustion, since the air is significantly used for cooling and sealing purposes, the energy release rate is still substantially greater than that of a piston engine of the same size.

Gas turbines can be very powerful for their size since they are able to move more air through an engine and thus burn more fuel. However, it should be noted that gas turbines are costly to manufacture, due to the expensive materials required for the combustor and turbine, since they have to withstand continuous high temperatures.

1.2 Gas Turbines for Industrial Power Generation

The location of many power generation engines, often near to centres of habitation, requires ultra-low emissions of nitrogen oxides and carbon monoxide. Modern industrial gas turbines are very clean engines, with combustion features not found on today's aero-engines, such as multiple combustor zones or water injection to ensure optimum control of flame temperatures.

Today's gas turbines play a major role in the huge power generation market, with orders of around 30GW per year [4]. The success is partly due to the large reserves of natural gas, which provide a cheap fuel rich in hydrogen, and produces less carbon dioxide than other liquid fuels. Another major factor is their thermal efficiency, which can reach about 60% for combined cycle power plants. The other advantage of gas turbines is their very wide range of power levels, which reaches up to 300 MW for simple cycle engines and 500 MW for combined cycle engines.

The configuration of simple cycle gas turbine engines is similar to that of a turbojet, apart from the intake and the exhaust. The main difference is that all the available pressure at entry to the turbine, is expanded to ambient pressure to produce shaft power, except for a small pressure loss at the exhaust. This results in the turbine power being considerably larger than that required to drive the compressor, where the excess power drives a load, such as an electrical generator which can be seen in Figure 1.3. However, the temperature of the gas at the exhaust is typically 250 °C to 350 °C hotter than ambient temperature, which represents a considerable amount of waste heat for an industrial application.

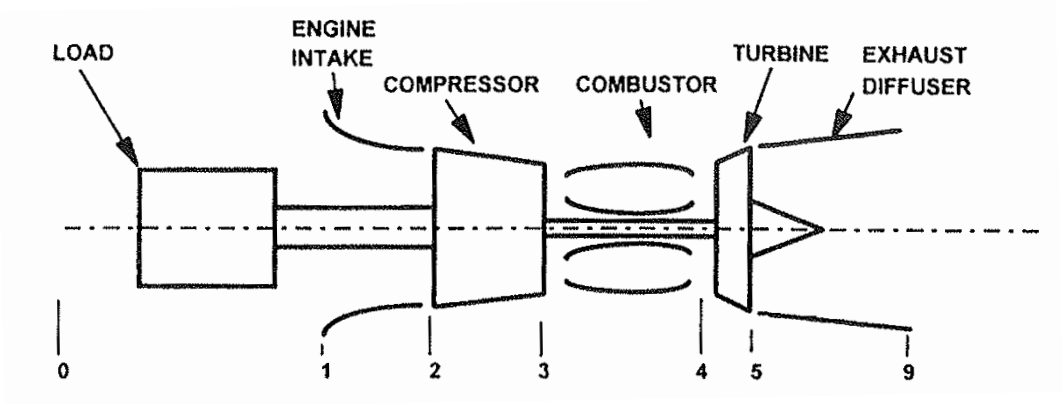

Figure 1.3 Single spool shaft power engine configuration [4]

Combined cycle gas turbines are similar to a simple cycle configuration, however with a significant difference, the waste heat is recovered in a Heat Recovery Steam Generator (HRSG). It consists of a heat exchanger, with the gas turbine exhaust on the hot side, and water, which forms into steam, on the cold side. The first part of the HRSG is the economiser, where the water is heated until it vaporises. Once the steam has fully vaporized, the temperature is further increased in the superheater.

The high pressure and high temperature steam is then expanded across a steam turbine, which provides up to an extra 45% power in addition to that from the gas turbine. Upon exiting the steam turbine, the rest of the steam is condensed to water, which is then passed into the pumps, ready to be circulated again. The steam plant of this combined cycle gas turbine is therefore considered as a 'closed cycle', as can be seen in Figure 1.4.

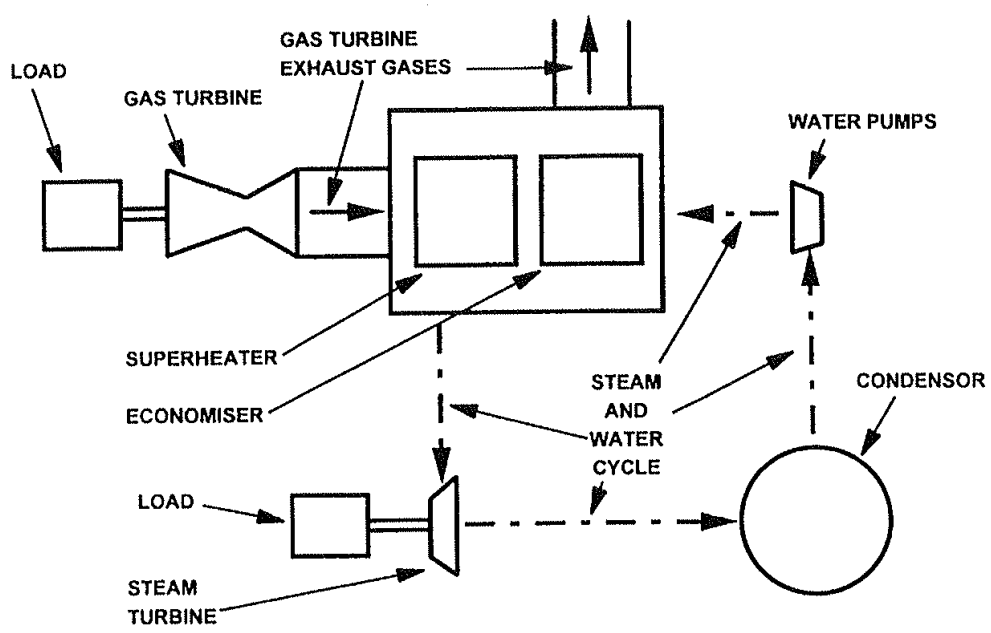

Figure 1.4 Single pressure combined cycle shaft power engine configuration [4]

Power generation applications and the type of plant (engine) used are described below.

1.2.1 Standby generators

Standby generators are employed for emergency use, where there may be a loss of main power supply which cannot be allowed. Examples include hospitals, and public buildings in areas such as Japan which may be prone to earthquakes. The power generated by these units is used locally since they are not connected to the grid system. Diesel engines are the most popular for this application, primarily due to the surplus of engines in the required power range (automotive and marine industry), also the reduced unit cost due to high production volume.

The key requirements for selecting the engine type are determined by the low utilisation, and are outlined below in order of importance:

1. Low unit cost.
2. Often low unit weight and volume are critical, i.e. Gas turbines have made some progress, particularly where weight and volume must be limited, for example if the generator is located on the roof with limited load bearing capability.
3. Fast start and acceleration to rated power times may be very important.
4. Thermal efficiency and emission levels are of secondary importance.

1.2.2 Small scale combined heat and power (CHP)

This application typically utilises the waste heat in an industrial process. The heat may be used directly in drying processes or generally it is converted by an HRSG into steam for other uses. Most CHP systems burn natural gas fuel, where the electricity generated is often used locally, and any excess is exported to the grid.

The key requirements for selecting the power plant are outlined below in order of importance:

1. Thermal efficiency, for both CHP and simple cycle operation, the latter is more appropriate if for parts of the year the full exhaust heat is not used.
2. Heat to power ratio is important as electricity is considered a more valuable commodity than heat. Thus a low ratio is an advantage as the unit may be sized for the heat requirement and any excess electricity sold to the grid.
3. The temperature of the heat is very important, in that whatever the industrial process is, it usually demands a high temperature.
4. Owing to the high utilisation, low unit cost, start and acceleration times are all of secondary importance, as are weight, volume and part speed torque.

Gas turbine engines best meet the above criteria, and are therefore the market leader in these applications. Diesel engines still retain a strong presence, particularly for applications where substantial low grade heat is acceptable or where simple cycle thermal efficiency is paramount.

1.2.3 Large scale CHP

This application exclusively utilises the waste heat to raise steam, which is then used in a large process application such as a paper mill or district heating. The electricity generated can be used locally or exported to the grid. The engine selection performance criteria are similar as for small scale CHP, with the exception that emissions legislation is more severe at the larger engine size.

Gas turbines are used almost exclusively for this application, where high grade heat is essential, and the weight and volume of diesel engines is prohibitive at these power outputs. The gas turbines used are often applicable to other markets such as oil and gas, and marine, which increase the production volume, and thus reduce unit cost. Aero-derivative gas turbines are most common, since they employ the core from a large civil turbofan as a gas generator, with a custom free power turbine for industrial use. Though some heavyweight engines are also used, these are designed specifically for industrial applications and are much heavier than their aero-derivative counterparts.

1.2.4 Applications which supply solely to a grid system

Power plants which supply to the grid fall into three categories:

1. *Peak lopping* engines, which have a low utilisation, typically less than 10%. They are used to satisfy the peak demand for electrical power which may occur in mid-weekday evenings as people return home and switch on a multitude of appliances.
2. *Base load power plants*, which achieve as near to 100% utilisation as possible to supply the continuous need for electrical power.
3. *Mid merit power plants*, which typically have a 30-50% utilisation. They serve the extra demand for electricity which is seasonal, such as the winter period in temperate climates where demand increases for domestic heating and lighting.

The considerations in selecting the type of power plant for a base load power station are as follows:

1. Thermal efficiency and availability are critical.
2. Unit cost is of high importance as the capital investment, and period of time before the power station comes on line to generate a return on the investment are large.

3. Cost of electricity is a key factor in selecting the type of power plant, and fuel price is a major contributor to this. Coal, nuclear and oil fired plants all compete with the gas turbine.

For all power plant cases, weight and volume are of secondary importance, while other specific criteria are presented below:

- For base load plants, start and acceleration times are unimportant.
- For peak lopping power stations, unit cost is crucial, time onto full load is very important and thermal efficiency is relatively unimportant.
- Mid merit power stations compromise between base load plants and peak lopping engines, where increased unit cost is acceptable in return for a moderate gain in thermal efficiency.

Peak loppers are generally simple cycle gas turbines, burning either diesel or natural gas, since the unit cost and time onto load are much lower than other available alternatives.

Base load power plants generally use gas turbines in combined cycle, to achieve the maximum possible thermal efficiency. The gas turbines compete with coal and nuclear fired steam plants for base load applications. Coal-powered plants use to have the biggest market share, however in recent years the combined cycle gas turbine has taken an increasing number of new power station orders due to the availability of natural gas, leading to a more competitive fuel price, higher thermal efficiency and lower emissions, and the fact that the power stations may often be built with a lower capital investment. This has also been supported by advances in gas turbine technology, which has increased both thermal efficiency and the feasible power output from a single engine.

Mid merit power stations use simple cycle gas turbines of a higher technology level than those used for peak lopping applications. The higher unit cost is justified by the higher thermal efficiency and the higher utilisation.

1.3 INTERNAL COOLING

Gas turbine engine designers are constantly trying to improve the power output for a given engine, reducing its weight, and/or decrease the fuel consumption for a given output. One way to achieve these improvements is by getting as high a turbine inlet temperature as possible.

Another important consideration gas turbine engineers face is the need to ensure that certain parts of the engine do not absorb heat to the extent that is detrimental to their safe operation. This is achieved by using cooling air to control the temperature of the compressor shafts and discs, ensuring an even temperature distribution and therefore improved engine efficiency by controlling thermal growth and hence maintaining minimum blade tip and seal clearances. Figure 1.5 shows the typical cooling and sealing airflows in a gas turbine engine.

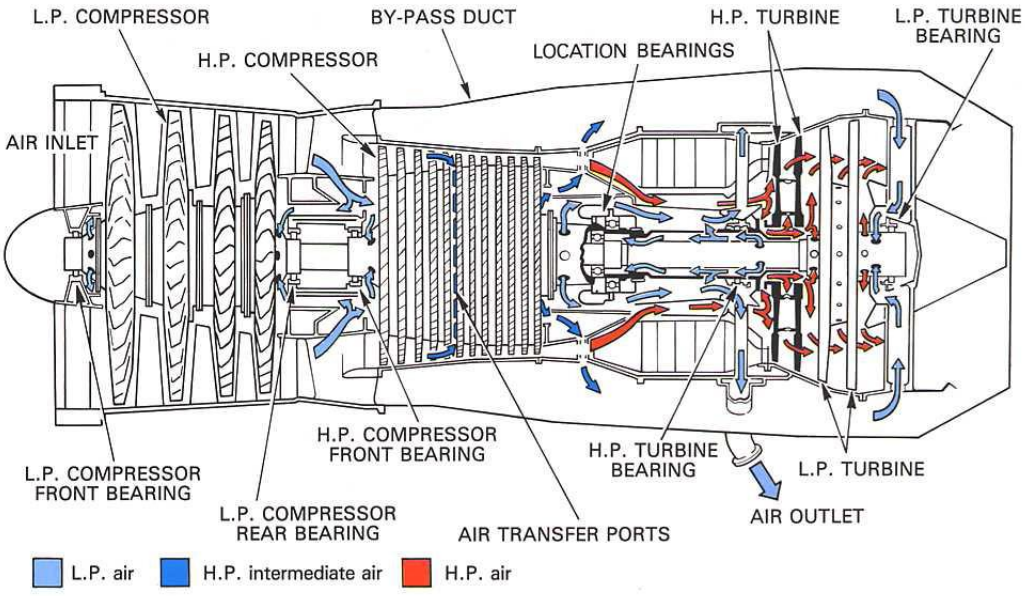

Figure 1.5 Gas turbine engine internal air system [3]

Turbine cooling was first developed by German designers in 1935, just prior to concentrated efforts during World War II. Since then, most, if not all, engine designers have used turbine cooling in their designs. The thermal efficiency of a gas turbine engine is highly dependent upon turbine entry temperature, which is limited by the nozzle guide vane and turbine blade materials. To increase the turbine entry temperature past the material's melting point without affecting the blade and vane integrity, continuous cooling of these components is necessary. The turbine discs also need to be

cooled due to the heat conducted from the turbine blades, which could cause thermal fatigue and uncontrolled expansion and contraction of the discs. Turbine inlet temperatures increased at a rate of approximately 8° C per year due to the advancements in metal alloys. However when turbine cooling was introduced, the rate at which turbine inlet temperatures increased was approximately doubled [5].

Around 20% of the compressed air is diverted for cooling and sealing purposes, where the extracted air from the main-gas path is distributed by the internal air system at several axial locations. Figure 1.6 shows in more detail the secondary air flow being used to cool the engine components, such as the nozzle guide vanes and turbine blades depicted in Figure 1.7. The sealing air is also used to prevent ingestion of hot mainstream gas on the disc surfaces to which the blades are attached and to seal the bearing chambers.

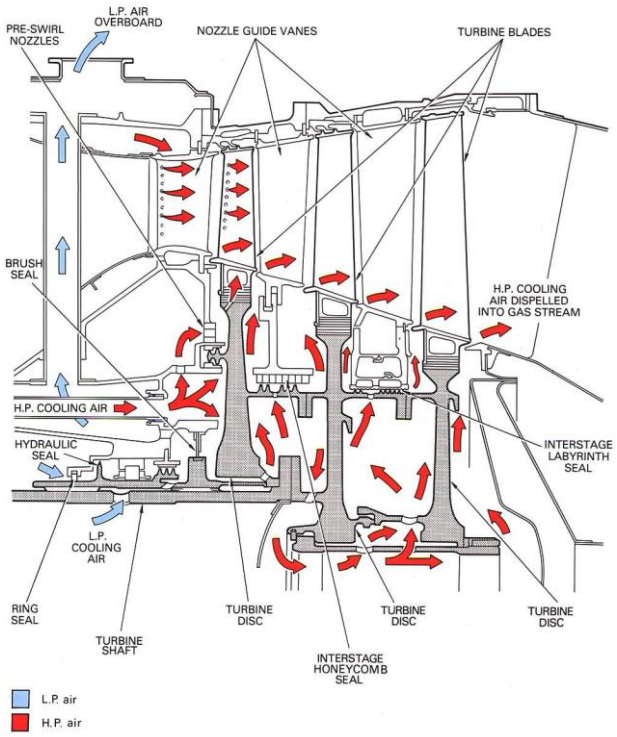

Figure 1.6 Turbine internal cooling and sealing air system [3]

Figure 1.7 illustrates an air cooled high pressure nozzle guide vane and turbine blade assembly. The life expectancy of the turbine blades and vanes depends not only on their structure but also on the method of cooling, which means that the flow design of the internal passages is important.

Pre-swirl nozzles (shown in Figure 1.7) reduce the temperature and pressure of the cooling air, which is fed to the disc for blade cooling by generating a substantial swirl velocity to assist with the efficient entry of the air into the rotating cooling passages.

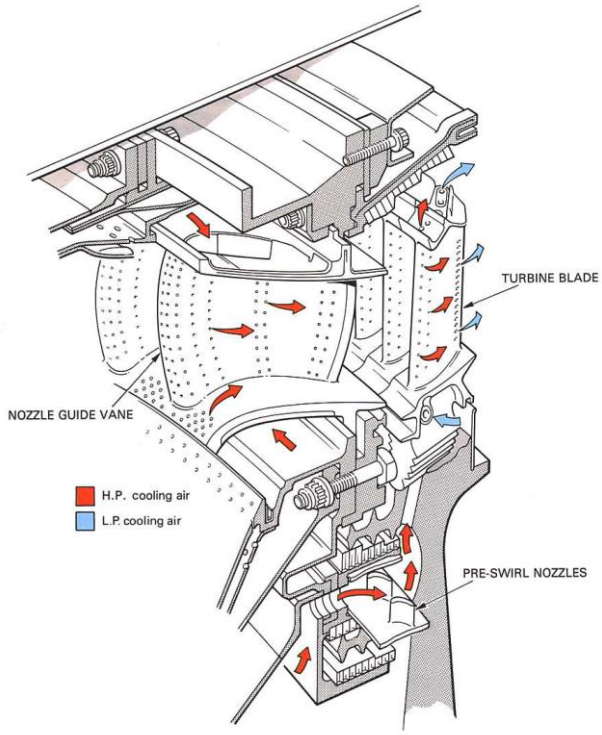

Figure 1.7 Nozzle guide vane and turbine blade cooling [3]

Advancements in materials allow for a limited increase in the turbine inlet temperature. Therefore engine designers have had to find an alternative way to further increase the turbine inlet temperature beyond that which the materials would tolerate. The solution was the use of turbine cooling, which allowed to increase the turbine inlet temperature while maintaining a constant blade (material) temperature.

The conventional coolant used for turbine cooling is air, which is readily available. It is extracted from the compressor, channelled to the turbine blade and vanes and used as a coolant. There are four methods used for turbine cooling, which are: 1) convection cooling, 2) impingement cooling, 3) film cooling and 4) transpiration cooling.

Convection cooling is the simplest and was the first turbine cooling method used. In this method, the coolant flows outward from the base of the turbine blade to the end through internal passages within the blade. Several possible blade configurations using convection cooling are shown in Figure 1.8. Early blade designs used circular passageways as shown in Figure 1.8a, however it had major shortcomings, such as the

large amount of cooling air required, and the fact that this method failed to effectively cool the thin trailing edge of the blades, since this portion of the blade is so thin. Figure 1.8d and Figure 1.8e illustrate later designs, which divided the blades into several passageways of varying size and shape, controlling the amount of cooling air to each passageway. The leading and trailing edge regions receive more cooling air than the midsection for appropriate cooling, with blades changing their flow path from Figure 1.8b to Figure 1.8f.

The effectiveness of convection cooling is limited by the size of the internal passages within the blade and the restriction on amount of cooling air available. Thus, when designing the internal passageways, the engine designer has to take into account the most effective geometry from a heat transfer view and the most economical from a manufacturing perspective.

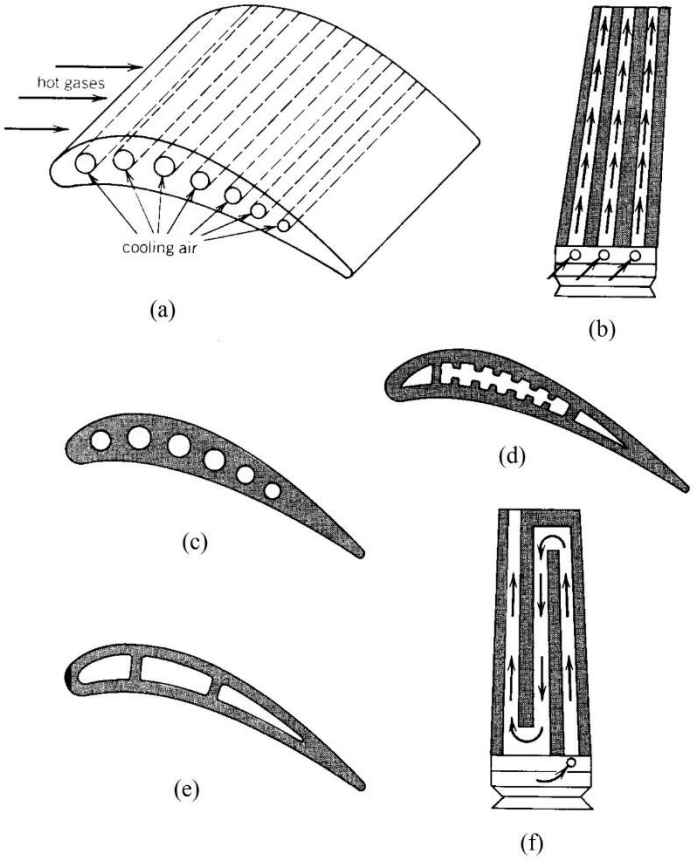

Figure 1.8 Various blade designs for convection cooling [5]

Impingement cooling is another form of convection cooling, however the main difference being that instead of the air flowing radially through the sections of the blade, the cooling air is ducted radially through a centre core of the blade, then turned normal to the radial direction, and passed through a series of holes so that it impinges on the inside of the blade, usually opposite from the stagnation point of the blade.

This cooling technique is a very effective method for local areas and can be easily adapted to stator (nozzle guide) vanes. It is usually employed at the leading edge of the blades, and can also be used in other areas if desired. The method is shown schematically in Figure 1.9a, with a possible design of impingement cooling shown in Figure 1.9b.

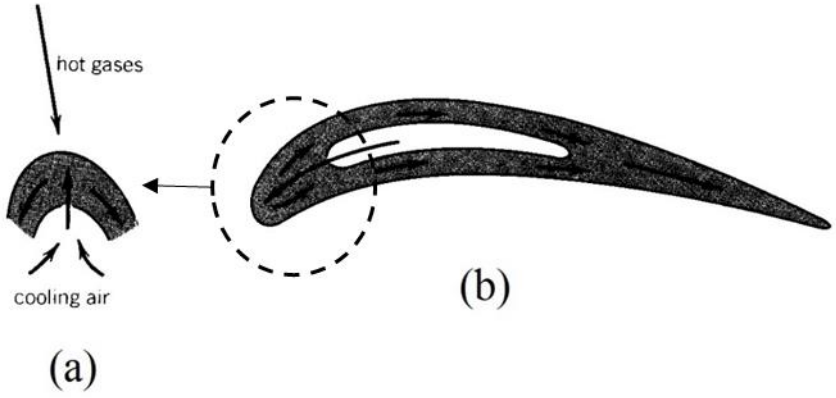

Figure 1.9 (a) General impingement cooling technique; (b) Example of impingement cooling design [5]

Film cooling is an effective way to protect the blade surface from hot gases, it involves the injection of the cooling air into the boundary layer of the hot gas, providing a protective, cool film along the surface. This method is more effective than convection cooling or impingement cooling, since the cooling air absorbs energy as it travels inside the blade and through the holes, then further reducing the metal temperature by reducing the amount of energy transferred from the hot gas to the blade. Film cooling is illustrated schematically in Figure 1.10a, with a possible design of film cooling shown in Figure 1.10b.

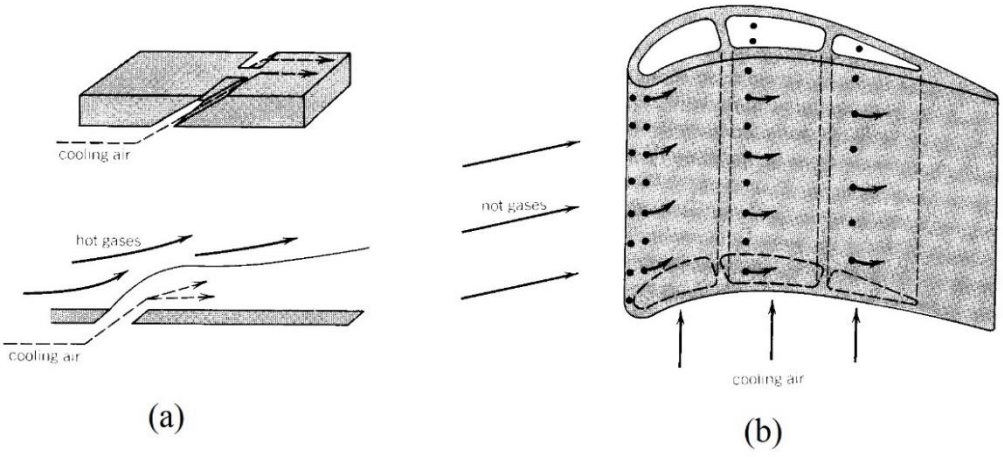

Figure 1.10 (a) General film cooling technique; (b) Example of film cooling design [5]

Transpiration cooling is the most efficient air-cooling method available, which is also known as full-blade film cooling or porous blade cooling. The method involves forcing the cooling air through a porous material which travels into the boundary layer, forming a cool, insulating film or layer. For transpiration cooling to be effective, the pores should be small, however it can lead to the pores becoming blocked due to oxidation and foreign material.

Even though all the turbine blade cooling methods mentioned allow for higher turbine inlet temperatures, there are some detrimental effects that might result from turbine cooling. The negative effects for all the cooling techniques include:

1. Added cost of producing turbine blades.
2. Turbine blade reliability.
3. Loss of turbine work due to the cooling air bypassing one or more of the turbine stages.
4. Loss due to the cooling air being mixed with the hot mainstream gas.
5. Decrease in steam enthalpy when the cooling air is mixed with the hot mainstream gas.

Inevitably, there is a limit to the maximum amount of cooling air that can be supplied for turbine blade cooling, since the cooling air is extracted from the compressor outlet, where the pressure is a maximum.

1.4 INGESTION

A typical high pressure gas turbine stage is illustrated in Figure 1.11a, where the cooling air ensures the integrity and operating life of the nozzle guide vanes and turbine blades. As previously mentioned, the other important function of the secondary air flow is to reduce and prevent the ingestion of hot mainstream gas through the rim-seal (Figure 1.11b) at the vane and blade platforms. The reduction of ingestion is achieved by supplying a sealing flow (also referred to as purge flow) of pressurised air into the wheel-space or disc cavity between the rotor and stator discs. This sealing flow allows tolerable metal disc temperatures to be maintained, while any excessive flow leaves the wheel-space into the annulus through the rim-seal gap.

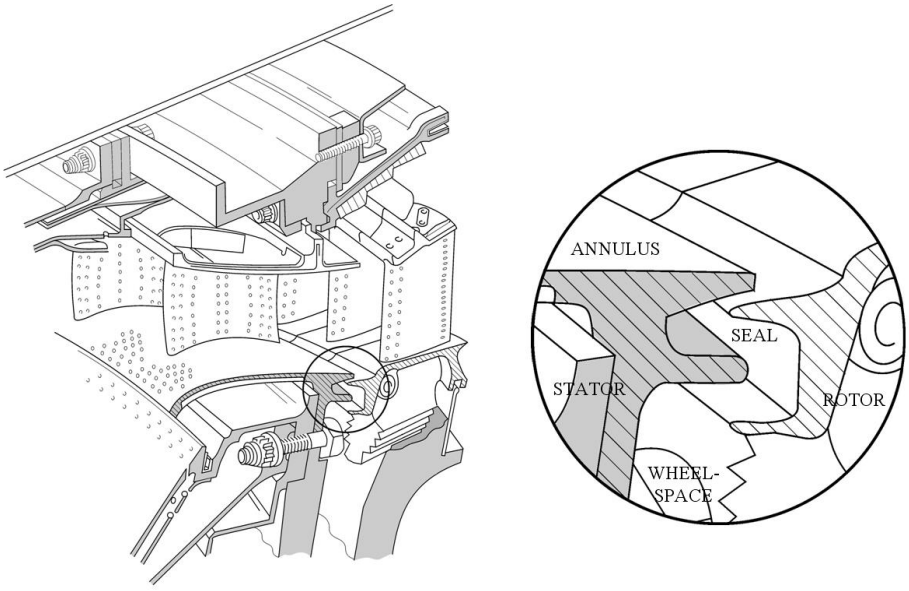

Figure 1.11 (a) Typical high pressure gas turbine stage; (b) rim-seal detail [6]

Designing and optimising the turbine stage for hot gas ingestion is an intricate job, since supplying excessive sealing flow reduces the engine efficiency, whilst supplying too little sealing flow can cause damage to the components in the turbine stage. The design of the rim-seal between the annulus and the wheel-space plays an important role in reducing and preventing ingress and egress.

Ingestion into the wheel-space of a turbine stage of an engine has been extensively researched at the University of Bath, and two different types of ingestion occurring in wheel-spaces have been identified. Firstly, the flow past the stationary vanes and rotating blades in the annulus causes an unsteady three-dimensional pressure variation

radially outward of the rim-seal, causing a non-axisymmetric type of ingestion, known as Externally-Induced ingress (EI ingress). Ingress and egress occur through parts of the seal clearance where the external pressure is higher and lower to that in the wheel-space, as shown in Figure 1.12.

The other type of ingestion is known as Rotationally-Induced ingress (RI ingress), which occurs when the rotating fluid in the wheel-space causes a radial pressure gradient which causes the pressure inside the wheel-space to be lower to that of the annulus. Egress occurs due to the so-called 'disc-pumping effect' near the rotating disc, whilst ingress occurs through the rim-seal due to the low pressure in the wheel-space.

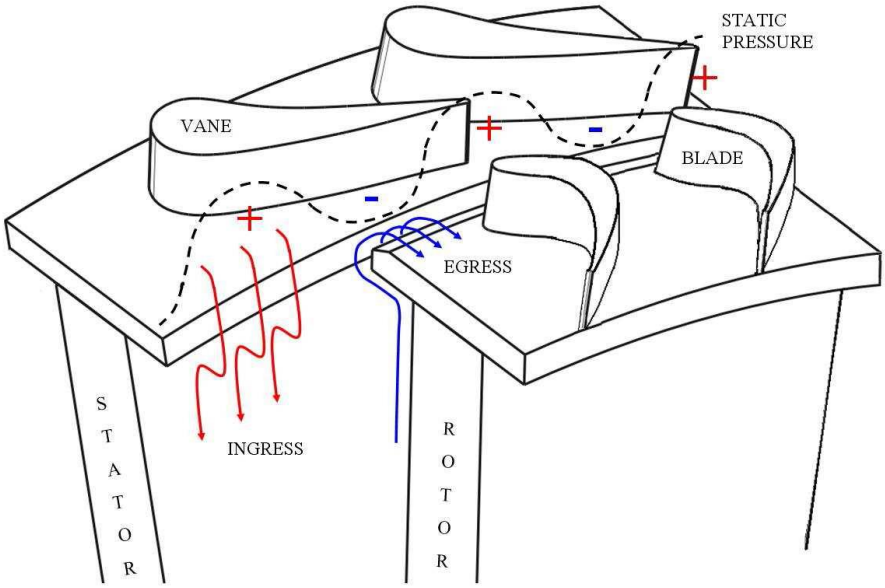

Figure 1.12 Pressure variation in turbine annulus [6]

The fluid dynamics and flow structure within the wheel-space of a turbine stage, will be discussed in increasing order of flow complexity as illustrated in Figure 1.13.

Figure 1.13a shows a simplified flow structure for a rotor-stator system without ingress. The wheel-space gap ratio is large enough to ensure separate boundary layers on the two discs, both starting at $r = a$. Both the inlet and the shroud have a clearance between the discs, with a superposed radial flow with swirl at $r = a$. The fluid moves radially outwards in the rotor boundary layer and inwards in the stator boundary layer. The total flow rate in both boundary layers must be equal to the superposed flow rate. The fluid moves axially from the stator boundary layer across the rotating inviscid core into the rotor boundary layer.

It should be noted that the entrainment by the rotor boundary layer decreases as the core swirl ratio increases. Also, there can be no axial gradients of the tangential and axial components of velocity in the core and the radial components must be zero, since all radial flow is confined to the boundary layers on the rotor and stator.

The superposed flow enters the rotating system via an inner region which ranges to $r = r_{in}$, where all the flow has been entrained by the rotor boundary layer. In the outer region, $r_{out} < r < b$, the fluid with an equal flow rate to that of the superposed flow, leaves the system through the rim-seal. The additional fluid entrained by the rotor boundary layer flows axially across the outer region into the stator boundary layer. The inner and outer regions are the sources for the flow in the rotor and stator boundary layers respectively.

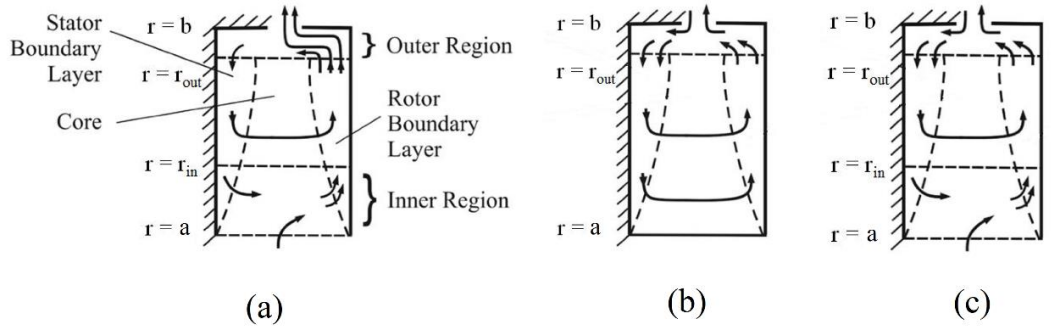

Figure 1.13 Simplified flow structure diagram for a rotor-stator system. (a) with superposed sealing flow and no ingress; (b) with ingress and no superposed sealing flow; (c) with superposed sealing flow and ingress [7]

Figure 1.13b shows the flow structure for the case where there is ingress but no superposed sealing flow; this case has similarities with Figure 1.13a though there is no inner region. The main difference occurs in the outer region, where the ingress and egress (of equal flow rates) mix; the swirl, concentration and temperature of the fluid in the outer region are determined by the conservation of mass, angular momentum and energy. This region is the source of the flow in the stator boundary layer, while outside the outer region, the flow rates in the rotor and stator boundary layers will be equal.

Figure 1.13c shows the flow structure for a case where there is a superposed radial flow with swirl, also with ingress through the rim-seal. The flow structure is a combination of those shown in Figure 1.13a and Figure 1.13b, where outside the inner and outer regions, the fluid leaves the stator boundary layer to be entrained into the rotor boundary layer through the core, thus concentration and temperature increase with radius.

It should be noted that if the fluid is fully mixed in the outer region, the concentration effectiveness and temperature of the fluid in the stator boundary layer, and the neighbouring core, will be invariant with radius. However the concentration and temperature of the rotor boundary layer increases with radius due to the axial migration of the flow through the core region. Also as the sealing flow rate is increased, the core region decreases in size and is pushed radially outwards.

While the sealing flow can reduce ingress, too much air reduces the engine efficiency and too little can cause overheating, resulting in damage to the turbine blade roots. Therefore the engine designer wants to know, in terms of the secondary airflow (internal air system), the most effective seal geometry and the amount of sealing air required to prevent ingestion. The designer also wants to know the amount of hot gas entering the wheel-space and the effects of the ingested fluid on the flow structure within the wheel-space.

1.5 AIM AND OBJECTIVES

The main aim of this research is to create a simple three dimensional steady-state computational model for predicting the flow structure within the wheel-space of gas turbines. The model is also capable of providing the sealing effectiveness for EI ingress in gas turbines. The 3D steady model is a simplified symmetrical 11.25° (1/32) sector model of a typical full 360° domain, which is computationally much more inexpensive than traditional 3D unsteady CFD codes run by companies such as Siemens. This provides engine designers with a quick, simple and economical design tool for predicting the effectiveness and fluid dynamics in the wheel-space for the different rim-seal geometries used in gas turbines engines.

The key objectives completed for this thesis are outlined below:

1. The experimental objective is to measure the sealing properties and flow structure in the wheel-space for a series of generic radial-clearance seals, which would inform and confirm the suppositions of the consequences for varying the radial overlap and clearance of a generic radial-clearance seal.
2. Two different axisymmetric rotor-stator models with no ingress are generated to understand the fundamental fluid-dynamic behaviour occurring within a rotor-

stator wheel-space. The effect of geometry is tested and validated against experimental data from the literature and a mathematical model produced at the University of Bath.

3. Two initial steady CFD models for predicting ingress are developed and validated against experimental data gathered at the University of Bath. The first model is a geometric alteration of the seal into a thin seal (baffle) model, which was later changed to the actual geometry, however with the rotor blade fixed at a relative position and computed with the "frozen rotor" method.
4. The finalised steady CFD model is established using the understanding gained from the previous models and recent literature on ingestion. The axial-clearance seal is firstly considered and the effects of mesh size/density and turbulence model are studied. The sealing effectiveness (on the stator and rotor), fluid dynamics and flow structure are inspected and shown to be in good agreement with the experimental results from the University of Bath.
5. Various other seal geometries have been computed and are presented in this thesis, such as the radial-clearance seal, and several of the double axial/radial seals. Similar analysis to the axial-clearance seal is presented for the other seal geometries and compared to experimental data, in terms of the sealing effectiveness and the flow structure in the wheel-space. Finally, the performance of the computed geometries is ranked in terms of sealing effectiveness.

1.6 THESIS OVERVIEW

Chapter 1 gives an introduction to the historical development of gas turbines and their impact and application in power generation. The concepts and issues of internal cooling in gas turbines is also discussed in this chapter, with the phenomenon of ingress stated and briefly introduced.

Chapter 2 presents a comprehensive literature review of research of rotor-stator systems and hot gas ingestion, discussing previous and current research in areas such as experimental, computational and theoretical modelling.

Chapter 3 describes the layout of the experimental gas turbine facility at the University of Bath. Experimental data for three radial-clearance seals are presented for a series of conditions for both the Externally-Induced and Rotationally-Induced ingestion

situations. The data is shown to agree well with the orifice model theory and highlights the benefits of using the parameters derived from the theoretical orifice model.

Chapter 4 describes the computational method used in this thesis and presents the turbulence model equations used in the CFD code. The various boundary and fluid settings applied to the CFD model are also described in this chapter, alongside with the mesh generation process. Finally, two axisymmetric rotor-stator models (different geometries) with no ingress are computed, discussing the fluid dynamics in the wheel-space and the effects of geometry. Results show good agreement to experimental data from the literature and calculated data from a mathematical model at the University of Bath.

Chapter 5 presents two preliminary axial-clearance seal models developed for predicting EI ingress, with modifications prompted by research carried out at partner institutions. Results are compared with experimental data measured at the University of Bath, with certain weaknesses identified.

Chapter 6 presents the final 3D steady CFD model which was the aim of this thesis. The model is comprised of the real geometry, however with the exclusion of the rotor blade. The axial-clearance seal CFD model is extensively validated against experimental data measured at the University of Bath. The sealing effectiveness, both on the stator and rotor, as well as the fluid dynamics of the annulus and wheel-space are discussed, also the effects of turbulence models and mesh size are considered. Good agreement with experimental data is found.

Chapter 7 presents computed results for the various other seal geometries considered in this study. The sealing effectiveness and fluid dynamics in the wheel-space are compared to experimental data, and the seal geometries are ranked in terms of sealing effectiveness performance.

Chapter 8 presents the main conclusions of this thesis and the possibility of future work.

1.7 PUBLICATIONS

This thesis has produced two main publications. The first was presented at the 2013 ASME Conference in San Antonio, Texas.

Sangan, C. M., Lalwani, Y., Owen, J. M., and Lock, G. D., 2013, "Experimental Measurements of Ingestion through Turbine Rim Seals. Part 5: Fluid Dynamics of Wheel-Space," *ASME Paper GT2013-94148*. [7]

This paper has been accepted for publication in the IMechE Journal for Power and Energy. The second publication, which is found from the results of chapters 6 and 7, has been submitted to the IMechE Journal of Power and Energy and is currently under peer review.

2 REVIEW OF PREVIOUS WORK

2.1 ROTATING DISC SYSTEMS

Rotating disc systems are important in a wide range of applications varying from hard disk drives, automotive disk brakes, flywheels, gear wheels, and most applicable to this research, the discs supporting the rotor blades in gas turbines. The power required to overcome the frictional drag which influences the heat transfer of the rotating systems, is dictated by the shear stresses between the disc and the fluid in which it is rotating.

Figure 2.1 illustrates some typical geometrical configurations which are of interest in disc flows. The most common configuration in engineering applications is that of the rotor-stator wheel-space, which is formed between a rotating disc and a stationary disc (i.e. Figure 2.1e - Figure 2.1j).

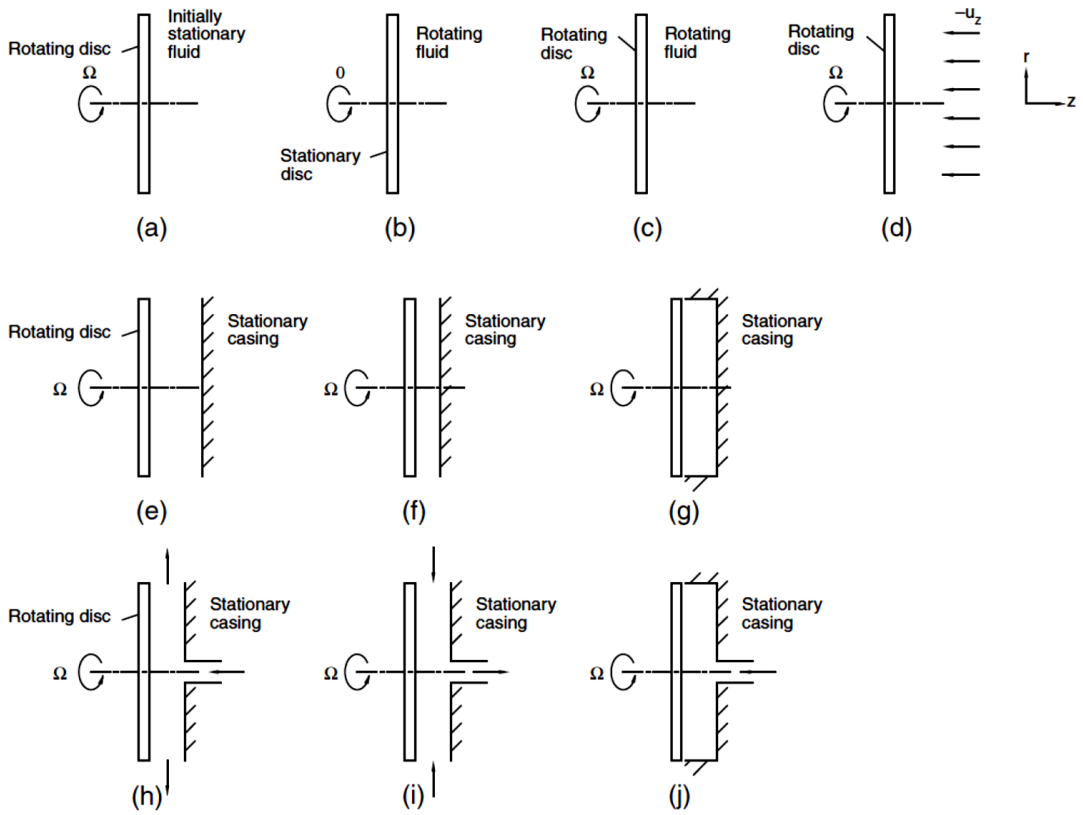

Figure 2.1 Selected disc flow configurations (a) The free disc. A rotating disc in an initially static flow. (b) Stationary disc in a rotating flow. (c) Rotating disc in a rotating flow. (d) Rotating disc with an impinging flow. (e) Rotor-stator disc wheel-space with a large gap. (f) Rotor-stator disc wheel-space with a narrow gap. (g) Enclosed rotor-stator disc wheel-space. (h) Rotor-stator disc wheel-space with radial outflow. (i) Rotor-stator disc wheel-space with radial inflow. (j) Rotor-stator disc wheel-space with stationary shroud and radial outflow. [8]

2.1.1 The Free Disc

Figure 2.1a shows a disc rotating at a constant angular velocity in an initially stationary fluid, which is commonly known as the 'free disc'. Analysing the free disc case, with a no-slip condition on the disc surface, a boundary layer is formed on the disc where the tangential velocity of the fluid is sheared from the disc speed (Ωr) to zero tangential velocity outside the boundary layer. The shear between the rotating disc and the fluid creates centrifugal forces which cause a radial outflow of the fluid in the boundary layer, commonly known as the 'free-disc pumping effect'. The radial velocity is zero at both the disc surface and outside the boundary layer, thus to satisfy the conservation of mass and enable the radial outflow, fluid is entrained axially into the boundary layer. The radial and tangential boundary layers for the free disc case are shown in Figure 2.2.

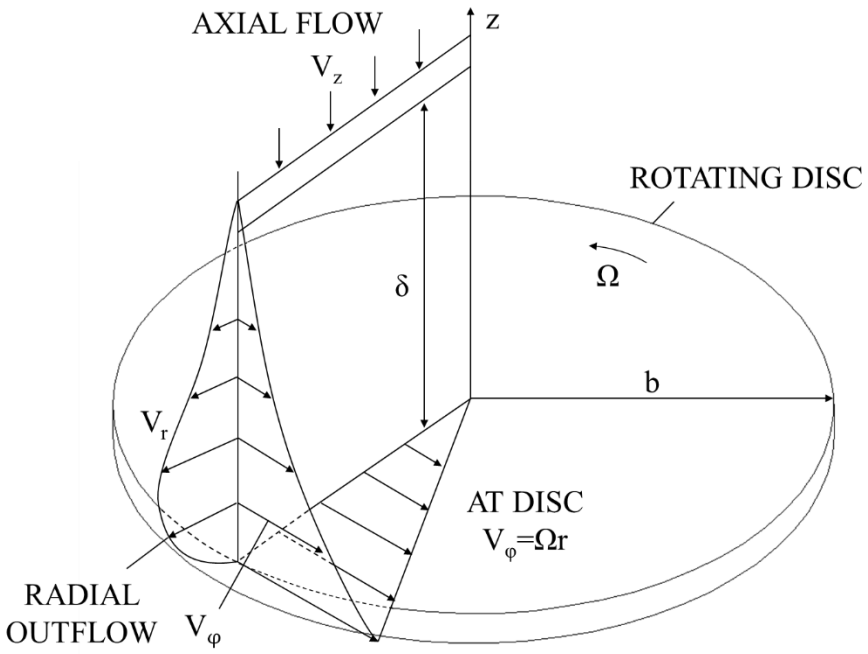

Figure 2.2 Radial and tangential boundary layers and associated inflow and outflow induced by a rotating disc. Adapted from [8]

2.1.2 Rotating Fluid over a Stationary Disc

Figure 2.1b shows a stationary disc with a rotating fluid, which is a typical behaviour of a stator disc within a gas turbine wheel-space. The fluid in the boundary layer near the stationary surface has less centrifugal force than the rotating fluid, causing the fluid to flow radially inwards. Therefore to satisfy the conservation of angular momentum of the inward flow, the tangential velocity has to be slightly higher than the free stream rotational speed, while the fluid flows axially away from the surface. The radial and tangential boundary layers of a rotating fluid over a stationary disc are shown in Figure 2.3.

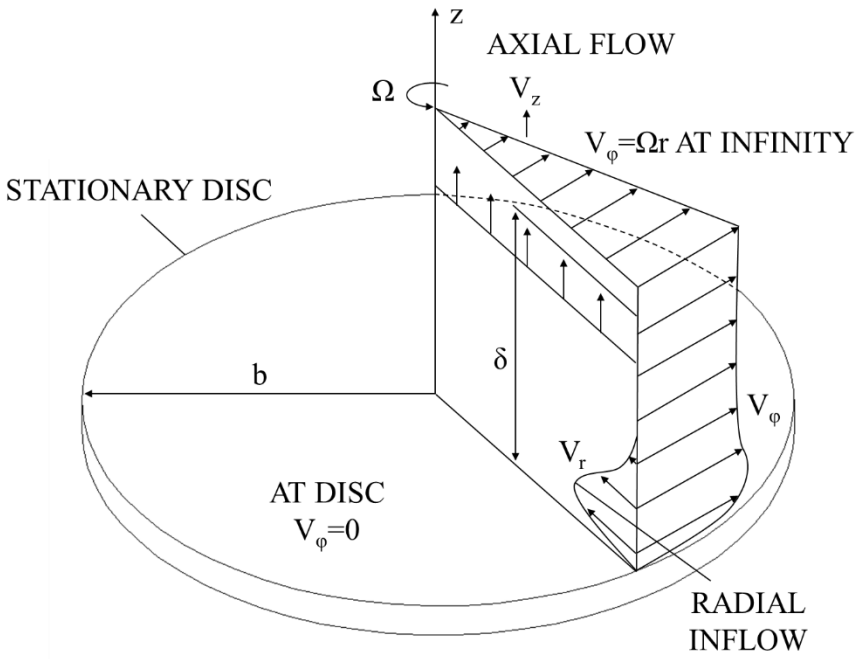

Figure 2.3 Radial and tangential boundary layers and associated inflow and outflow induced by a rotating fluid adjacent to a stationary disc. Adapted from [8]

2.2 ROTOR-STATOR SYSTEMS

A rotor-stator system is comprised of a coaxial rotating and stationary disc, which form a rotor-stator cavity or wheel-space. The gap between the discs, the flow conditions in the boundaries, and the purge flow supplied to the wheel-space all have a significant influence on the fluid dynamics within the wheel-space.

Prior to the large amount of experimental data and numerical solutions available, several theories were developed for the flow structure within a rotor-stator wheel-space. Batchelor [9] suggested that there is a core of fluid between the rotating and stationary discs, which rotates at an angular velocity with a value between that of the rotor and stator. This theory implied the existence of separate boundary layers on both the rotor and stator. Thus, in order to supply the rotor boundary layer, fluid had to be entrained from the core and pumped radially outward on the rotor. While on the stator, the fluid flows radially inwards and axially away from the stator boundary layer into the core.

However, Stewartson [10] proposed that the flow is more like that of the 'free disc', where the tangential velocity in the rotor boundary layer reduces from the rotor speed to zero outside the boundary layer with no core rotation. It is known as the Batchelor-Stewartson controversy, with characteristic velocity profiles for the two theories shown in Figure 2.4.

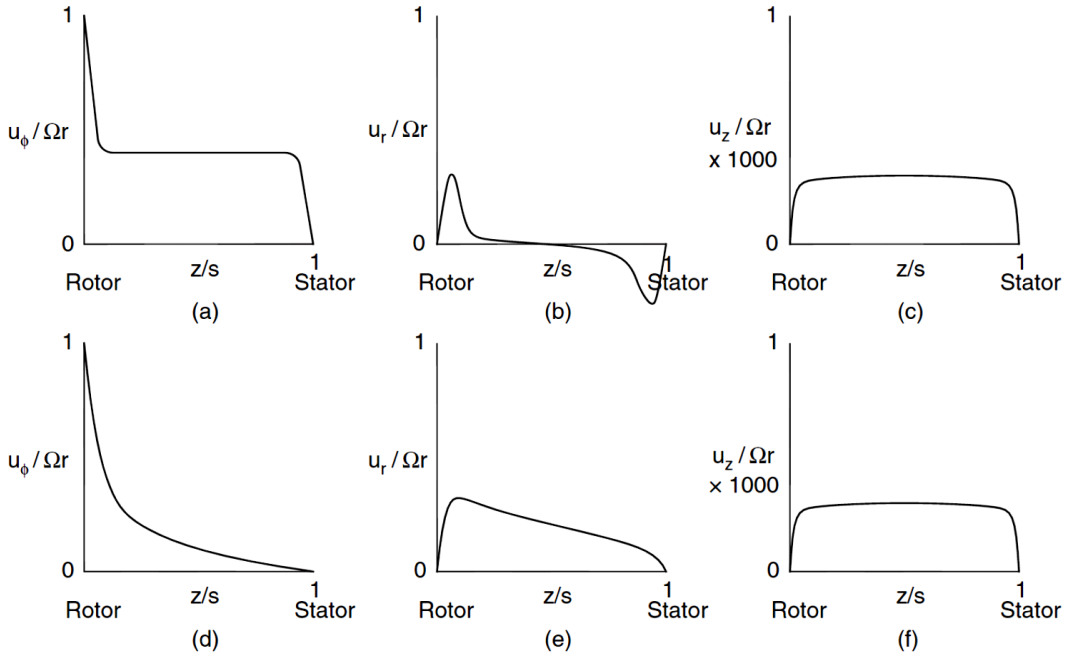

Figure 2.4 Characteristic velocity profiles in a rotor-stator wheel-space: (a) to (c) Batchelor flow; (d) to (f) Stewartson flow. [8]

The flow characteristics in a rotor-stator system are also dependent on the nature of the flow, meaning whether it is laminar or turbulent. Daily and Nece [11] performed experimental measurements for an enclosed rotor-stator wheel-space, allowing them to identify four flow regimes and categorising them as a function of gap ratio, *G*, and rotational Reynolds number, Re_ϕ, depicted in Figure 2.5. The four flow regimes identified are:

- Regime 1: laminar flow, small clearance, merged boundary layers
- Regime 2: laminar flow, large clearance, separate boundary layers
- Regime 3: turbulent flow, small clearance, merged boundary layers
- Regime 4: turbulent flow, large clearance, separate boundary layers

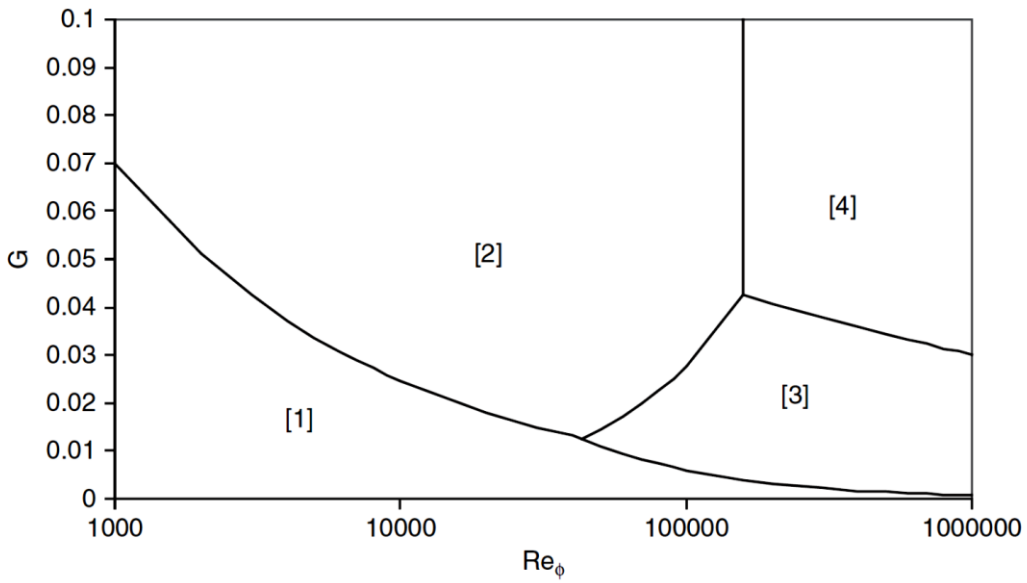

Figure 2.5 Regimes of flow for an enclosed rotor-stator wheel-space. [1] Laminar flow and small clearance; [2] Laminar flow and large clearance; [3] Turbulent flow and small clearance; [4] Turbulent flow and large clearance. [11]

Chen *et al.* [12] experimentally investigated a rotor-stator system which was represented by a wheel-space enclosed by a rotor disc and stator disc in a turbine stage. Laser Doppler Anemometry (LDA) was used to measure the circumferential and radial velocities at various radial locations in the wheel-space. The flow structure observed in this setup was similar to that described by Batchelor, with radial outflow on the rotor and radial inflow on the stator, and a rotating inviscid core between both boundary layers. Chen *et al.*'s experiments also showed that by increasing the superposed flow, the core swirl ratio is reduced.

2.2.1 Non-Dimensional Variables

This section defines a set of non-dimensional fluid dynamic variables which are commonly used in the study of rotor-stator systems, and have a significant influence in the flow structure within a rotor-stator wheel-space.

Rotational Reynolds number, $Re_\phi = \frac{\rho \Omega b^2}{\mu}$ *Equation (2.1)*

Non-dimensional flow rate, $C_w = \frac{\dot{m}}{\mu b}$ *Equation (2.2)*

Turbulent flow parameter, $\lambda_T = \frac{C_w}{Re_\phi^{0.8}}$ *Equation (2.3)*

Swirl ratio, $\beta = \frac{V_\phi}{\Omega r}$ *Equation (2.4)*

where b is the radius of the seal, ρ is the density, μ is the dynamic viscosity and $\dot{m}$ is the mass flow rate of the fluid.

In addition, the Reynolds number of the axial flow in the turbine annulus, Re_W, will influence the amount of ingress.

Axial Reynolds number, $Re_W = \frac{\rho W b}{\mu}$ *Equation (2.5)*

where W is the axial velocity of the fluid in the annulus.

2.3 INGESTION

Bayley and Owen [13] carried out ingestion experiments on a simple rotor-stator system with an axial-clearance rim-seal without an external annulus. The rotating flow in the system created a sub-atmospheric pressure inside the wheel-space which caused external air to be drawn into the wheel-space, however by increasing the sealing flow rate, the pressure inside the wheel-space increased and in turn reduced the amount of ingested air. At high sealing flow rates, where $C_{w,o} \geq C_{w,min}$, ingestion was not experienced.

Using a fluid-dynamic model where the seal-clearance was treated as an orifice, Bayley and Owen showed that $C_{w,min}$ was proportional to Re_ϕ and G_c, providing the following correlation known as the *Bayley-Owen criterion for RI ingress*:

$$C_{w,min} = 0.61 G_c Re_\phi \qquad \textit{Equation (2.6)}$$

Phadke and Owen [14-17] broadened the research on RI ingress by using flow visualization, concentration and pressure measurements for seven different rim-seal geometries and various seal-clearances to determine $C_{w,min}$. They proved that radial-clearance seals are more effective than axial-clearance seals.

Graber *et al.* [18] presented extensive concentration measurements for a rotating-disc rig. The measurements were used to determine the effects of the rim-seal geometry, rotational Reynolds number, Re_ϕ, and the swirl level in the annulus on the sealing effectiveness. The measurements revealed that the swirl level in the external annulus had no effect on the sealing effectiveness.

Abe *et al.* [19] was the first to show that ingestion is dominated by the external annular flow rather than the rotational disk speed, using a turbine rig with vanes located upstream of the rim-seal in the annulus. Various rim-seal geometries were tested and three parameters which affected ingress were identified:

- The ratio of the velocities of the sealing air and the annulus flow
- The rim-seal clearance
- The shape of the rim-seal

Phadke and Owen [14-16] determined the minimum sealing flow rate required to prevent ingress, $C_{w,min}$, in a simple rotor-stator system by considering different scenarios, such as different rim-seal geometries, with and without external air flow in the annulus. The stator-rotor system used by Phadke and Owen did not have vanes or blades in the annulus, instead wire mesh was used to block sections in the annulus to create the circumferential pressure asymmetries. Both RI and EI ingress were observed by Phadke and Owen, where $C_{w,min}$ increases with increasing Re_ϕ for RI ingress, and $C_{w,min}$ is independent of Re_ϕ and increases with Re_w for EI ingress.

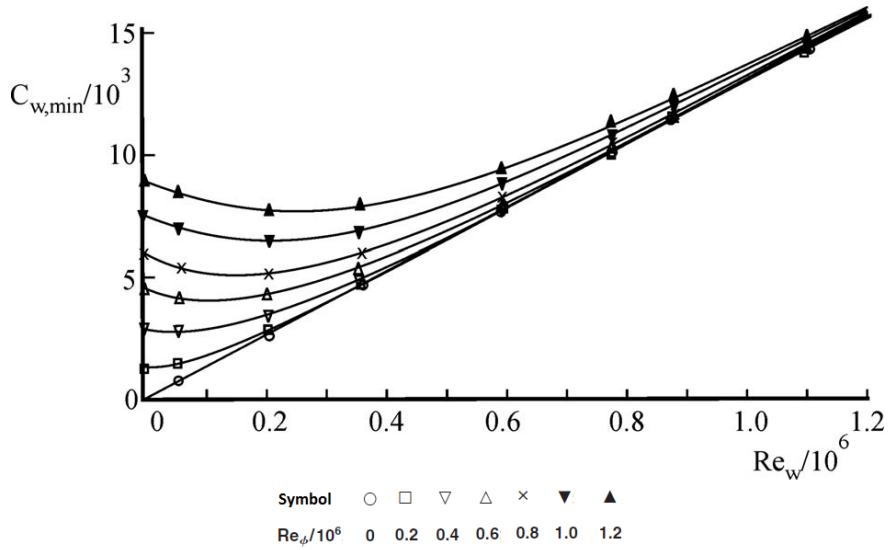

Figure 2.6: Variation of $C_{w,min}$ with Re_w for axial-clearance seal [16]

Figure 2.6 shows that when $Re_w = 0$ (RI ingress), $C_{w,min}$ is proportional to Re_ϕ; however for large values of Re_w (EI ingress), $C_{w,min}$ is proportional to Re_w. Phadke and Owen [16] correlated the results for EI ingress for a number of different seal geometries, which is expressed through the following empirical relationship:

$$C_{w,min} = 2\pi K G_c P_{max}^{1/2} \qquad \textit{Equation (2.7)}$$

where,

$$P_{max} = \frac{1}{2} C_{p,max} Re_w^2 \qquad \textit{Equation (2.8)}$$

Here $C_{p,max}$ is the non-dimensional pressure difference in the external annulus, and K is an empirical constant. The data shown in Figure 2.7 was correlated using $K = 0.6$. Hamabe and Ishida [20] performed measurements of the sealing effectiveness in a turbine rig fitted with upstream vanes but with no downstream blades; they correlated their data and obtained a similar empirical relationship to that of Phadke and Owen [16]. Hamabe and Ishida also showed that the discharge coefficient for egress, $C_{d,e}$, decreases as the external flow rate increases.

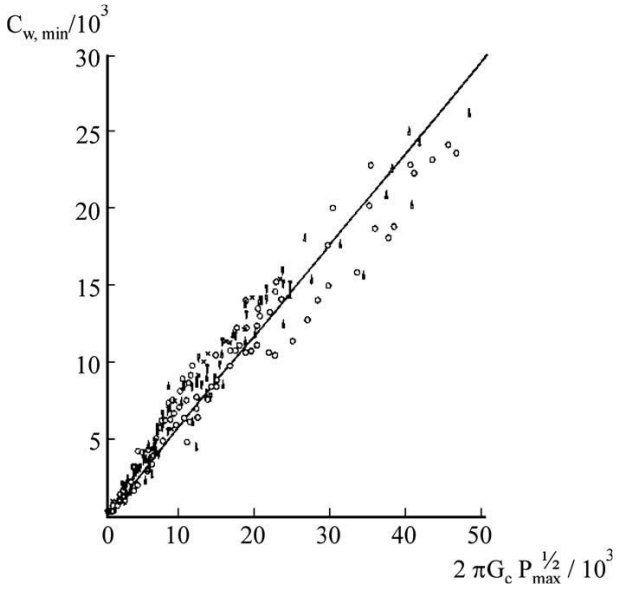

Figure 2.7: Variation of $C_{w,min}$ with P_{max} [16]

Chew *et al.* [21] performed effectiveness measurements in a rig with upstream vanes in the annulus. Measurements of the discharge coefficients for the rim-seal were carried out when the disc was not rotating. Similar to Hamabe and Ishida, the measurements from Chew *et al.* also showed that $C_{d,e}$ decreases with increasing external flow rate.

Green and Turner [21] were the first to publish data for a turbine rig with both vanes and blades. They found that at low sealing flow rates, the addition of rotating blades reduced ingress, compared to the case where only vanes were used.

The Aachen group [22-26] have carried out many ingress studies in turbine rigs with vanes and blades. The most relevant paper by Bohn and Wolff [23], presents a correlation for four rim-seal geometries in terms of $C_{w,0}$, G_c and $C_{p,max}$, and is shown in Figure 2.8. The figure shows a linear variation of $C_{w,min}$ with ${C_{p,max}}^{1/2}$, similar to the correlation found by Phadke and Owen [14-16]; however, Bohn and Wolff [23] found a different K value to the one found by Phadke and Owen for the axial-clearance seal. Bohn and Wolff suggested that $K = 0.6$ provides a conservative estimate for $C_{w,min}$.

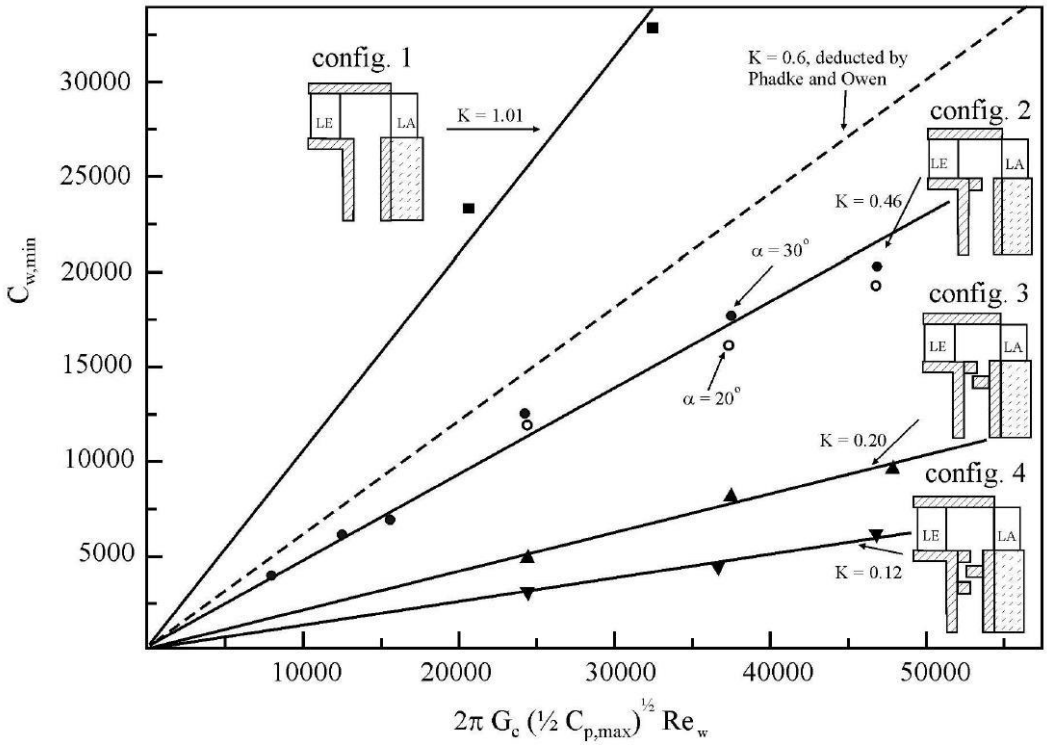

Figure 2.8: Variation of $C_{w,min}$ with $C_{p,max}$ [23]

The research group at Arizona State University and their associated research institutes have significantly contributed to the research of hot gas ingestion. Roy *et al.* [27] performed experiments in a single-stage axial-flow turbine model using two vane-blade configurations, where the difference between the two configurations was the vane turning angle. Recorded measurements included the unsteady time-averaged static pressure distributions and wheel-space distributions of time-average ingestion. The measurements suggested that the pressure field in the annulus is fundamental for EI ingress. The parameters controlled in the experiments, which are believed to influence the unsteady 3D pressure field, were the mainstream flow rate, the sealing flow rate and the rotor speed.

Roy *et al.* [28] carried out experiments in a single-stage turbine featuring vanes, blades and an axially overlapping radial-clearance rim-seal. Time-resolved velocity maps of the flow in the wheel-space, obtained by particle image velocimetry (PIV), are shown in Figure 2.9 for two sealing flow rates. The experiment showed that when the sealing flow rate is low, the ingested fluid entered the wheel-space with high tangential velocity from the mainstream annulus (seen as the red and yellow regions). Whereas at high sealing flow rate, the tangential velocity is low throughout the wheel-space,

meaning there is no ingestion, and large-scale unsteady structures with fluctuating velocities appear in the wheel-space; while the egress flow transports low tangential velocity fluid from the wheel-space to the annulus.

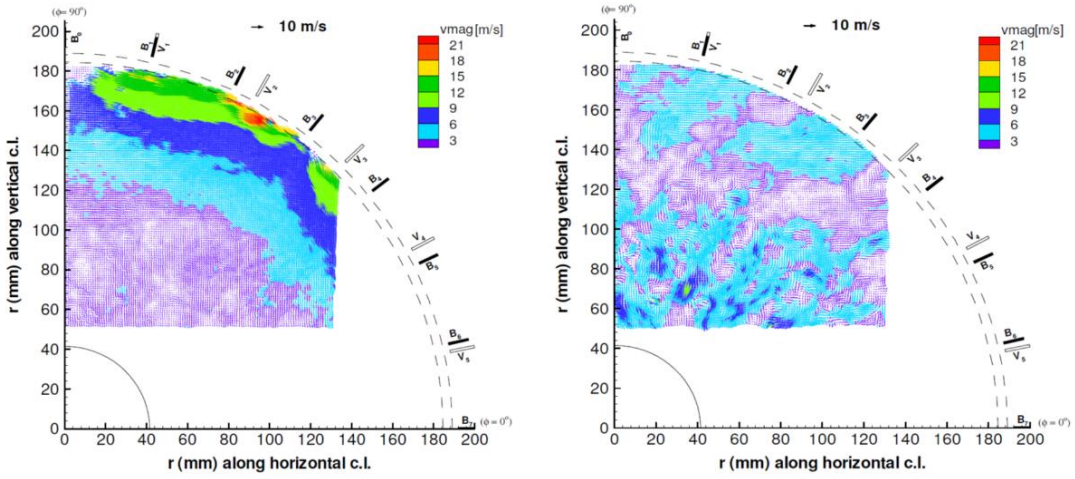

(a) (b)

Figure 2.9 Measured instantaneous velocity vector map (r-φ plane) in the disk cavity. (a) $Re_w = 9.27 \times 10^4$, $Re_\phi = 4.63 \times 10^5$, $C_w = 1574$; (b) $Re_w = 1.12 \times 10^5$, $Re_\phi = 5.86 \times 10^5$, $C_w = 8656$ [28]

Zhou *et al.* [29] performed similar experimental measurements on the single-stage turbine described above for Roy *et al.* [28], however the investigation was carried out for three wheel-space configurations differing in their aspect ratios (height / width), while maintaining the same rim-seal geometry. They were also able to identify regions of ingress and egress close to the rim-seal through their PIV images at low sealing flow rates. Their effectiveness measurements revealed that as the wheel-space aspect ratio reduces, ingestion decreased and in turn the sealing effectiveness increased.

Gentilhomme *et al.* [30] performed concentration and pressure measurements in the wheel-space of a single-stage turbine. The pressure measurements revealed that at low sealing flow rates, the high swirling ingested fluid from the annulus increased the swirl level within the wheel-space.

Recently, the Bath research group [6, 7, 31-33] has carried out many ingress studies which experimentally modelled hot gas ingestion into the wheel-space of an axial turbine stage. The performance of various generic (engine representative) rim-seal geometries were assessed in terms of concentration effectiveness by measuring the carbon dioxide (CO_2) gas concentration in the rim-seal region inside the wheel-space. The Bath group presented the experimental data with respect to the non-dimensional

sealing parameter Φ_0 (defined in Equation (2.9)), which combines different terms ($C_{w,0}$, G_c and Re_ϕ) into a single parameter, as shown in Figure 2.10.

Further details on the derivation of the non-dimensional sealing parameter, Φ_0, can be found in section 2.5.2.

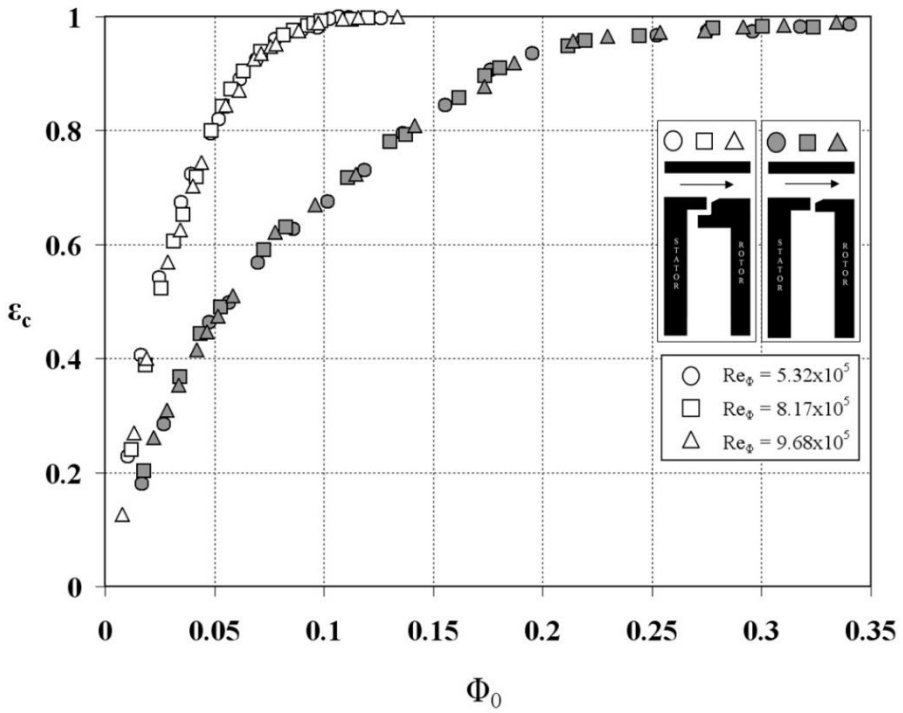

Figure 2.10: Measured variation of sealing effectiveness with Φ_0 for EI ingress for generic radial and axial clearance seals [6]

2.4 COMPUTATIONAL FLUID DYNAMICS

Roy *et al.* [28] performed 3D unsteady CFD simulations for a single-stage axial turbine with similar geometry to their experimental rig, which includes vanes, blades and an axially overlapping radial-clearance seal. The computed model consisted of a sector which included one vane and one blade, along with the rim-seal and the wheel-space. Figure 2.11 shows the velocity vectors in the axial-radial plane, which show the ingestion process from the main gas path, to the seal region, through the seal gap, and down the stator wall. The formation of a recirculation region can be seen downstream of the vane platform, while another recirculation region exists besides the rotor side of the rim-seal. The additional velocity contours exposed that the axial and tangential velocity components are greater for ingress than for egress, which is consistent with their experimental measurements.

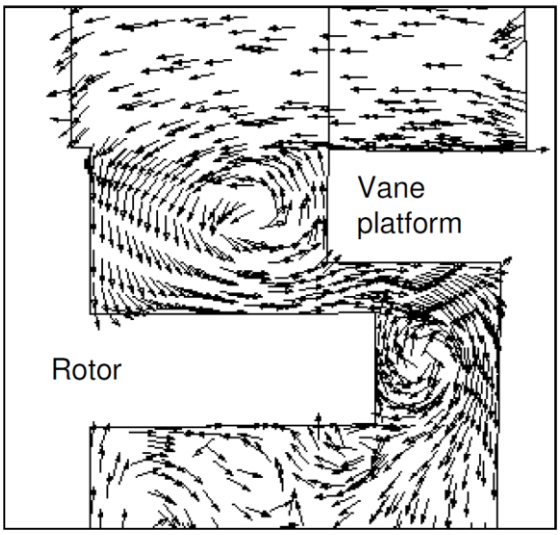

Figure 2.11 CFD velocity vectors in r-x plane of seal region [28]

Zhou *et al.* [29] performed 3D unsteady CFD computations for a 14.4° sector model corresponding to a similar rig geometry to their experimental setup. The computed results under-predicted ingestion into the wheel-space compared to their experimental results. One possible reason for this under-prediction was that the sector model cannot capture the circumferential rotating low-pressure zones predicted in the wheel-spaces by the full 360° CFD simulations, which are thought to increase ingestion.

Dunn *et al.* [34] performed an extensive computational study of the flow in a single-stage gas turbine model. The computational model is that of a 1/14 sector of the experimental rig, consisting of four rotor blades and four stator vanes. The effects of two turbulence models were considered, as well as considering a steady frozen rotor approach and a time-dependent unsteady approach. The solutions showed good agreement with experimental measurements.

Gentilhomme *et al.* [30] performed a CFD study of the annulus flow which showed reasonable agreement with the experimental pressure measurements. They also found that the pressure asymmetry at the rim-seal created by the nozzle guide vanes (NGVs) is only slightly affected by the presence of the rotor blades. On the other hand, the pressure asymmetry due to the rotor is highly influenced by the NGVs.

Lewis and Wilson [35] performed a computational study of a simplified gas-turbine rotor-stator wheel-space with an axial-clearance rim-seal, the mainstream annulus included a stator vane which created the non-axisymmetric flow conditions. The study

was performed to investigate the effects of the axial spacing between the vane trailing edge and the rim-seal. The computed results exposed that the circumferential variation of C_p, decreases with increasing distance from the vane trailing edge.

Mirzamoghadam *et al.* [36, 37] performed 3D CFD computations for a full-stage high pressure turbine disc cavity. Through their computed results, they found that the asymmetrical pressure in the annulus can cause ingress even at high levels of sealing flow rates. Their studies also showed that the stator wake has a greater influence on ingress that the rotor blade bow wave.

Three-dimensional unsteady CFD simulations were carried out by Zhou *et al.* [38] for a simple axial-clearance seal, comprised of one stator vane and rotor blade. The model employed a scalar equation to represent the seeded tracer gas used in experiments at the University of Bath [6], to determine the sealing effectiveness of the model. Zhou *et al.* [38] confirmed, via unsteady computations, that the magnitude of the peak-to-trough pressure difference in the annulus is the principal driving mechanism for ingestion into the wheel-space.

The pressure difference mentioned above is used in an orifice model [39, 40] (discussed in section 2.5) to predict the sealing effectiveness; however, the magnitude of the pressure difference depends on the locations chosen in the annulus and wheel-space (Figure 2.12). Zhou *et al.* [38] used the CFD model to investigate the relevance of the chosen locations for the evaluation of the pressure difference. They also investigated the relationship between the time-dependent unsteady simulations and steady computations which do not contain a blade, where they found that the use of the blade increased the pressure asymmetry in the annulus. Although the magnitude of the pressure distribution in the annulus predicted for both the unsteady and steady models were similar, the sealing effectiveness for the steady model was over-predicted.

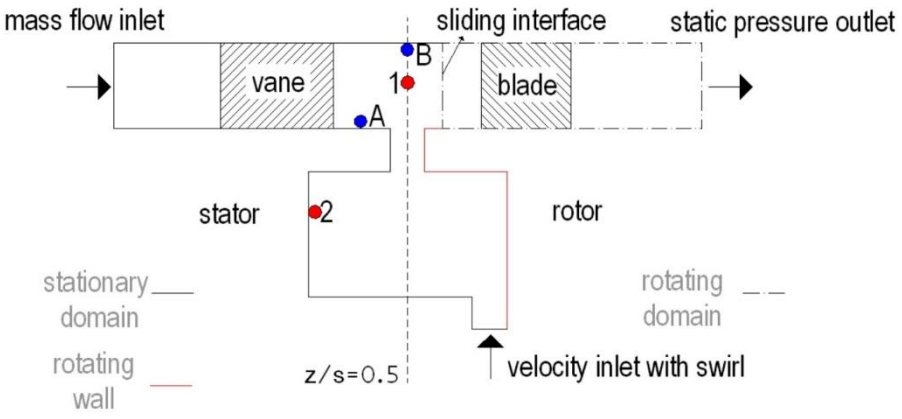

Figure 2.12: Geometrical model of axial-clearance seal and relevant locations for evaluation of pressure distribution in annulus [38]

Consequently, Zhou *et al.* [38] used a "thin seal" geometric approximation for the steady model, which predicted similar effectiveness results as the unsteady model. The "thin seal" approach made the rim-seal, as thin as permissible by the meshing program. This approximation was employed, to relax the formation of an unrealistic vortex inside the seal-clearance, allowing accurate results to be obtained much more economically compared to the unsteady model.

Rabs *et al.* [41] investigated simplifications to the CFD model of gas turbine rim-seal cavities, focusing on hot gas ingestion. Several studies were carried out, such as adjusting the vane-to-blade pitch ratio in the CFD model to accurately match the experiment, which provided a slight improvement over the smaller sector models. Another study was a comparison between steady state and unsteady models, using several blade positions in the steady-state computations (Figure 2.13). It was identified that the worst case position, which gave the least ingestion, occurred when the blade and vane were in close proximity. This study presented an alternative to the traditional time-intensive unsteady simulations, where the relative position of the blade, which contributes to the greatest ingestion levels, can be utilized to carry out successful steady-state computations.

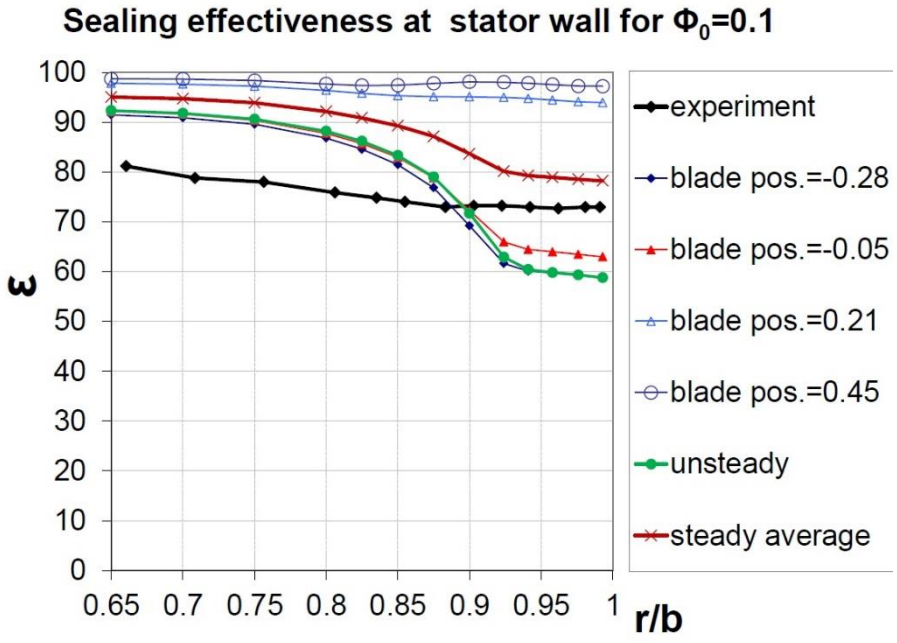

Figure 2.13: Comparison between steady state (different blade positions) and unsteady simulations [41]

Jakoby *et al.* [42] carried out unsteady simulations and identified energetic large-scale flow structures which perturbed the pressure in the wheel-space at low sealing flow rates and increased ingestion levels. Increasing the sealing flow rate was found to dissipate these large-scale flow structures; these findings have been supported by recent unsteady computations by Julien *et al.* [43] and Dunn *et al.* [34].

Laskowski *et al.* [44] performed steady and unsteady computations for ingestion. Their computed results showed a difference in the contours of effectiveness between both approaches. The steady results showed no ingestion for any of the circumferential planes in the wheel-space, whereas the time-averaged unsteady results experienced ingestion in the rim-seal and wheel-space for all circumferential planes.

An alternative study involving Unsteady Reynolds-Averaged Navier-Stokes (URANS) computations and Large Eddy Simulations (LES) on rim-seal ingress was carried out by O'Mahoney *et al.* [45]. The results of both computational results were compared to experimental data, and it was found that LES results gave better sealing effectiveness prediction, however at the expense of much larger computational cost.

Teuber *et al.* [46] carried out URANS computations on two-different rim-seal geometries based on the experimental rig at the University of Bath. Two different pitch ratio models were investigated, a 1:1 sector model (corresponding to 32 vanes and 32

blades), and a 4:5 model (corresponding to 32 vanes and 40 blades), which more closely represents the pitch variation in the experimental rig. The two models computed a virtually similar peak-to-trough pressure distribution in the annulus (ΔC_p); which is known to be the driving mechanism of ingestion, establishing that a sector model (1/32) is capable of simulating proper annulus pressure behaviour at incompressible flow regimes, whilst keeping computational cost down. They were also able to reproduce swirl ratios and sealing effectiveness distributions in the wheel-space over a range of sealing flow rates for both an axial and radial-clearance seal.

2.5 THEORETICAL RESEARCH AT THE UNIVERSITY OF BATH

2.5.1 Orifice Model for EI Ingress

The orifice model [39, 40] developed recently has proven successful in calculating the sealing effectiveness of rim-seal for EI and RI ingress. The models assume the seal clearance to be an orifice and use adaptations of Bernoulli's equation to correlate the sealing flow rate to the pressure drop across the seal-clearance; this is done by including properties of rotating flows into the equation such as swirl terms.

The orifice model equations are derived for inviscid incompressible flow. Losses are introduced through the use of two different discharge coefficients for ingress and egress, respectively denoted as $C_{d,i}$ and $C_{d,e}$. These discharge coefficients must be determined empirically.

The magnitude of the peak-to-trough circumferential difference in pressure in the annulus (see Figure 1.12) dominates EI ingress, and the pressure distribution profile is of lesser importance for the ingress calculation. A simple equation which represents the sealing effectiveness, ε, in terms of the non-dimensional sealing flow parameter, Φ_o, is given by the orifice model.

The aforementioned discharge coefficients ($C_{d,i}$ and $C_{d,e}$) are the only two empirical parameters associating the orifice model with the experimentally measured values of ε and Φ_o. The model has the additional benefit of providing an estimate of the minimum sealing flow rate to prevent ingress, $\Phi_{min,EI}$; this estimate is determined from the (ε, Φ_o) data points. The capability of providing $\Phi_{min,EI}$ without any knowledge of the

pressure distribution in the annulus or the associated discharge coefficients makes the orifice model a powerful tool for rim-seal design.

The principal solutions to the equations of the orifice model for EI ingress are given below; further details on the orifice model solutions for RI ingress, will be covered on section 2.5.4.

2.5.2 Non-Dimensional Sealing Flow Parameter

The non-dimensional sealing flow parameter is defined as:

$$\Phi_o = \frac{C_{w,o}}{2\pi G_c Re_\phi} \qquad \textit{Equation (2.9)}$$

The above parameter, Φ_o, is an inertial parameter, as both Re_ϕ and $C_{w,o}$ include viscous terms which cancel in the above equation. Hence the use of a more appropriate equation equivalent to Equation (2.9) :

$$\Phi_o = \frac{U}{\Omega b} \qquad \textit{Equation (2.10)}$$

U is the bulk mean radial velocity of sealing air through the seal clearance, such that:

$$U = \frac{\dot{m}}{2\pi\rho b s_c} \qquad \textit{Equation (2.11)}$$

The non-dimensional sealing flow parameters for egress, ingress and sealing flow are represented respectively with the following subscripts: *e*, *i* and *o*. When the system is sealed, $C_{w,o} = C_{w,min}$, then $\Phi_o = \Phi_{min}$. Such that:

$$\Phi_{min} = \frac{U_{min}}{\Omega b} = \frac{C_{w,min}}{2\pi G_c Re_\phi} \qquad \textit{Equation (2.12)}$$

From the continuity equation:

$$\Phi_o = \Phi_e - \Phi_i \qquad \textit{Equation (2.13)}$$

The sealing effectiveness can be calculated from Equation (2.14), when $\Phi_o < \Phi_{min}$:

$$\varepsilon = 1 - \frac{\Phi_i}{\Phi_e} = \frac{\Phi_o}{\Phi_e} = \frac{\Phi_o}{\Phi_o + \Phi_i} \qquad \textit{Equation (2.14)}$$

Thus, when $\Phi_o = 0$ then $\varepsilon = 0$, and when $\Phi_o = \Phi_{min}$ then $\varepsilon = 1$.

Effectiveness is a convenient parameter, however the rim-seal designer needs to know the amount of hot gas being ingested into the wheel-space when $\Phi_o < \Phi_{min}$, which involves calculating Φ_i from Equation (2.14), hence:

$$\frac{\Phi_i}{\Phi_o} = \varepsilon^{-1} - 1 \qquad \textit{Equation (2.15)}$$

The ratio of the discharge coefficients, Γ_c, is another important parameter in the orifice model, and it is defined as:

$$\Gamma_c = \frac{C_{d,i}}{C_{d,e}} \qquad \textit{Equation (2.16)}$$

As previously mentioned, it should be noted that $C_{d,i}$ and $C_{d,e}$ are empirical constants. It was also mentioned that EI ingress is governed by the non-dimensional pressure difference ΔC_p, which is defined as:

$$\Delta C_p = \frac{\Delta p}{1/2\,\rho\Omega^2 b^2} \qquad \textit{Equation (2.17)}$$

Δp is the time-average peak-to-trough static pressure difference in the annulus.

2.5.2.1 Wheel-space Parameters

The swirl ratio of the fluid in the inviscid core between the boundary layers in the wheel-space is previously defined in Equation (2.4). Here V_ϕ is the tangential component of velocity in the core. In a rotating inviscid fluid (rotating core) the radial component of velocity must be zero and the axial gradients of the axial and tangential components of velocity must also be zero. All radial flow occurs inside the boundary layers, and the swirl (β) value adjusts to satisfy the continuity of the flow rates in the boundary layers.

The swirl ratio also controls the radial distribution of static pressure p in the wheel-space, and the pressure coefficient is defined as:

$$C_p = \frac{p - p_{ref}}{1/2\,\rho\Omega^2 b^2} \qquad \textit{Equation (2.18)}$$

where p_{ref} is a convenient reference pressure.

The flow structure in the wheel-space is dominated by the turbulent flow parameter, λ_T, previously defined in Equation (2.3). Note that for the free disc case, where there is

no stator, the entrained flow rate is characterized by $\lambda_{T,fd} \approx 0.22$. Following from Equation (2.3) and Equation (2.9):

$$\lambda_T = 2\pi G_c Re_\phi^{0.2} \Phi_o \qquad \textit{Equation (2.19)}$$

2.5.3 Orifice Model Solutions for EI Ingress – Effectiveness Equations

The circumferential pressure distribution in the annulus can be approximated using the 'saw-tooth model', hence allowing the orifice equations to be solved analytically, such that:

$$\Phi_{min,EI} = 2/3\, C_{d,e} \Delta C_p^{1/2} \qquad \textit{Equation (2.20)}$$

The constant K is expressed in terms of $\Phi_{min,EI}$ and ΔC_p:

$$\Phi_{min,EI} = \frac{C_{w,min,EI}}{2\pi G_c Re_\phi} = K\sqrt{\frac{\Delta C_p}{2}} \qquad \textit{Equation (2.21)}$$

The two aforementioned empirical constants from the orifice equations, $C_{d,i}$ and $C_{d,e}$, are replaced with two unknown parameters, $\Phi_{min,EI}$ and Γ_c, creating effectiveness equations in a convenient, explicit form, such that for $\Phi_o < \Phi_{min,EI}$:

$$\frac{\Phi_o}{\Phi_{min,EI}} = \frac{\varepsilon}{\left[1 + \Gamma_c^{-2/3}(1-\varepsilon)^{2/3}\right]^{3/2}} \qquad \textit{Equation (2.22)}$$

When $\Phi_o > \Phi_{min,EI}$, $\varepsilon = 1$. The two unknown parameters, $\Phi_{min,EI}$ and Γ_c are estimated using a statistical model that fits the experimental data.

The parameter $\Phi_{min,EI}$, which defines the amount of sealing air required to prevent ingress is of equal importance to the ratio of the discharge coefficients, Γ_c. Therefore, following Equation (2.14) and Equation (2.22):

$$\frac{\Phi_{i,EI}}{\Phi_{min,EI}} = \frac{1-\varepsilon}{\left[1 + \Gamma_c^{-2/3}(1-\varepsilon)^{2/3}\right]^{3/2}} \qquad \textit{Equation (2.23)}$$

When $\Phi_o = 0$, it follows that $\varepsilon = 0$; which is the maximum possible value for the non-dimensional ingested flow rate. Hence, Equation (2.23) reduces to:

$$\frac{\Phi^*_{i,EI}}{\Phi_{min,EI}} = \frac{1}{\left[1 + \Gamma_c^{-2/3}\right]^{3/2}} \qquad \textit{Equation (2.24)}$$

2.5.4 Orifice Model for RI Ingress

The orifice model developed to calculate RI ingress has had good success in calculating the sealing effectiveness of rim-seal. The orifice equations for the model are based on an actuator disc which has a discontinuous pressure change across an imaginary surface, which can be called the sealing ring (thin, permeable membrane with dimension of seal clearance), where ingress and egress occur simultaneously across the sealing ring. Similar to the EI ingress equations, they are derived for inviscid and incompressible flow, however discharge coefficients $C_{d,e}$ and $C_{d,i}$, are introduced to account for losses.

The main solutions of the orifice model equations for RI ingress are presented below, where the radial components of egress and ingress are expressed as:

$$\frac{V_{r,e}}{\Omega b} = C_{d,e}\sqrt{C_{\beta_1} - C_p} \qquad \textit{Equation (2.25)}$$

$$\frac{V_{r,i}}{\Omega b} = C_{d,i}\sqrt{C_p - C_{\beta_2}} \qquad \textit{Equation (2.26)}$$

where,

$$C_p = \frac{p_2 - p_1}{1/2\,\rho\Omega^2 b^2}, C_{\beta_1} = \beta_1^2\left(1 - \frac{r_1^2}{r_2^2}\right), C_{\beta_2} = \beta_2^2\left(\frac{r_2^2}{r_1^2} - 1\right) \qquad \textit{Equation (2.27)}$$

and the swirl ratio, β, is previously defined in Equation (2.4).

Equation (2.25) and Equation (2.26) reveal that the swirl in the wheel-space increases egress (known as 'disc-pumping effect'), while swirl in the annulus decreases ingress.

The driving force for RI ingress is the internal swirl parameter, C_{β_1}, since there is no circumferential pressure variation in the annulus and the annular flow is axisymmetric. The orifice model has the ability of providing an estimate of $\Phi_{min,RI}$ from the recorded experimental data points, ε and Φ_o without requiring any additional details such as the pressure distribution or the wheel-space swirl.

2.5.5 Orifice Model Solutions for RI Ingress – Effectiveness Equations

$$\Phi_{min,RI} = C_{d,e} C_{\beta_1}^{1/2} \quad \textit{Equation (2.28)}$$

The swirl parameter C_{β_1} is defined in Equation (2.27). The effectiveness Equation (2.29) is used when $\Phi_o < \Phi_{min,RI}$, however when $\Phi_o > \Phi_{min,RI}$, $\varepsilon = 1$.

$$\frac{\Phi_o}{\Phi_{min,RI}} = \frac{\varepsilon}{[1 + (1-\varepsilon)^{1/2}][1 + \Gamma_c^{-2}(1-\varepsilon)]^{1/2}} \quad \textit{Equation (2.29)}$$

Combining Equation (2.14) and Equation (2.29), the equation is presented in terms of the ingress parameter, $\Phi_{i,RI}$, such that:

$$\frac{\Phi_{i,RI}}{\Phi_{min,RI}} = \frac{1-\varepsilon}{[1 + (1-\varepsilon)^{1/2}][1 + \Gamma_c^{-2}(1-\varepsilon)]^{1/2}} \quad \textit{Equation (2.30)}$$

Considering the limiting case, when $\Phi_o = 0$ and $\varepsilon = 0$, Equation (2.30) reduces to:

$$\frac{\Phi_{i,RI}^*}{\Phi_{min,RI}} = \frac{1}{2[1 + \Gamma_c^{-2}]^{1/2}} \quad \textit{Equation (2.31)}$$

2.6 CHAPTER OVERVIEW

This chapter covers published literature from the basic subject of rotating disc systems, to more complicated cases such as rotor-stator systems, finally leading to ingestion. Literature on ingestion is included in great detail, ranging from experiments to computational fluid dynamics, and theoretical modelling.

The literature review revealed that there is a wide range of experiments and CFD studies previously published on ingress, further increasing the understanding of ingestion. However there is a gap in the literature, which would benefit from further research to be carried out on all three aspects (experiments, CFD and theoretical modelling). These research gaps are listed below:

- Need detailed experiments in rigs specifically designed for instrumentation access, not just engine scale rigs where it is hard to measure data
- Need fast CFD techniques
- Theoretical model supports both experiments and CFD

3 EXPERIMENTAL MEASUREMENTS

3.1 TEST FACILITY

The University of Bath has an experimental test facility which models a turbine stage with 32 vanes and 41 blades (manufactured from nylon by rapid-prototyping), as shown in Figure 3.1. Symmetric blades are attached to a disc which can be rotated up to speeds of 4000 rpm by an electric motor ($Re_\phi = 1.1 \times 10^6$).

The stationary and rotating discs are manufactured from transparent polycarbonate which allows optical view to the wheel-space for the application of heat transfer measurements using thermo-chromic liquid crystals. The vanes and blades are attached to these polycarbonate discs via an aluminium platform between both surfaces.

There are 32 circular pipes (25.4 mm diameter) which feed compressed air into the mainstream annulus of the turbine stage of the test rig, passing through the vanes and blades, and then being exhausted into the atmosphere. Figure 3.2 displays some of the supply pipes. All flow rates to the experimental test section are measured using calibrated orifice plates (EN ISO 5167-2).

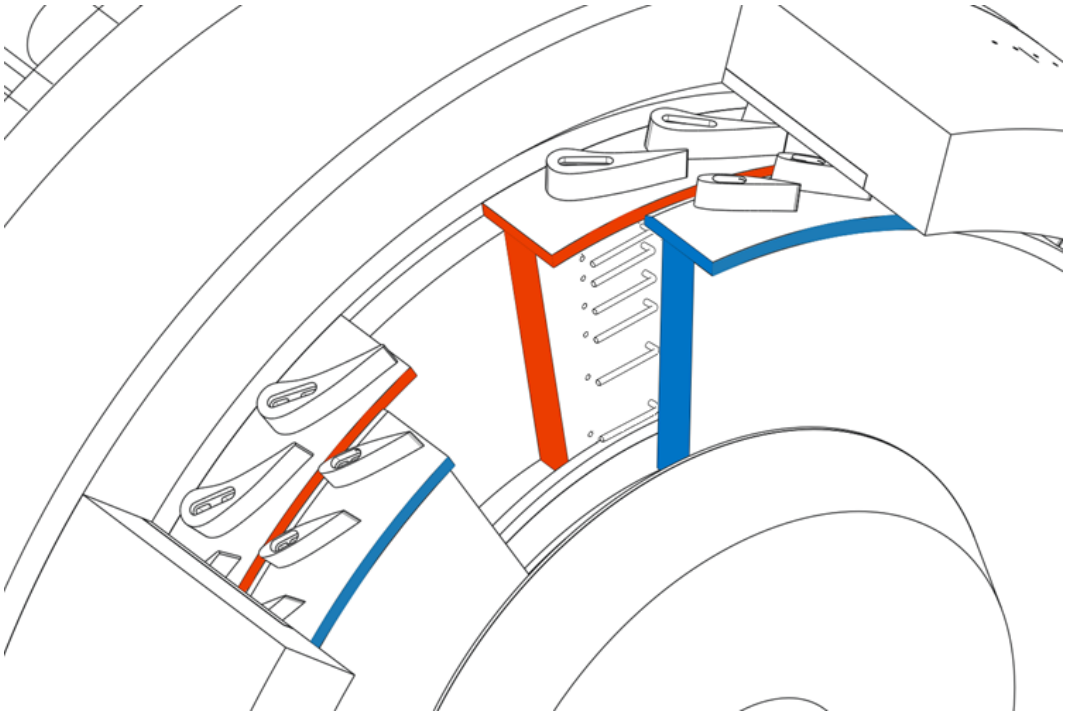

Figure 3.1 Rig test section highlighting pressure instrumentation (red = stationary; blue = rotating). [7]

It has been shown that for rotating flows, the turbulent flow structure in the boundary layers is minimally affected by the Re_ϕ and is governed mainly by the turbulent flow parameter λ_T. Therefore the flow structure in the rig should be representative of that found in engines.

The sealing air enters the wheel-space at a low radius through an inner seal. The amount of ingestion occurring is measured by seeding the sealing flow with carbon dioxide tracer gas. The CO_2 concentration is controlled at two locations: the seal flow inlet to the wheel-space, c_o, and the unseeded annular flow, c_a. A radial variation of concentration c_s ($0.55 < r/b < 0.993$) is determined along the stator disc in the wheel-space via 15 sampling taps of 1.6 mm diameter. The sampling taps can be seen in Figure 3.1, where the gas is drawn into the taps by a pump, which in turn is sent to an infrared gas analyser.

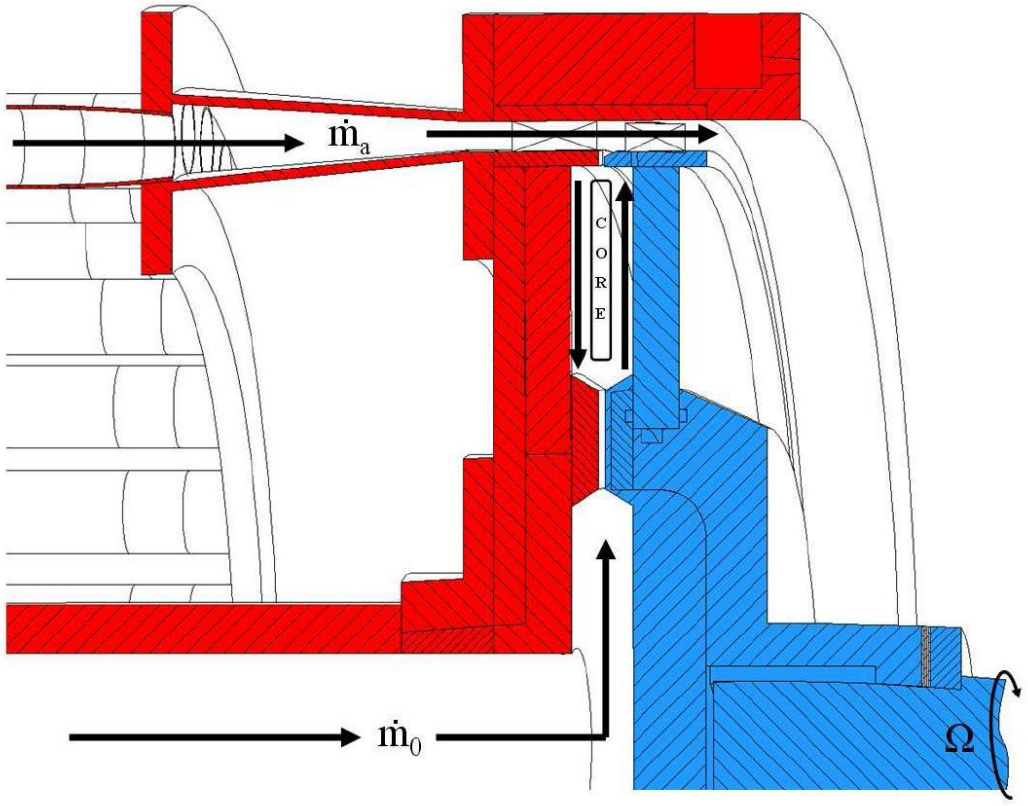

Figure 3.2 Rig test section displaying mainstream and sealing flows (red = stationary surfaces; blue = rotating surfaces). [6]

To measure the gas concentration effectiveness, ε_c, the following equation is used:

$$\varepsilon_c = \frac{c_s - c_a}{c_o - c_a}$$ *Equation (3.1)*

The equation above can be expressed in terms of the ingress parameter, Φ_i by means of Equation (2.15):

$$\frac{\Phi_{i,EI}}{\Phi_o} = \frac{c_o - c_s}{c_s - c_a}$$ *Equation (3.2)*

Therefore it follows that when there is no ingress, $\varepsilon_c = 1$, and when the sealing flow rate is zero, $\varepsilon_c = 0$. The rim-seal effectiveness is based on one radial location on the stator; hence the data is collected at *r/b* = 0.958.

The effectiveness measurements are time averaged and completing a full radial concentration test takes approximately 10 minutes. The multi-gas analyser is a Signal Group 9000MGA product, which carries out concentration measurements by using an infrared filter-correction technique which calculates seed-gas concentration levels. The uncertainty of the concentration measurements taken with the multi-gas analyser are within ± 1.5% of the recorded value.

The gas analyser is calibrated linearly by using two different gases as the two points of the line; pure alpha-grade N_2 gas as the zero-gas and 3% CO_2 in N_2 gas as the span-gas. There is a ± 3% uncertainty in the previously mentioned orifice plate for the sealant flow-rate (CO_2 seed).

There are static pressure taps of 0.5 mm diameter at 15 radial stations, as well as the concentration taps; also seven pitot-tubes (sketched in Figure 3.1) allow the measurement of the radial distribution of static and total pressure, while also enabling to capture V_ϕ, the tangential velocity of the fluid in the core outside the boundary layer. The measured V_ϕ allows determining the swirl ratio at set locations.

The different rim-seals that were experimentally investigated are shown in Figure 3.3, while the corresponding geometric details (static and rotating) are given in Table 3.1. The generic radial-clearance seal shown in Figure 3.3 shows that the vane and blade platforms at the edge of the parallel stator and rotor discs, with an axial overlap from a lower radial positioned seal lip on the rotating disc. The radial-clearance seal is bolted onto the rotor under the rotating platform.

The axial deflection of the disc was measured using displacement transducers. It was found that the axial clearance of the seal increases slightly when the disc is rotating and when the sealing flow pressurises the wheel-space. Displacement transducers were also used to measure the radial growth of the disc, rotor platform and the radial-clearance seal under rotation, which allowed determining the operating seal clearances.

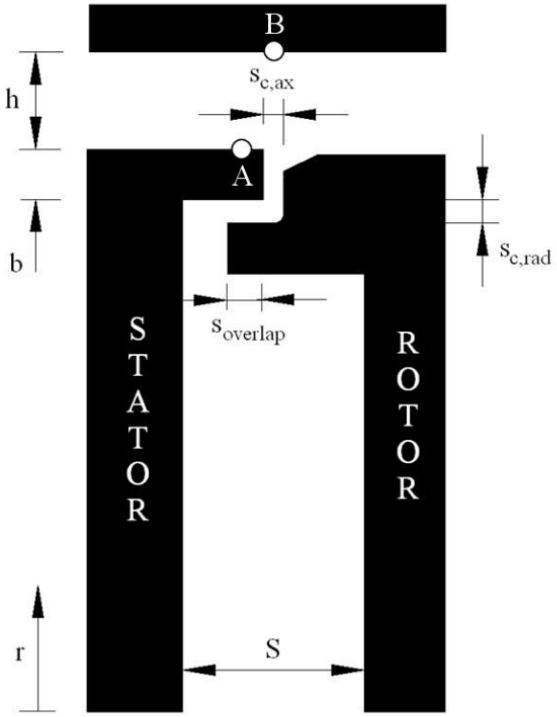

Figure 3.3 Radial-clearance seal

Geometric Symbol	Radial-clearance seal 1 (S2a)	Radial-clearance seal 2 (S2b)	Radial-clearance seal 3 (S2c)
h	10 mm		
b	190 mm		
S	20 mm		
$s_{c,ax}$	2 mm		
$G_{c,ax}$	0.0105		
$s_{overlap}$	3.7 mm	1.86 mm	1.86 mm
$s_{c,rad}$ **(0 rpm)**	2.4 mm	2.4 mm	1.28 mm
$G_{c,rad}$ **(0 rpm)**	0.0126		
$G_{c,rad}$ **(2000 rpm)**	0.0124		
$G_{c,rad}$ **(3000 rpm)**	0.0121		
$G_{c,rad}$ **(3500 rpm)**	0.0119		

Table 3.1 Geometric properties for seal configurations

Figure 3.4 shows the geometry of the vanes and blades in the annulus which produce a flow structure similar to those in engines. The blades used in this test rig are NACA 0018 symmetric aerofoils, which avoid the need of a dynamometer to absorb any energy. The vane trailing edge and blade leading edge are separated by an axial clearance of 12 mm. The 2 mm seal gap is equidistant between the vane trailing edge and the blade leading edge.

15 static pressure taps of 0.5 mm diameter each, are located in the vane platform 2.5 mm downstream the vane trailing edge (Location A) and above the seal-clearance centre line on the outer casing (Location B), these positions are shown in Figure 3.3. These taps are positioned across one vane pitch to capture the circumferential pressure variation driving the ingestion of the mainstream annulus flow.

The velocity triangles for the turbine stage are shown in Figure 3.4. α is the vane exit angle. The air has velocity C and a corresponding Mach number, $M = C/a$. W is the axial component of velocity, with the corresponding axial Reynolds number $Re_W = \rho W b/\mu$.

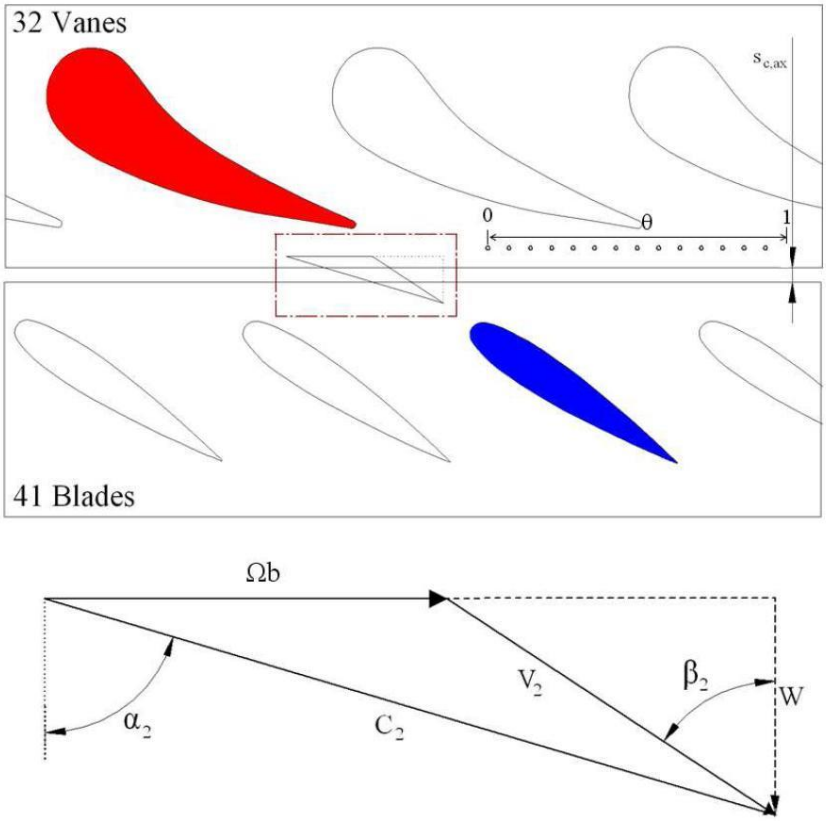

Figure 3.4 Vane and blade geometry and associated velocity triangles [6]

The flow leaving the vanes is incompressible and close to atmospheric pressure; by means of the static temperature and pressure measured inside the wheel-space on the stator at r/b = 0.993, the density ρ, speed of sound a, and air viscosity μ is determined. β is the rotor inlet angle and V is the velocity. The rig is operated at design condition, where $\beta = \beta_o$. The rig has the following properties: β_o = 56°, α = 73°, and $Re_W/Re_\phi = 0.538$. All effectiveness data presented in this report are for design operating conditions of the rig, with the velocity triangles for the three operating points listed in Table 3.2.

Parameter	**Disc Speed (rpm)**		
	2000	3000	3500
$\boldsymbol{Re_\phi}$	5.32 x 10^5	8.17 x 10^5	9.68 x 10^5
$\boldsymbol{Re_W}$	2.86 x 10^5	4.40 x 10^5	5.21 x 10^5
$\boldsymbol{Re_W/Re_\phi}$	0.538	0.538	0.538
$\boldsymbol{M}$	0.225	0.339	0.398

Table 3.2 Design operating conditions for test rig

3.2 EFFECTIVENESS MEASUREMENTS

This section presents the experimental data collected using the variations of radial-clearance seals displayed in Figure 3.3 with associated properties listed in Table 3.1. The rim-seal effectiveness is measured using the concentration effectiveness, ε_c Equation (3.1), collected on the stator at r/b = 0.958. Data is presented in terms of $C_{w,o}$, the widely used non-dimensional sealing flow rate and Φ_o, the non-dimensional flow parameter used in the orifice equations. The collected experimental data is compared against the theoretical calculations from the orifice model using the effectiveness Equation (2.23), $\frac{\Phi_{i,EI}}{\Phi_{min,EI}}$.

3.2.1 Effectiveness Measurements in terms of $C_{w,o}$

The variation of effectiveness with $C_{w,o}$ for the different tested radial-clearance seals is shown in Figure 3.5 and Figure 3.6, for EI and RI ingress respectively. Measurements were made at three different values of Re_ϕ corresponding to the three operational conditions listed in Table 3.2. Illustrative sketches of the different seal configurations are shown on all the following figures. The external flow is from the stator to the rotor (left to right) in these sketches.

The data shows that ε_c increases with increasing $C_{w,o}$, as the sealing flow pressurises the wheel-space and reduces ingestion of main-stream flow from the annulus. As Re_ϕ (hence Re_W) increases, a larger non-dimensional sealing flow rate, $C_{w,o}$ is required to maintain a certain level of effectiveness; $C_{w,min}$, the non-dimensional sealing flow required to seal the wheel-space, increases consistently with Re_ϕ and Re_W. The radial-clearance seal with the tighter radial-clearance gap (S2c) is shown to require a significantly smaller $C_{w,min}$ than the other two radial-clearance seals (S2a and S2b) for the same Re_ϕ, showing that a smaller radial-clearance gap makes the radial-clearance seal a more superior geometric design for sealing the rim-seal of the wheel-space.

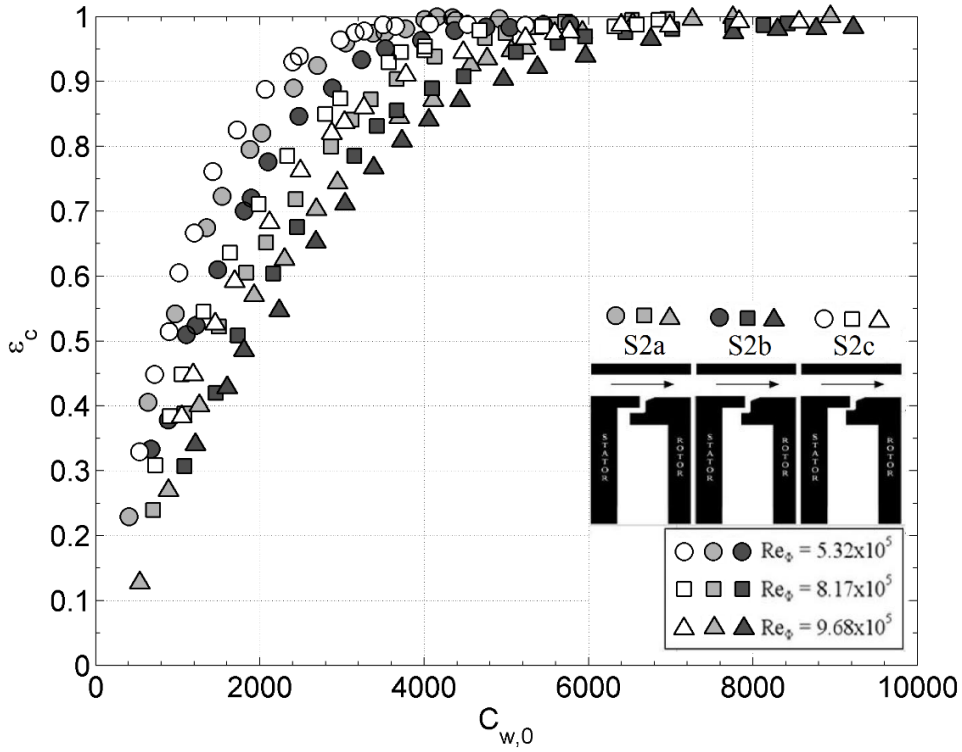

Figure 3.5 Effect of Re_ϕ on measured variation of ε_c with $C_{w,o}$ for EI ingress on variations of tested radial-clearance rim-seals

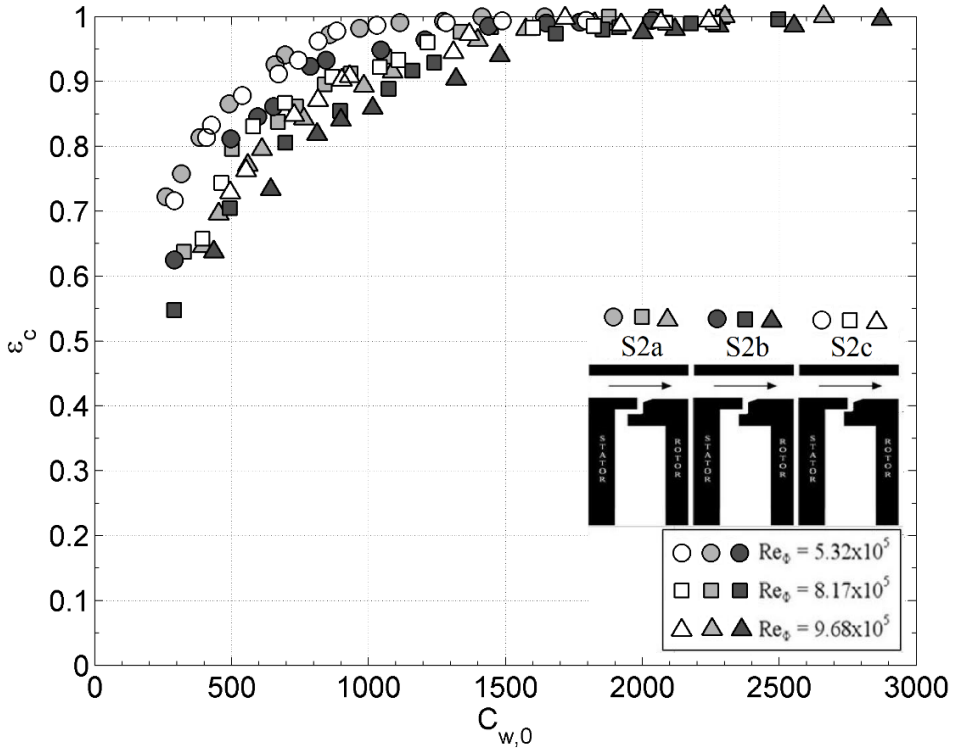

Figure 3.6 Effect of Re_ϕ on measured variation of ε_c with $C_{w,o}$ for RI ingress on variations of tested radial-clearance rim-seals

3.2.2 Effectiveness Measurements in terms of Φ_o

The data in Figure 3.5 and Figure 3.6 has been re-plotted as ε_c versus Φ_o and is shown in Figure 3.7 and Figure 3.8 respectively. From Table 3.1, it can be noted that the value of G_c varies with different Re_ϕ for the different radial-clearance seal. The parameter Φ_o combines $C_{w,o}$, G_c and Re_ϕ into a single flow parameter, avoiding the use of separate correlations for the effects of G_c and Re_ϕ on ε. For the design condition, $Re_W/Re_\phi = 0.538$, the rim-seals can be characterized by a simple value of $\Phi_{min,EI}$ (for EI ingress) and $\Phi_{min,RI}$ (for RI ingress).

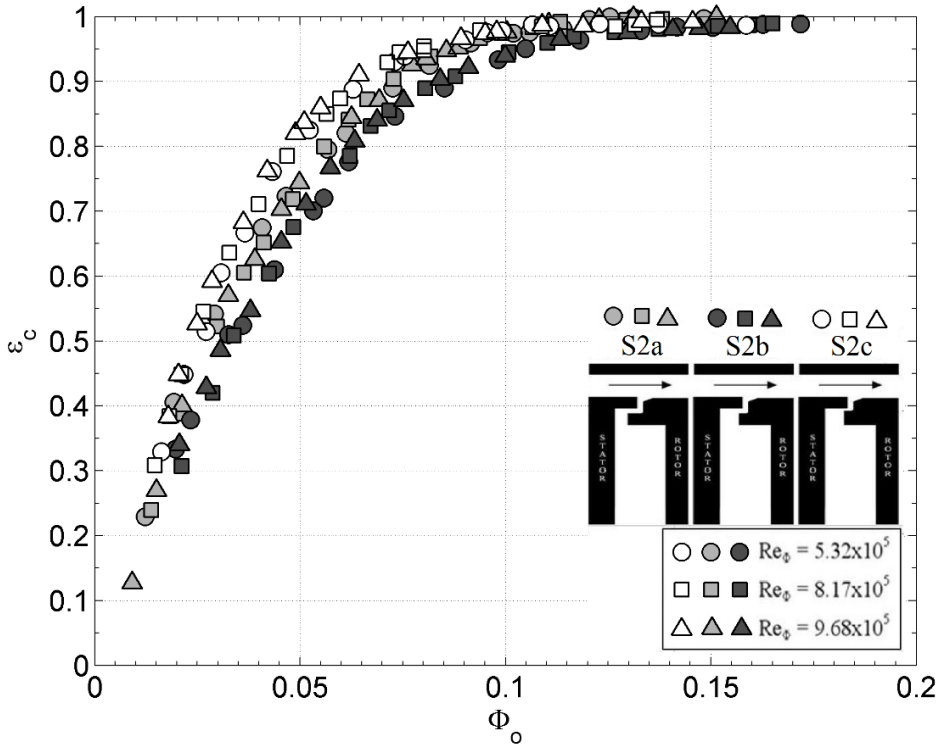

Figure 3.7 Measured variations of sealing effectiveness with Φ_o for EI ingress at $Re_W/Re_\phi = 0.538$

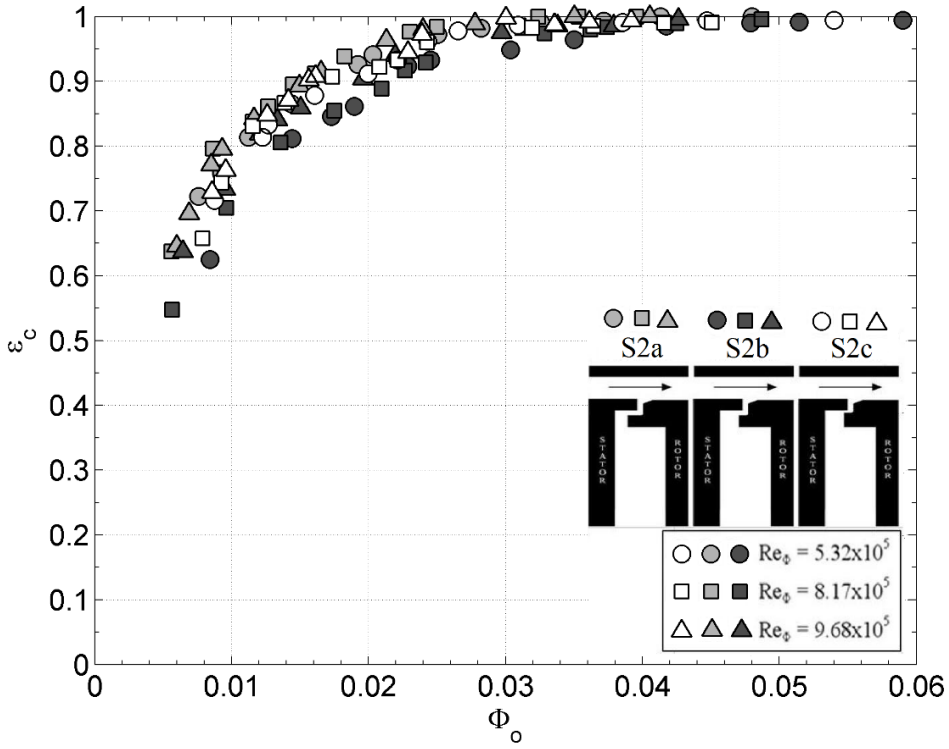

Figure 3.8 Measured variations of sealing effectiveness with Φ_o for RI ingress at $Re_W/Re_\phi = 0.538$

A comparison between EI and RI ingress for the three different radial-clearance seals; S2a, S2b, and S2c are presented in Figure 3.9, Figure 3.10 and Figure 3.11, respectively.

Also shown on these figures are the theoretical effectiveness curves from the orifice model. The figures are plotted by fitting the effectiveness equations to the measured data in terms of ε and Φ_o. Using the statistical 'fitting' model in conjunction with the orifice model, allows optimising the data and presenting it in terms of Φ_{min}, Φ_i and Γ_c. This optimised curve also shows the ratio Φ_i/Φ_{min} against the minimum seal flow rate, Φ_{min} for both EI and RI ingress. This permits the designer to estimate the maximum possible ingestion due to EI and RI ingress for similar seals when $\Phi_o = 0$.

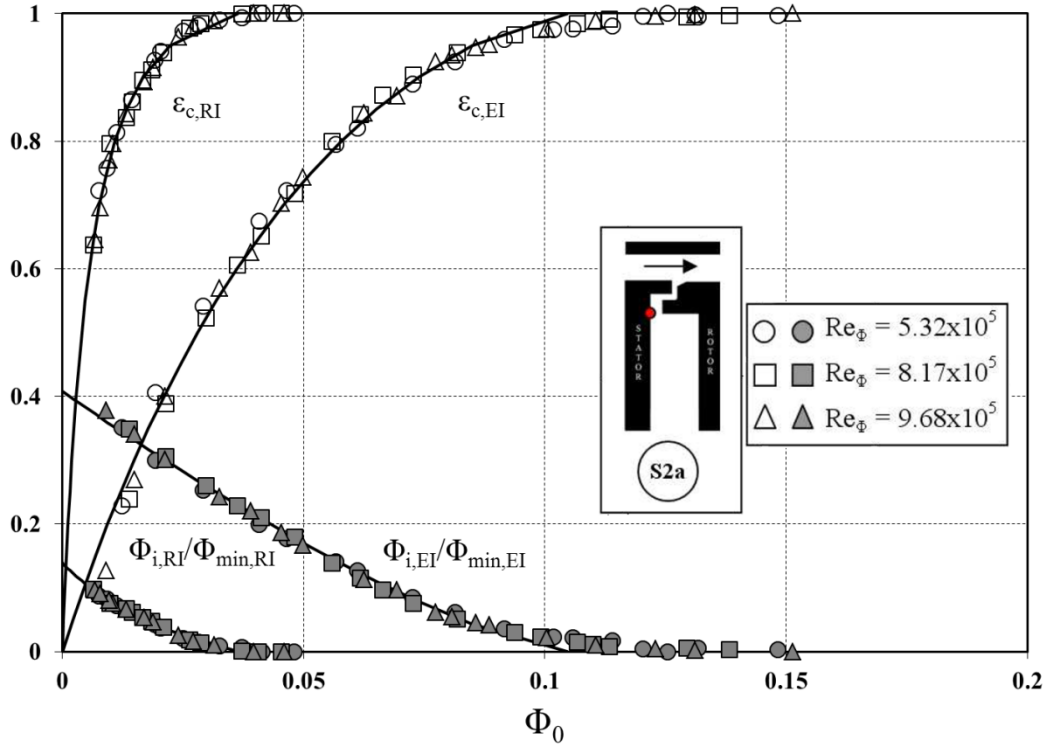

Figure 3.9 Comparison between theoretical effectiveness curves and experimental data for radial-clearance seal (S2a) with EI and RI ingress for $Re_W/Re_\phi = 0.538$

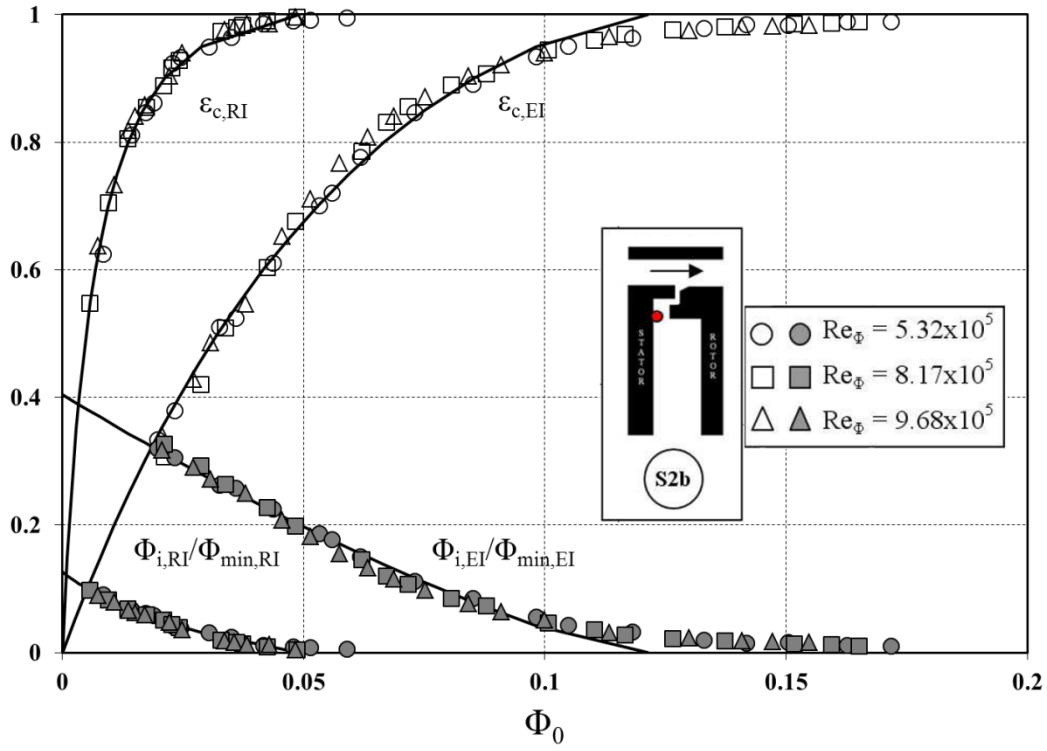

Figure 3.10 Comparison between theoretical effectiveness curves and experimental data for radial-clearance seal (S2b) with EI and RI ingress for $Re_W/Re_\phi = 0.538$

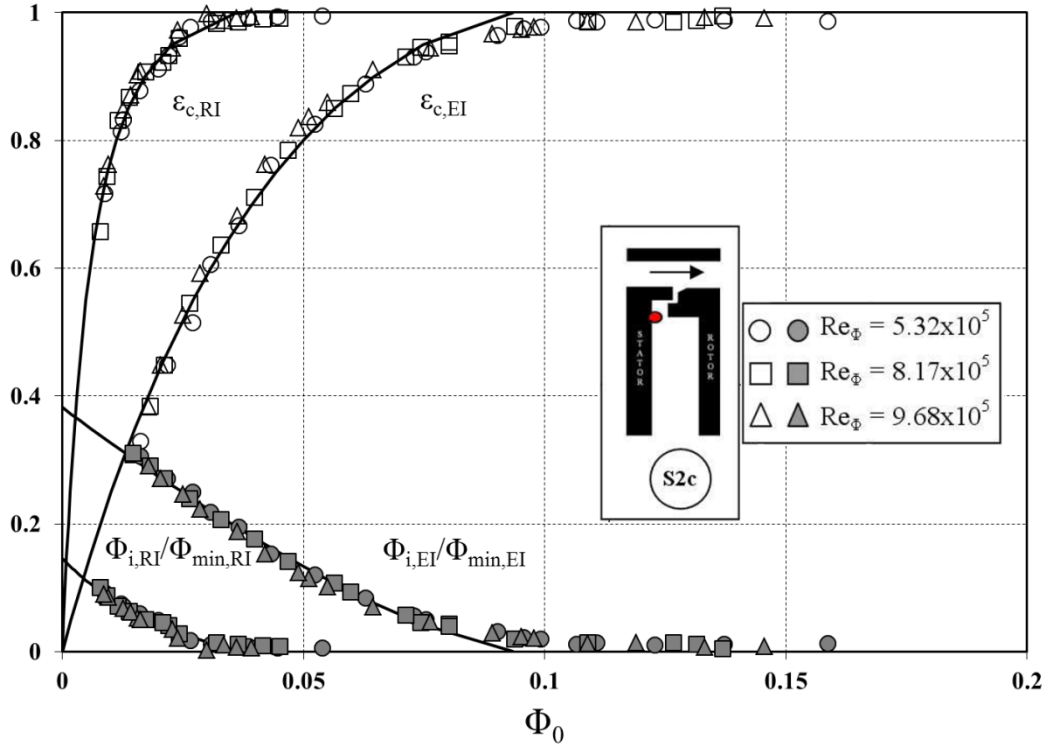

Figure 3.11 Comparison between theoretical effectiveness curves and experimental data for radial-clearance seal (S2c) with EI and RI ingress for $Re_W/Re_\phi = 0.538$

Table 3.3 shows data of the three variations of the radial-clearance seals for EI and RI ingress, such as the values of Φ_{min}, Γ_c and σ, the standard deviation between the equations and the data. The value of Φ_i^* for EI and RI ingress is also displayed by calculating $\Phi_{i,EI}^*$ and $\Phi_{i,RI}^*$ using Equation (2.24) and Equation (2.31), respectively. Φ_i^* is the maximum value of Φ_i, which occurs when $\Phi_o = 0$ for both EI and RI ingress. This theoretical value of Φ_i^* cannot be clearly determined from experimental concentration measurements. The accuracy of the statistical method improves with larger number of data points [47].

	EI Ingress			**RI Ingress**		
Seal	**S2a**	**S2b**	**S2c**	**S2a**	**S2b**	**S2c**
$\boldsymbol{\Phi_{min}}$	0.105	0.121	0.093	0.036	0.049	0.036
$\boldsymbol{\Phi_i^*}$	0.408	0.404	0.382	0.139	0.126	0.146
$\boldsymbol{\Gamma_c}$	1.351	1.323	1.170	0.289	0.261	0.305
$\boldsymbol{n}$	54	54	54	54	54	54
$\boldsymbol{\sigma}$	0.017	0.019	0.019	0.008	0.010	0.013

Table 3.3 Parameters for variations of radial-clearance seals

Table 3.3 shows that, for EI ingress, the three variations of the radial-clearance seal exhibit different sealing characteristics. Decreasing the length of the axial overlap of the radial-clearance seal has a negative impact on the sealing characteristics of the seal as shown in Figure 3.7. On the other hand the other radial-clearance seal tested, with the tighter radial-clearance gap, reveals that the effectiveness of the seal is significantly more effective than the other two radial-clearance seals (S2a and S2b).

Using Table 3.3, Φ_{min} for EI ingress can be calculated for the variations of the radial-clearance seals. The decreased axial overlap radial-clearance seal (S2b) has a 16% higher $\Phi_{min,EI}$ value than that of the base-line radial-clearance seal (S2a). While the tighter radial-clearance gap seal (S2c) has an 11% lower $\Phi_{min,EI}$ value than that of the base-line radial-clearance seal (S2a), rendering seal S2c the most effective seal in terms of $\Phi_{min,EI}$ for the three radial-clearance seals.

3.2.3 Rim-Seal Discharge Coefficients

Table 3.4 shows values for ΔC_p, which was recorded and calculated via the 15 static pressure taps located across one vane pitch at Locations A and B previously mentioned. The values of Φ_{min} and Γ_c were estimated via the statistical method applied to the experimental data (ε and Φ_o). The values of $C_{d,e}$, $C_{d,i}$ and K were obtained using Equation (2.20), Equation (2.16) and Equation (2.21) respectively.

The value of $C_{d,e}$ for radial seal S2c is approximately 88% of that of radial seal S2a, and consecutively the $C_{d,e}$ of radial seal S2a is approximately 85% of that of radial seal S2b. Regarding the ratio of $C_{d,i}$, radial seal S2c is approximately 76% of that of radial seal S2a, and the $C_{d,i}$ ratio of radial seal S2a is approximately 86% of that of radial seal S2b.

Analysing the presented data in Table 3.4, it can be observed that the value of $C_{d,e}$ for any of the three seals is always below the $C_{d,i}$ value of its respective seal, which means that ingress dominates over egress. This occurrence could be explained by the 'impinging jet phenomenon', where the rotating-disc for a radial-clearance seal creates a radial jet, similar to a fluid wall which impinges on the stationary disc of the seal.

Seal	ΔC_p	Φ_{min}	Γ_c	$C_{d,e}$	$C_{d,i}$	K
Location A S2a	0.82	0.105	1.351	0.17	0.23	0.16
Location A S2b	0.82	0.121	1.323	0.20	0.27	0.19
Location A S2c	0.82	0.093	1.170	0.15	0.18	0.15
Location B S2a	0.42	0.105	1.351	0.24	0.33	0.23
Location B S2b	0.42	0.121	1.323	0.28	0.37	0.26
Location B S2c	0.42	0.093	1.170	0.22	0.25	0.20

Table 3.4 Discharge coefficients and K values for radial-clearance seal variations

3.3 WHEEL-SPACE MEASUREMENTS

3.3.1 Effectiveness Measurements

Figure 3.12 compares the radial variation of concentration effectiveness ε_c on the stator surface for the three radial-clearance seals S2a/b/c, all for $\lambda_T \approx 0.05$ and 0.07.

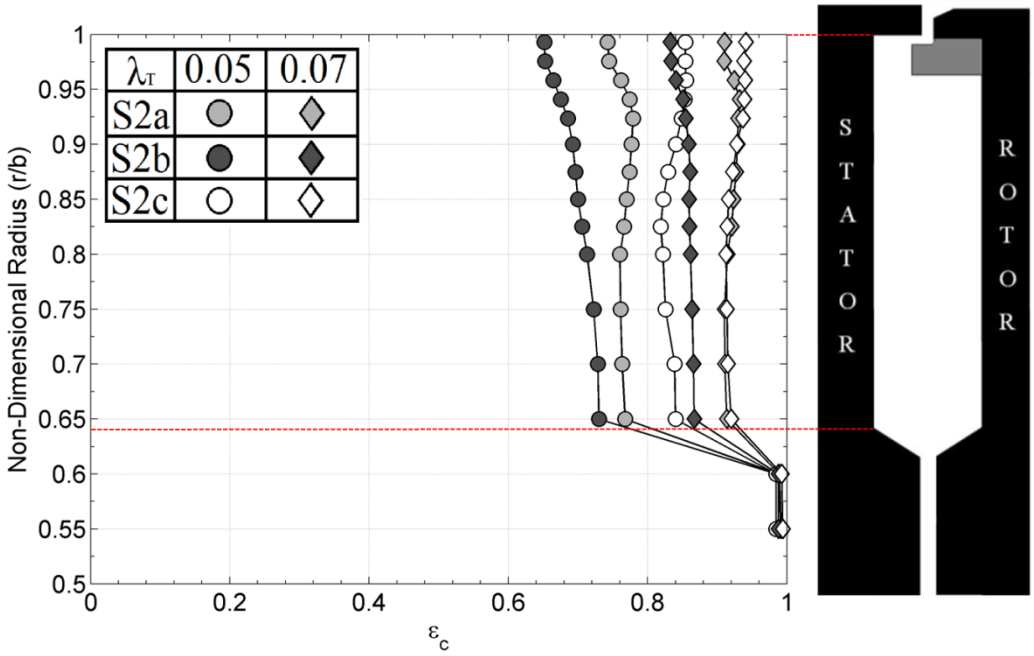

Figure 3.12 Radial variation of effectiveness for radial-clearance seals (S2a-c) for $\lambda_T \approx 0.05$ and 0.07

Figure 3.12 shows that for all seals the effectiveness is mainly invariant with radius for $r/b > 0.65$, suggesting that most of the mixing has occurred in a region very close to the rim-seal. The instant increase in ε_c at low radii is caused by the presence of the sealing inlet seal, which nearly prevents the ingestion of fluid into the region where the sealing flow is introduced.

Note that if the flow were not to be completely mixed, there would be concentration effectiveness gradients in the stator boundary layer and hence a radial variation in effectiveness.

As expected (discussed in section 3.2.2), seal S2b with the smaller axial overlap and larger radial-clearance gap, is the worst performing seal in terms of sealing performance. With reference to seal S2b, the increase in the axial overlap for seal S2a improves the performance; however a greater improvement is gained by reducing the radial-clearance gap for seal S2c. Though not tested, a seal with both a larger axial

overlap and reduced radial-clearance would be expected to produce a much better performance.

3.3.2 Swirl Ratio Measurements

Figure 3.13 illustrates the variation of swirl ratio with non-dimensional radius for the radial-clearance seal (S2a). The measurement points for total pressure in the wheel-space (at *z/S*=0.25) are shown on the right of the figure. The tests were conducted at Re_ϕ= 8.2x10^5 for several values of λ_T and hence Φ_o; in all cases ingress occurred with β_a = 1.8.

The data for λ_T = 0, shows a similar flow structure in the wheel-space to that illustrated in Figure 1.13b. There is no superposed flow and the core rotation $\beta = \beta^* \approx$ 0.44 for *r/b* < 0.8. The swirl ratio at larger radii increases radially outward to $\beta \approx 0.9$ at the wheel-space periphery due to the influence of the high-swirling ingress. The case for λ_T = 0 has the maximum ingress and the concentration effectiveness is zero everywhere in the wheel-space.

Increasing the purge flow causes a reduction in the core rotation as can be seen in Figure 3.13. The level of swirl also diminishes at the wheel-space periphery, as the wheel-space is pressurised and reduces ingestion from the annulus. Further increasing the sealing flow, amplifies these effects. At small values of λ_T, the flow structure is similar to that depicted in Figure 1.13c, however the area of the outer region is difficult to measure.

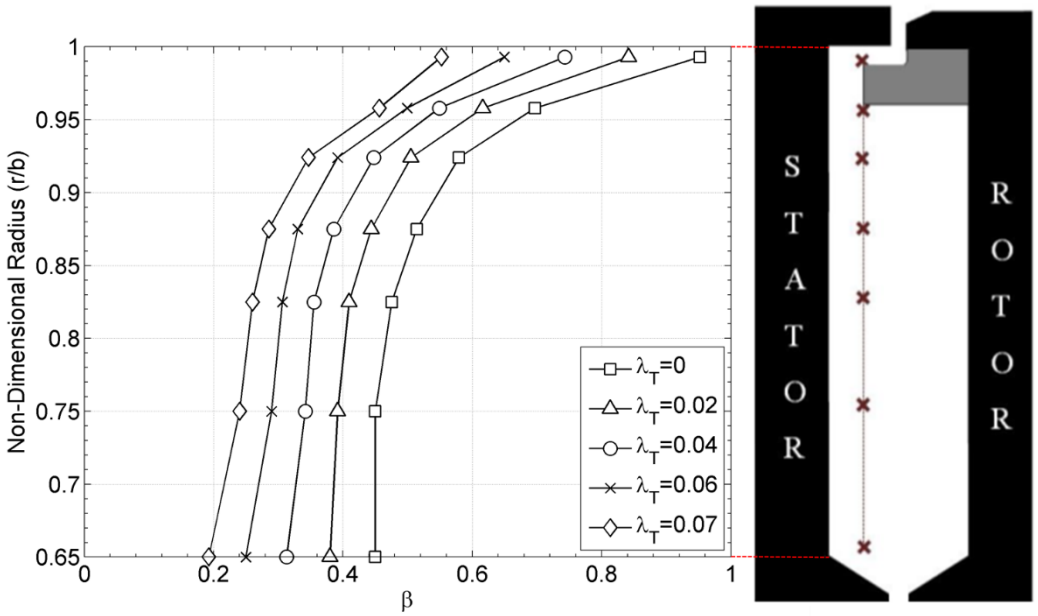

Figure 3.13 Variation of swirl ratio with radius for radial-clearance seal (S2a) for different λ_T at $Re_\phi = 8.2 \times 10^5$

Figure 3.14 compares the variation of swirl ratio for the three radial-clearance seals. The measurements were made at Re_ϕ= 8.2x10^5 with λ_T = 0, 0.02 and 0.07. As shown in Figure 3.12, there is substantial differences in the ingress levels into the wheel-space for the three radial-clearance seals. Regardless of the differences in ingestion levels, the measured swirl appears only to vary near the outer periphery of the wheel-space, confirming that the flow structure is governed principally by λ_T.

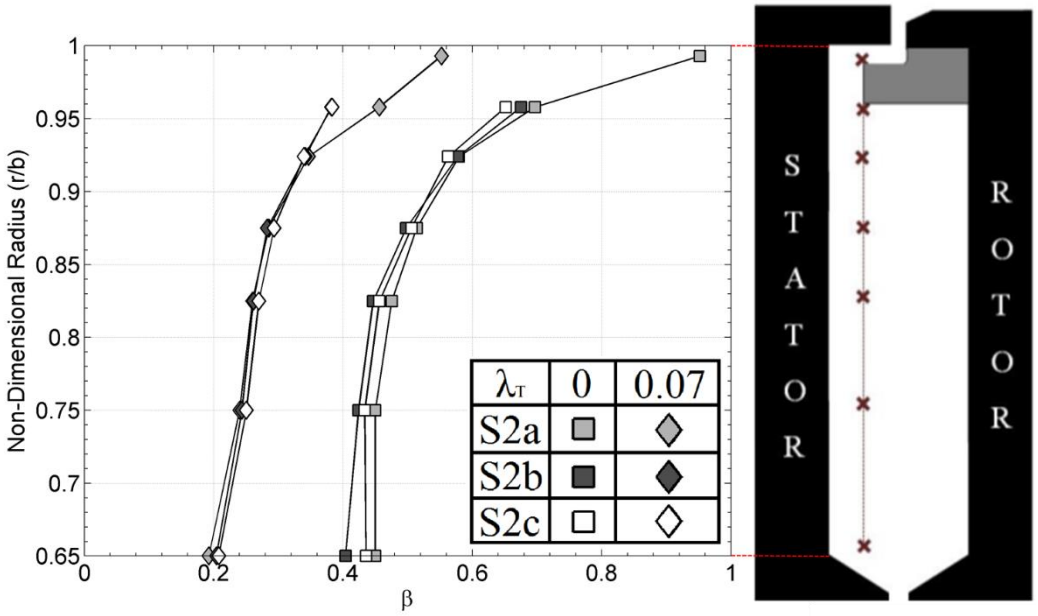

Figure 3.14 Variation of swirl ratio with radius for radial-clearance seals (S2a-c) for three different λ_T values at $Re_\phi = 8.2 \times 10^5$

Initially it may be surprising that different ingestion levels for the same λ_T have such a little effect on the velocity distribution in the core region. As previously explained in section 0, ingress will affect the swirl in the outer region, which is the source of the boundary layer on the stator. This affects the flow in the stator boundary layer, which in turn affects the flow in the rotor boundary layer and the swirl in the core. Changes to the swirl in the outer region have a small effect outside it, since boundary layers are insensitive to initial conditions, which decay with distance from the outer region.

3.3.3 Static Pressure Measurements

For a rotating inviscid core, the radial momentum equation reduces to a balance between the pressure force and the centripetal acceleration, such that:

$$\frac{1}{\rho}\frac{dp}{dr} = \frac{V_\phi^2}{r} \qquad \textit{Equation (3.3)}$$

Using the definitions of C_p and β in section 2.5.2.1, Equation (3.3) can be integrated to provide:

$$C_p = \frac{p - p_{ref}}{0.5\rho\Omega^2 b^2} = 2\int_{x_{ref}}^{x} x\beta^2 dx \qquad \textit{Equation (3.4)}$$

where p_{ref} is the pressure at $x = r/b = x_{ref}$; for the results presented in this thesis x_{ref} = 0.6. The numerical integration was carried out using Simpson's rule, with values of β obtained from a least-squared cubic spline fitted to the experimental swirl data.

Figure 3.15 show comparisons between the distributions of C_p calculated from Equation (3.4) and the values obtained from the measured static pressures on the stator wall. There is very good agreement between the calculated and measured distributions of C_p. This confirms two important things: (1) the radial distribution of the swirl ratio determines the radial distribution of pressure in the wheel-space, (2) the distributions of swirl and pressure are controlled by λ_T.

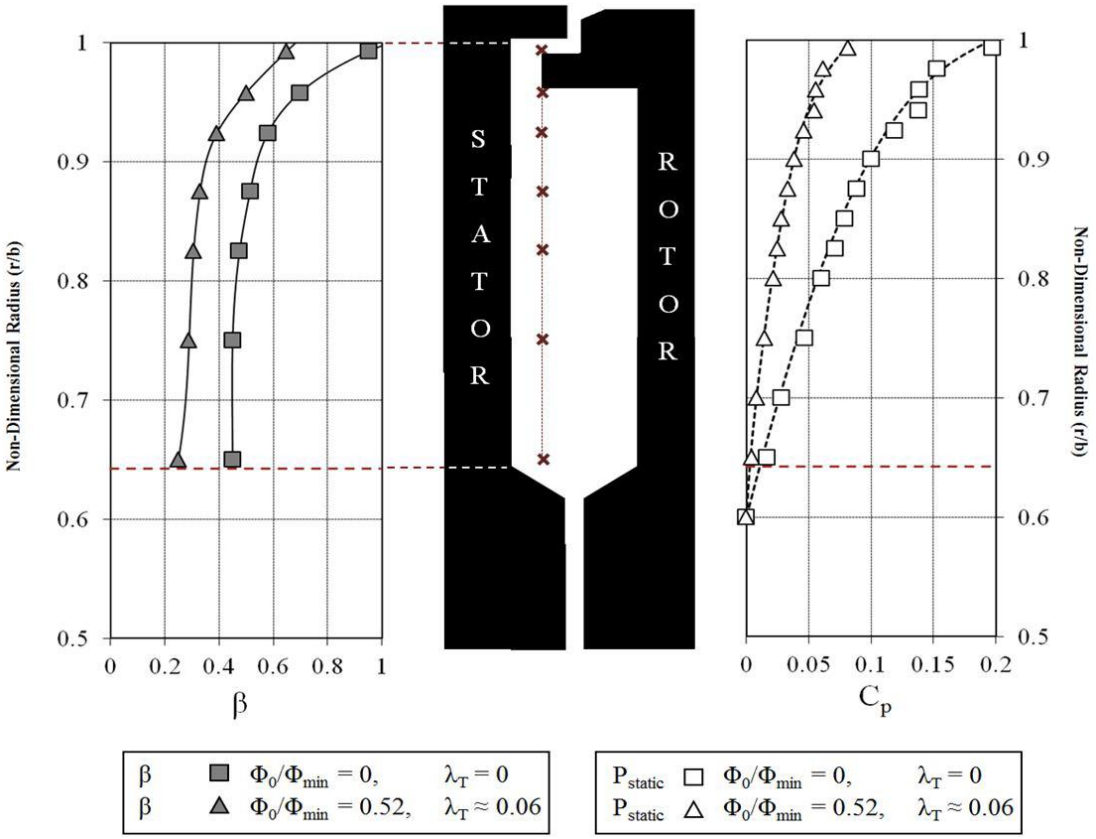

Figure 3.15 Effect of λ_T on radial distribution of swirl ratio and pressure coefficient (static) for radial-clearance seal (S2a). Symbols denote measured values; lines denote fitted distribution for β and calculated distribution for C_p [7]

3.4 CHAPTER OVERVIEW

This experimental chapter has described the research facility at the University of Bath which models hot gas ingestion into the wheel-space of an axial turbine stage. CO_2 gas concentration measurements were taken along the stator wall inside the wheel-space and used to determine the performance of three radial-clearance seals in terms of gas concentration effectiveness (ε_c). The sealing parameter, Φ_o, was used to present the data as it combines the different variables G_c, $C_{w,o}$ and Re_ϕ into a single parameter. The data was presented in two different aspects, ε_c and $\Phi_{i,EI}$ versus Φ_o.

Although the ingestion through the rim-seal is a consequence of an unsteady, three dimensional flow field and the cause-effect relationship between pressure and the sealing effectiveness is complex, the experimental data is shown to be successfully calculated by simple effectiveness equations developed from a previously published theoretical model. The data illustrates that the effectiveness can be correlated using the non-dimensional sealing parameter, Φ_o. Equation (3.1) and Equation (3.2) are the

effectiveness equations from the model which predict the variation of ε and $\Phi_{i,EI}$ against Φ_o. These equations provide an estimate of the minimum non-dimensional sealing flow rate to stop ingress, Φ_{min}, without requiring any data on the annular pressure distribution. To use these equations, it is necessary to determine two empirical constants from the experimental data using a statistical fitting method.

The effectiveness equations predict the form of the experimental data for the three variations of the radial-clearance seals very well. Seal S2c proved to be the most adept at preventing ingress compared to the other two-radial clearance seals (S2a and S2b). The data shows that reducing the axial overlap of the radial-clearance seal (S2b) has a negative impact on the performance of the seal in terms of preventing ingress. Decreasing the radial-clearance gap improved the performance of the radial seal (S2c). The EI ingress results exhibited that a 50% decrease in axial overlap of the radial-clearance seal increased the Φ_{min} value by 15%, whereas a 53% decrease in the radial-clearance gap of the seal decreased the Φ_{min} value by 12%.

The radial variation of effectiveness for all three seals is mainly invariant with radius, suggesting that most of the mixing has occurred at high radius, in the outer region very close to the rim-seal.

The swirl ratio measurements revealed that the ingested fluid enters the wheel-space with high swirl, increasing the swirl ratio at high radius. Also shown is that, increasing the sealing flow rate reduces the core rotation, while the swirl at the wheel-space periphery is also reduced due to the wheel-space pressurisation and reduction of ingress from the annulus. The swirl measurements shown in Figure 3.13 and Figure 3.14, clearly show that the flow structure in the wheel-space is principally governed by λ_T.

The static pressure measurements on the stator wall reveal that the radial distribution of swirl determines the radial distribution of pressure in the wheel-space; while λ_T controls the swirl and pressure distributions in the wheel-space.

4 COMPUTATIONAL METHOD

4.1 DISCRETIZATION

ANSYS CFX utilises an element-based finite volume method, which initially involves discretizing the spatial domain using a mesh. The mesh is used to construct finite volumes, to which are applied conservation conditions for relevant quantities such as mass, momentum and energy. All computations in this study use a three dimensional mesh, but for simplicity, the process is shown for two dimensions.

Figure 4.1 shows a typical two-dimensional mesh, where all solution variables and fluid properties are stored at the nodes. A control volume is constructed around each mesh node using the median dual (lines connecting the centres of the edges and element centres).

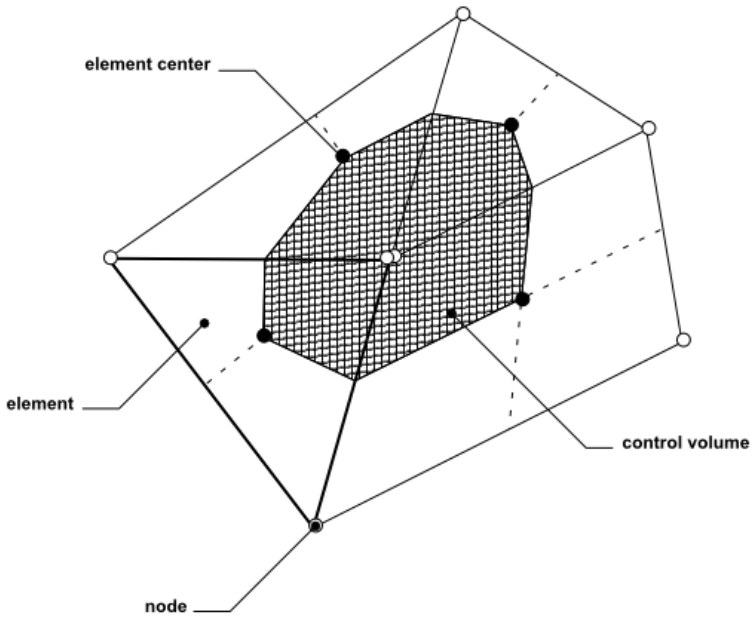

Figure 4.1 Control (finite) volume shown from top view [48]

The next step in the numerical algorithm is the discretization of the volume and surface integrals, which is illustrated by considering a single element like the one shown in Figure 4.2. The volume integrals are discretized within each element sector and accumulated to the control volume to which the sector belongs. On the other hand, surface integrals are discretized at the integration points located at the centre of each surface segments within an element and then distributed to the adjacent control volumes.

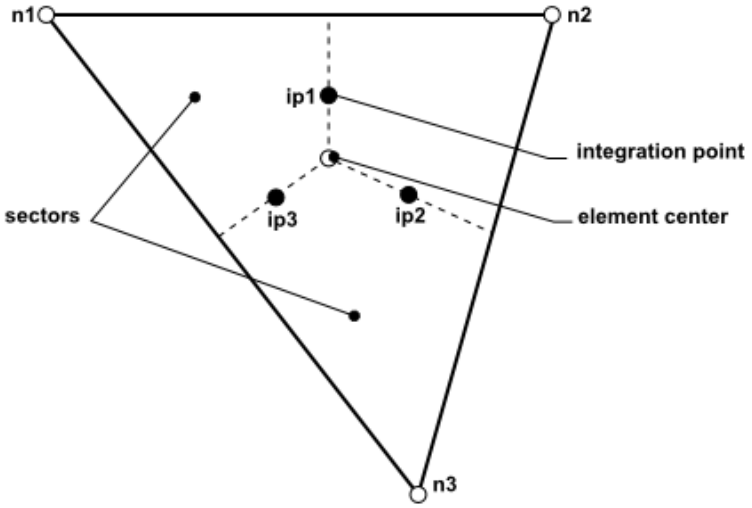

Figure 4.2 Finite volume element [48]

Advection schemes are numerical mechanisms for transporting given quantities (velocity, temperature, etc.) through the solution domain. The form of the advection scheme is shown in Equation (4.1), where $0 < \beta \leq 1$ and the choice yields different schemes. Details on the evaluation of β can be found in ANSYS CFX Reference Guide [48].

$$\phi_{ip} = \phi_{up} + \beta\phi \qquad \textit{Equation (4.1)}$$

During this study two advection schemes were considered, 1) Upwind Differencing Scheme and 2) High Resolution Scheme.

4.1.1 Upwind Differencing Scheme (UDS)

A first order Upwind Differencing Scheme is obtained when a value of β = 0 is selected. This scheme is very robust, but introduces diffusive discretization errors that tend to smear steep spatial gradients.

4.1.2 High Resolution Scheme (HRS)

The High Resolution Scheme uses a nonlinear formula for β at each node, which is computed to be as close to 1 as possible. The formula for β is based on the principles of boundedness used by Barth and Jesperson [49].

4.2 TURBULENCE MODELS

Two-equation turbulence models are widely used due to their offering of a good compromise between numerical effort and computational accuracy, and are therefore generally used in fundamental flow computations. These two-equation turbulence models solve the velocity and length scales using separate transport equations, and the turbulent viscosity is modelled as the product of both the velocity and length scale.

4.2.1 $k - \varepsilon$ Turbulence Model

The $k - \varepsilon$ model is one of the most prominent turbulence models, which has been implemented in most general purpose CFD codes and is regarded as an industry standard model. The model has proven to be stable and numerically robust, as it offers a good compromise in terms of accuracy and robustness.

In the k - ε turbulence model, the turbulent velocity is calculated from the turbulent kinetic energy, k, which is defined as the variation in velocity fluctuations. Whilst the turbulent length scale is calculated from both the turbulent kinetic energy and the turbulence eddy dissipation rate, ε, which is defined as the rate at which the velocity fluctuations dissipate. The model introduces these two new variables into the system of equations. The continuity and momentum equations then become:

$$\frac{\partial \rho}{\partial t} + \frac{\partial}{\partial x_j}\left(\rho U_j\right) = 0 \qquad \textit{Equation (4.2)}$$

$$\frac{\partial \rho U_i}{\partial t} + \frac{\partial}{\partial x_j}\left(\rho U_i U_j\right) = -\frac{\partial p}{\partial x_i} + \frac{\partial}{\partial x_j}\left[\mu_{eff}\left(\frac{\partial U_i}{\partial x_j} + \frac{\partial U_j}{\partial x_i}\right)\right] + S_M \qquad \textit{Equation (4.3)}$$

In Equation (4.3), μ_{eff} is the effective viscosity accounting for turbulence, such that:

$$\mu_{eff} = \mu + \mu_t \qquad \textit{Equation (4.4)}$$

The turbulence viscosity, μ_t, is linked to the turbulence kinetic energy and eddy dissipation rate through the following relationship:

$$\mu_t = C_\mu \rho \frac{k^2}{\varepsilon} \qquad \textit{Equation (4.5)}$$

In Equation (4.5), C_μ is a constant. While the values of k and ε are solved via two additional differential transport equations, one for the turbulence kinetic energy and another for the turbulence eddy dissipation rate, which are shown below:

k – equation:

$$\frac{\partial(\rho k)}{\partial t}+\frac{\partial}{\partial x_j}\left(\rho U_j k\right)=\frac{\partial}{\partial x_j}\left[\left(\mu+\frac{\mu_t}{\sigma_k}\right)\frac{\partial k}{\partial x_j}\right]+P_k-\rho\varepsilon+P_{kb} \qquad \textit{Equation (4.6)}$$

ε – equation:

$$\frac{\partial(\rho\varepsilon)}{\partial t}+\frac{\partial}{\partial x_j}\left(\rho U_j \varepsilon\right)= \qquad \textit{Equation (4.7)}$$
$$\frac{\partial}{\partial x_j}\left[\left(\mu+\frac{\mu_t}{\sigma_\varepsilon}\right)\frac{\partial \varepsilon}{\partial x_j}\right]+\frac{\varepsilon}{k}\left(C_{\varepsilon 1}P_k-C_{\varepsilon 2}\rho\varepsilon+C_{\varepsilon 1}P_{\varepsilon b}\right)$$

In the above equations, $C_{\varepsilon 1}$, $C_{\varepsilon 2}$, σ_k, and σ_ε are constants. P_k is the turbulence production rate due to viscous forces, which is obtained using:

$$P_k=\mu_t\left(\frac{\partial U_i}{\partial x_j}+\frac{\partial U_j}{\partial x_i}\right)\frac{\partial U_i}{\partial x_j}-\frac{2}{3}\frac{\partial U_k}{\partial x_k}\left(3\mu_t\frac{\partial U_k}{\partial x_k}+\rho k\right) \qquad \textit{Equation (4.8)}$$

P_{kb} and $P_{\varepsilon b}$ represent the influence of buoyancy forces; however buoyancy is neglected in the present computations, due to the prescribed flow conditions.

The constants in the above equations are given below in Table 4.1.

C_μ	$C_{\varepsilon 1}$	$C_{\varepsilon 2}$	σ_k	σ_ε
0.09	1.44	1.92	1.00	1.30

Table 4.1 k – ε turbulence model constants

While the $k-\varepsilon$ model provides good predictions for many types of flows, there are certain applications for which this model is not suitable, such as:

- Flows with boundary layer separation
- Flows with sudden changes in the mean strain rate
- Flows in rotating fluids
- Flows over curved surfaces

This is due to the inability of the model to handle low turbulent Reynolds number computations, since it requires complex damping functions as well as the requirement of highly refined near-wall grid resolution ($y^+ < 0.2$).

4.2.2 $k - \omega$ Turbulence Model

The $k - \omega$ model presents a major advantage over the previous turbulence model, which is the near wall treatment for low-Reynolds number computations, making it more accurate and robust. This model does not involve complex nonlinear damping functions, and the requirement for a near wall resolution is increased from $y^+ < 0.2$, to $y^+ < 2$. The $k - \omega$ model assumes that the turbulence viscosity is linked to the turbulent kinetic energy, k, and the turbulent frequency, ω, through the following relation:

$$\mu_t = \rho \frac{k}{\omega} \qquad \textit{Equation (4.9)}$$

Wilcox [50] developed the $k - \omega$ model, which similarly to the $k - \varepsilon$ model, solves two transport equations, which are presented below:

k – equation:

$$\frac{\partial(\rho k)}{\partial t} + \frac{\partial}{\partial x_j}(\rho U_j k) = \frac{\partial}{\partial x_j}\left[\left(\mu + \frac{\mu_t}{\sigma_k}\right)\frac{\partial k}{\partial x_j}\right] + P_k - \beta' \rho k \omega + P_{kb} \qquad \textit{Equation (4.10)}$$

ω – equation:

$$\frac{\partial(\rho \omega)}{\partial t} + \frac{\partial}{\partial x_j}(\rho U_j \omega) = \frac{\partial}{\partial x_j}\left[\left(\mu + \frac{\mu_t}{\sigma_\omega}\right)\frac{\partial \omega}{\partial x_j}\right] + \alpha \frac{\omega}{k} P_k - \beta \rho \omega^2 + P_{\omega b} \qquad \textit{Equation (4.11)}$$

The constants in the above equations are given below in Table 4.2.

β'	α	β	σ_k	σ_ω
0.09	5/9	0.075	2	2

Table 4.2 k – ω turbulence model constants

The main issue with the $k - \omega$ Wilcox model is its strong sensitivity to free stream conditions; such that, depending on the value specified for ω at the inlet, it can give a significant variation in the results.

4.2.3 Shear-Stress-Transport (SST) Model

To solve the problem experienced by the $k - \omega$ model, Menter [51] developed a modified version of it. This new model blends between the $k - \omega$ model near the surface and the $k - \varepsilon$ model in the outer region. This model combines the two turbulence models ($k - \omega$ and $k - \varepsilon$) into two parts of the model, which is known as the Shear Stress

Transport (SST) $k-\omega$ model. The SST $k-\omega$ model accounts for the transport of the turbulent shear and gives highly accurate predictions of the onset and the amount of flow separation under adverse pressure gradients by including transport effects into the eddy-viscosity formulation.

The turbulent eddy-viscosity is modified through the following relation:

$$\mu_t = \rho \frac{\alpha_1 k}{max(\alpha_1 \omega, SF_2)} \qquad \textit{Equation (4.12)}$$

The two transport equations are transformed into the following equations:

k – equation:

$$\frac{\partial(\rho k)}{\partial t} + \frac{\partial}{\partial x_j}(\rho U_j k) = \frac{\partial}{\partial x_j}\left[\left(\mu + \frac{\mu_t}{\sigma_{k3}}\right)\frac{\partial k}{\partial x_j}\right] + P_k - \beta'\rho k\omega + P_{kb} \qquad \textit{Equation (4.13)}$$

ω – equation:

$$\frac{\partial(\rho\omega)}{\partial t} + \frac{\partial}{\partial x_j}(\rho U_j \omega) = \frac{\partial}{\partial x_j}\left[\left(\mu + \frac{\mu_t}{\sigma_{\omega 3}}\right)\frac{\partial \omega}{\partial x_j}\right] + \frac{(1-F_1)2\rho}{\sigma_{\omega 2}\omega}\frac{\partial k}{\partial x_j}\frac{\partial \omega}{\partial x_j} + \alpha_3 \frac{\omega}{k} P_k - \beta_3 \rho \omega^2 + P_{\omega b} \qquad \textit{Equation (4.14)}$$

In Equation (4.12), S is an invariant measure of the strain rate. While F_1 and F_2 are blending functions which are critical to the SST $k-\omega$ model. Their formulation is based on the distance to the nearest surface and on the flow variables, F_1 is a function of the wall distance, and is equal to 1 near the surface and decreases to 0 outside the boundary layer. F_2 restricts the limiter to the wall boundary layer.

The superior performance of the SST $k-\omega$ model has been verified in a large number of validation studies by Bardina *et al.* [52]. The model is more suited for high accuracy boundary layer simulations, where previously in section 1.4, it has been explained that the flow structure within the wheel-space is dominated by the boundary layers in the stator and rotor discs. In this thesis, the SST $k-\omega$ model has been used for all computations other than the results presented in section 6.1, which present a turbulence model sensitivity study on the pressure distribution in the annulus.

4.3 WALL FUNCTIONS

ASNYS CFX uses scalable wall-functions, which is an extension of Launder and Spalding's method [53], to reduce the computational cost related with integrating the flow properties to the wall. The advantage of using wall-functions is that the spacing between the wall and the first mesh point can be greatly increased, thus by applying the law-of-the-wall approximation at this first point (assumed to be located in the log region of the boundary layer profile), the shear stress and velocity can be calculated. The minimum non-dimensional distance to the wall, y^+ (defined in Figure 4.3), for the high Reynolds number $k-\varepsilon$ and $k-\omega$ based models (including SST) is $y^+ \approx 11$.

Figure 4.3 illustrates the iterative method used to calculate the shear stress and velocity near the wall. The turbulent kinetic energy, k, is estimated by solving the transport equations for the appropriate turbulence model. It is then substituted into the wall shear stress equation, τ_ω, which in turn is used to calculate the non-dimensional distance to the wall, y^+. The law-of-the-wall associates y^+ to the near wall velocity, u^+, which is used to calculate the wall tangential velocity, U_t, which is finally inputted back into the transport equations.

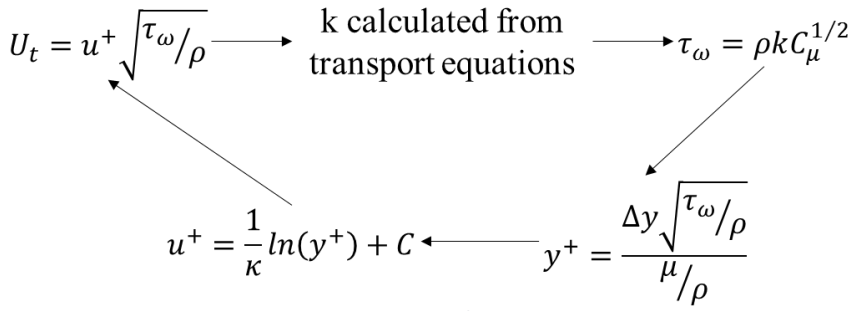

Figure 4.3 Wall-function method

In rotating disc systems where the flow structure is dominated by the boundary layers in the stator and rotor discs, the performance of the wall function is especially sensitive to the value of y^+; which if, is too high, will over-estimate u^+ and in turn also the shear stress. Δy is the distance from the wall, κ is the von Karman constant and C is a log-layer constant which depends on the wall roughness.

4.4 FLUID PROPERTIES, BOUNDARY SETTINGS AND ADDITIONAL VARIABLE FOR CONCENTRATION

All computations in this thesis utilise air at 15 °C as the ideal gas for fluid properties, through which density is calculated from the Ideal Gas Law:

$$\rho = \frac{wp_{abs}}{R_0 T} \qquad \textit{Equation (4.15)}$$

where w is the molecular weight, p_{abs} is the absolute pressure, and R_0 is the universal gas constant.

The following boundary conditions were applied at the two inlets and outlet:

- Inlets – mass flow rate normal to boundary with a 5% turbulence intensity.
- Outlet – average static pressure over the whole boundary with atmospheric pressure, this allows the pressure profile at the outlet to vary based on upstream influences while constraining the average pressure to the specified value.

An additional scalar variable, in the form of an additional mass transport equation, is introduced into the computations with a kinematic diffusivity of 1.6×10^{-5} m^2/s, in order to calculate the concentration sealing effectiveness. To calculate the concentration effectiveness, ε_c, of a computed case, Equation (3.1) is used.

4.5 MESH GENERATION

The accuracy of the computed solutions is highly dependent on the mesh, where increasing the number of mesh cells and decreasing their size, improves the accuracy of the results (since more physical flow behaviours can be captured) at the cost of higher computing times and power requirements. Throughout this study, the mesh has been generated using ANSYS ICEM CFD. The methodology used by ICEM consisted in firstly creating a structured surface mesh before converting it into an unstructured volume mesh.

There are various types of elements which can be used to discretise the flow domain; these include hexahedral and tetrahedral elements. Tetrahedral elements are suitable for complex geometries and are generally used by automatic discretisation programs; however they require 9 times the amount of elements to fill the same domain as a

hexahedral element of the same length scale, and are also not ideal for flows near the wall. Generally, numerical diffusion is reduced when element faces are parallel and normal to the flow direction. In the boundary layers of rotating disc systems, the mean flow direction is generally parallel to the wall, such that tetrahedral elements would have face angles acute to the flow, hence suffering from losses in numerical accuracy.

Instead, hexahedral or quadrilateral elements, are placed in the wall region, which have faces aligned with the flow direction and do not experience small internal angles when their resolution is changed. The elements are built to a prescribed number of layers, with increasing thickness away from the wall. This allows for better control of the distance of the first node from the wall boundary (good control of y^+ values), and thus a smooth transition in the element sizing between the wall boundary and the main volume mesh is possible.

The three different mesh domains are attached into a single multi-body model using Generic Grid Interfaces (GGI) and/ or Reference Frame Change Interfaces (RFCI), i.e. Frozen Rotor Interface.

A comprehensive mesh sensitivity analysis has been carried out to ensure that the computed results are balanced between numerical accuracy and computational time. Figure 4.4 shows the structured hexahedral surface mesh for the three domains of the CFD model. The boundary layers for all the solid surfaces were appropriately modelled, accounting for the required value of $y^+ \leq 10$ for the SST turbulence model.

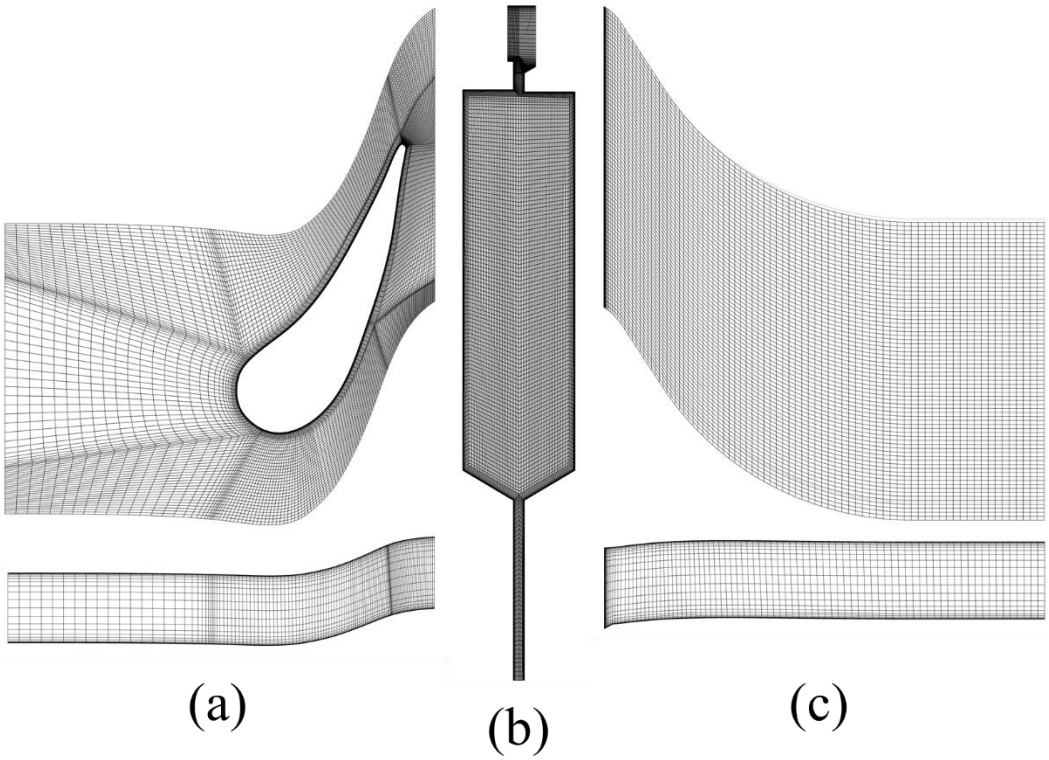

Figure 4.4 Surface mesh for each domain of the CFD model. (a) Stator domain (top and lateral view respectively); (b) Wheel-space domain (periodic side view only); (c) Rotor domain without blade (top and lateral view respectively)

4.6 PARALLEL APPROACH

Present day simulations keep drastically reducing computing times by solving computational models in parallel. Another alternative to further reducing computing times, is the use of high-performance computers (HPC), which are designed and built to reduce system bottlenecks. Computations in this study were solved using Aquila, the high-performance computer at the University of Bath; it consists of 100 nodes, each node with 8x 2.8 GHz cores (800 cores total), with 2GB RAM/core. A parallel computing analysis was performed, with 8 cores per simulation being the most optimum, since all the cores of a single node are utilised. The limiting factor for the computations in ANSYS CFX was found to be the number of parallel licenses available.

The parallel implementation of CFX-Solver is based on running identical versions of the code in multiple processors. The mesh is partitioned into a number of different segments, each of which is solved on a separate processor.

4.7 CODE VALIDATION

The commercial code, ANSYS CFX, is validated against two test cases for rotating flows: 1) experimental results from Chen *et al.* [12] for a rotor-stator system with radial outflow, 2) and a mathematical model with superposed sealing flow and no ingress developed at the University of Bath, similar to that depicted in Figure 1.13a.

4.7.1 Rotor-Stator Model by Chen *et al.*

In this section, computational results for a 3D rotor-stator model with no ingress (radial outflow) is compared against published experimental data by Chen *et al.* [12]. Computed results for two different configurations are compared in order to study the effect of the wheel-space geometry on the fluid dynamics. In terms of fluid dynamics, velocity profiles in the wheel-space are compared and the effects of the advection scheme is also presented. The computational results show very good agreement with the experimental data, especially at locations of higher radius, validating the 3D axisymmetric CFD rotor-stator model for predicting the flow structure and fluid dynamics in the wheel-space.

Figure 4.5 displays the two axisymmetric rotor-stator wheel-space models used for the validation. Figure 4.5a shows the geometry of the first model, which is identical to that of the experimental rotor-stator rig used by Chen *et al.* [12], referred to as the Chen rig model. The Chen rig model has an axial inlet for the sealing flow which is located at the axis of rotation. Figure 4.5b shows the geometry of the second model, which is based on an experimental test rig used for ingestion experiments at the University of Bath, referred to as the Bath rig model. This model has a radial inlet for the sealing flow located at a/b = 0.45. For both models, the sealing flow introduced into the system has zero inlet swirl.

All computations in this section are carried out using the SST turbulence model, which is supported by the findings of Zhou *et al*. [38], Rabs *et al*. [41] and Teuber *et al.* [46]. The computations are carried out at $Re_\phi = 1.25 \times 10^6$ and for a non-dimensional sealing flow rate value of C_w = 6100, similar to Chen *et al*.'s experiment [12].

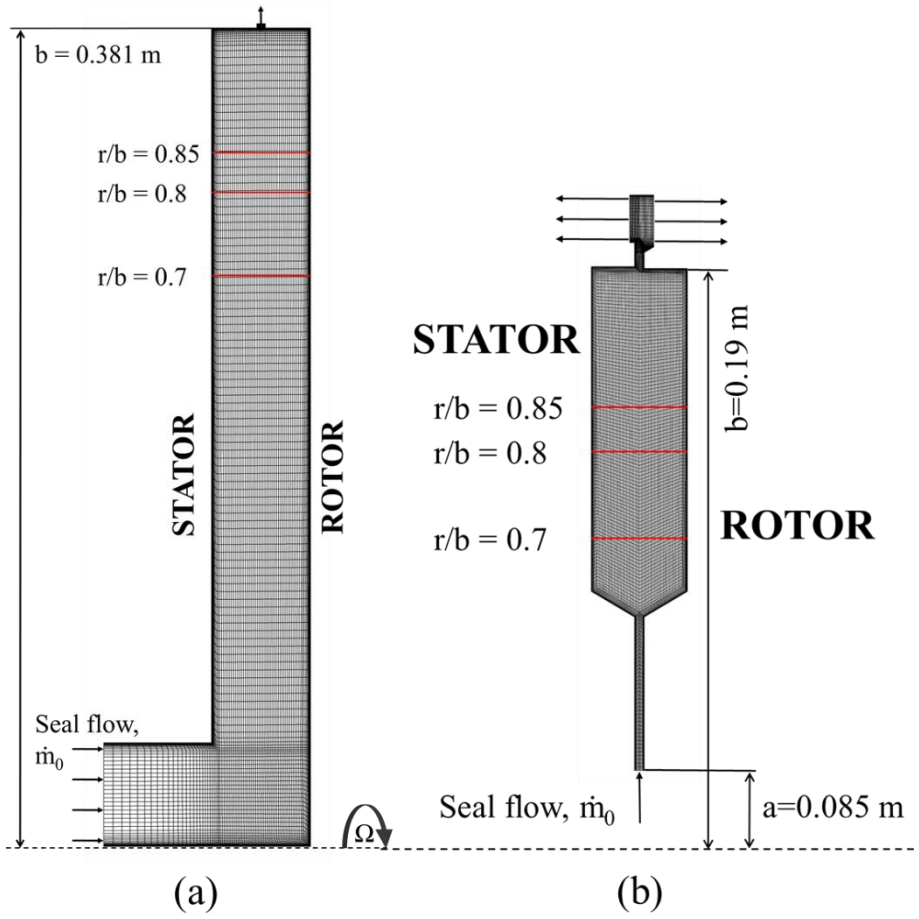

Figure 4.5 Mesh grid for axisymmetric rotor-stator models. (a) Chen rig model; (b) Bath rig model

To understand the fluid dynamics within a rotor-stator wheel-space, computed velocity profiles for the Chen rig and Bath rig models (upwind and high resolution advection schemes) are presented in Figure 4.6 (with radial velocity plots on the left, and tangential velocity plots on the right); alongside Chen *et al.*'s [12] experimental data for comparison purposes at $\lambda_T = 0.081$. Figure 4.5a shows the three radial locations ($0.7 \leq r/b \leq 0.85$) for which measured axial distributions of non-dimensional radial and tangential velocities have been recorded by Chen *et al.* [12]. The horizontal axis in the plots represent the non-dimensional axial location, *Z/s*, where *Z/s* = 0 is the stator wall and *Z/s* = 1 is the rotor wall.

The computed results for both geometries show good agreement with the experimental data and with each other, exhibiting geometric independence in terms of fluid dynamics within the wheel-space. The radial velocity (V_r / Ω*r*) results show typical rotor-stator flow behaviour, with the flow moving radially inward on the stator (*Z/s* = 0), and radially outward on the rotor (*Z/s* = 1), and no radial flow in the core similar to

Batchelor's type of flow. The computed result for the Chen rig model displays very good agreement with the experimental data at all radial locations. The computed results for the Bath rig model shows some disagreement at $r/b = 0.7$ with the experimental data, confirming that the computed results are influenced by the slanted surfaces in the lower part of the wheel-space. However this effect diminishes and nearly disappears with increasing non-dimensional radius (r/b).

The tangential velocity (V_φ / Ωr = swirl ratio) results also show typical rotor-stator flow behaviour, exhibiting separate boundary layers on the stator and rotor at each radial location similar to Batchelor type flow. The swirl ratio at the stator = 0 and at the rotor = 1, as expected, with a core of constant swirl ratio which increases with increasing radial location. The computed results give very good agreement with the experimental data, and show very little effect of geometry on the swirl ratio.

The Bath rig model was computed using two different settings, the Upwind Differencing Scheme and High Resolution Scheme. This was carried out to check whether the fluid dynamics, hence velocity profiles, within the rotor-stator wheel-space were influenced by the advection scheme. Figure 4.6 shows that the computed results of the fluid dynamics in the wheel-space are insensitive to the advection scheme. Another point to be noted, is that the convergence level achieved by the Upwind Differencing Scheme is better than that of the High Resolution Scheme, since it doesn't require a nonlinear formulation for β at each node of the model.

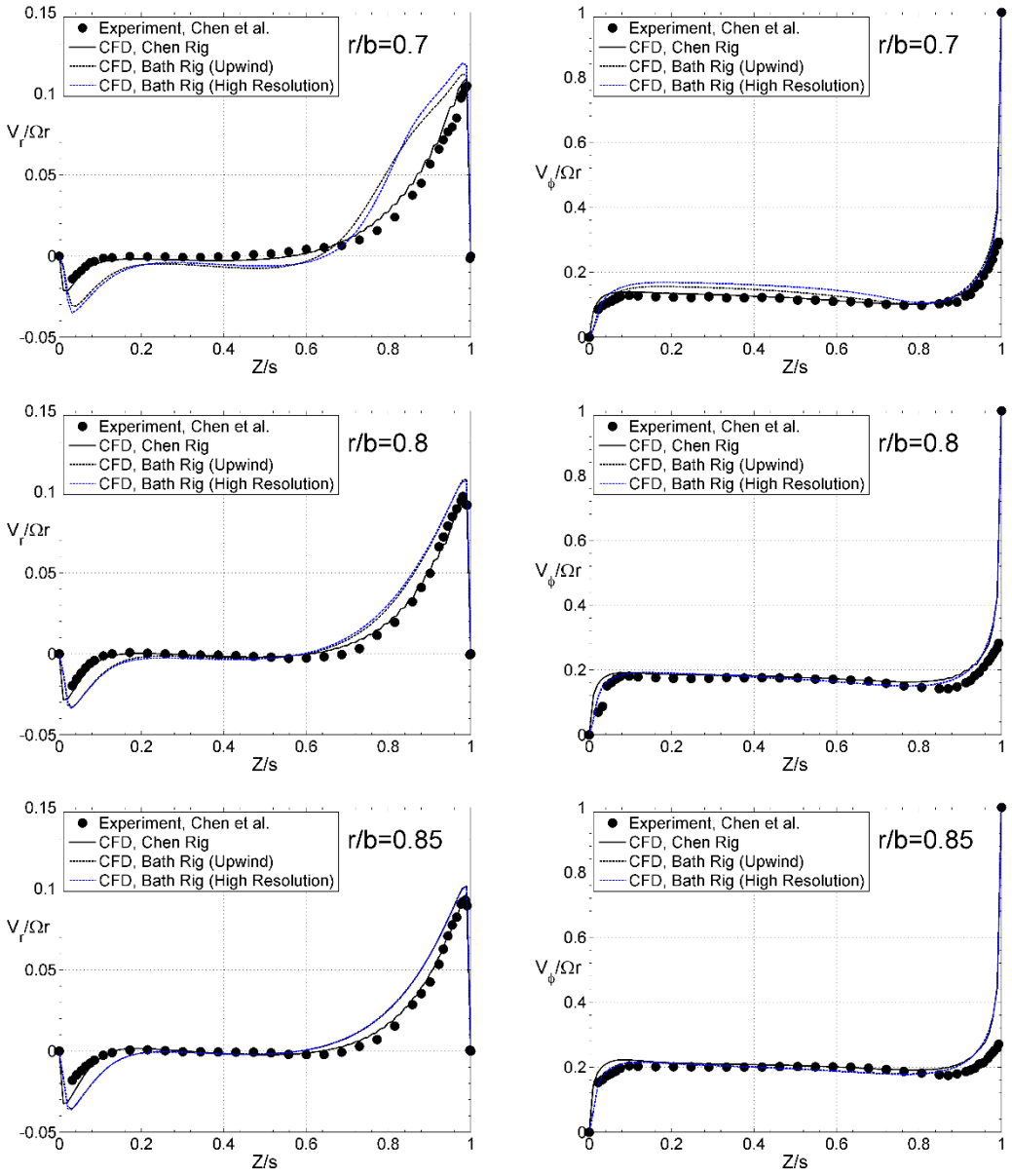

Figure 4.6 Comparison of velocity profiles for experimentally measured data and computed CFD models for the Chen Rig and Bath Rig (upwind and high resolution advection schemes) for $\lambda_T = 0.081$ at $Re_\phi = 1.25 \times 10^6$

The effect of sealing flow rate on the velocity distributions is also investigated; where the turbulent flow parameter, $\lambda_T = C_{w,o} Re_\phi^{-0.8}$, is used to represent the sealing flow rate at $\mathrm{Re}_\Phi = 8.2 \times 10^5$. Four sealing flow rates are chosen to show this effect, varying from λ_T = 0 to λ_T = 0.11. Figure 4.7 shows computed radial and tangential velocity distributions at $x = r/b = 0.8$ for the four different values of λ_T for the Bath rig model as a radial outflow case as depicted in Figure 4.5b. As λ_T is increased, the magnitude of the inward radial velocity on the stator decreases and the outward radial velocity on the rotor increases. In terms of the circumferential velocity, increasing λ_T

reduces the magnitude of the swirl ratio in the core, which shows that higher values of sealing flow rates reduce the core rotation.

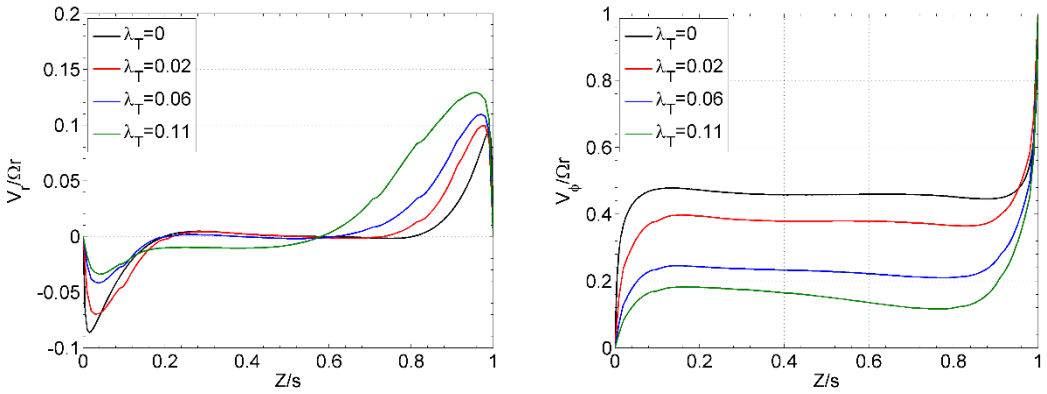

Figure 4.7 Computed velocity profiles for the Bath rig model at different λ_T values

4.7.2 Rotor-Stator with Radial Outflow at University of Bath

A numerical mathematical model developed at the University of Bath is used to compare and further validate the computational results for the 3D rotor-stator system with no ingress (shown in Figure 4.5b). Computed results at various values of λ_T for the Bath rig model are compared in order to study the effect of the sealing flow on the flow structure. In terms of the fluid dynamics, radial distributions of swirl ratio in the wheel-space at Z/s = 0.25 are compared between the CFD results and the mathematically calculated results. The computational results show good agreement with the mathematical model results at lower radius. This further supports the 3D axisymmetric CFD model for the prediction of flow structure within the wheel-space.

The mathematical model used for the comparison is that of a closed system with sealing flow and no ingress as shown in Figure 1.13a. The model is developed by starting off from the Navier-Stokes equations, from which the boundary layer equations are obtained in the form of Partial Differential Equations (PDEs). Subsequently, the momentum integral equations, in the form of Ordinary Differential Equations (ODEs) which are easier to solve, are used to approximate the boundary layer equations. To solve the mathematical model, it requires three input variables, which are provided from the computational results: 1) λ_T (turbulent flow parameter), 2) β_o (an initial swirl value), and 3) x_o (the starting radial location for β_o).

Figure 4.8 shows radial distributions of swirl ratio at *Z/s* = 0.25 for various values of λ_T for the computed and mathematical model results. The figure illustrates that for both sets of results, the swirl ratio in the wheel-space reduces as the sealing flow rate increases, which causes a reduction in the core rotation. Further increasing the sealing flow amplifies this effect. This behaviour of the flow structure with increasing sealing flow is to be expected, as shown by previous literature [7, 12]. The figure shows good similarity between the computed CFD swirl ratio and the mathematically calculated swirl distribution, especially at *r/b* < 0.9. The divergence between both sets of data (computation and mathematical models) at high radius, can be attributed to the different outlet boundary conditions set for the two models; in the CFD case, the outlet is set to an average static pressure corresponding to atmospheric conditions.

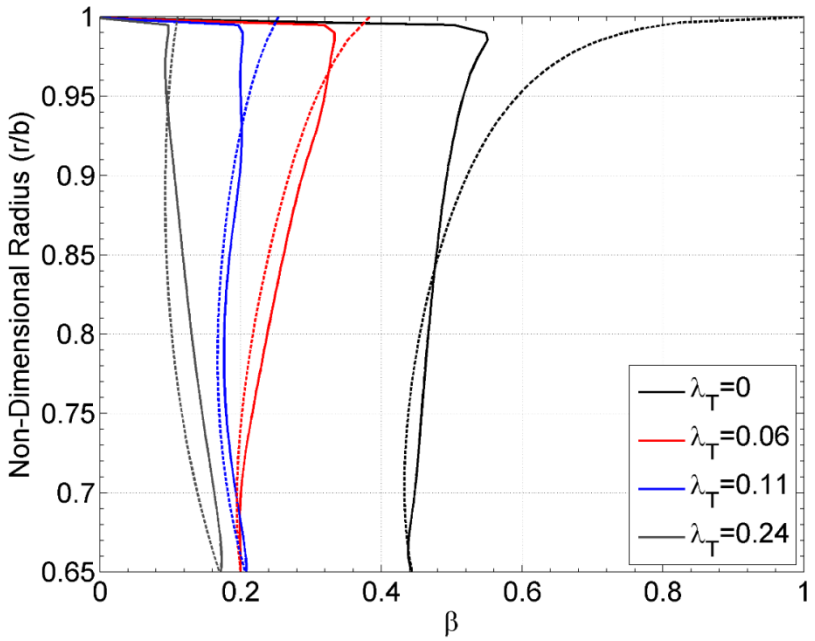

Figure 4.8 Comparison of swirl ratio at Z/s = 0.25 for computed CFD model (solid lines) and mathematical model (dashed lines) for various λ_T values at $Re_\phi = 8.2 \times 10^5$

4.8 CONVERGENCE OF AXISYMMETRIC MODEL

The computed CFD results were completed when the target convergence was met; this is when the root-mean square (RMS) residual target value reached 10^{-6}, also monitoring points were set on the model, so that when the monitored pressures in the wheel-space reached a stable solution, the results were considered converged.

4.9 CHAPTER OVERVIEW

This chapter covered the development process of the computational model to be used in this study. The methodology and process used by ANSYS CFX is covered, such as the discretization method, the advection schemes, turbulence models, additional scalar equations and mesh generation process of the CFD model.

The CFD model (axisymmetric rotor-stator system with no ingress and superposed flow) is validated against experimental results and a mathematical model of a closed system with sealing flow and no ingress. The computed results show good agreement with the experimental results in terms of wheel-space axial distributions of radial and tangential velocities; and the mathematical model results in terms of wheel-space flow structure or radial distribution of swirl ratio.

5 PRELIMINARY METHODS FOR PREDICTING EI INGRESS

This chapter covers the early stage models which were developed to try to predict EI ingress. The models evolved through different stages as certain effects were encountered, changes such as the use of 'thin seals', reference frame selections, blade positioning, and the exclusion of the rotor blade.

5.1 THIN-SEAL APPROACH

This section covers a CFD study which investigated the use of a 'thin-seal' model for predicting EI ingress though an axial-clearance rim-seal, where the 'thin seal' means the radial dimension of the seal is made as thin as permitted by the meshing software. This study continued that of Zhou *et al*. [38], with 'on-design' conditions used for the steady state CFD model, attempting to predict similar results to the ones achieved by the experimental test rig at the University of Bath.

In this model, the rotor domain is modelled without the rotor blade (RB), since the early assumption was that the main driving force for ingestion is caused by the NGVs. Another reason for not incorporating the blade into the model is the fact that it is a steady-state simulation, and the selected Frozen Rotor (FR) frame change interface, requires a relative blade position to be set. The blade positioning can produce different results, thus the choice of not including the RB into the 'thin seal' model.

Figure 5.1 illustrates a schematic of the 'thin seal' model, where the system has two inlets: the sealing air inlet at low radius in the wheel-space and the external mainstream inlet which is upstream of the vane. The model shows the inlet and outlet boundary conditions, including the interfaces used for connecting the different domains. In this model the frame change interface is positioned between the wheel-space and the rotor domain, such that they each have a fixed relative position throughout the calculation. Equation transformations are made when the frame changes, and the fluxes are scaled by the pitch change when the pitch changes. The FR interface is most useful when the circumferential variation of the flow is large relative to the component pitch, also, the

model requires the least amount of computational effort of the three frame change/mixing models available [48].

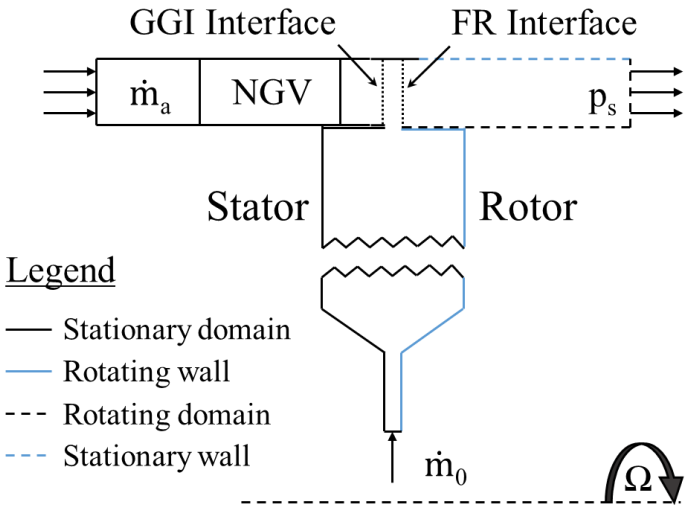

Figure 5.1 Schematic diagram of a generic axial-clearance seal, depicting the inlet/outlet boundary conditions and interfaces connecting the different domains; stator and wheel-space domains in stationary frame of reference, and rotor domain in rotating frame of reference

Figure 5.2a shows the real geometry of the axial-clearance seal which has been experimentally used at the University of Bath. Whereas Figure 5.2b, is the 'thin seal' equivalent of the same seal, which is intended to prevent the formation of an unrealistic vortex inside the seal clearance in the steady computations, which would generally inhibit the ingested flow into the wheel-space [38].

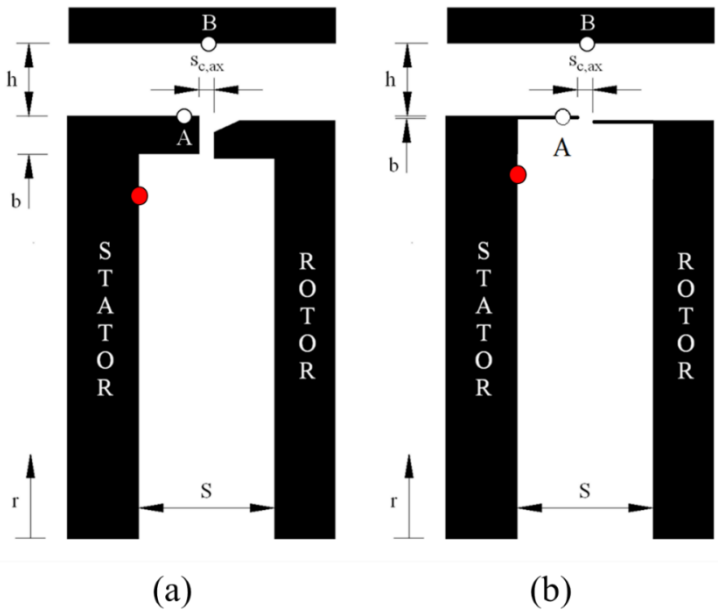

Figure 5.2 Axial-clearance seal. (a) Real geometry where b=190 mm; (b) Thin seal geometry where b=195 mm

Figure 5.3 shows the computed effectiveness curve (Φ_0 vs ε_c) at r/b = 0.958 for both axial-clearance seal geometries depicted in Figure 5.2 (red circles). The computed real geometry of the axial-clearance seal, greatly under-predicts ingestion (hence over predicting effectiveness). Zhou *et al*. [38] also experienced this effect and explained that it is caused by the formation of a vortex in the seal clearance. The computed thin seal seems to overcome this under-prediction of ingestion by minimizing the radial dimension of the seal clearance, which prevents the formation of the vortex. The plot illustrates that the thin seal performs better in predicting EI ingress, however ingestion is over predicted, which can be caused by the alteration of the seal clearance's dimension.

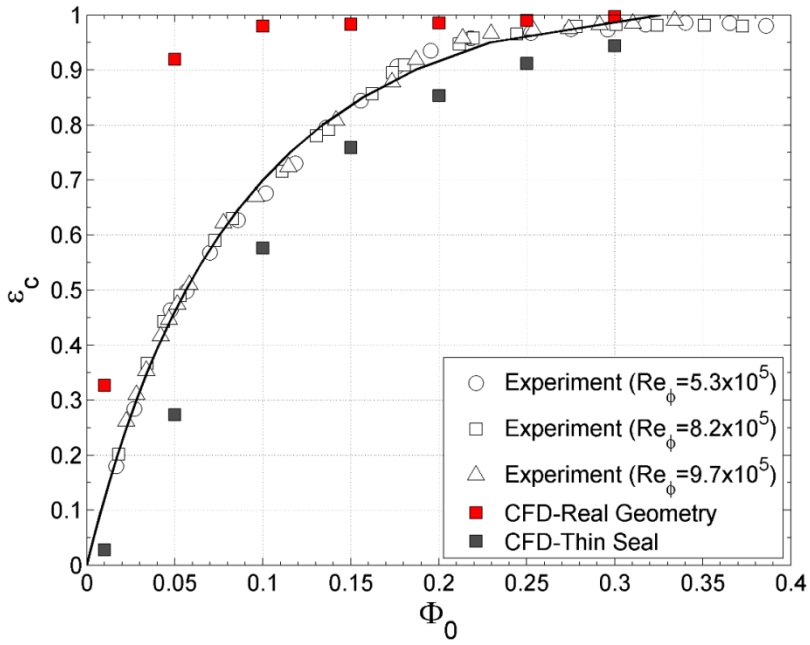

Figure 5.3 Comparison between experimental effectiveness curve and computed effectiveness (real and thin seal models) for axial-clearance seal with EI ingress for $Re_\phi = 8.2 \times 10^5$

This 'thin seal' method initially seemed a viable approach to overcome the formation of the unrealistic vortex in steady-state computations. However, as the method was tested for more complicated seal geometries (such as radial-clearance and/ or double-clearance seals) which are more representative of gas turbine engines, it was found that there are too many possible geometric alterations to account for when modifying the real geometry into a 'thin seal' version.

5.2 EFFECT OF FRAME OF REFERENCE ON MODEL DOMAINS

Rabs *et al.* [41] and Teuber *et al*. [46] carried out ingestion computations where the wheel-space domain was computed in the rotating frame of reference, although the latter consisted in unsteady computations; where both experienced high levels of ingestion, suggesting that the inclusion of the wheel-space in the rotating frame of reference inhibited the formation of the previously identified "numerical" vortex [38], or induced ingress.

The 3D steady CFD model was therefore adapted to use the real geometry (Figure 5.2a) with the inclusion of the rotor blade positioned at θ = -0.5 (see Figure 5.6a), and the wheel-space domain was computed in the rotating frame of reference, which means the FR interface is positioned between the stator and wheel-space domain, as can be seen in Figure 5.4. This new model has the same inlet and outlet boundary conditions as those set previously in the thin seal model.

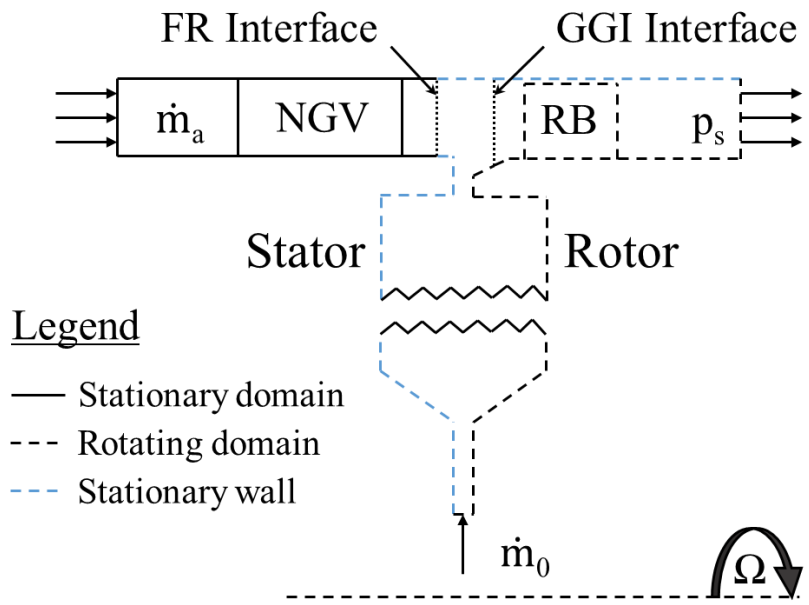

Figure 5.4 Schematic diagram of a generic axial-clearance seal, depicting the inlet/outlet boundary conditions and interfaces connecting the different domains; stator domain in stationary frame of reference, wheel-space and rotor domains in rotating frame of reference

Figure 5.5 shows the computed effectiveness curve (Φ_0 vs ε_c) at r/b = 0.958 for the axial-clearance seal geometry depicted in Figure 5.2a (red circle), with the two reference frame settings (stationary and rotating) applied to the wheel-space domain. The computed results for the wheel-space in the stationary frame of reference experiences great under prediction of ingestion due to the unrealistic vortex inhibiting ingress into the wheel-space as previously discussed. However, the computed results with the wheel-space in the rotating frame of reference, shows very good agreement with the experimental results, confirming that the steady CFD model can experience appropriate levels of ingestion. This dramatic effect of reference frame was first identified by Teuber [46] using the same CFX software.

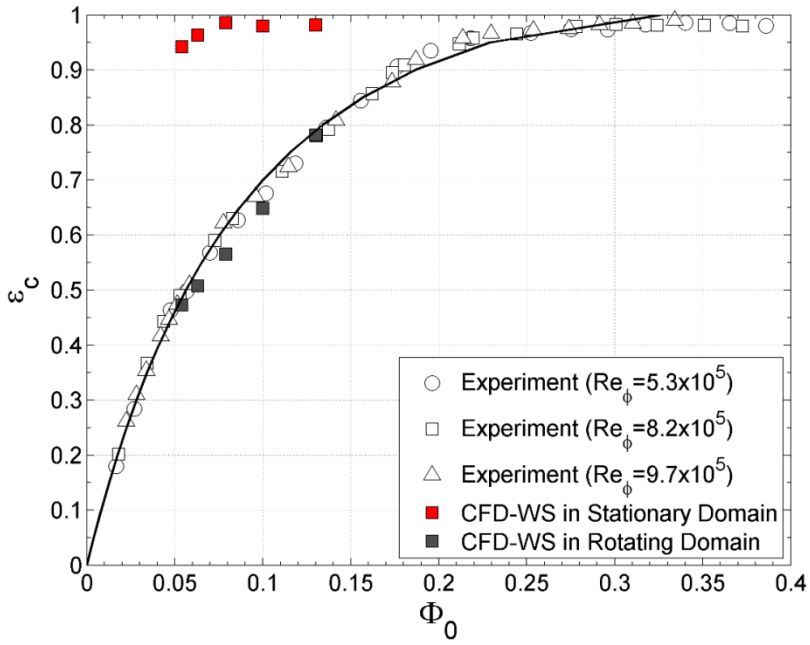

Figure 5.5 Comparison between experimental effectiveness curve and computed effectiveness (wheel-space in stationary and rotating frame of reference, with blade positioned at θ = -0.5) for axial-clearance seal for $Re_\phi = 8.2 \times 10^5$

This CFD model is able to appropriately predict ingestion into the wheel-space, however as previously discussed, the inclusion of the rotor blade into the model presents the question of its position and its effect.

5.3 FROZEN ROTOR - ROTOR BLADE POSITIONING

This section presents computational results for a 3D steady model with similar settings as those shown in Figure 5.4. The main difference is that for a given sealing flow rate case, four computations are carried out, each for a different blade position as depicted in Figure 5.6. The four blade positions chosen are similar to those chosen by Rabs *et al*. [41].

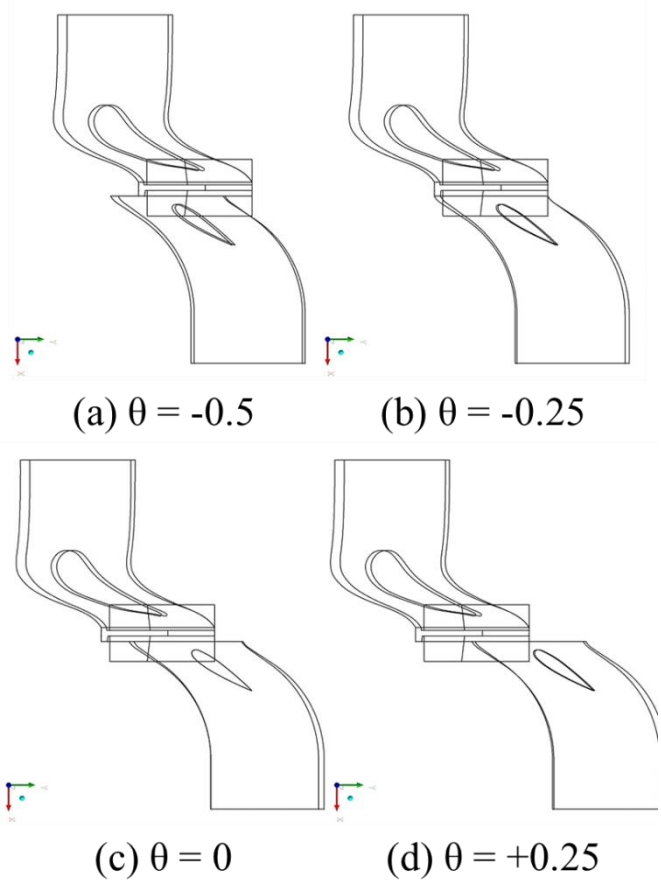

Figure 5.6 Rotor blade positioned at 4 different positions for Frozen Rotor blade computations

Figure 5.7 shows the computed effectiveness curve (Φ_0 vs ε_c) at r/b = 0.958 for the axial-clearance seal at the four blade positions depicted in the figure above. An average of the computed effectiveness for the four blade positions is also plotted in the figure. The plot also includes Rabs *et al*. [41] computed data for Φ_0 = 0.1 for the four positions and its corresponding average value.

The plot reveals that the blade position has a significant influence in the computed effectiveness results, especially at lower sealing flow rates. As the sealing flow rate is increased, to the point where effectiveness is above 90%, the computed results for each

blade position seems to vary very little. The encouraging aspect of this CFD model is that the average of the four blade positions has good agreement with the experimental data. The calculations from Rabs *et al.* [41] have a similar effectiveness trend as the present results, however Rabs results vary from the results in this study. This might be due to the sealing flow inlet being at a higher radius in the Rabs model.

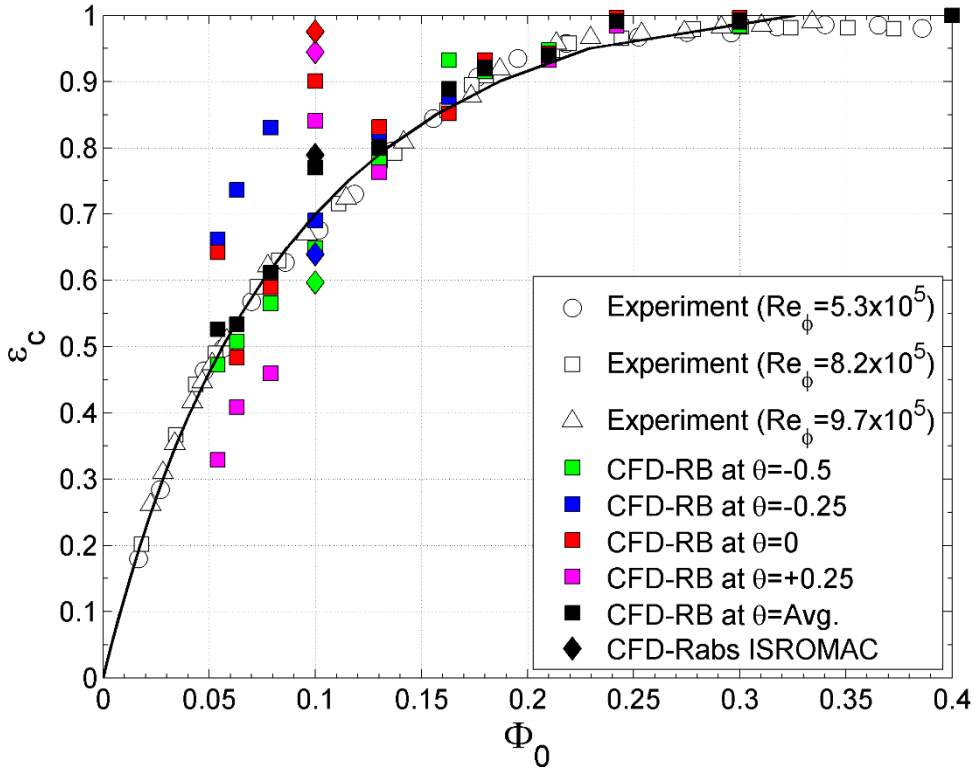

Figure 5.7 Comparison between experimental effectiveness curve and computed effectiveness (different rotor blade positions and average) for axial-clearance seal for $Re_\phi = 8.2 \times 10^5$; also included Rabs et al. [41] computational data at $\Phi_0 = 0.1$

5.3.1 Pressure Coefficient in Annulus

To further understand the difference in the computed results for each blade position (Figure 5.7), the circumferential pressure distribution in the annulus at location A (Figure 5.2a) was investigated. It has been previously stated that the main driving force for EI ingress is the pressure downstream of the NGV, therefore Figure 5.8 shows a comparison between the experimentally measured C_p in the annulus against computed results for the four blade positions shown in Figure 5.6. The average of the computed results is also presented, and as can be seen, the blade position has a significant influence on the pressure distribution at location A, with the average having reasonable agreement with the experimental data.

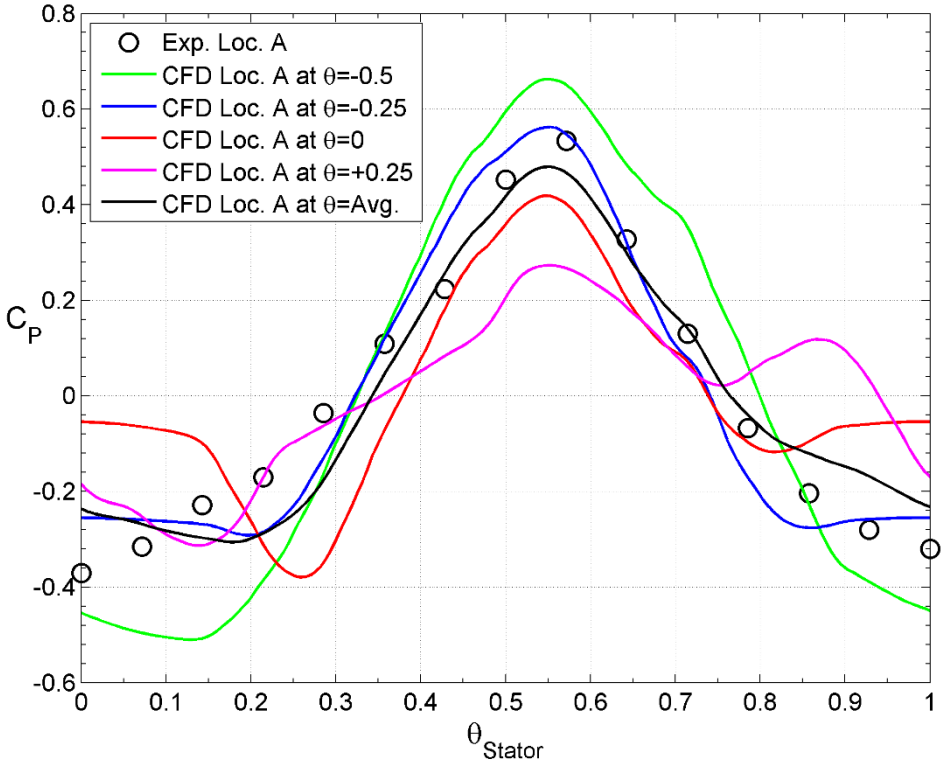

Figure 5.8 Effect of rotor blade position on circumferential distribution of C_p over non-dimensional vane pitch for $Re_\phi = 8.2 \times 10^5$ at location A

This steady CFD model successfully predicts EI ingress, however the requirement of running multiple computations for various blade positions makes this approach time consuming and complex when post processing. Even though the model is quick to compute, the question arises of how many positions and which positions should be computed, since the more positions that are computed the more closely the model represents the unsteady CFD situation.

5.4 CHAPTER OVERVIEW

This chapter covers the early stages of this research, where various CFD methods were developed to try and predict EI ingress. Each method led to the next, either by encountering certain issues in the computed results or by literature published by partner institutions. The various CFD models developed in the preliminary stages of this study were the 'thin seal' model, the frame of reference of the wheel-space, and the rotor blade positioning. Each model was assessed by having the computed data compared with the experimental data in terms of the effectiveness curves (Φ_0 vs ε_c), and for one of the models in terms of C_p at location A in the annulus.

The first approach showed that it was possible to eliminate the unrealistic vortex that previously inhibited ingestion by employing the 'thin-seal' axial-clearance model. The results for the 'thin-seal' model shows reasonable agreement with experimental data, however under-predicting effectiveness.

A review of relevant published literature gave insight on the effect of computing the wheel-space domain in the rotating frame of reference. Computed results for the wheel-space in the rotating frame of reference and the blade fixed at a given position, showed that for the real geometry of the axial-clearance seal, effectiveness values were in good agreement with experimental results.

The next logical step was to test the effect of positioning the rotor blade for the Frozen Rotor steady-state computation. Four blade positions were computationally tested for a range of sealing flow rates, and the C_p distribution at location A in the annulus presented. The blade position showed a strong effect on the C_p distribution at location A, and a significant influence in the computed effectiveness values, especially at low sealing flow rates ($\varepsilon_c < 90\%$). The average values of the four blade positions was found to be in good agreement with experimental measurements.

6 NON-BLADED APPROACH

This chapter presents the main steady-state CFD method of this study, which consists of a non-bladed model of the axial-clearance (and subsequently other) seals.

Literature reviewed by Teuber *et al*. [46] suggested very little effect of the rotor blades on the pressure distribution at location A, which is considered to be the main driving force of EI ingress. Scobie *et al*. [33] presented experimental data for off-design conditions, i.e. where the velocity vectors in the annulus vary from the design point, which showed little effect of the rotor blades on the pressure downstream the vanes. Therefore the previous Frozen Rotor CFD model was modified by excluding the rotor blade and computing the wheel-space and rotor domains in the rotating frame of reference, with the frame change interface located between the stator and wheel-space domain. This approach takes away the uncertainty and complexity of fixing the rotor blade at a given position, whilst also reducing the mesh size for the rotor domain.

It should be noted that this method was successful in terms of predicting ingress for the Bath University rig which featured symmetric blades. For other turbine stages with aerodynamically-loaded aerofoils there is likelihood to be an influence of the rotating blade.

6.1 TURBULENCE MODEL SENSITIVITY

A turbulence model sensitivity check was carried out on the non-bladed CFD model, to verify which turbulence model appropriately predicts the pressure distribution in the annulus. The $k - \varepsilon$, $k - \omega$ and SST turbulence models were tested with the two different advection schemes, Upwind Differencing Scheme and High Resolution Scheme. The computed results in terms of ΔC_p at locations A and B in the annulus, are presented in Table 6.1. It was found that the SST turbulence model best predicted the pressure distribution in the annulus, which is also supported by the findings of Zhou *et al*. [38], Rabs *et al*. [41] and Teuber *et al*. [46]. The Upwind Differencing Scheme was chosen as the most appropriate advection scheme, because it is able to predict the appropriate pressure in the annulus while also computing realistic fluid dynamics in the wheel-space as shown in the previous section. Also the Upwind scheme is able to converge to higher

convergence levels (RMS=10^{-7}) compared to the High Resolution scheme (RMS=10^{-4}). Thus the Upwind scheme was utilised in all of the following computations.

Turbulence Model	Advection Scheme	$\Delta C_{p,A}$	$\Delta C_{p,B}$	$\Delta C_{p,A}^{1/2}$	$\Delta C_{p,B}^{1/2}$
k – ε	Upwind	0.819	0.349	0.905	0.591
	High Resolution	0.804	0.332	0.896	0.577
k - ω	Upwind	0.851	0.371	0.922	0.609
	High Resolution	0.805	0.375	0.897	0.613
SST	Upwind	0.876	0.383	0.936	0.619
	High Resolution	0.832	0.388	0.912	0.623

Table 6.1 Effect of turbulence model and advection scheme on ΔC_p at locations A and B for $\Phi_o = 0$ at $Re_\phi = 8.2 \times 10^5$

6.2 PRESSURE COEFFICIENT IN ANNULUS

The circumferential distribution of C_p at location A (vane platform) is shown in Figure 6.1, and at location B (on the outer shroud at the axial location of the middle of the seal clearance) is shown in Figure 6.2. In both figures, the symbols denote experimental measurements and the coloured lines their equivalent computed values. The measurements were made at the design point (Table 3.2) for the case of no sealing flow, i.e. $\Phi_0 = \lambda_T = 0$ for three values of Re_ϕ. It should be noted that the flow is over a small range of Mach numbers.

It can be seen in Figure 6.1 and Figure 6.2 that, since Re_W/Re_ϕ is constant (Table 3.2), the three distributions at location A and B for both experiments and computations, are virtually independent of Re_ϕ. There is a significant difference between the distributions at location A and B, where the non-dimensional peak-to-trough pressure difference, ΔC_p, is greater at location A than that at location B. This pressure difference between both locations is expected, as the pressure is expected to decrease with axial distance from the vane, which causes the reduction at location B. This pressure reduction with axial distance from the vane trailing edge can be visualized from the computed figure in Figure 6.4. It should be noted that ΔC_p depends on where it is measured.

Figure 6.1 shows very good agreement between the measured and computed data at location A, which is considered to be the main driving force for EI ingress. The computed data is slightly higher at low values of C_p than the measured data, but this is nullified by the slightly higher C_p peak experienced by the computations, hence both computations and experiment end up having a virtually similar peak-to-trough pressure difference, ΔC_p. These were all computed at $\Phi_o = 0$ to match the experimental boundary condition.

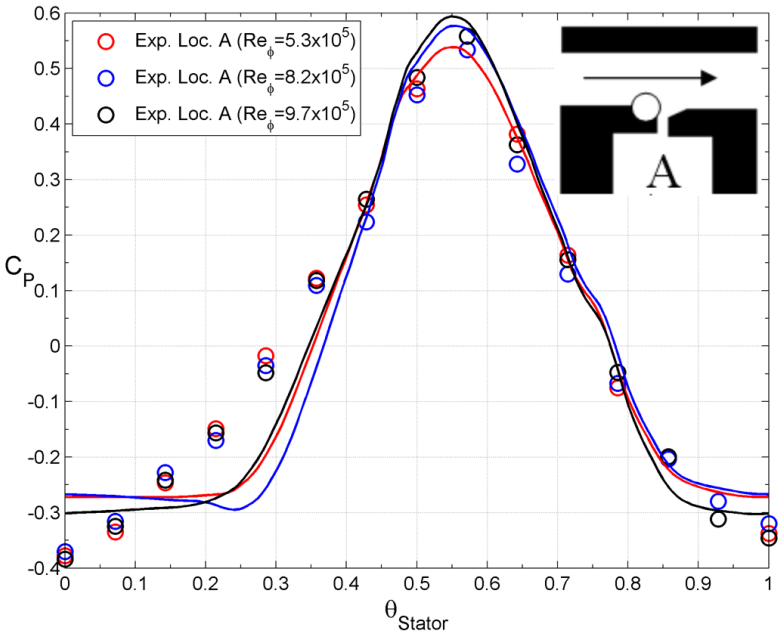

Figure 6.1 Effect of Re_ϕ on circumferential distribution of C_p over non-dimensional vane pitch for $Re_W/Re_\phi = 0.538$ at location A, $\lambda_T = \Phi_o = 0$

Figure 6.2 shows that there is a greater difference between the measured and computed data at location B. This major difference is probably because the CFD model does not model the rotor blade, which would be expected to have a greater influence in the pressure distribution at location B, due to the blade's proximity to this measurement location. Again the computations and experiments are at $\Phi_o = 0$.

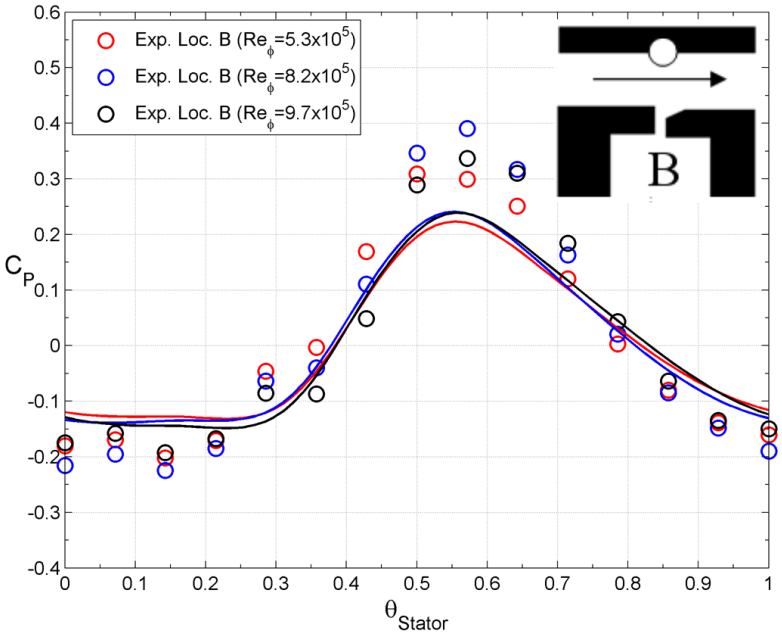

Figure 6.2 Effect of Re_ϕ on circumferential distribution of C_p over non-dimensional vane pitch for $Re_W/Re_\phi = 0.538$ at location B, $\lambda_T = \Phi_o = 0$

Table 6.2 presents the computed numerical values of ΔC_p for the three computations at different Re_ϕ for location A and B (Figure 6.1 and Figure 6.2). The tabulated results again show the independence of ΔC_p to Re_ϕ at both locations.

Re_ϕ	Disc Speed (RPM)	$\Delta C_{p,A}$	$\Delta C_{p,B}$	$\Delta C_{p,A}^{1/2}$	$\Delta C_{p,B}^{1/2}$
5.32 x 10^5	2000	0.813	0.359	0.902	0.599
8.17 x 10^5	3000	0.876	0.383	0.936	0.619
9.68 x 10^5	3500	0.900	0.391	0.949	0.625

Table 6.2 Effect of varying Re_ϕ on ΔC_p at locations A and B in the annulus for $Re_W/Re_\phi = 0.538, \lambda_T = \Phi_o = 0$

Figure 6.3 shows the measured and computed circumferential distribution of C_p for $Re_\phi = 8.2 \times 10^5$ at the design point at location A for three different values of λ_T. The peak-to-trough pressure difference decreases slightly as the sealing flow increases, which is attributed to the 'spoiling effect' of the egress as it interacts with the main flow in the annulus [6], which is consistent with the findings of Bohn *et al.* [54]. The figure shows relatively good predictions of the measured C_p distribution with increasing sealing flow rate. For the highest sealing flow case, the computation appears to experience a much greater 'spoiling effect', although the peak pressure trends are qualitatively similar.

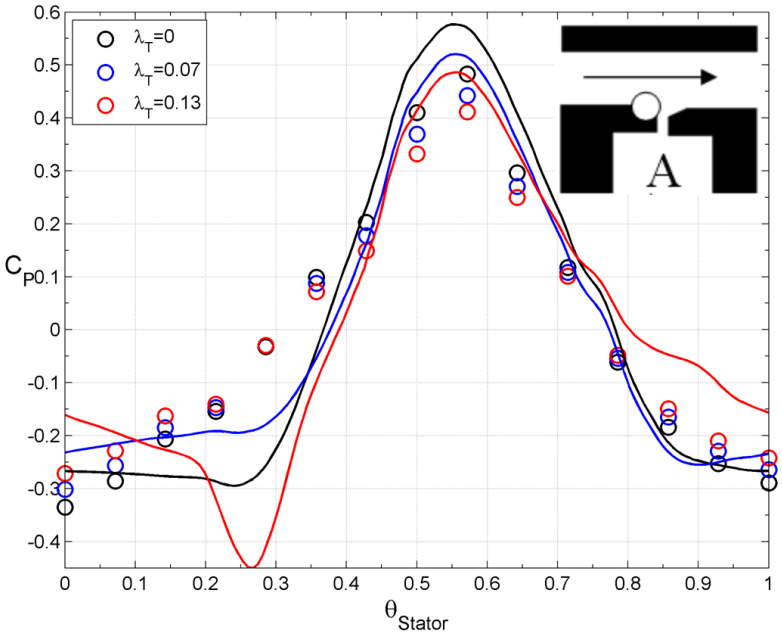

Figure 6.3 Effect of sealing flow on circumferential distribution of C_p over non-dimensional vane pitch for $Re_\phi = 8.2 \times 10^5$

Figure 6.4 shows an isometric axial-circumferential contour plot of the computed pressure distribution downstream of the vane trailing edge on the vane platform. The figure illustrates the pressure reduction with axial distance from the vane trailing edge, which emphasizes the importance of selecting the appropriate axial location (location A) for pressure measurements for the previously discussed orifice model [40].

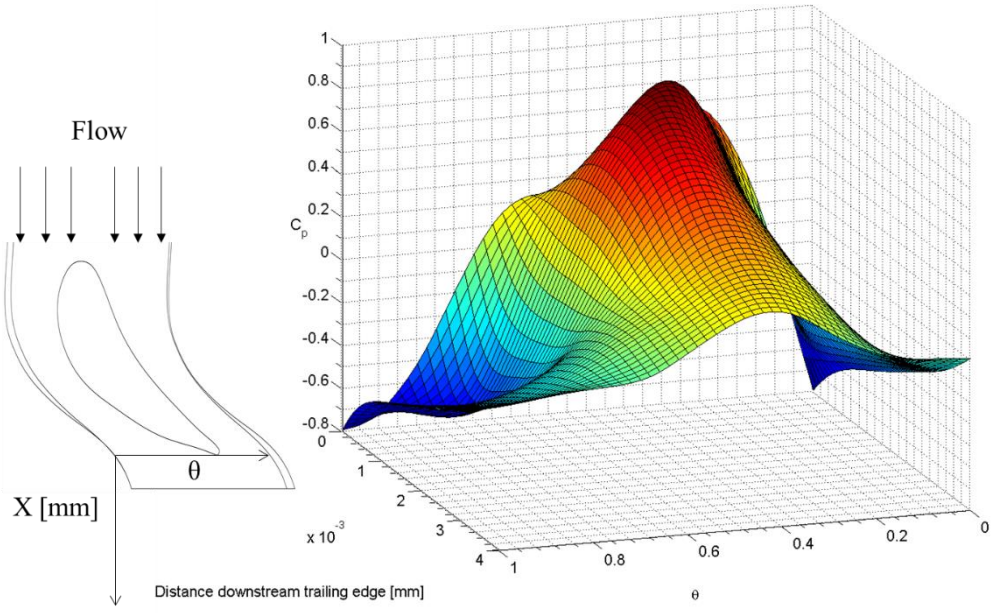

Figure 6.4 Axial-circumferential pressure distribution downstream vane trailing edge for axial clearance-seal for $Re_\phi = 8.2 \times 10^5$

Figure 6.5 shows the expected experimental measured variations of $\Delta C_p^{1/2}$ with Re_W/Re_ϕ at the two locations (A and B) in the annulus [6]. The experimental data was collected for $Re_\phi = 5.3 \times 10^5$ and 8.2×10^5 over the range $0 < Re_W < 4.9\text{x}10^5$. A computational study was carried out for different values of Re_W/Re_ϕ, with constant $Re_\phi = 8.2 \times 10^5$, to check if this non-bladed steady CFD model could capture the increase in $\Delta C_p^{1/2}$ with increasing Re_W/Re_ϕ. The value of β - β_o, i.e. the divergence angle for the design point at β - β_o = 0, is also shown at the top axis of this figure. The figure shows that this CFD model can capture the correct pressure distribution in the annulus for a range of Re_W/Re_ϕ, though at both low and high extreme end values the prediction diverges. The model is shown to accurately predict the correct pressure distribution for the design point $Re_W/Re_\phi = 0.538$, and over the range $-20 < \beta - \beta_o < 3$.

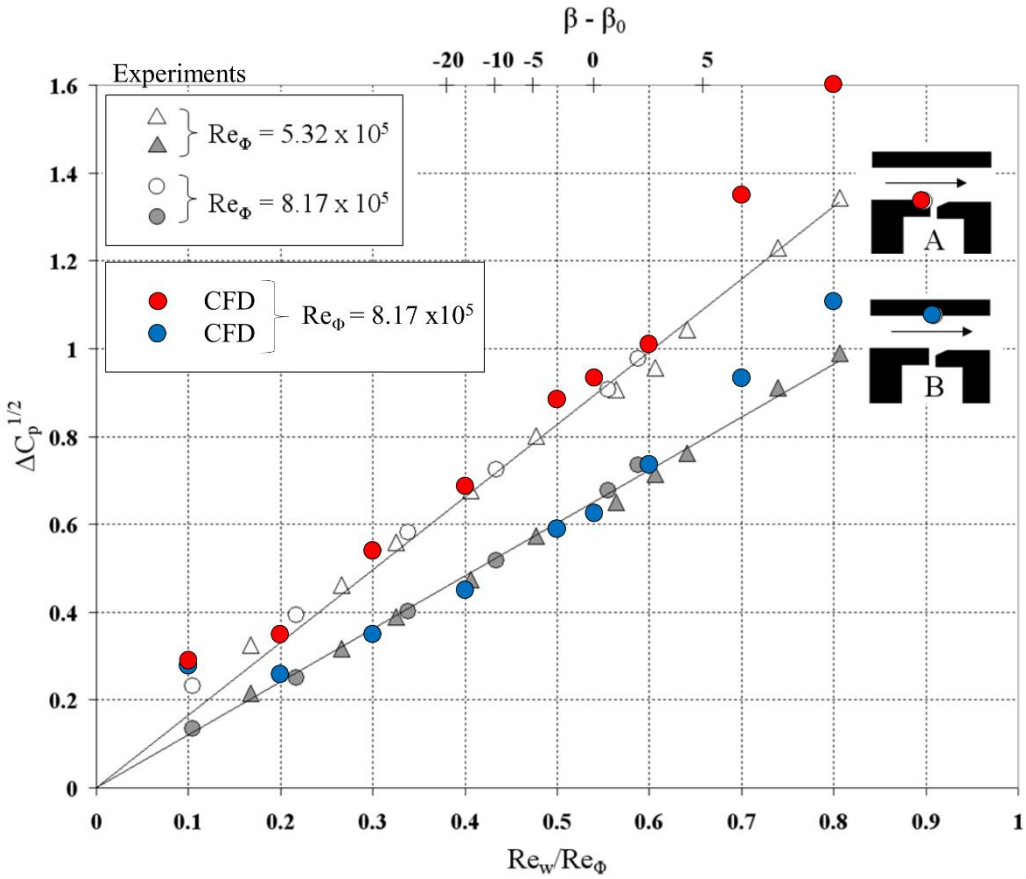

Figure 6.5 Effect of Re_W on variation of $\Delta C_p^{1/2}$ with Re_W/Re_ϕ at locations A and B in annulus; white and grey symbols – experiments, red and blue symbols – CFD

Table 6.3 presents the numerical peak-to-trough pressure values for the computed range of Re_W/Re_ϕ shown in Figure 6.5 for locations A and B.

(Re_w/Re_ϕ)	$\Delta C_{p,A}$	$\Delta C_{p,B}$	$\Delta C_{p,A}{}^{1/2}$	$\Delta C_{p,B}{}^{1/2}$
0.1	0.086	0.080	0.294	0.283
0.2	0.130	0.074	0.360	0.272
0.3	0.293	0.124	0.541	0.352
0.4	0.477	0.201	0.691	0.448
0.5	0.797	0.348	0.893	0.590
0.538	0.876	0.383	0.936	0.619
0.6	1.160	0.538	1.077	0.734
0.7	1.832	0.877	1.354	0.937
0.8	2.632	1.309	1.623	1.144

Table 6.3 Effect of varying Re_W on ΔC_p at locations A and B in the annulus for constant $Re_\phi = 8.2 \times 10^5, \lambda_T = \Phi_o = 0$

6.2.1 Swirl Ratio in Annulus

Figure 6.6 illustrates the fluid dynamics in the stator domain via a cross-sectional plane for the swirl ratio. The figure shows that the flow past the NGV has high swirl, with the swirl ratio at the vane trailing edge increasing from 1 to approximately 2, at measurement location A. The figure therefore illustrates that the ingested fluid from the annulus would enter the wheel-space with very high swirl, increasing the swirl ratio in the wheel-space at high radius and the overall core rotation, as shown in Figure 6.8 and Figure 6.9.

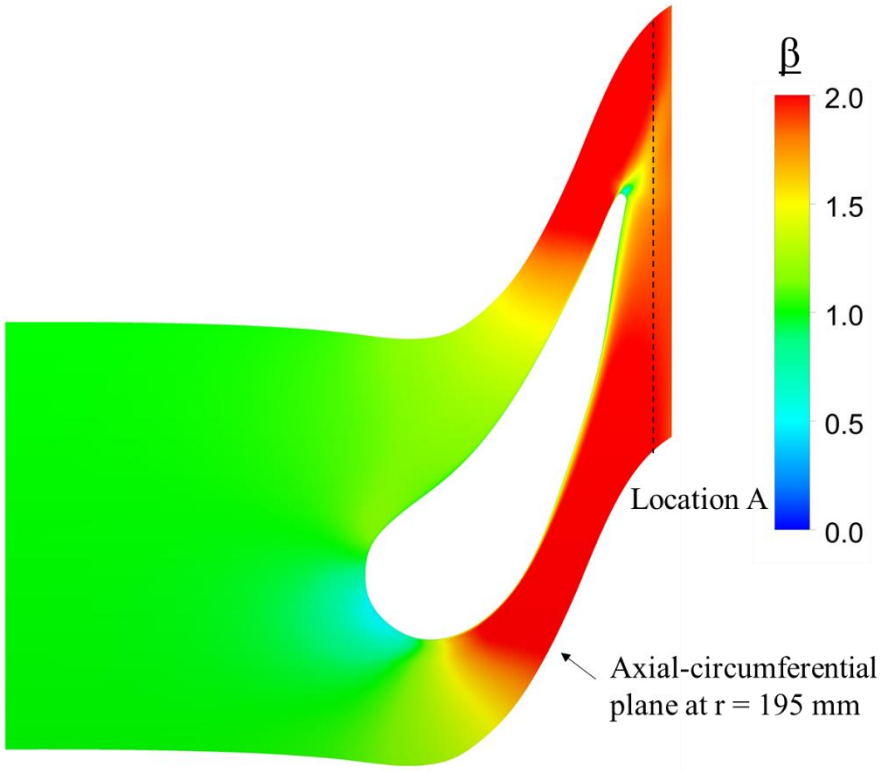

Figure 6.6 Swirl ratio at axial-circumferential plane at r=195 mm for $Re_W/Re_\phi = 0.538$

6.3 AXIAL-CLEARANCE SEAL

This section will validate the axial-clearance seal CFD model against the wide range of experimental data measured at the University of Bath, such as swirl ratio distributions, radial distributions of effectiveness, effectiveness curves and the static pressure on the stator wall.

6.3.1 Wheel-Space Fluid Dynamics

The effect of sealing flow rate on the velocity distributions is again investigated, though now for the full multi-body model with ingress; here the turbulent flow parameter, $\lambda_T = C_{w,o}Re_\phi^{-0.8}$, is used to represent the sealing flow rate. Four sealing flow rates are chosen to show this effect, varying from λ_T = 0 to λ_T = 0.11. Figure 6.7 shows computed radial and tangential velocity distributions $0.8 \leq r/b \leq 0.95$ (depicted in Figure 4.5b) for four different values of λ_T for the no-blade Bath rig model with EI ingress.

The horizontal axis in the plots represent the non-dimensional axial location, *Z/s*, where *Z/s* = 0 is the stator wall and *Z/s* = 1 is the rotor wall. As λ_T is increased, the magnitude of the inward radial velocity on the stator decreases and the outward radial velocity on the rotor increases. In terms of the circumferential velocity, increasing λ_T reduces the magnitude of the swirl ratio in the core, which shows that higher values of sealing flow rates reduce the core rotation. The fluid dynamics within the wheel-space are very much identical for the radial outflow case (Figure 4.7) as with the EI ingress case.

Figure 6.7 also illustrates that as a higher radial location is chosen, the swirl ratio in the core increases, this is because the ingested fluid enters the wheel-space with high swirl, which in turn causes the core rotation in the wheel-space to have higher swirl at higher radius. This effect diminishes at lower radius, as the flow is outside the mixing region. Another effect that is observed is that the peak radial velocity of the radial outflow on the rotor slightly decreases with increasing radius.

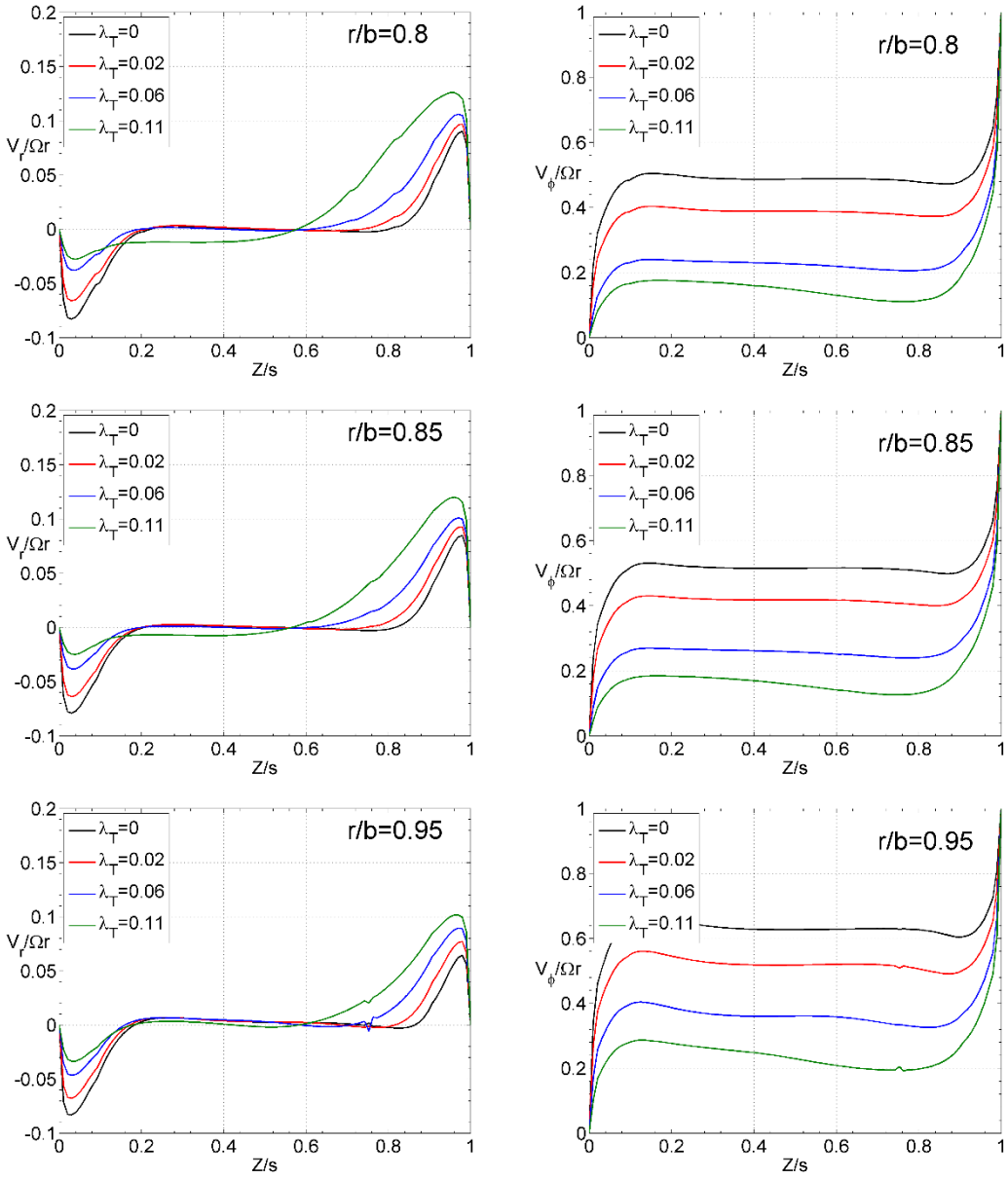

Figure 6.7 Computed velocity profiles for the no-blade CFD axial seal model for various radial locations at different λ_T values for $Re_\phi = 8.2 \times 10^5$

6.3.1.1 Swirl Ratio in the Wheel-Space

Figure 6.8 shows the circumferential-radial swirl variation in the wheel-space at *Z/s* = 0.25. The figure reveals that there is a non-axisymmetric swirl variation at high radius, which is attributed to the high swirling ingested fluid from the annulus. Comparisons of radial swirl variations are carried out by circumferentially averaging the computed data across the 11.25° sector model. This position is chosen as it is expected to be in the rotating, inviscid core outside the rotor and stator boundary layers and is the measurement place for the pitot-static tubes (see Figure 3.1).

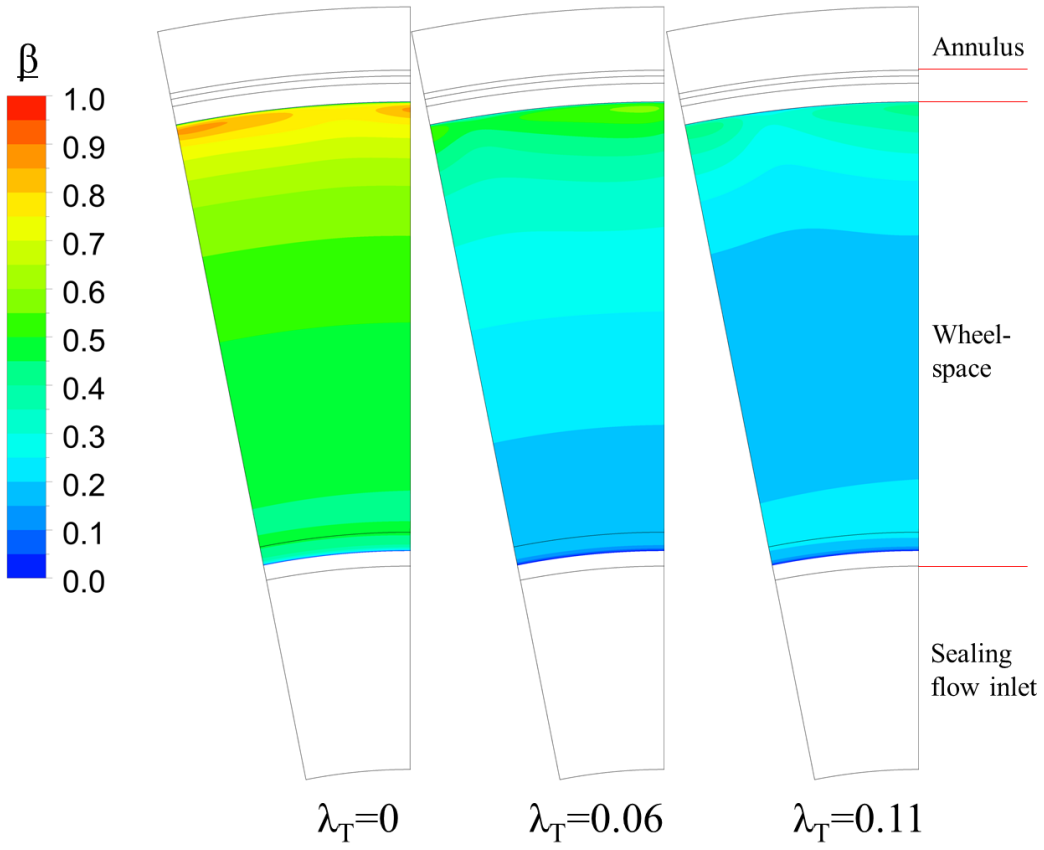

Figure 6.8 Swirl contours at Z/s = 0.25 for varying λ_T values and at $Re_\phi = 8.2 \times 10^5$ for the axial seal

Figure 6.9 shows the computed swirl ratio distributions at *Z/s* = 0.25 using the non-bladed 3D steady CFD model for the axial-clearance seal. Experimental measurements [7] are also shown in the figure. The figure shows that the swirl ratio in the wheel-space reduces as the sealing flow rate increases. In general, the computations have managed to properly predict the flow structure within the wheel-space. The greatest divergence between the measured and computed data is experienced at λ_T = 0.06. However for all other sealing flow rates the computations agree very well with the measured data for mostly all radii. There is a difference at the lowest radius, which arises due to the seal inlet boundary condition being set as mass flow rate with zero swirl, the initial zero swirl flow is allowed to develop along the long and narrow sealing inlet which can be seen in Figure 6.8.

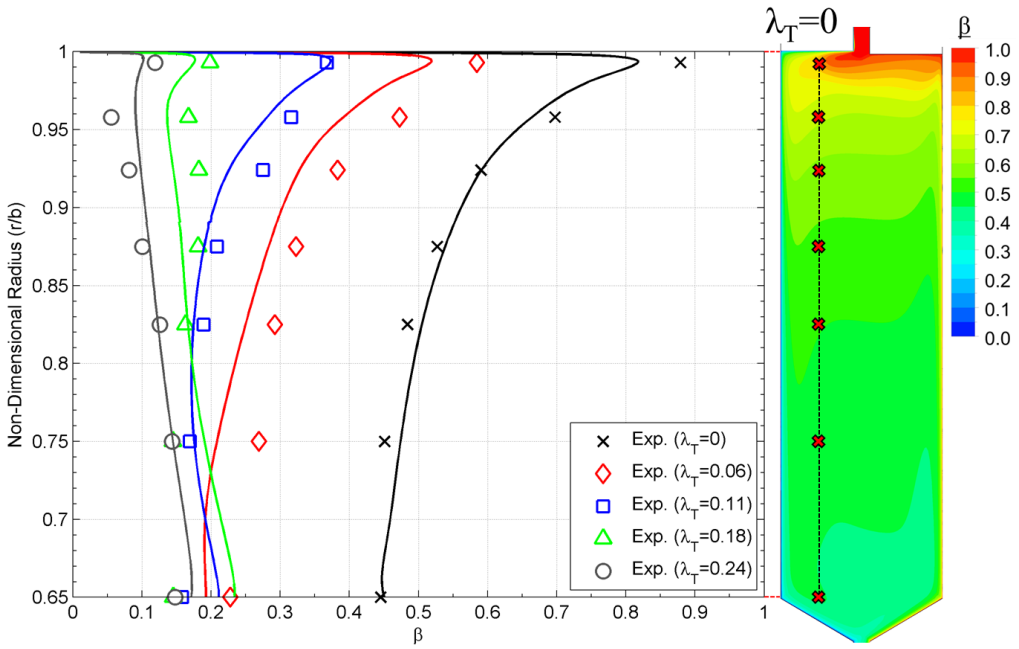

Figure 6.9 Comparison between measured and computed variation of swirl ratio with radius for axial-clearance seal for different λ_T at $Re_\phi = 8.2 \times 10^5$

Figure A - 1 in Appendix A shows axial-radial swirl contours in the wheel-space at the periodic surface for various λ_T cases, matching those from the plot above. The figure reveals that as ingestion occurs, the fluid enters the wheel-space with high swirl. The swirl ratio is zero on the stator disc and one on the rotating disc. With decreasing radius, the core rotation is seen to decrease. As the sealing flow is increased, the sealing flow enters the wheel-space with nearly zero swirl, thus reducing the wheel-space swirl or core rotation.

The effect of computing the inner wheel-space of the University of Bath rig (as can be seen in Figure 6.10) is also tested. Figure 6.11 illustrates that there is very little effect of adding the inner wheel-space into the computational model, as the flow structure is identical to the computations with only the outer wheel-space. There is only a slight noticeable difference which occurs at λ_T= 0.06 at low radius. It can be assumed that the tight sealing inlet between the inner and outer wheel-spaces is what governs the initial swirl entering the outer wheel-space, since it is where the sealing flow develops appropriate and realistic levels of swirl.

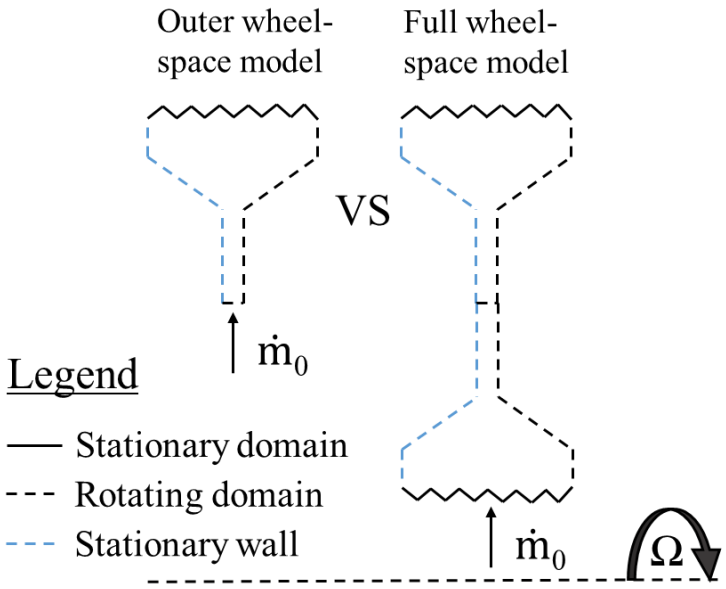

Figure 6.10 Schematic of outer wheel-space model and full wheel-space model (see Figure 3.2)

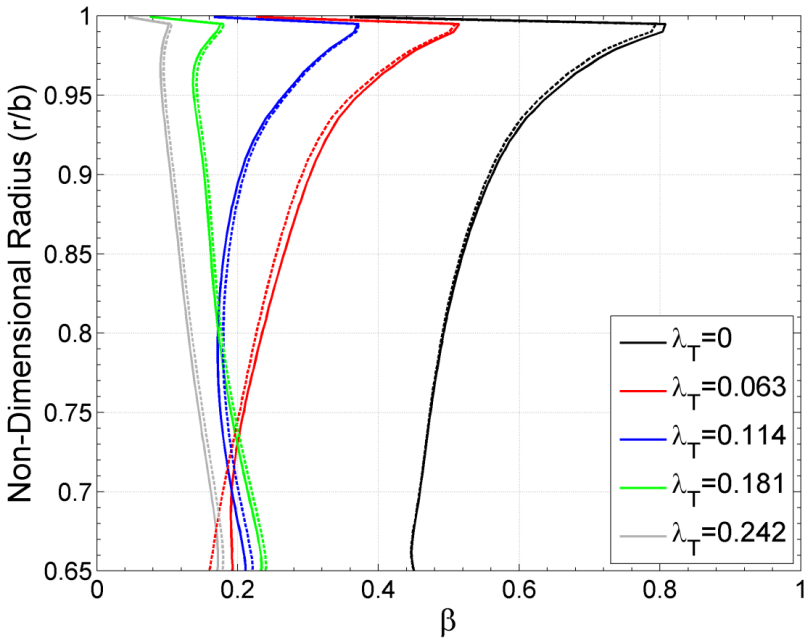

Figure 6.11 Comparison between computed variations of swirl ratio with radius for axial-clearance seal for different λ_T at $Re_\phi = 8.2 \times 10^5$ between full wheel-space model (solid lines) and outer wheel-space model (dashed lines)

Figure 6.12 shows the swirl distribution at Z/s = 0.25 for two different Re_ϕ values of λ_T for the axial-clearance seal. These are for equal Re_W/Re_ϕ, hence equal ΔC_p in the annulus. The computed results illustrate that Re_ϕ has no effect on the swirl ratio radial distribution, and that the turbulent flow parameter, λ_T, is the governing parameter for the flow structure in the wheel-space.

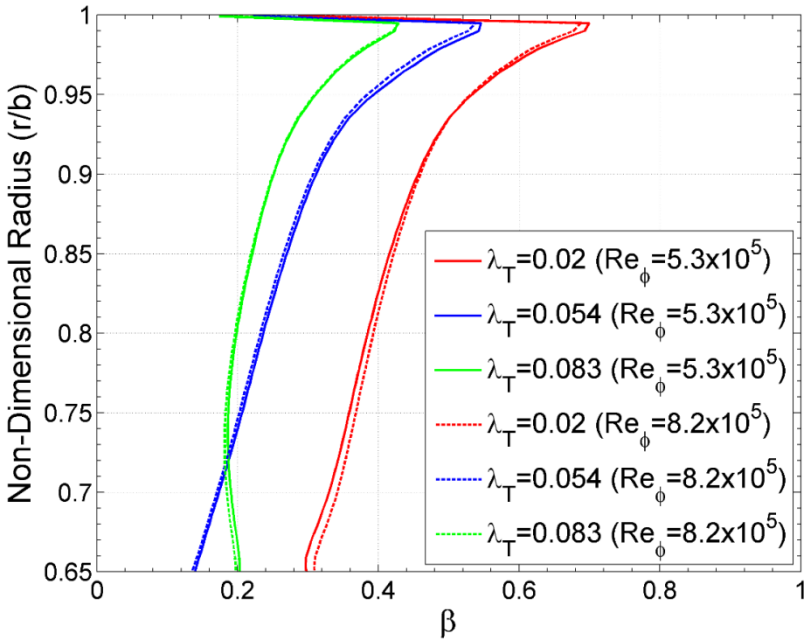

Figure 6.12 Comparison between computed swirl distribution for different Re_ϕ for axial-clearance seal at three λ_T values; for all cases $Re_W/Re_\phi = 0.538$, i.e. design condition

6.3.1.2 Swirl Fraction in Wheel-Space

The values of β and β^* are useful quantities which allow the swirl fraction to be quantified with and without superposed flow, where β^* is β for $\lambda_T = 0$. The variation of β/β^* with $\lambda_T/x^{13/5}$ has been widely investigated, with correlations from the studies of Daily *et al.* [55], Dadkhah [56] and more recently Micio [57] offering insight, as well as the Ekman approximation offered in [58] and [8]. Data from the computational study discussed in this section is shown alongside these empirical correlations in Figure 6.13.

Figure 6.13, once again, reveals that the core rotation or swirl fraction decreases with increasing values of λ_T. The swirl ratio, β, is recorded at various radial locations where the influence of external swirl is mostly negligible, r/b = 0.75, 0.8, 0.85 and 0.9; with β^* = 0.44, where the value is selected from the axial-clearance seal with no ingress computation in the core region. The computations show that the data obtained is slightly above the correlations, which is attributed to the ingested high swirling fluid at low sealing flow rates, increasing the core rotation, hence the higher predicted swirl fraction than the correlations offered by other studies where no external flow was present. However, at the higher values of λ_T, where the sealing flow rates are higher and ingestion is mostly suppressed, the computed swirl fraction is relatively insensitive to the chosen radial position. In general, the computed swirl fraction has a very similar

trend to the correlations offered by other studies where no external flow was present, and any slight over-predictions are attributed to the Externally-Induced ingestion present in the computations.

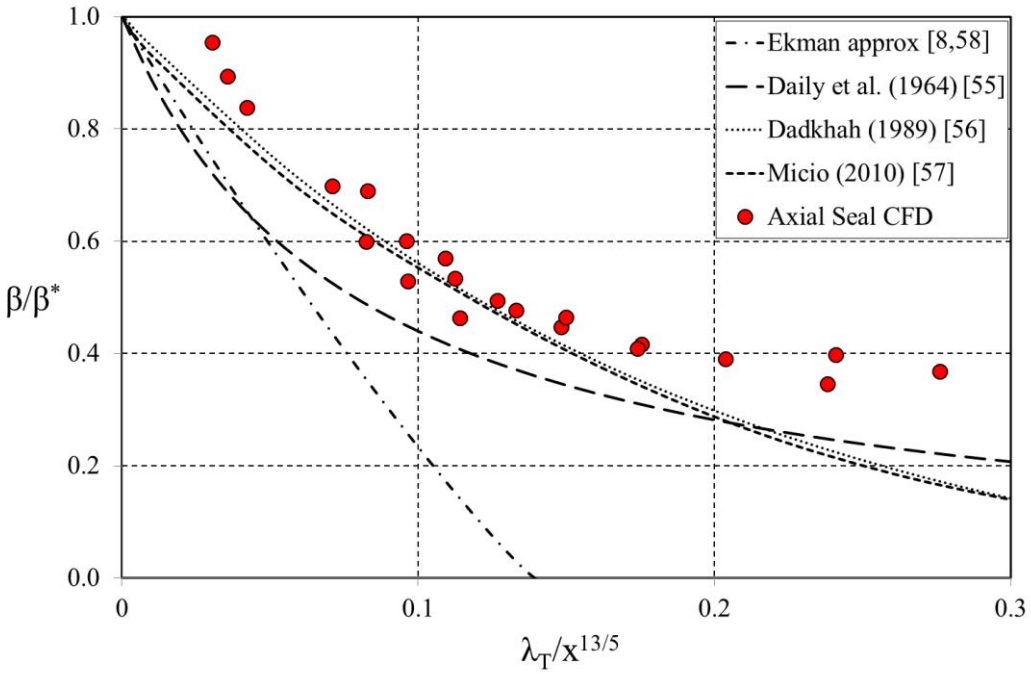

Figure 6.13 Variation of β/β with $\lambda_T/x^{13/5}$ for axial-clearance seal*

6.3.2 Radial Distribution of Effectiveness

Figure 6.14 shows the circumferential-radial effectiveness variation in the wheel-space at *Z/s* = 0 (stator surface). The figure reveals that there is an axisymmetric variation of effectiveness on the stator wall, which is attributed to the fact that concentration effectiveness is expected not to have any circumferential variation.

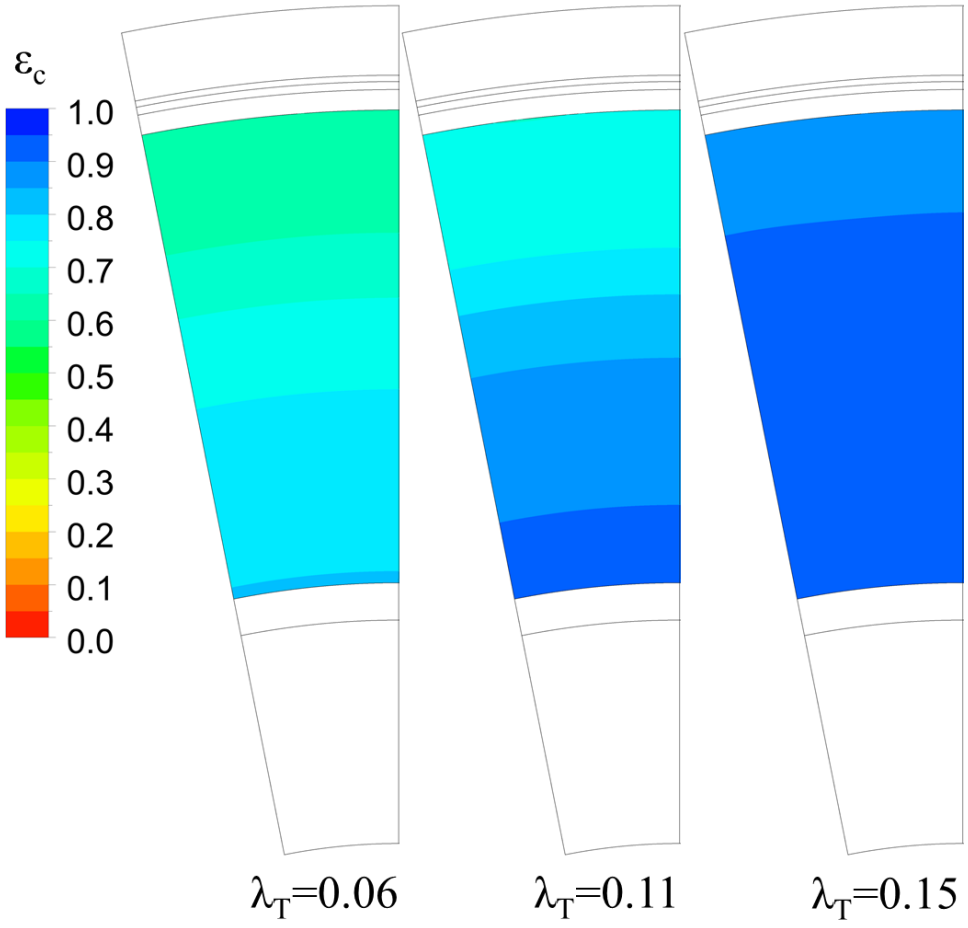

Figure 6.14 Effectiveness contours at Z/s = 0 for varying λ_T values

Figure 6.15 shows the computed radial distribution of effectiveness on the stator, where experimental data is also included for comparison [59]. The symbols represent the experimental data, which suggests that the ingress flow is fully mixed at the rim-seal region (mixing region), such that the concentration effectiveness of the fluid in the stator boundary layer has little variation with radius. The computed results have a similar trend to the experimental data, with the low sealing flow rates indicating that further mixing occurs in the stator boundary layer in the wheel-space. However, for the higher sealing flow rates, it seems that the computations are able to properly predict a fully mixed out flow. There is some over-prediction of the computed effectiveness values, especially for low sealing flows at lower radius, which is attributed to the fact that the computations do not produce such fully mixed flow in the wheel-space.

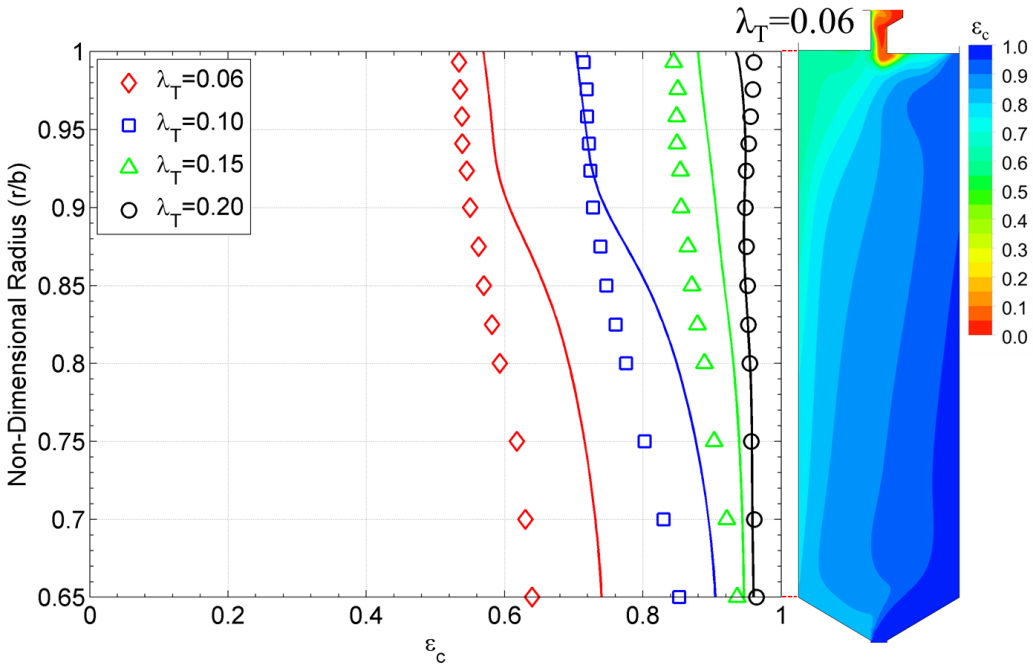

Figure 6.15 Comparison between measured and computed radial variation of effectiveness on the stator for axial-clearance seal for different λ_T at $Re_\phi = 8.2 \times 10^5$

Figure B - 1 in Appendix B shows axial-radial effectiveness contours in the wheel-space at the periodic surface. It can be seen that at low sealing flows, the ingested fluid is not fully mixed before entering the wheel-space, hence the radial gradient of effectiveness on the stator wall. The effectiveness contour beside the plot reveals that the sealing flow impinges on the rotating disc. As the sealing flow is increased, mixing of the ingested fluid occurs outside the wheel-space, at the rim-seal clearance. The sealing flow rapidly fills the wheel-space, covering all of the rotating disc, showing that the rotor is more shielded than the stator due to the impingement of the sealing flow on the rotating disc (see Figure B - 1). Another phenomenon that can be seen from the contours is that as the sealing flow is increased, egress takes place across the seal-clearance, where part of the sealing flow exits the wheel-space due to the previously 'disc-pumping effect'.

Figure 6.16 shows the radial distribution of effectiveness for two different Re_ϕ for similar values of λ_T for the axial-clearance seal. The computed results illustrate that Re_ϕ presents a difference on the effectiveness distribution for lower sealing flow rates, however the disparity diminishes with increasing sealing flow rates. This difference is not trivial, since industrial gas turbines run at very high rotational speeds and the sealing effectiveness is expected to be in the range of $0.8 < \varepsilon_c < 0.95$.

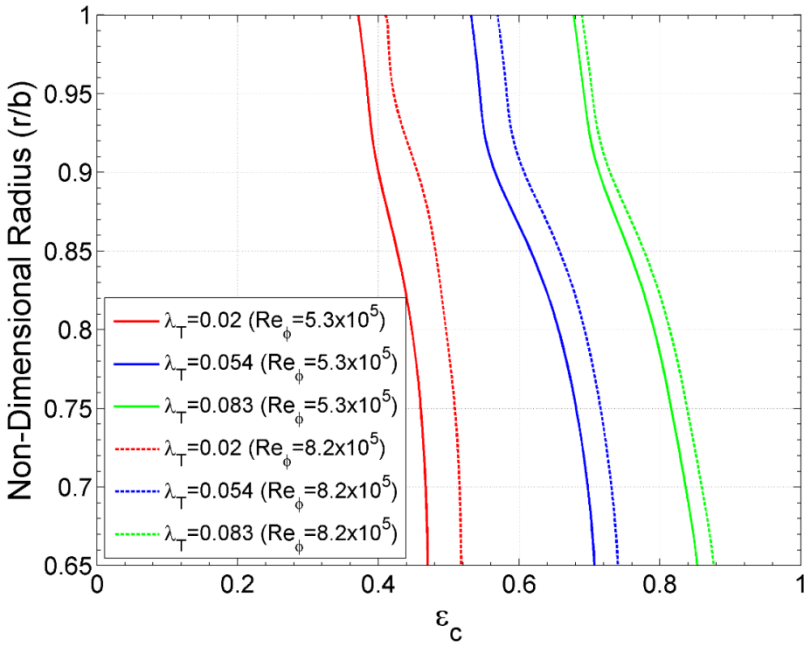

Figure 6.16 Comparison of radial variation of effectiveness on the stator for different Re_ϕ for axial-clearance seal at similar λ_T

Figure 6.17 shows a comparison between the computed radial distribution of effectiveness on the rotor and the measured adiabatic effectiveness on the rotor for the axial-clearance seal. The measured adiabatic effectiveness, ε_{ad}, is used since it was not possible to measure concentration on the rotating disc (without the complexity of slip-rings). For consistency, all definitions of sealing effectiveness should equal unity when the ingress is zero and should equal zero when there is no sealing flow, hence, the adiabatic effectiveness is defined by:

$$\varepsilon_{ad} = \frac{T_{ad} - T_a}{T^*_{ad} - T_a} \qquad \textit{Equation (6.1)}$$

where T^*_{ad} is the value of T_{ad} when there is no ingress, and T_a is the total temperature of the air in the annulus, which is the expected value of T_{ad} when there is zero sealing flow, as frictional heating was small. In the experiments, $9 < T_a < 15$ °C and $55 < T^*_{ad} < 60$ °C. Hence the definition above satisfies the necessary conditions that $\varepsilon_{ad} = 1$ when there is zero ingress and $\varepsilon_{ad} = 0$ when there is zero sealing flow.

Comparing the radial distribution of effectiveness on the stator surface (Figure 6.15) to that on the rotor surface (Figure 6.17), it can be observed that the rotor experiences higher values of sealing effectiveness, which is attributed to the sealing flow impinging

on the rotor disc and providing a thermal protective layer of cool sealing flow air. The computations display the same trends as the experimental measurements. The computed results over-predict the effectiveness on the rotor for the lower value of λ_T, which can be explained by the stator effectiveness also being over-predicted, where the fluid migrates from the stator boundary layer into the rotor boundary layer through the core region. The computed rotor effectiveness shows very good agreement with the measured data, for the higher value of λ_T. Both experiments and computed results show that the rotating disc is better protected from the effect of ingestion than the stator disc.

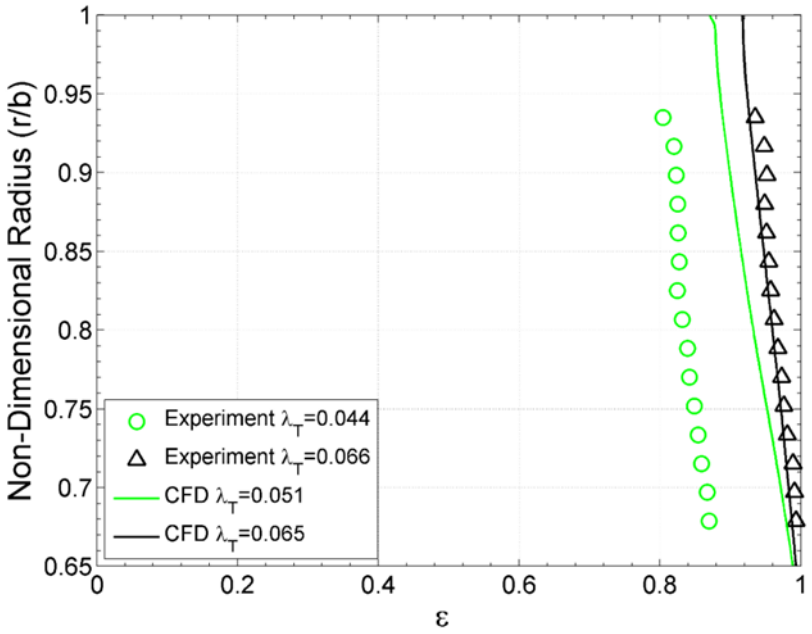

Figure 6.17 Comparison between measured adiabatic effectiveness and computed concentration effectiveness on the rotor for axial-clearance seal for different λ_T at $Re_\phi = 8.2 \times 10^5$

6.3.3 Effectiveness Curve

From the previous experimental section, it is known that the sealing flow can be represented by the non-dimensional sealing parameter, Φ_o. The variation of the computed sealing effectiveness (monitor location at *r/b* = 0.958 on the stator, illustrated on the inset diagram) with Φ_o is shown in Figure 6.18 and Figure 6.19. The computed results are denoted by the closed red symbols, while the experimental measurements [6] are shown as open symbols and the theoretical curve fit for the measured effectiveness is also shown.

Figure 6.18 presents a very small effect of Re_ϕ on the computed effectiveness curve, with the greatest disparity occurring at very low sealing flow rates (see Figure 6.16), which is out of the range of operating conditions for industrial gas turbines. Figure 6.18 illustrates that the computed effectiveness for the different Re_ϕ replicates the experimental trend reasonably well.

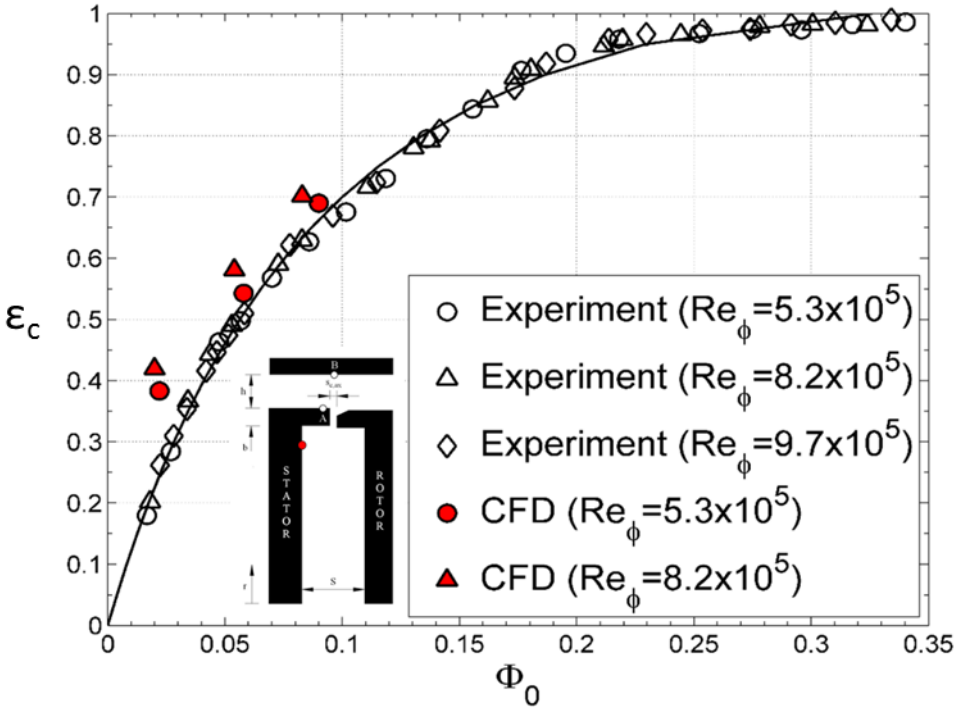

Figure 6.18 Comparison between experimental effectiveness curve and computed effectiveness for axial-clearance seal with EI ingress for $Re_W/Re_\phi = 0.538$

Figure 6.19 shows the computed effectiveness curve at the stator and rotor for $Re_\phi = 8.2 \times 10^5$. The computed results show good agreement with the experimental data (and theoretical fit), however the effectiveness on the stator is over-predicted for $\Phi_o < 0.1$, and with some fluctuation occurring on the stator at $\Phi_o < 0.15$. The figure also shows the variation of computed and measured adiabatic effectiveness on the rotor (at the monitor location $r/b = 0.9$, also illustrated on the inset diagram) with Φ_o. The adiabatic effectiveness data on the rotor has been experimentally measured at the University of Bath only for the axial-clearance seal, which allows it to be further validated. The computed data shows a very close similarity to the measured data. The effectiveness is expected to be higher on the rotor, since the sealing flow provides it with a thermal protective layer.

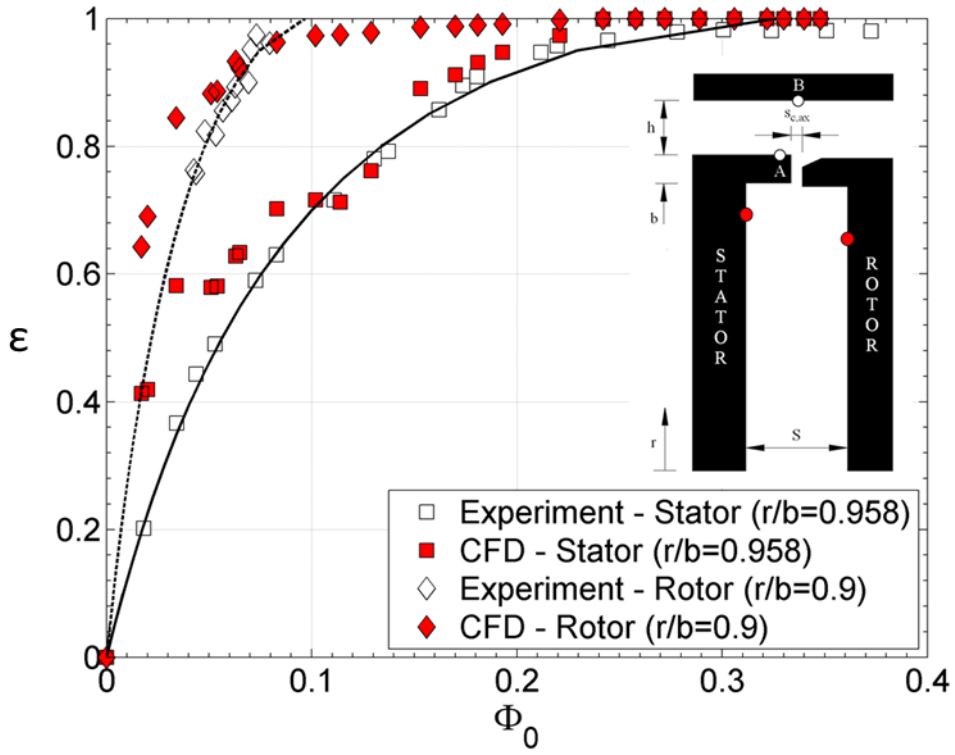

Figure 6.19 Comparison between experimental effectiveness curve and computed effectiveness for axial-clearance seal with EI ingress for $Re_\phi = 8.2 \times 10^5$ on rotor (adiabatic effectiveness) and stator (concentration effectiveness)

6.3.4 Static Pressure on Stator Wall

Figure 6.20 shows contours for the static pressure on the stator wall, which can be seen to have great variation in the circumferential direction at high radius. Previously the effectiveness concentration values are seen to have an axisymmetric distribution, however the pressure seems to be largely affected by the flow through the NGV, which causes the non-axisymmetric pressure distribution expected to drive EI ingress. To compare the radial pressure distribution on the stator wall with experimental data, the pressure is averaged across the circumferential direction.

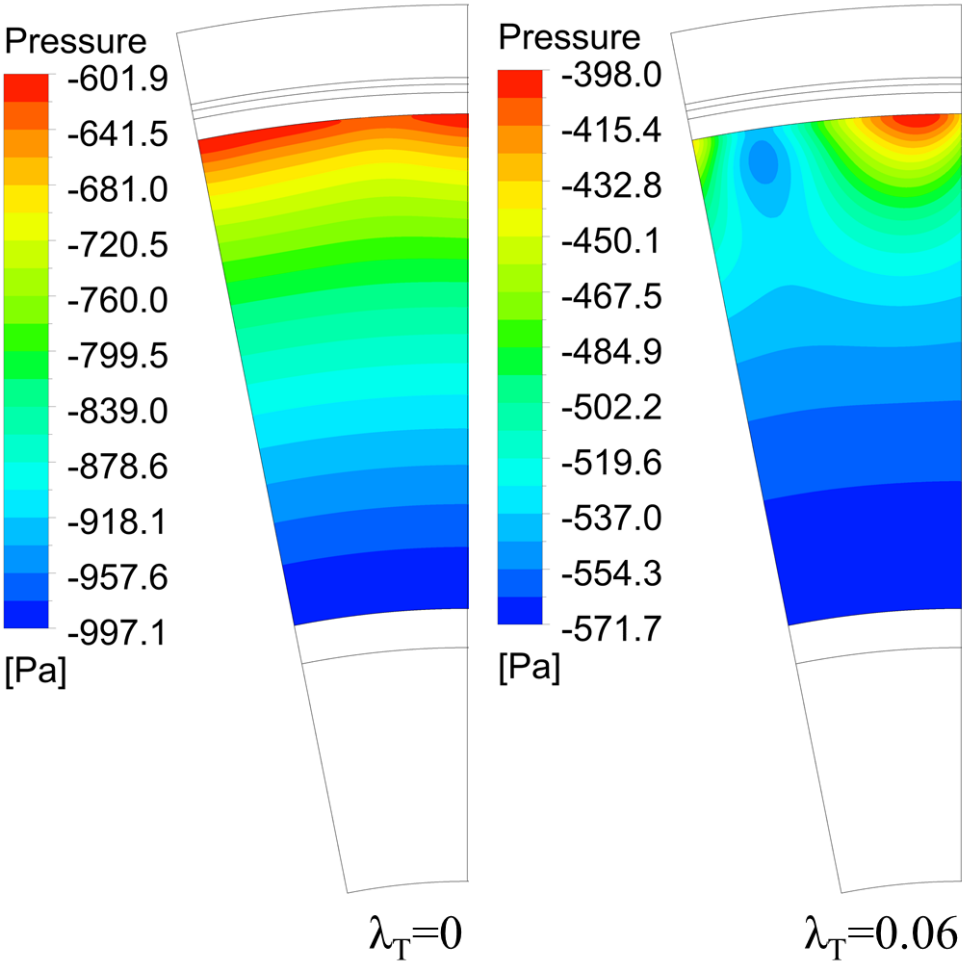

Figure 6.20 Pressure contours at Z/s = 0 for varying λ_T values

Figure 6.21 shows comparisons between the distributions of C_p calculated from Equation (3.4) and the values obtained from the measured static pressures on the stator wall, for both experiments and computations. For the no sealing flow case, there is very good agreement between the calculated and measured distributions of C_p between the experiment and the CFD data. Since the distributions of β are well predicted for the axial clearance seal, it is not surprising that the calculated distributions of C_p are also similar. There is a slight variation for the case where λ_T = 0.06, and this could be expected due to the difference in the flow structure previously seen in Figure 6.9. Also, the computed C_p in the stator wall is highly dependent on the value of p_{ref}, which as previously stated, is at $x_{ref} = r/b = 0.6$. Even though the computations do not predict the static pressure values in the annulus and wheel-space, the pressure difference is very similar to that measured in the experiments.

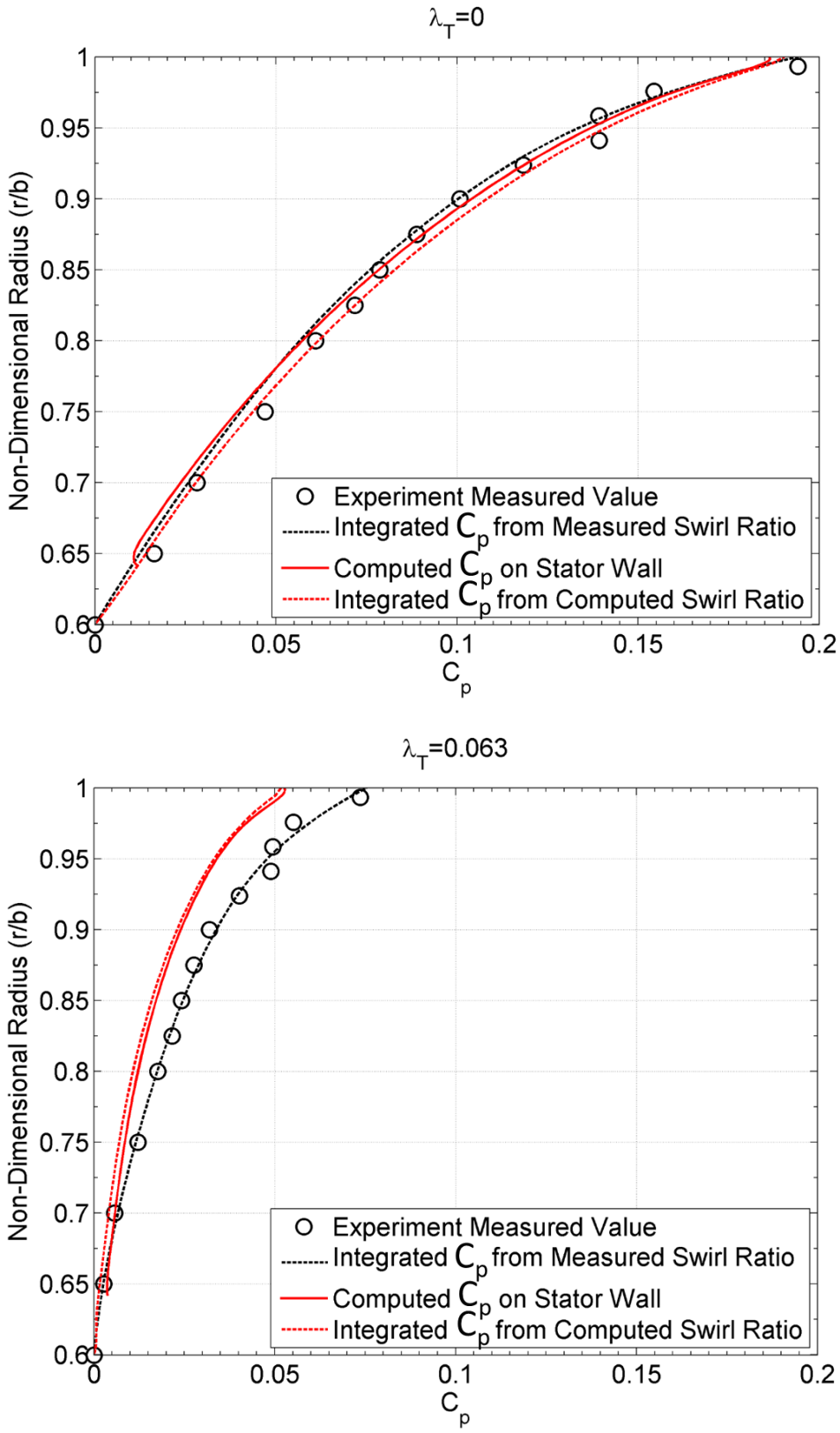

Figure 6.21 Comparison between measured and computed radial distribution of pressure coefficient (static) for axial-clearance seal. Dashed-lines denote calculated distribution for C_p, from Equation (3.4)

6.3.5 Moment Coefficient on Rotor Wall

This section will present the variation of the moment coefficient on the rotor wall ($C_M Re_\varphi^{1/5}$) with λ_T for a rotor-stator rig. The moment coefficient has been shown to become asymptotic to the free disc-value as $\lambda_T \rightarrow 0.22$, this behaviour is supported by the approximate theory (an analytical model), computations by Vaughan [60] for $G = 0.069$, experimental correlations of Daily *et al.* [55] and subsequent computations by Chew and Vaughan [61], all of which studied a rotor-stator rig with no ingestion. Previous numerical evaluations have shown that for the particular case where $C_W = 0$ (no sealing flow), $C_M Re_\varphi^{1/5} = 0.04$, approximately 55% of the free-disc value.

Figure 6.22 shows the measured moment coefficients of Daily *et al.* [55] for three gap ratios, $G = 0.0276$, 0.069 and 0.124, for a range of Reynolds number, $2\text{x}10^6 \leq Re_\varphi < 10^7$ and for $0 \leq \lambda_T < 0.06$, which are correlated via:

$$C_M = C_M^*\left(1 + 13.9\beta^*\lambda_T G^{-1/8}\right) \qquad \textit{Equation (6.2)}$$

The figure also presents the computed moment coefficients in the wheel-space on the rotating disc, for the no ingress model shown in Figure 4.5b and the non-bladed model with ingress, previously discussed in this chapter. As can be seen, the computed results show that $C_M Re_\varphi^{1/5}$ tends towards the free disc-value as λ_T approaches 0.22, which would be expected as the sealing flow rate is increased which would cause an increase in the moment on the rotor. The computed $C_M Re_\varphi^{1/5}$ value for $\lambda_T = 0$ is lower than the numerical evaluation of 0.04, while the computed results also show a lower $C_M Re_\varphi^{1/5}$ than the empirical correlations of Daily *et al.* [55] for $\lambda_T < 0.06$.

This difference in the moment coefficient between previous research and the computations, can be attributed to the fact that the rotor surface area of the computed model is smaller ($x_{min,rotor} = 0.642$), which would affect the moment and in turn the moment coefficient. Both computed models show an identical rotor moment behaviour without ingress and with ingress, with major difference at very low sealing flow rates, which can be attributed to the vast difference in ingestion levels, which seems to slightly reduce the moment on the rotor.

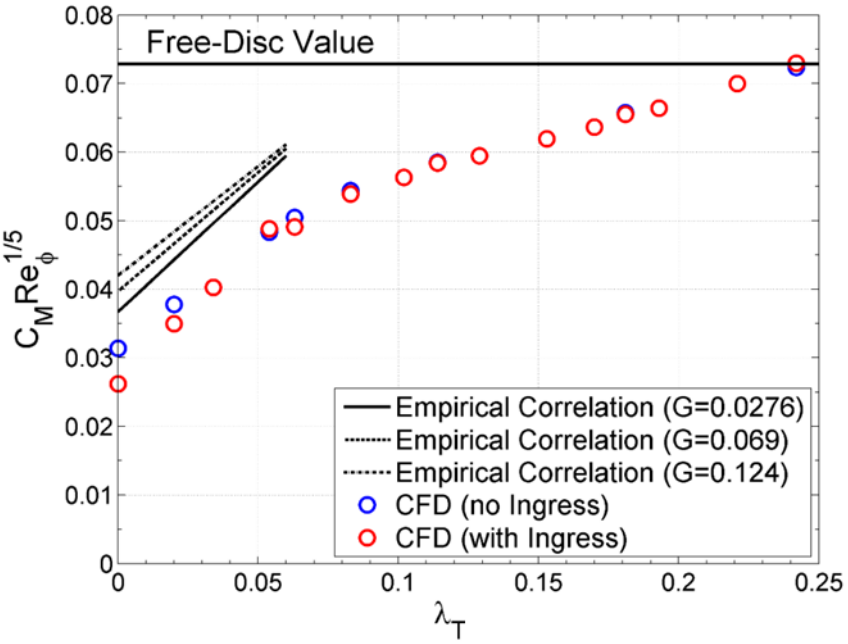

Figure 6.22 Variation of moment coefficient with λ_T for empirical correlations and computed results (with and without ingress)

6.4 CHAPTER OVERVIEW

This chapter covers a non-bladed steady-state 3D CFD model for an axial-clearance seal, which is extensively validated against experimental correlations and data. The pressure distribution in the annulus is compared to experimentally measured data and shows good agreement for location A (downstream of the vane trailing edge). Analysis is carried out on the annulus pressure distribution in terms of verifying the effects of varying the rotational Reynolds number, sealing flow rate and axial Reynolds number.

Computed axial distributions of radial and tangential velocity at various radial locations are studied and seen to show traditional rotor-stator behaviour. Validation of the computed results is carried out against experimental data in terms of radial distributions of pressure, swirl ratio, and effectiveness (for the stator and rotor), which show very good agreement. The computed sealing effectiveness with Φ_o is also presented, and shows good agreement with its experimental counterpart. Lastly, the moment on the rotor disc is also calculated and compared against empirical correlations, and showing it also becomes asymptotic to the free-disc value as λ_T approaches 0.22.

7 OTHER SEAL GEOMETRIES

This chapter demonstrates the predictive capabilities of the non-bladed 3D steady CFD model developed for the axial-clearance seal, for five other seal geometries: a radial-clearance seal, a double-axial-clearance seal, a radial-axial-clearance seal, another variation of the radial-clearance seal (with a shorter axial overlap and a tighter radial gap), and a double-radial-clearance seal. Figure 7.1 illustrates the computational meshes for the five different seals considered in this chapter. As with the axial-clearance seal, the CFD model is that of a multi-domain body, with a stator and rotor (without a blade) domain attached, via a frame change and GGI interface respectively to the wheel-space domain considered below. For all the wheel-space domains shown in Figure 7.1, the stator domain is attached to the left side of the annular region whilst the rotor domain is fixed to the right side.

Since in the previous chapter it was shown that including the inner wheel-space of the experimental rig had little effect on the computed results, all models will exclude the inner wheel-space for a faster computing turnaround time. All of the seals presented in this chapter have previously been experimentally tested at the University of Bath, therefore there is a wealth of experimental data available for validation purposes, such as radial distributions of swirl ratio and effectiveness and effectiveness curves for each seal.

The fluid dynamics in the wheel-space and the sealing effectiveness for each seal is compared and validated against experimental data, also the sealing performance in terms of Φ_o vs ε_c, for all seal geometries is compared. Carrying on from the previous chapter, all computations in this chapter are carried out at $Re_\phi = 8.2 \times 10^5$.

It should be noted that axial-radial contours for the swirl ratio and sealing effectiveness in the wheel-space, for different sealing flows and for each of the seals considered in this chapter, are presented in Appendix A and Appendix B, respectively.

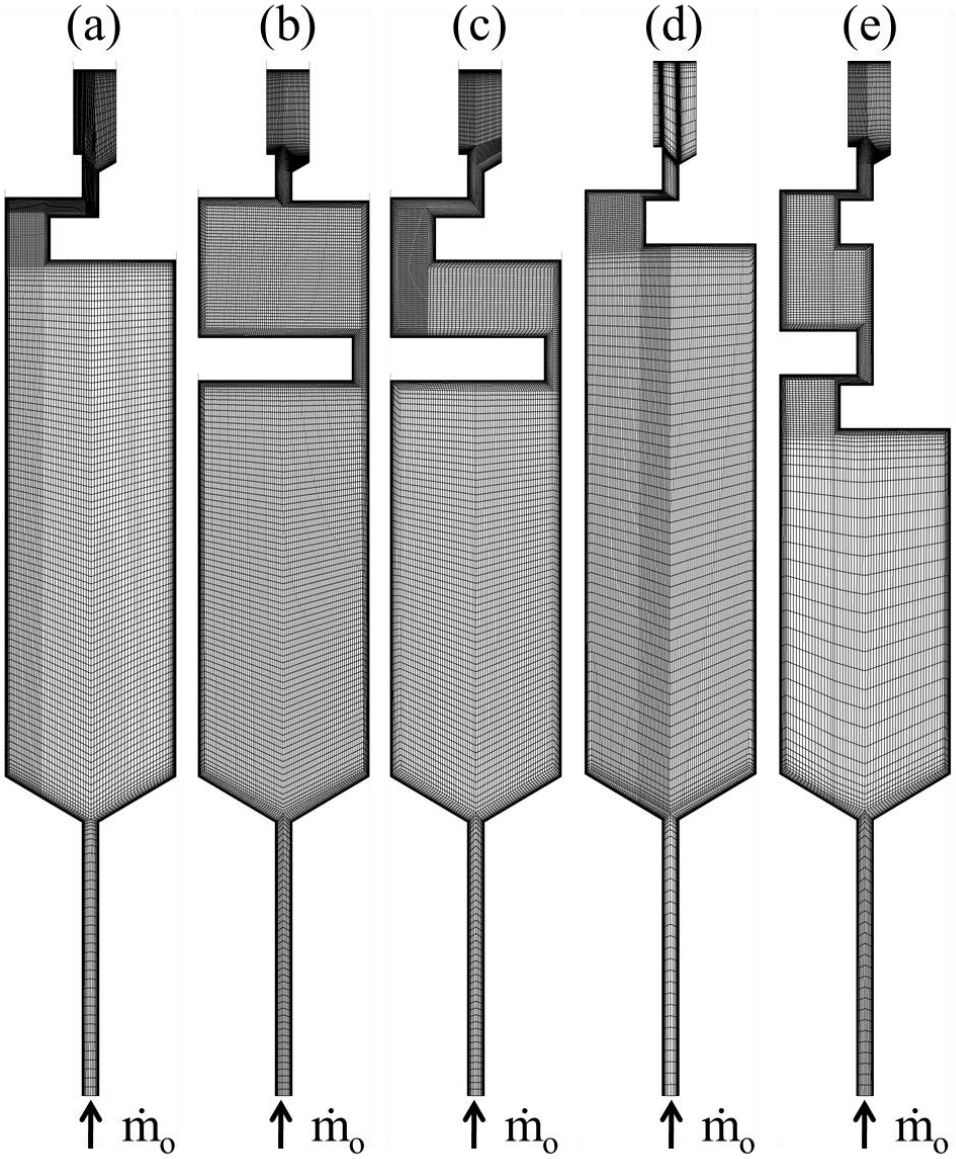

Figure 7.1 Wheel-space surface mesh for different rim-seal geometries (left side – stator; right side – rotor). (a) Radial-clearance seal; (b) Double-axial-clearance seal; (c) Radial-axial-clearance seal; (d) Radial-clearance seal; and (e) Double-radial-clearance seal

7.1 RADIAL-CLEARANCE SEAL

The radial-clearance seal shown in Figure 7.1a is a generic seal experimentally tested at the University of Bath and is previously presented in the experimental chapter (Figure 3.3), and is referred to as radial-clearance seal S2a. The radial-clearance seal includes an axial overlap section on the rotating disc, under the rotor platform, which rotates with the rotating disc. Previous literature has shown that a radial-clearance seal performs better than a generic axial-clearance seal.

Figure 7.2 shows the radial distribution of swirl ratio at *Z/s* = 0.25 in the wheel-space for the radial-clearance seal. The symbols denote experimental data, while the lines represent the computed swirl for the same conditions. Both the experiments and computations show that increasing the sealing flow causes a reduction in the swirl in the wheel-space. The computed swirl ratio is in good agreement with the experimental data, however with some differences at low radius (*r/b* < 0.75), which could be attributed to the sealing flow inlet boundary condition of $\beta = 0$, set up in the computational model. This comparison shows again that the computational model is capable of predicting the swirl ratio in the wheel-space reasonably well.

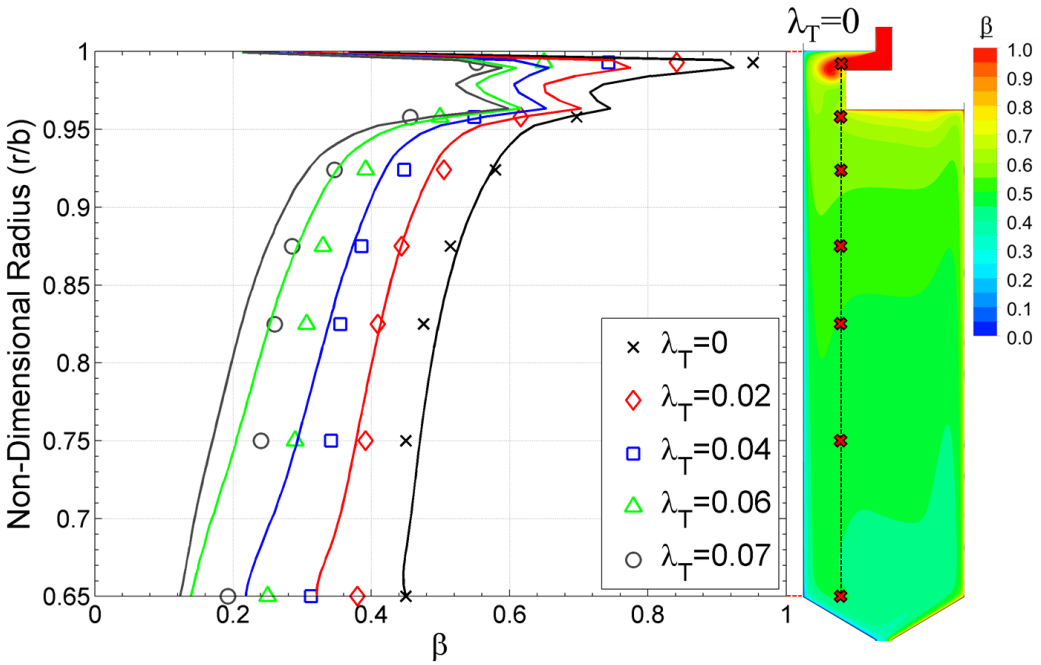

Figure 7.2 Comparison between measured and computed variation of swirl ratio with radius for radial-clearance seal for different λ_T at $Re_\phi = 8.2 \times 10^5$

Figure 7.3 presents a comparison of computed distributions of swirl ratio between the radial-clearance seal and axial-clearance seal for similar λ_T. The swirl ratio for both seals is virtually identical for *r/b* < 0.95, with the main difference occurring at high radius near the rim-seal. This is to be expected, since in the case of the radial-clearance seal, the high swirl ingested fluid enters the wheel-space and is influenced by the rotating axial overlap, causing the difference at high radius.

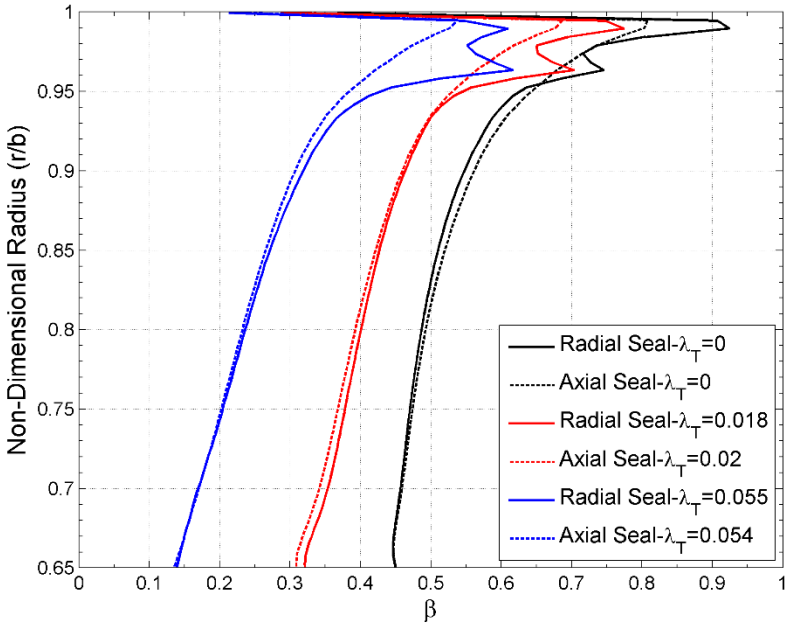

Figure 7.3 Comparison between computed variation of swirl ratio with radius for radial-clearance seal and axial-clearance seal for similar λ_T values at $Re_\phi = 8.2 \times 10^5$

Figure 7.4 shows the computed radial distribution of effectiveness on the stator. Experimental data is also included for comparison. The symbols represent the experimental data, which similar to the axial-clearance seal, suggests that the ingress flow is fully mixed at the rim-seal region, such that the concentration of the fluid in the boundary layer on the stator has little variation with radius. The computed results have properly captured the trend of the experimental data, however at high radius (r/b > 0.95), the computations indicate that mixing is still occurring in the stator boundary layer in the wheel-space. On the other hand, the computations are able to properly predict a fully mixed out flow at lower radius (constant effectiveness gradient), with some over-prediction on the computed effectiveness values.

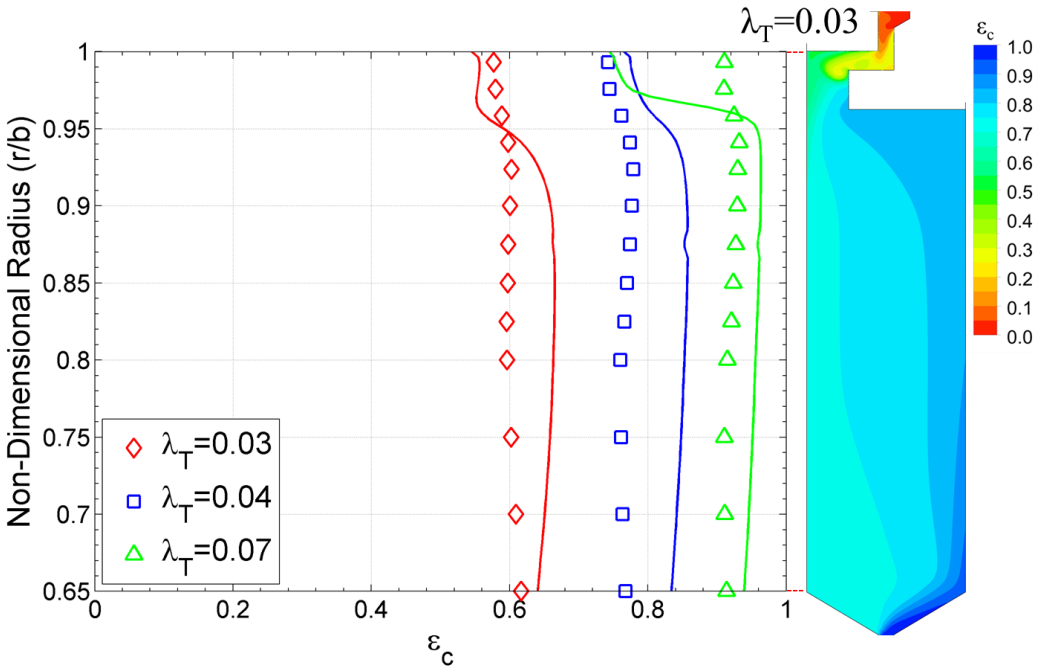

Figure 7.4 Comparison between measured and computed radial variation of effectiveness for radial-clearance seal for different λ_T at $Re_\phi = 8.2 \times 10^5$

Figure 7.5 shows a comparison of the radial distribution of effectiveness between the radial-clearance seal and the axial-clearance seal. The figure shows that the radial seal performs better than the axial seal in terms of sealing effectiveness, which is supported by previous literature. However for the lowest sealing flow case (λ_T = 0.02), it is seen that the axial-clearance seal seems to be more effective; this is due to the over-prediction of sealing effectiveness experiences by the axial-clearance seal at low sealing flow rates, which was identified in the previous chapter (Figure 6.19).

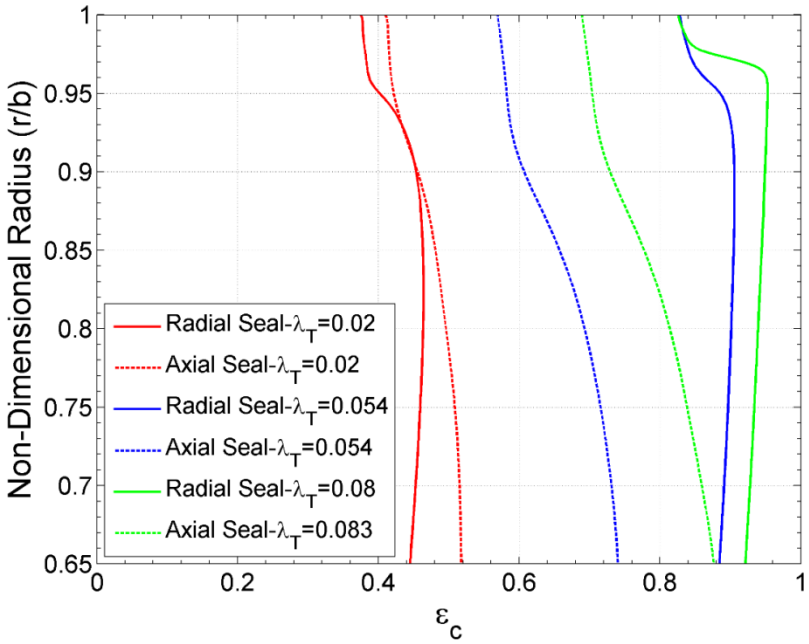

Figure 7.5 Comparison between computed variation of effectiveness with radius for radial-clearance seal and axial-clearance seal for similar λ_T values at $Re_\phi = 8.2 \times 10^5$

The performance of a rim-seal can be measured through the sealing effectiveness, and it was previously shown that the variation of sealing effectiveness with Φ_o is independent of Re_ϕ. Therefore in this chapter, the variation of sealing effectiveness with Φ_o is presented for all the different rim-seal geometries. Figure 7.6 shows the computed and measured variation of sealing effectiveness with Φ_o for the radial-clearance seal. The open symbols denote the experimental data for the radial-clearance seal for different Re_ϕ at r/b = 0.958, while the closed red symbols represent the computed effectiveness on the stator disk at the same radius, and the black line is the orifice model theoretical curve fitted to the experimental data. The figure shows very good agreement between computed and measured data, with some slight over-prediction of the computed effectiveness at mid-levels of sealing flow. However, the overall trend is properly captured and the computations properly predict the better sealing performance of the radial-clearance seal over the axial-clearance seal.

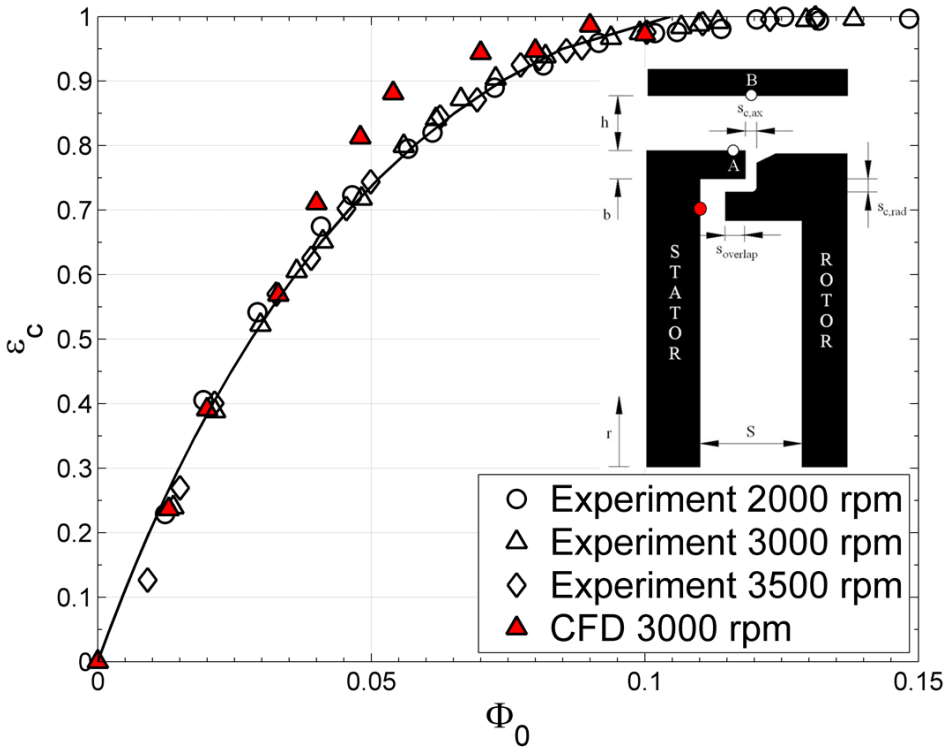

Figure 7.6 Comparison between experimental effectiveness curve fit and computed effectiveness for radial-clearance seal with EI ingress for $Re_W/Re_\phi = 0.538$; where Re_φ = 5.3 x 10^5, 8.2 x 10^5 and 9.7 x 10^5 for 2000, 3000 and 3500 rpm respectively

7.2 DOUBLE-AXIAL-CLEARANCE SEAL

Figure 7.1b shows the double-axial-clearance seal, which features similar axial-clearances for both inner and outer seals. The inner axial-clearance seal separates the wheel-space into an inner and outer wheel-space.

The performance of double-clearance seals was assessed by Sangan *et al.* [32]. Double seals are commonly used in turbine applications, where the outer wheel-space between the inner and outer seals act as a damping chamber, so that the circumferential pressure distribution generated in the annulus by the vanes can be attenuated. The amount of sealing air required to prevent ingress through the inner seal (into the inner wheel-space) is much lower than that required for a single-clearance seal.

Figure 7.7 shows the radial distribution of swirl ratio at *Z/s* = 0.25 in the wheel-space for the double-axial-clearance seal. The symbols denote the experimental data [59], while the lines represent the computed swirl for the same conditions. The computed results are in good agreement with experimental data in the inner wheel-space, with some swirl over-prediction occurring in the outer wheel-space for high values of sealing flow rates, which is be attributed to the higher level of ingestion (with high swirl) experienced in the outer wheel-space. Both the experiments and computations show that increasing the sealing flow causes a reduction of the core swirl in both the inner and outer wheel-space. The overall computed swirl ratio trend is qualitatively captured in the outer wheel-space and quantitatively captured in the inner wheel-space.

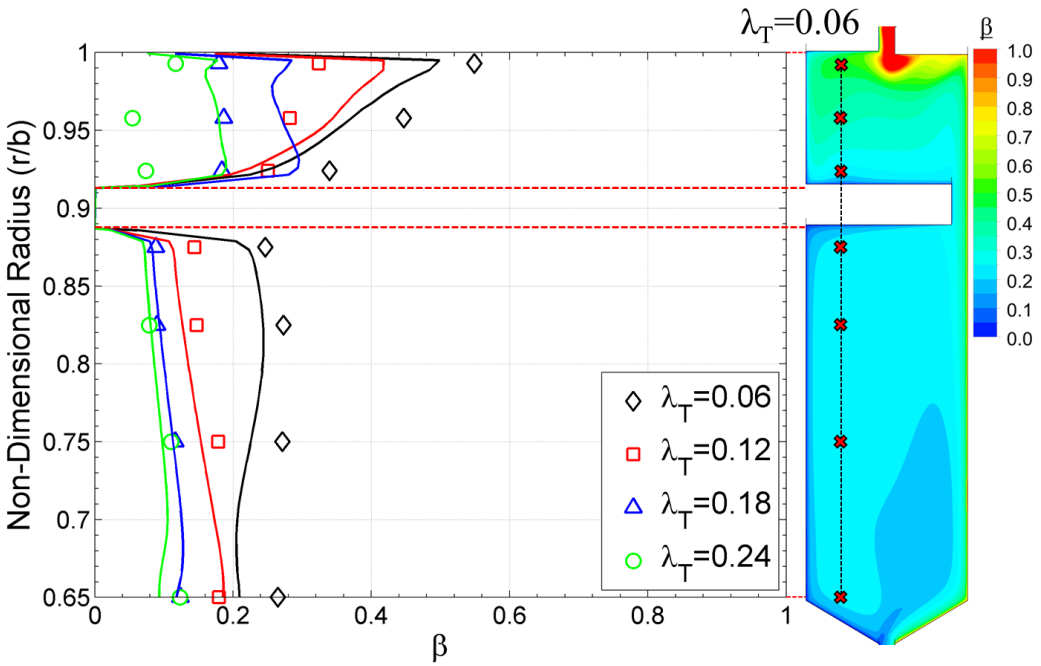

Figure 7.7 Comparison between measured and computed variation of swirl ratio with radius for double-axial--clearance seal for different λ_T at $Re_\phi = 8.2 \times 10^5$

Figure 7.8 shows a comparison of the computed distribution of swirl ratio between the double-axial-clearance seal and single axial clearance-seal for similar λ_T. The swirl for both seals is very similar, with the double-axial seal experiencing a slightly lower swirl in the inner wheel-space, which is attributed to the high swirl ingested fluid being contained in the outer wheel-space.

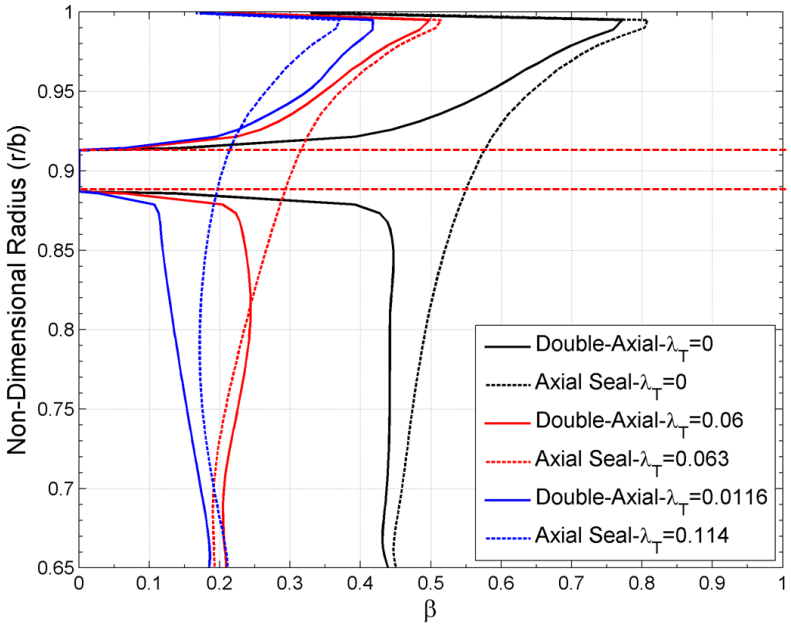

Figure 7.8 Comparison of computed variation of swirl ratio with radius between double-axial-clearance seal and axial-clearance seal for similar λ_T values at $Re_\phi = 8.2 \times 10^5$

Figure 7.9 shows the radial distribution of sealing effectiveness on the stator for the double-axial-clearance seal. Experimental data is also included for comparison [59]. Both computational results and experimental data show an increased sealing effectiveness in the inner wheel-space, which is attributed to the outer wheel-space acting as a buffer chamber which retains most of the high swirling ingested flow from the annulus. The computations seem to qualitatively predict the sealing effectiveness, with over-prediction of effectiveness occurring in the outer wheel-space for low sealing flow rates. The effectiveness in the inner wheel-space is over-predicted for most of the range of sealing flow rates.

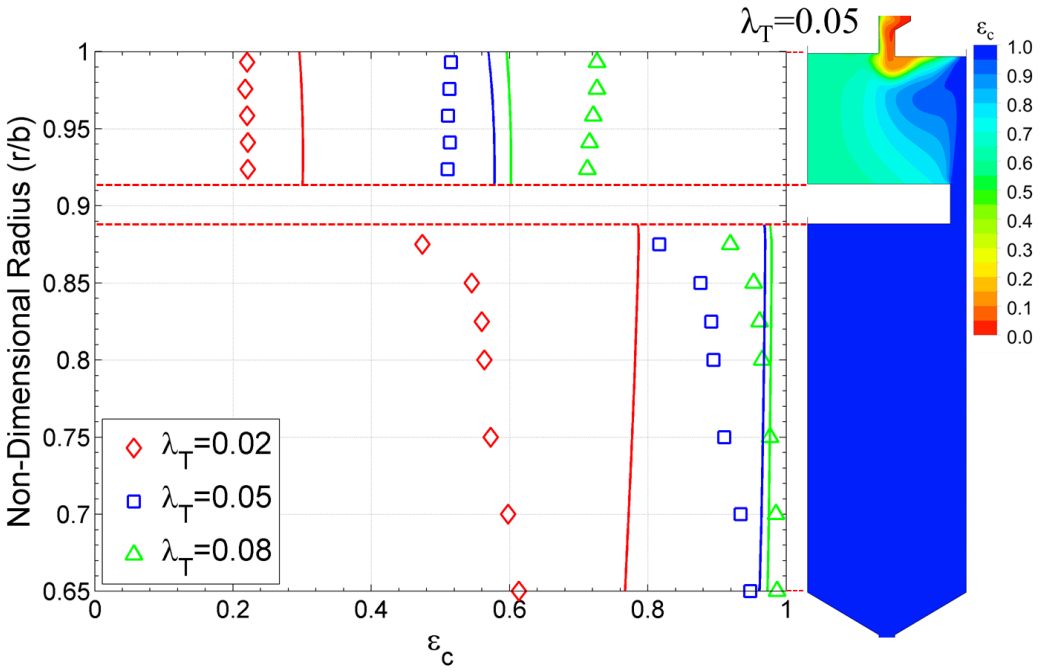

Figure 7.9 Comparison between measured and computed radial variation of effectiveness for double-axial-clearance seal for different λ_T at $Re_\phi = 8.2 \times 10^5$

Figure 7.10 compares the radial distribution of effectiveness between the double-axial-clearance seal and the axial-clearance seal. The figure shows that the double seal has a much higher sealing effectiveness performance for the inner wheel-space than the single axial-clearance, which is supported by previous literature, since the outer chamber for the double seal dampens and contains most of the ingested fluid, protecting the inner wheel-space. However the outer chamber of the double seal shows a lower sealing effectiveness performance than its single seal counterpart, which is to be expected, since it entraps most of the ingested fluid in this outer wheel-space.

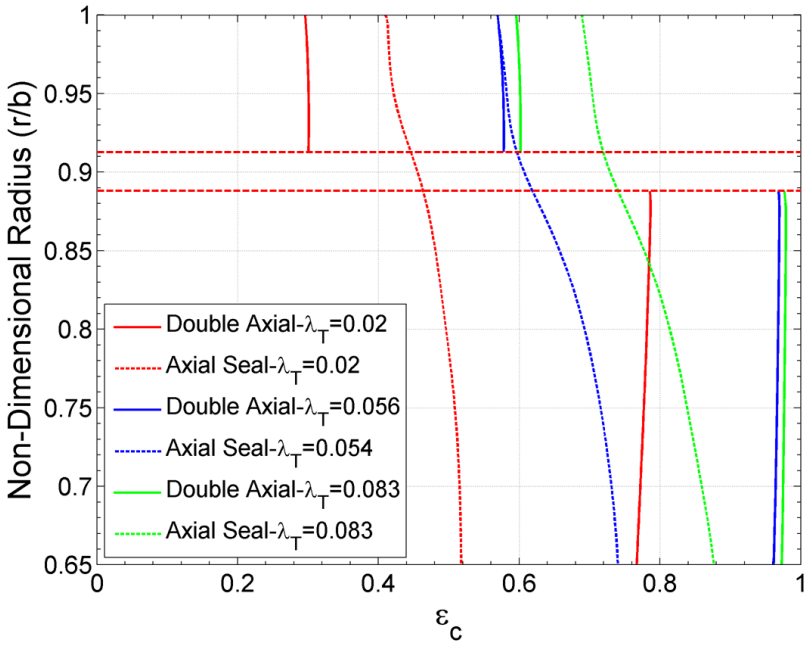

Figure 7.10 Comparison between computed variation of effectiveness with radius for double-axial-clearance seal and axial-clearance seal for similar λ_T values at $Re_\phi = 8.2 \times 10^5$

Due to having two wheel-spaces, the double-axial-clearance seal has two sampling points. The sampling point in the outer wheel-space is at *r/b* = 0.958, similar to that of the single-clearance seal, whilst the inner sampling point is at r/b=0.85. The definitions for sealing effectiveness at both sampling points is the same as that for the single-clearance seals, as presented in Equation (3.1).

Figure 7.11a and b present the computed and measured variation of sealing effectiveness with Φ_o for the inner and outer sampling points for the double-axial-clearance seal. The open symbols denote the experimental data [32] for the double-axial-clearance seal for different Re_ϕ at *r/b* = 0.958 and *r/b* = 0.85 respectively, while the closed red symbols represent the computed effectiveness on the stator disk at same radius, and the black line is the orifice model theoretical fitted curve for the experimental data.

The computed results for the outer sampling point are in reasonable agreement with experimental data and theoretical curve, with slight over-prediction of sealing effectiveness at low sealing flow rates and then switching to slight under-prediction of effectiveness at higher sealing flow rates. On the other hand, the computations at the inner sampling point show over-prediction of effectiveness. Both the computational results and experimental measurements show that the effectiveness is higher for the

inner sampling point than that at the outer sampling point for the same sealing flow rate value, which is supported by previous literature.

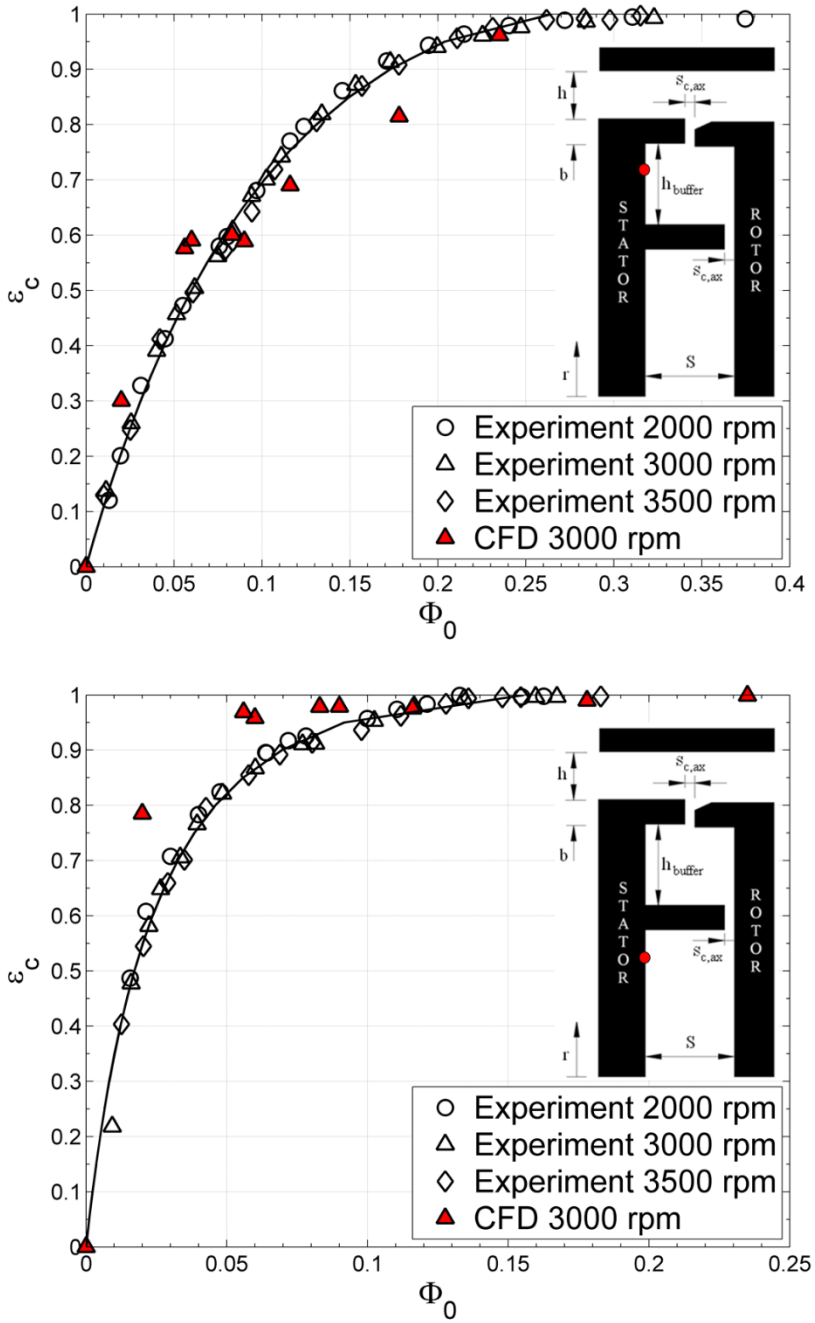

Figure 7.11 Comparison between experimental effectiveness curve fit and computed effectiveness for double-axial-clearance seal with EI ingress for $Re_W/Re_\phi = 0.538$; where Re_φ = 5.3 x 10^5, 8.2 x 10^5 and 9.7 x 10^5 for 2000, 3000 and 3500 rpm respectively. (a) Outer sampling point; (b) Inner sampling point

7.3 RADIAL-AXIAL-CLEARANCE SEAL

Figure 7.1c shows the radial-axial-clearance seal, which features a radial-clearance as the outer seal and an axial-clearance as the inner seal. The inner axial-clearance seal separates the wheel-space into an inner and outer wheel-space.

Figure 7.12 shows the radial distribution of swirl ratio at Z/s = 0.25 in the wheel-space for the radial-axial-clearance seal. The symbols denote the experimental data [7], while the lines represent the computed swirl for the same conditions. The computed results are in good agreement with experimental data in both the inner and outer wheel-space, with some swirl under-prediction occurring in the inner wheel-space at low radius and high sealing flows, which can be attributed to an increased damping of swirl occurring in the outer wheel-space. Again, both computations and experiments show that increasing the sealing flow reduces the core swirl in both the inner and outer wheel-spaces. Overall the computed swirl ratio trend is properly captured in both inner and outer systems.

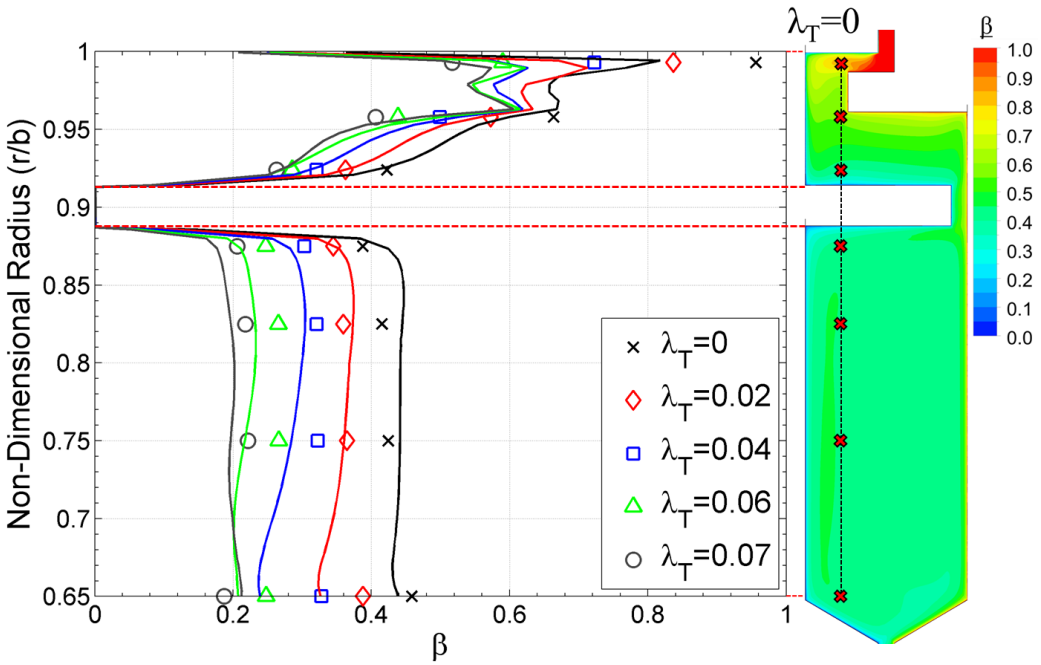

Figure 7.12 Comparison between measured and computed variation of swirl ratio with radius for radial-axial-clearance seal for different λ_T at $Re_\phi = 8.2 \times 10^5$

Figure 7.13 shows a comparison of the computed distribution of swirl between the radial-axial-clearance seal and the single radial-clearance seal for similar λ_T. The swirl for both seals is very similar in the outer wheel-space, however in the inner wheel-space the double seal presents a lower swirl than the single seal, which is due to the outer wheel-space containing most of the high swirl ingested fluid.

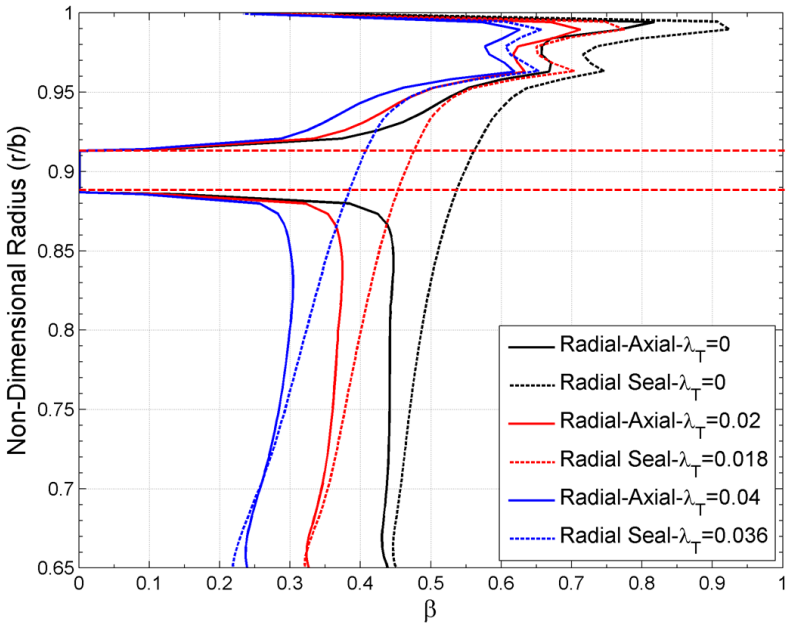

Figure 7.13 Comparison between computed variation of swirl ratio with radius for radial-axial-clearance seal and radial-clearance seal for similar λ_T values at $Re_\phi = 8.2 \times 10^5$

Figure 7.14 shows the radial distribution of sealing effectiveness on the stator for the radial-axial-clearance seal. Experimental data is also included for comparison [7]. Both computational results and experimental data show an increased sealing effectiveness in the inner wheel-space than the outer wheel-space, which is attributed to the outer wheel-space acting as a buffer chamber which retains most of the high swirling ingested flow from the annulus. The computations show good effectiveness prediction for the inner wheel-space, with over-prediction of effectiveness occurring in the outer wheel-space. The computed effectiveness in the inner wheel-space has good agreement with experimental data, and reasonable qualitative agreement for the outer wheel-space.

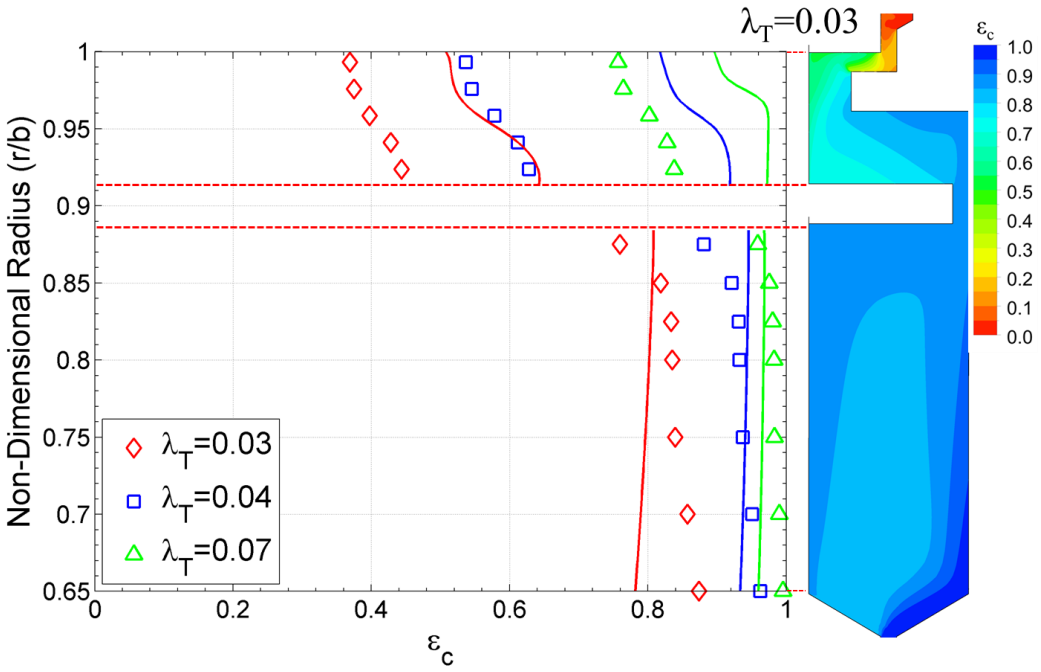

Figure 7.14 Comparison between measured and computed radial variation of effectiveness for radial-axial-clearance seal for different λ_T at $Re_\phi = 8.2 \times 10^5$

Figure 7.15 compares the radial distribution of effectiveness between the radial-axial-clearance seal and the radial-clearance seal for similar λ_T. The figure shows that the double seal has a higher effectiveness in both the inner and outer wheel-spaces for most of the sealing flows than the single radial seal. With the exception of the single radial seal having higher effectiveness at high radius for the lowest λ_T case. Overall, the computed data shows that the inner wheel-space is better protected due to the use of the double seal compared to that of a single seal. Also, the increase in sealing flow increases the effectiveness of all the wheel-space, especially it has a higher effect on the sealing of the inner wheel-space.

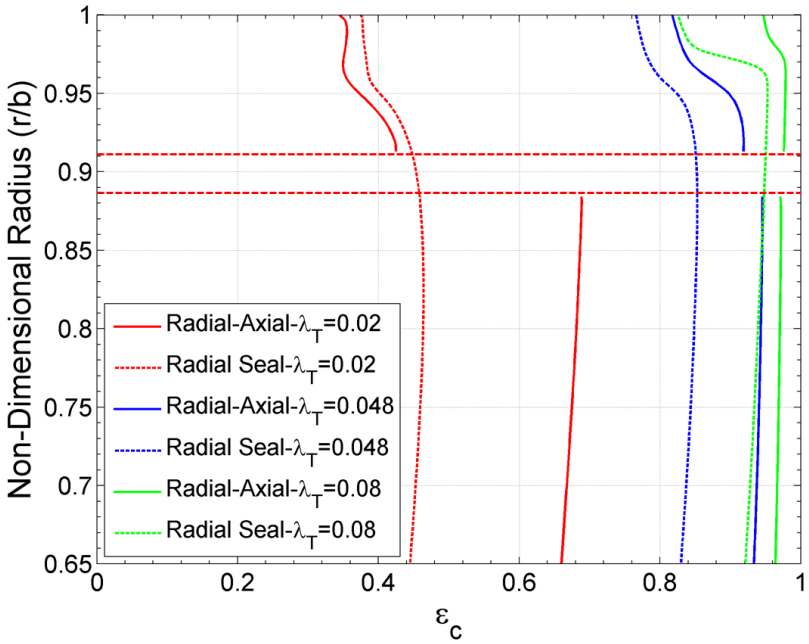

Figure 7.15 Comparison between computed variation of effectiveness with radius for radial-axial-clearance seal and radial-clearance seal for similar λ_T values at $Re_\phi = 8.2 \times 10^5$

Figure 7.16a and b present the computed and measured variation of sealing effectiveness with Φ_o for the inner and outer sampling points (previously covered) for the radial-axial-clearance seal. The open symbols denote the experimental data [59] for the radial-axial-clearance seal for different Re_ϕ at r/b = 0.958 and r/b = 0.85 respectively, while the closed red symbols represent the computed effectiveness on the stator disk at same radius, and the black line is the orifice model theoretical fitted curve for the experimental data.

The computed results for the outer sampling point over-predict the effectiveness in the outer wheel-space compared to the experimental data and theoretical curve, which is to be expected by seeing Figure 7.14, which showed that the computations over-predict the effectiveness in the outer wheel-space. On the other hand, the inner sampling point for the computations shows very good agreement with the experimental data. Both the computational results and experimental measurements show that the effectiveness is higher for the inner sampling point than that at the outer sampling point for the same sealing flow rate value.

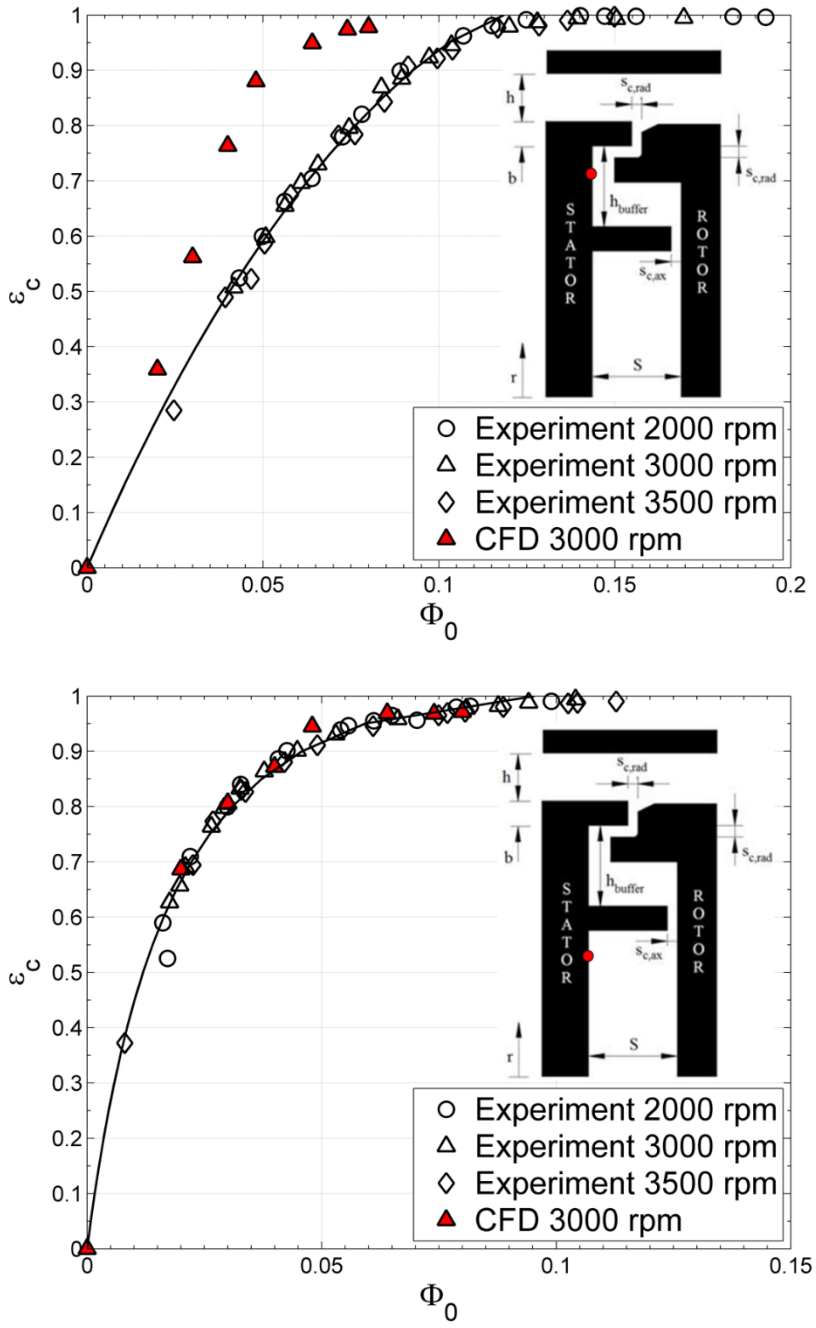

Figure 7.16 Comparison between experimental effectiveness curve fit and computed effectiveness for radial-axial-clearance seal with EI ingress for $Re_W/Re_\phi = 0.538$; where Re_φ = 5.3 x 10^5, 8.2 x 10^5 and 9.7 x 10^5 for 2000, 3000 and 3500 rpm respectively. (a) Outer sampling point; (b) Inner sampling point

7.4 TIGHTER RADIAL-CLEARANCE SEAL

A variation of the previously discussed radial-clearance seal is shown in Figure 7.1d, which has a shorter axial overlap and a tighter radial gap. The experimental section of this thesis, in Chapter 3, showed that tightening the radial gap greatly increased the sealing performance of the radial-clearance seal. This variation of the radial-clearance

seal has been computed and is presented so that comparisons can be made to the following (next section) double-clearance-radial seal, which has similar radial-seal dimensions as this one.

Figure 7.17 illustrates the variation of swirl ratio with non-dimensional radius for the radial-clearance seal. The experimental measurement locations for total pressure in the wheel-space (at Z/s = 0.25) are shown on the right of the figure. The experiments and computations were carried out at Re_φ = 8.2 x10^5 for various values of λ_T. The symbols denote the experimental data, while the lines represent the computed swirl for the same conditions. The swirl distribution shows very good agreement between the computations and measurements, suggesting good prediction of the amount of ingestion entering the wheel-space. The figure shows that as the sealing flow rate is increased, there is a reduction in the core rotation. The swirl near the periphery of the wheel-space also reduces, as the sealing flow increases and pressurises the wheel-space, hence reducing the amount of ingestion from the annulus.

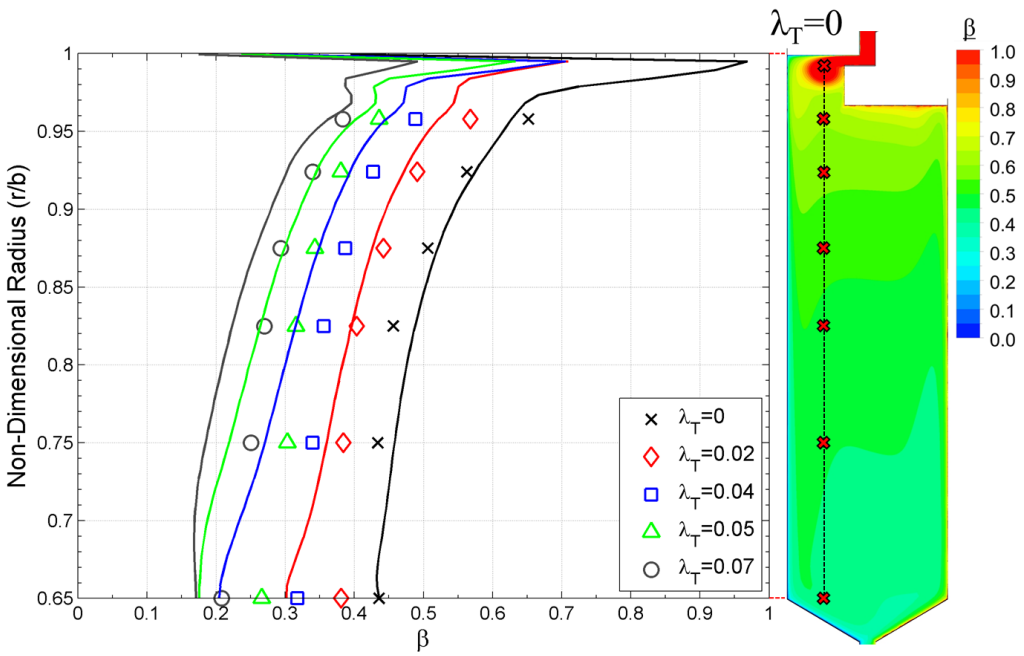

Figure 7.17 Comparison between measured and computed variation of swirl ratio with radius for radial-clearance seal for different λ_T at $Re_\phi = 8.2 \times 10^5$

Figure 7.18 shows the computed and measured radial variation of sealing effectiveness along the stator wall for three different sealing flow rates at Re_φ = 8.2 x 10^5. The symbols represent the experimental, while the computations are represented by the lines. The computed results show good agreement with the experimental distribution

for r/b < 0.9. However at higher radius, the computations show a divergence from the measured data, which is attributed to the CFD experiencing fluid mixing within the wheel-space at high radius (0.9 < r/b < 1).

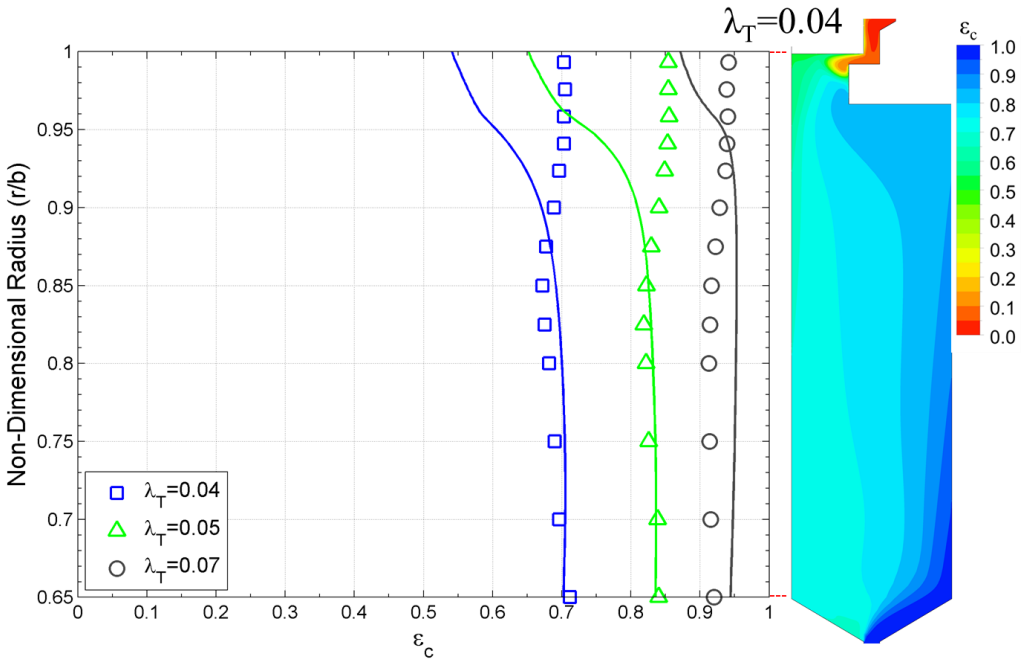

Figure 7.18 Comparison between measured and computed radial variation of effectiveness for radial-clearance seal for different λ_T at $Re_\phi = 8.2 \times 10^5$

Figure 7.19 presents the computed and measured variation of sealing effectiveness with Φ_o for the tighter radial-clearance seal. The open symbols represent the experimental data for different Re_ϕ at r/b = 0.958, while the closed red symbols represent the computed effectiveness on the stator disc at same radius, and the black line is the orifice model theoretical fitted curve for the experimental data. The figure shows reasonable qualitative agreement between computations and experiments, with the computations presenting over-predictive and under-predictive effectiveness fluctuations for the chosen monitored point. This disparity can be explained by seeing Figure 7.18, where it appears that there is a substantial mixing region which is located inside the wheel-space at high radius, giving rise to the difference in effectiveness.

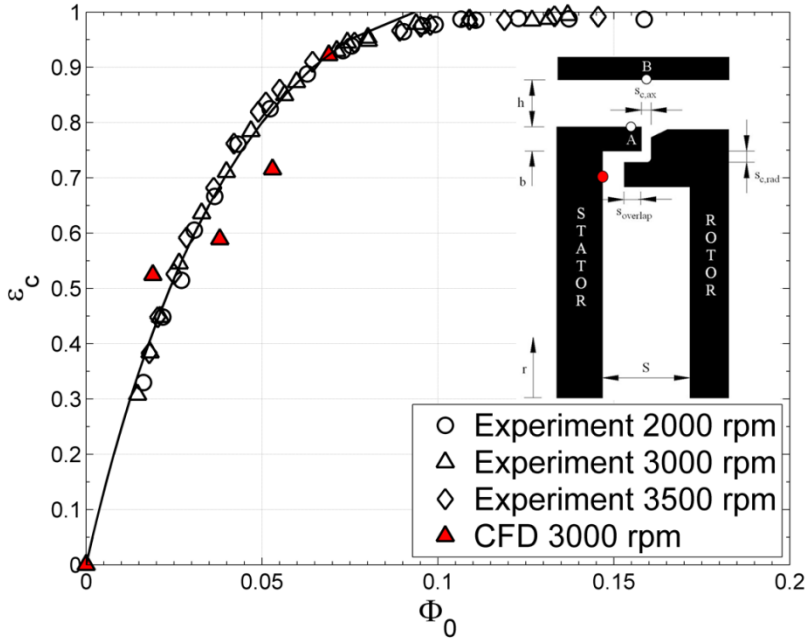

Figure 7.19 Comparison between experimental effectiveness curve fit and computed effectiveness for tighter gap radial-clearance seal with EI ingress for $Re_W/Re_\phi = 0.538$; where Re_φ = 5.3 x 10^5, 8.2 x 10^5 and 9.7 x 10^5 for 2000, 3000 and 3500 rpm respectively

7.5 DOUBLE-RADIAL-CLEARANCE SEAL

Figure 7.1e shows the double-radial-clearance seal, which features similar radial-clearances as the seal in section 7.4 for both inner and outer seals. The inner radial-clearance seal separates the wheel-space into an inner and outer wheel-space.

Figure 7.20 shows the radial distribution of swirl ratio at *Z/s* = 0.25 in the wheel-space for the double-radial-clearance seal. The symbols denote the experimental data [7], while the lines represent the computed swirl for the same conditions. The computed results are in reasonable agreement with experimental measurements, with the computed swirl under-predicted in the outer and inner wheel-spaces for most sealing flows. However the qualitative trend is properly predicted, and the sudden increase of swirl at *r/b* ≈ 0.875 is due to the rotating radial insert. As previously discussed and again shown by Figure 7.20, increasing the sealing flow rate causes a reduction in the swirl ration in both the inner and outer wheel-spaces for both the computed and experimental results.

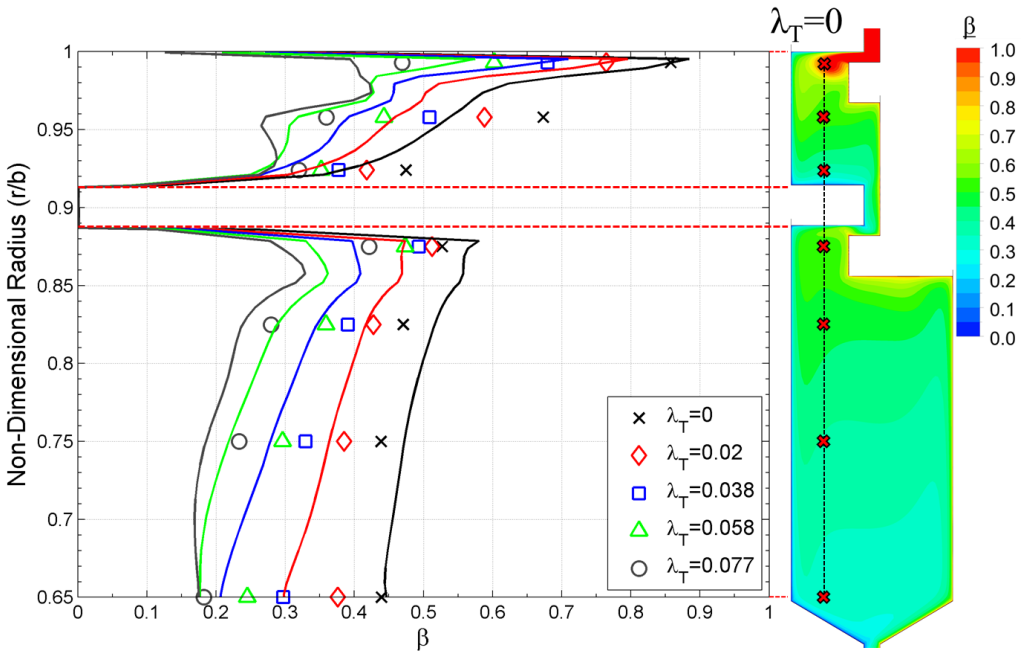

Figure 7.20 Comparison between measured and computed variation of swirl ratio with radius for double-radial-clearance seal for different λ_T at $Re_\phi = 8.2 \times 10^5$

Figure 7.21 presents a comparison between the double-radial-clearance seal and the tighter radial-clearance seal for the swirl ratio distribution for similar λ_T. The swirl for both seals is virtually identical with two major differences identified; firstly the double-radial seal experiences a lower swirl in the outer wheel-space than the single radial seal for similar λ_T, which can be explained by the fact that the double seal has a smaller volume (due to the radial inserts), thus requiring less sealing flow to pressurise the wheel-space, hence reducing ingestion. Secondly, the double-radial-clearance seal has higher swirl at $r/b > 0.85$, which can be explained by the rotor insert on the rotating disc.

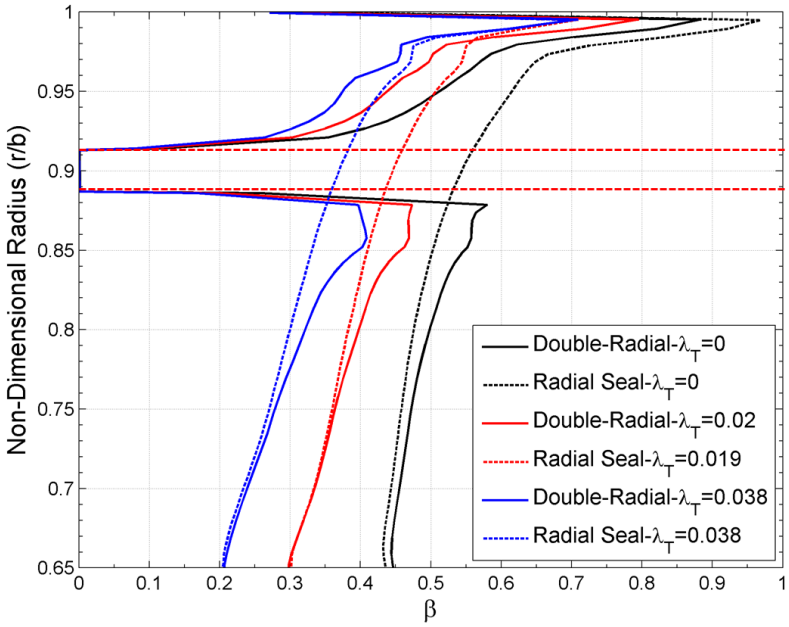

Figure 7.21 Comparison of computed variation of swirl ratio with radius between double-radial-clearance seal and tighter radial-clearance seal for similar λ_T values at $Re_\phi = 8.2 \times 10^5$

Figure 7.22 shows the radial distribution of sealing effectiveness on the stator for the double-radial-clearance seal. Experimental data is also included for comparison [7]. Both computational results and experimental data show an increased sealing effectiveness in the inner wheel-space, which is attributed to the outer wheel-space acting as a buffer chamber which retains most of the high swirling ingested flow from the annulus. The computations qualitatively reproduce trends in the measured sealing effectiveness in the outer wheel-space, but with under-prediction of the measured effectiveness. The effectiveness in the inner wheel-space has good agreement with the experimental data.

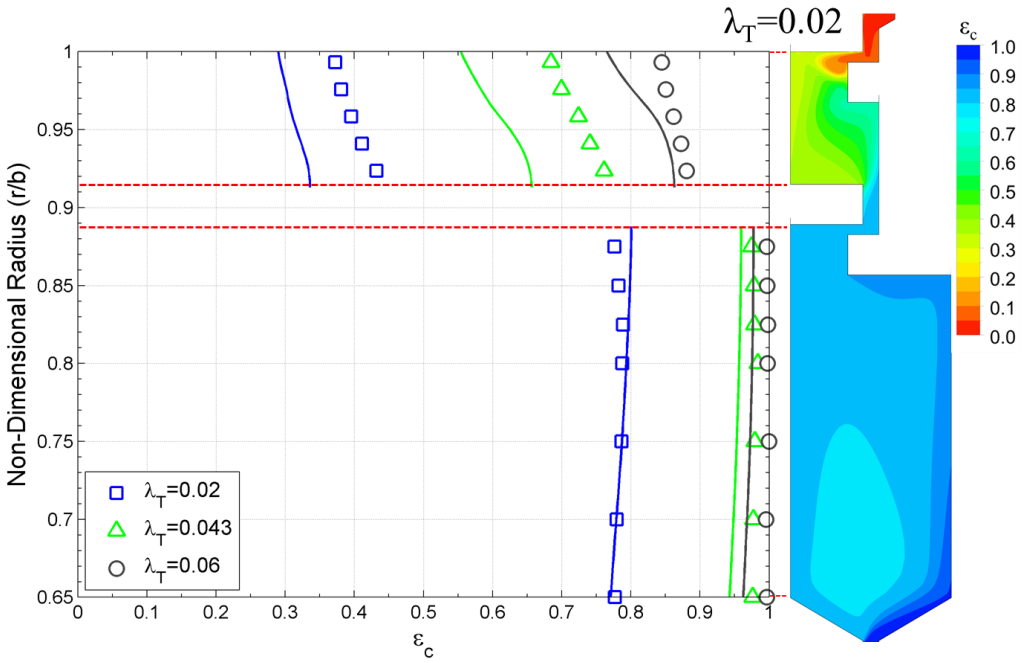

Figure 7.22 Comparison between measured and computed radial variation of effectiveness for radial-clearance seal for different λ_T at $Re_\phi = 8.2 \times 10^5$

Figure 7.23 presents a comparison of the radial distribution of effectiveness between the double-radial-clearance seal and the tighter radial-clearance seal. Both seals present an almost invariant effectiveness for $r/b < 0.875$, suggesting the fluid is fully mixed by this point, i.e. inner wheel-space. However both seals show mixing is occurring at high radius in the wheel-space, i.e. outer wheel-space. Again, the double seal shows a better sealing effectiveness for the inner wheel-space than the single radial-clearance seal, supporting the statement that the outer wheel-space acts as a buffer chamber which contains and dampens most of the ingested fluid for the inner wheel-space.

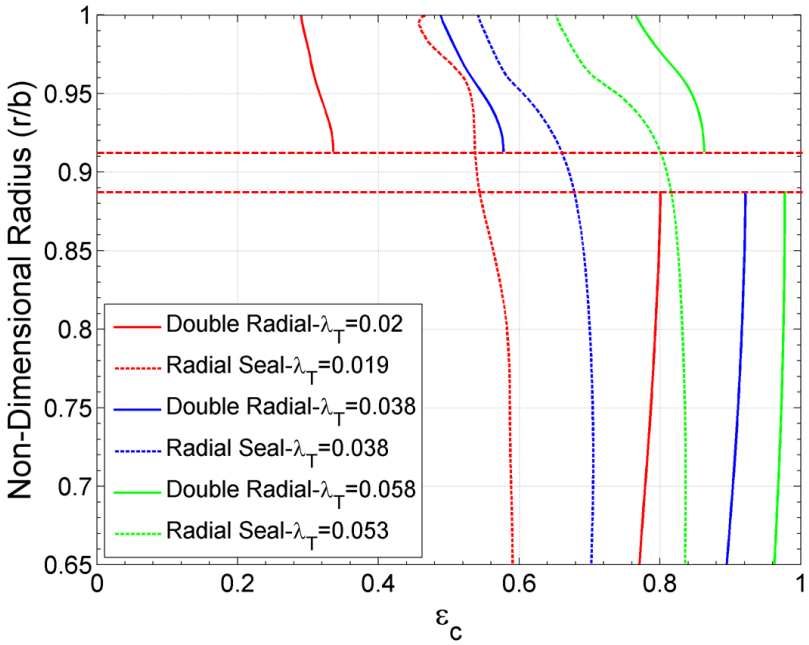

Figure 7.23 Comparison of computed variation of effectiveness with radius between double-radial-clearance seal and tighter radial-clearance seal for similar λ_T values at $Re_\phi = 8.2 \times 10^5$

Figure 7.24a and b present the computed and measured variation of sealing effectiveness with Φ_o for the inner and outer sampling points (previously covered) for the double-radial-clearance seal. The open symbols denote the experimental data [32] for the double-radial seal for different Re_ϕ at r/b = 0.958 and r/b = 0.85 respectively, while the closed red symbols represent the computed effectiveness on the stator disk at same radius, and the black line is the orifice model theoretical fitted curve for the experimental data.

The computed results for the outer sampling point under-predict the effectiveness in the outer wheel-space for $\Phi_o < 0.05$ compared to the experimental data and theoretical curve. On the other hand, the inner sampling point for the computations shows very good agreement with the experimental data. Both the computational results and experimental measurements show that the effectiveness is higher for the inner sampling point than that at the outer sampling point for the same sealing flow rate value.

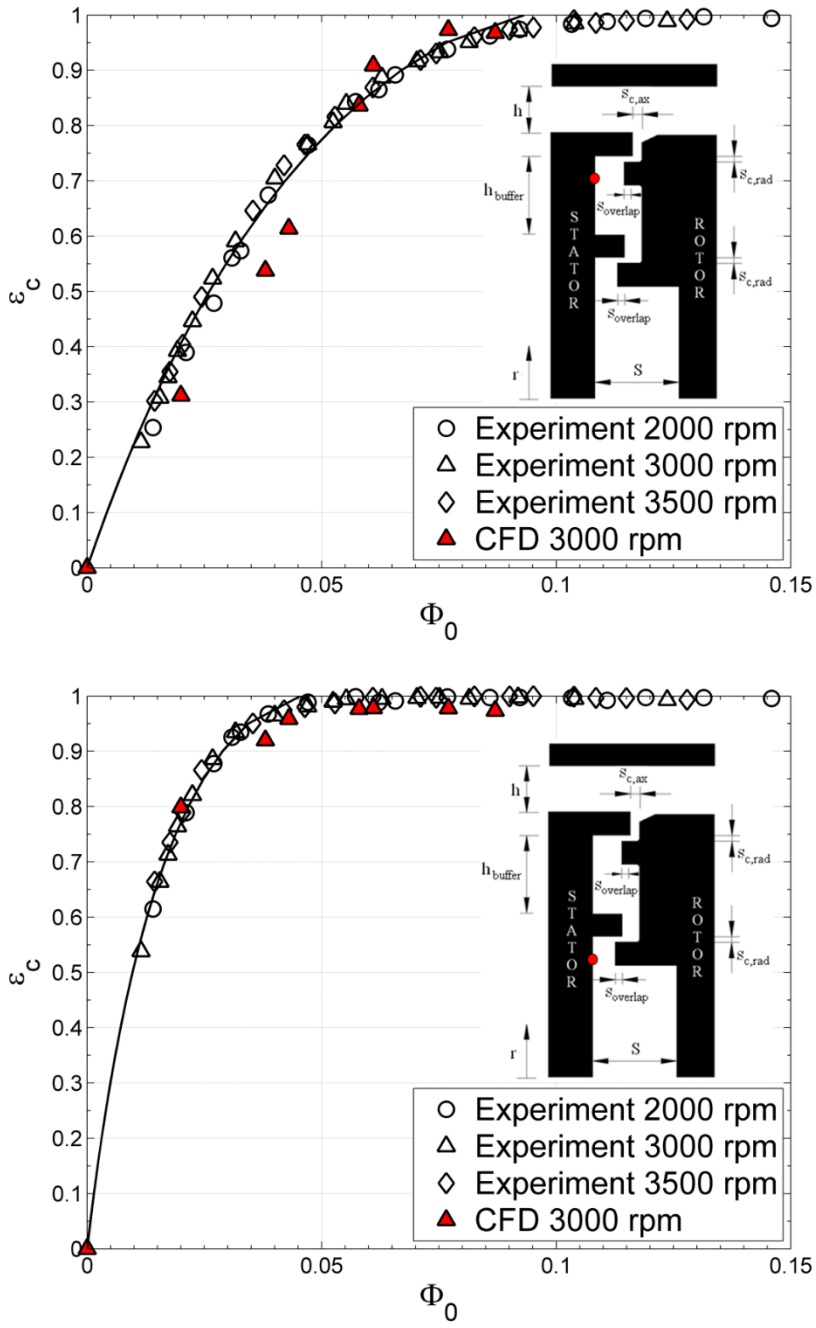

Figure 7.24 Comparison between experimental effectiveness curve fit and computed effectiveness for radial-clearance seal with EI ingress for $Re_W/Re_\phi = 0.538$; where Re_φ = 5.3 x 10^5, 8.2 x 10^5 and 9.7 x 10^5 for 2000, 3000 and 3500 rpm respectively. (a) Outer sampling point; (b) Inner sampling point

7.6 SEALING PERFORMANCE FOR ALL COMPUTED RIM-SEAL GEOMETRIES

Figure 7.25 shows the computed and fitted curve of measured variation of sealing effectiveness with Φ_o for all the rim-seal geometries considered in this study at the monitoring point, r/b = 0.958; which is in the outer wheel-space for the double seals. The worst performing seals are the single and double axial-clearance seals, which is over-predicted and under-predicted respectively. The worst predicted effectiveness at this monitoring location was for the radial-axial-clearance seal, where the computed effectiveness was greatly over-predicted. On the other hand, the two single radial-clearance seals and double-radial-clearance seal show good predictive capabilities, with some effectiveness fluctuation encountered, however the qualitative behaviour is captured.

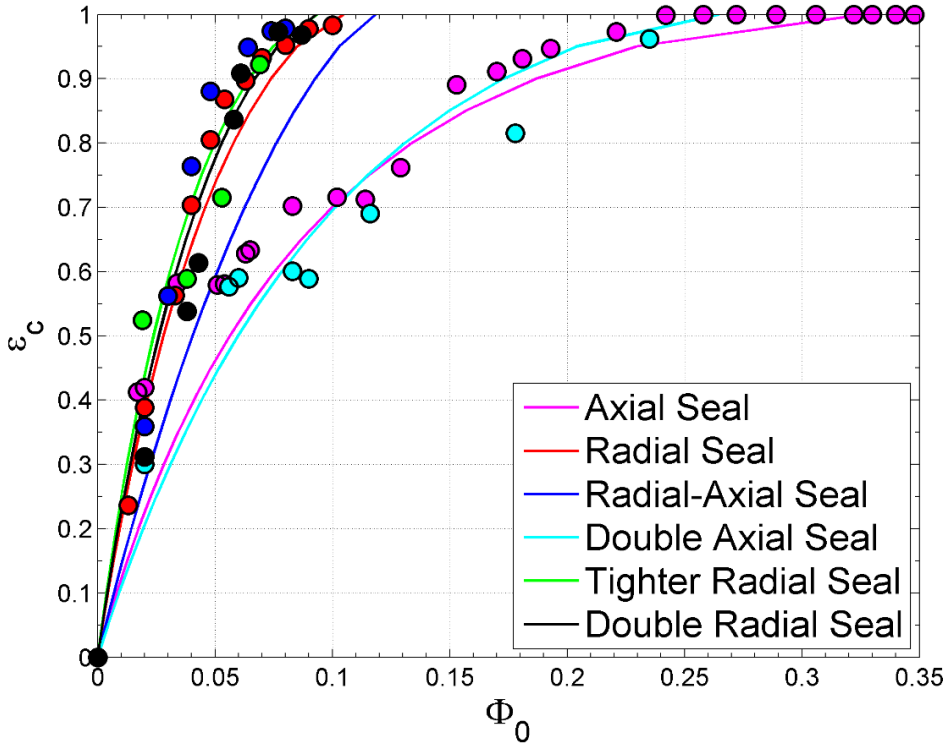

Figure 7.25 Computed variation of effectiveness with Φ_o for all rim-seal geometries at r/b=0.958 (lines denote orifice model theoretical fitted curve for experimental data; symbols represent computed effectiveness).

Figure 7.26 shows the computed and fitted curve of measured variation of sealing effectiveness with Φ_o for all the double seals at the inner sampling point of r/b = 0.85. For this sampling point, the double-axial-clearance seal largely over-predicts the effectiveness. However the radial-axial and double-radial seals show very good agreement with the fitted experimental curve. Overall, the double-clearance seals are able to capture the improvement of effectiveness at low radius, which is due to the inner seal creating a damping chamber (outer wheel-space) to protect the inner wheel-space.

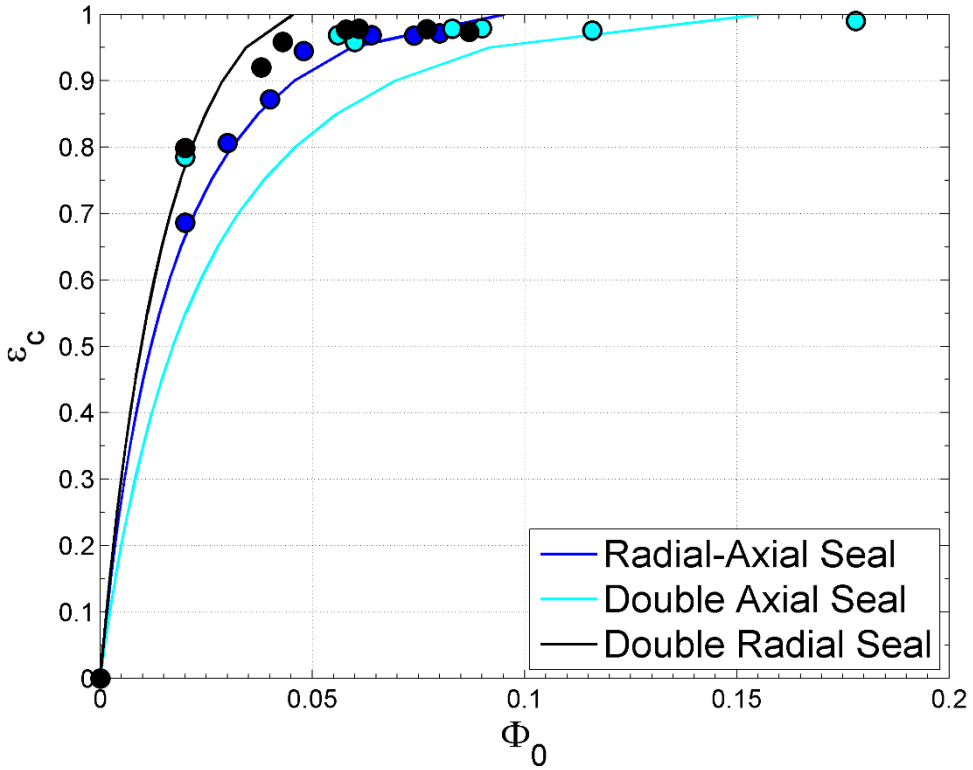

Figure 7.26 Computed variation of effectiveness with Φ_o for all double seal geometries at r/b=0.85 (lines denote orifice model theoretical fitted curve for experimental data; symbols represent computed effectiveness).

7.7 CHAPTER OVERVIEW

The non-bladed 3D steady CFD model has some limitations when predicting ingress for double-clearance seals, however it is shown to properly capture the flow structure in the wheel-space for different sealing flow rates. The 3D steady model is shown to capture qualitative effectiveness trends and have very good predictive capabilities for the flow structure for all rim-seal geometries compared to experimental results.

This 3D model is less computationally intensive than traditional 3D unsteady models, whilst still allowing it to predict proper non-axisymmetric annular flow behaviour in comparison to traditional 2D axisymmetric models. Therefore the model can be considered as a convenient and relatively quick computational tool for an engine designer who needs to know and understand the flow structure in the wheel-space for a given rim-seal, or even qualitatively evaluate the sealing performance of a given rim-seal geometry, when experimental facilities are not available.

8 CONCLUSIONS AND FUTURE WORK

A 3D steady CFD model without rotor blades is presented in this thesis for the study of Externally-Induced ingress. The model is an 11.25° circumferential sector and includes three domains: the stator domain (which includes a vane), wheel-space domain, and rotor domain (excludes rotor blade); the domains are joined into a multi-body model via a frame change interface, which is located between the stator and wheel-space domains. The boundary conditions set for both inlets (main flow and sealing flow) is with mass flow rate, and with an average static pressure set on the outlet. This model is a quick computational tool compared with 3D unsteady CFD codes.

8.1 AXISYMMETRIC MODEL

The verification of the procedure in creating a CFD model and its mesh was carried out by comparing the computational results of a 3D axisymmetrical rotor-stator model with no ingress against published experimental results. The effect of wheel-space geometry and advection scheme was tested and found to have negligible effect on the fluid dynamics within the wheel-space (axial distributions of velocity).

Computations show very good agreement with experimental data, where the radial and tangential velocities show typical Batchelor rotor-stator flow behaviour. This means that the flow moves radially inwards on the stator and radially outwards on the rotor, and no radial flow in the core (located outside the separate boundary layers). The swirl is seen to be zero at the stator and one on the rotor, with a constant swirl ratio in the core.

8.2 PRELIMINARY INGESTION MODELS

This research evolved through various CFD models for the steady prediction of ingress through gas turbine rim-seals. The first model to be developed was the ‘thin seal’ model, which was a continuation of a previous research at the University of Bath, however the development being that ‘on-design’ conditions were used. A ‘thin seal’ model, which consisted of modifying the radial dimension of a seal to as thin as permissible by meshing configurations, was found to under-predict effectiveness, however having reasonable qualitative agreement with experimental data. This model

was found to be too cumbersome to be applied to more complicated rim-seal geometries, due to the large number of geometric alterations possible.

The steady CFD model eventually led to the use of the real rim-seal geometry (including the rotor blade) with a Frozen Rotor interface. The rotor blade was positioned and computed at four locations for a range of sealing flow rates, producing varied effectiveness results at low sealing flows. It was seen that the average of the four blade positions gave good agreement with the experimental data, however the requirement of computing several blade positions for a given case was found to be too time consuming, giving rise to questions of how many and which positions should be computed.

8.3 NON-BLADED 3D STEADY MODEL

Recent published literature gave proper insight on the very little effect rotor blades have on the pressure distribution downstream of the vanes (location A), which is the driving force for EI ingress. Thus the CFD model was modified to exclude the rotor blade from the rotor domain, and extensively tested for the axial-clearance seal.

A turbulence and advection scheme sensitivity analysis was performed for the no sealing flow case, and the Shear Stress Transport turbulence model with upwind scheme selected as the most appropriate setting due to its convergence level, supported by previous literature and good agreement with the pressure distribution in the annulus. The pressure distribution in the annulus was extensively analysed for different rotational Reynolds number computations, differing sealing flows and varying ratios of Re_W/Re_ϕ; all the cases showed good agreement with experimentally measured data at the University of Bath.

Further validation was carried out between the computed results and the measured data within the wheel-space in terms of radial distributions of swirl ratio, effectiveness and static pressure (C_p). The computations show very good agreement with experiments for swirl ratio and C_p at the stator wall, with reasonable agreement in terms of effectiveness.

Finally, the non-bladed steady method was used to perform further computations for generic radial-clearance and double-clearance seals experimentally tested at the

University of Bath. For each computed seal, the swirl ratio and sealing effectiveness in the wheel-space is validated against measured data, also the sealing performance is compared for each seal. The radial-clearance seal is seen to have improved sealing capabilities than the axial-clearance seal as confirmed by previous literature too, however no significant improvement is seen for the swirl. Therefore to reduce the swirl ratio within the wheel-space, double-clearance seals are computed, where the outer wheel-space created by the inner seal is seen to act as a damping chamber which holds and contains most of the ingested fluid, thus drastically improving the effectiveness and reducing the core swirl within the inner wheel-space. The computed results for all the other seals show reasonable sealing effectiveness agreement with experiments, while the flow structure (swirl ratio) is properly captured.

The non-bladed CFD model is a useful 3D tool for a turbine design engineer. The lack of experimental facilities and/ or data would make this 3D model an indispensable CFD tool for quantitatively predicting the flow structure within the wheel-space, and qualitatively predicting the sealing effectiveness for any given rim-seal geometry.

8.4 FUTURE WORK

The 3D steady CFD model has shown to be able to provide useful information for the prediction of EI ingress, however some limitations and/ or improvements have been identified, which will be listed below for the possibility of further improving this method.

1. Produce a similar non-bladed CFD model to the one described in this study, however for another experimental rig geometry, which includes non-symmetric rotor blades and blade axial location relative to the seal, to verify that the blade geometry (symmetrical/ non-symmetrical) has no effect on this CFD approach.
2. Set more accurate boundary conditions which would make the computations more robust and reliable in predicting the flow field information (i.e. pressure). This would require the experimental rig to incorporate total pressure taps at the inlets and static pressure taps at the outlet; these boundary conditions have been identified to give better converged and accurate solutions.

3. Set the CFD model to include the energy equation, which would allow for the prediction of heat transfer in the rotor-stator system, and hence temperature validations can be carried out for the rotor disc. However, an in depth sensitivity study would be required, since much more care is usually required to properly capture the heat transfer in a rotor-stator system.
4. Low rotational Reynolds number computations have been performed and validated against experimental data in this study, however the use of CFD tools usually takes place in industry. Gas turbine engines operate at much higher rotational speeds, which would require this steady CFD model to be scaled and validated for engine conditions.

Work presented and discussed in chapter 3 has been published (see Appendix C). The results for the non-bladed model, presented and discussed in chapters 6 and 7, is currently being written up for publication.

REFERENCES

[1] Lock, G. D. (2007). Aircraft Propulsion - Lecture Course Notes.

[2] Pfenninger, H. (1953). "Operating Experience with Brown Boveri Gas-Turbine Installations." Brown Boveri Rev. 40: pp. 144-166.

[3] Rolls-Royce (1996). The Jet Engine, Rolls-Royce PLC. ISBN 0902121235.

[4] Walsh, P. P. and Fletcher, P. (2004). Gas Turbine Performance, 2nd Edition, Blackwell Publishing. ISBN 063206434X.

[5] Bathie, W. W. (1996). Fundamentals of Gas Turbines, 2nd Edition, Wiley. ISBN 9780471311225.

[6] Sangan, C. M., Pountney, O. J., Zhou, K., Wilson, M., Owen, J. M. and Lock, G. D. (2013). "Experimental Measurements of Ingestion through Turbine Rim Seals. Part I: Externally-Induced Ingress." Journal of Turbomachinery 135(2).

[7] Sangan, C. M., Lalwani, Y., Owen, J. M. and Lock, G. D. (2013). "Experimental Measurements of Ingestion through Turbine Rim Seals. Part 5: Fluid Dynamics of Wheel-Space." ASME Paper GT2013-94148.

[8] Childs, P. R. N. (2010). Rotating Flow, Butterworth-Heinemann. ISBN 0123820987.

[9] Batchelor, G. K. (1951). "Note on a Class of Solutions of the Navier-Stokes Equations representing Steady Rotationally-Symmetric Flow." Quart. J. Mech. Appl. Maths 4: pp. 29-41.

[10] Stewartson, K. (1953). "On the Flow between Two Rotating Coaxial Discs." Proceedings of the Cambridge Philosophical Society 49: pp. 333-341.

[11] Daily, J. W. and Nece, R. E. (1960). "Chamber Dimension Effects on Induced Flow and Frictional Resistance of Enclosed Rotating Disks." Journal of Basic Engineering 82(1): pp. 217-230.

[12] Chen, J. X., Gan, X. and Owen, J. M. (1996). "Heat Transfer in an Air-Cooled Rotor-Stator System." Journal of Turbomachinery 118: pp. 444-451.

[13] Bayley, F. J. and Owen, J. M. (1970). "The Fluid Dynamics of a Shrouded Disk System with a Radial Outflow of Coolant." ASME Journal of Engineering Power 92: pp. 335-341.

[14] Phadke, U. P. and Owen, J. M. (1988). "Aerodynamic Aspects of the Sealing of Gas-Turbine Rotor-Stator Systems. Part 1: The Behavior of Simple Shrouded Rotating-Disk Systems in a Quiescent Environment." International Journal of Heat and Fluid Flow 9(2): pp. 98-105.

[15] Phadke, U. P. and Owen, J. M. (1988). "Aerodynamic Aspects of the Sealing of Gas-Turbine Rotor-Stator Systems. Part 2: The Performance of Simple Seals in a Quasi-Axisymmetric External Flow." International Journal of Heat and Fluid Flow 9(2): pp. 106-112.

[16] Phadke, U. P. and Owen, J. M. (1988). "Aerodynamic Aspects of the Sealing of Gas-Turbine Rotor-Stator Systems. Part 3: The Effect of Non-Axisymmetric External Flow on Seal Performance." International Journal of Heat and Fluid Flow 9(2): pp. 113-117.

[17] Phadke, U. P. and Owen, J. M. (1983). "An Investigation of Ingress for an 'Air Cooled' Shrouded Rotating Disk System with Radial Clearance Seals." ASME Journal of Engineering Power 105: pp. 178-183.

[18] Graber, D. J., Daniels, W. A. and Johnson, B. V. (1987). Disk Pumping Test: Final Report, Air Force Wright Aeronautical Laboratories.

[19] Abe, T., Kikuchi, J. and Takeuchi, H. (1979). "An Investigation of Turbine Disk Cooling (Experimental Investigation and Observation of Hot Gas Flow into a Wheel Space)." CIMAG – 13th International Congress on Combustion Engines.

[20] Hamabe, K. and Ishida, K. (1992). Rim Seal Experiments and Analysis of a Rotor-Stator System with Non-Axisymmetric Main Flow. ASME Paper 92-GT-160.

[21] Chew, J. W., Green, T. and Turner, A. B. (1994). Rim Sealing of Rotor-Stator Wheel-Spaces in the Presence of External Flow. ASME Paper 94-GT-126.

[22] Bohn, D. E., Decker, A., Ma, H. and Wolff, M. (2003). Influence of Sealing Air Mass Flow on the Velocity Distribution in and Inside the Rim of the Upstream Cavity of a 1.5-Stage Turbine. ASME Paper GT2003-38459.

[23] Bohn, D. and Wolff, M. (2003). Improved Formulation to Determine Minimum Sealing Flow: Cw,min - for Different Sealing Configurations. ASME Paper GT2003-38465.

[24] Bohn, D., Johann, E. and Krueger, U. (1995). Experimental and Numerical Investigations of Aerodynamic Aspects of Hot Gas Ingestion in Rotor-Stator Systems with Superimposed Cooling Mass Flow. ASME Paper 95-GT-143.

[25] Bohn, D., Rudzinski, B., Sürken, N. and Gärtner, W. (1999). Influence of Rim Seal Geometry on Hot Gas Ingestion into the Upstream Cavity of an Axial Turbine Stage. ASME Paper 99-GT-248.

[26] Bohn, D., Rudzinski, B., Sürken, N. and Gärtner, W. (2000). Experimental and Numerical Investigation of the Influence of Rotor Blades on Hot Gas Ingestion into the Upstream Cavity of an Axial Turbine Stage. ASME Paper 00-GT-284.

[27] Roy, R. P., Feng, J., Narzary, D. and Paolillo, R. E. (2005). "Experiment on Gas Ingestion through Axial-Flow Turbine Rim Seals." Journal of Engineering for Gas Turbines and Power 127(3): pp. 573-582.

[28] Roy, R. P., Zhou, D. W., Ganesan, S., Wang, C. Z., Paolillo, R. E. and Johnson, B. V. (2007). The Flow Field and Main Gas Ingestion in a Rotor-Stator Cavity. ASME Paper GT2007-27661.

[29] Zhou, D. W., Roy, R. P., Wang, C. Z. and Glahn, J. A. (2009). Main Gas Ingestion in a Turbine Stage for Three Rim Cavity Configurations. ASME Paper GT2009-59851.

[30] Gentilhomme, O., Hills, N. J., Turner, A. B. and Chew, J. W. (2003). "Measurement and Analysis of Ingestion through a Turbine Rim Seal." Journal of Turbomachinery 125(3): pp. 505-512.

[31] Sangan, C. M., Pountney, O. J., Zhou, K., Owen, J. M., Wilson, M. and Lock, G. D. (2013). "Experimental Measurements of Ingestion through Turbine Rim Seals. Part II: Rotationally-Induced Ingress." Journal of Turbomachinery 135(2).

[32] Sangan, C. M., Pountney, O. J., Scobie, J. A., Wilson, M., Owen, J. M. and Lock, G. D. (2012). Experimental Measurements of Ingestion through Turbine Rim Seals. Part 3: Single and Double Seals. ASME Paper GT2012-68493.

[33] Scobie, J. A., Sangan, C. M., Teuber, R., Pountney, O. J., Owen, J. M., Wilson, M. and Lock, G. D. (2013). Experimental Measurements of Ingestion through Turbine Rim Seals. Part 4: Off-Design Conditions. ASME Paper GT2013-94147.

[34] Dunn, D. M., Zhou, D. W., Saha, K., Squires, K. D., Roy, R. P., Kim, Y. W. and Moon, H. K. (2010). Flow Field in a Single-Stage Model Air Turbine Rotor-Stator Cavity with Pre-Swirled Purge Flow. ASME Paper GT2010-22869.

[35] Lewis, P. and Wilson, M. (2007). "Three-Dimensional Computations of Ingress in Gas Turbine Cooling Systems." Proceedings of the International Gas Turbine Congress.

[36] Mirzamoghadam, A. V., Heitland, G., Morris, M. C., Smoke, J., Malak, M. and Howe, J. (2008). "3D CFD Ingestion Evaluation of a High Pressure Turbine Rim Seal Disk Cavity." Proceedings of the ASME Turbo Expo 4: pp. 1443-1452.

[37] Mirzamoghadam, A. V., Heitland, G. and Hosseini, K. M. (2009). "The Effect of Annulus Performance Parameters on Rotor-Stator Cavity Sealing Flow." Proceedings of the ASME Turbo Expo 3: pp. 1163-1172.

[38] Zhou, K., Wilson, M., Owen, J. M. and Lock, G. D. (2013). "Computation of Ingestion through Gas Turbine Rim Seals." Proceedings of the Institution of Mechanical Engineers. Part G, Journal of Aerospace Engineering 227(7): pp.1101-1113.

[39] Owen, J. M. (2011). "Prediction of Ingestion through Turbine Rim Seals. Part I: Rotationally Induced Ingress." Journal of Turbomachinery 133(031005-1-9).

[40] Owen, J. M. (2011). "Prediction of Ingestion through Turbine Rim Seals. Part II: Externally Induced and Combined Ingress." Journal of Turbomachinery 133(031006-1-9).

[41] Rabs, M., Benra, F. K., Dohmen, H. J., Lock, G. D. and Schneider, O. (2012). Model Simplifications for Numerical Simulation of Ingestion through Gas Turbine Rim Seals. ISROMAC Paper.

[42] Jakoby, R., Zierer, T., Devito, L., Lindblad, K., Larsson, J., Bohn, D. E., Funcke, J. and Decker, A. (2004). "Numerical Simulation of the Unsteady Flow Field in an Axial Gas Turbine Rim Seal Configuration." Proceedings of the ASME Turbo Expo 4: pp. 431-440.

[43] Julien, S., Lefrancois, J., Dumas, G., Boutet-Blais, G., Lapointe, S. and Caron, J.-F. (2010). Simulations of Flow Ingestion and Related Structures in a Turbine Disk Cavity. ASME Paper GT2010-22729.

[44] Laskowski, G. M., Bunker, R. S., Bailey, J. C., Ledezma, G., Kapetanovic, S., Itzel, G. M., Sullivan, M. A. and Farrell, T. R. (2009). "An Investigation of Turbine Wheel-Space Cooling Flow Interactions with a Transonic Hot Gas Path – Part 2: CFD Simulations." Proceedings of the ASME Turbo Expo 3: pp. 1095-1111.

[45] O'Mahoney, T. S. D., Hills, N. J., Chew, J. W. and Scanlon, T. (2010). "Large-Eddy Simulation of Rim Seal Ingestion." Proceedings of the ASME Turbo Expo 4: pp. 1155-1165.

[46] Teuber, R., Li, Y. S., Maltson, J., Wilson, M., Lock, G. D. and Owen, J. M. (2013). "Computational Extrapolation of Turbine Sealing Effectiveness from Test Rig to Engine Conditions." Proceedings of the Institution of Mechanical Engineers, Part A: Journal of Power and Energy 227(2): pp. 167-178.

[47] Zhou, K., Wood, S. N. and Owen, J. M. (2011). Statistical and Theoretical Models of Ingestion through Turbine Rim Seals. ASME Paper GT2011-45139.

[48] ANSYS (2010). ANSYS CFX Reference Guide, Release 13.0.

[49] Barth, T. J. and Jesperson, D. C. (1989). The Design and Application of Upwind Schemes on Unstructured Meshes. AIAA Paper 89-0366.

[50] Wilcox, D. C. (1988). "Multiscale Model for Turbulent Flows." AIAA Journal 26(11): pp. 1311-1320.

[51] Menter, F. R. (1994). "Two-Equation Eddy-Viscosity Turbulence Models for Engineering Applications." AIAA Journal 32(8): pp. 1598-1605.

[52] Bardina, J. E., Huang, P. G. and Coakley, T. J. (1997). Turbulence Modeling Validation. AIAA Paper 97-2121.

[53] Launder, B. E. and Spalding, D. B. (1974). "The Numerical Computation of Turbulent Flows." Comp. Meth. Appl. Mech. Eng. 3: pp.269-289.

[54] Bohn, D. E., Decker, A., Ohlendorf, N. and Jakoby, R. (2006). Influence of an Axial and Radial Rim Seal Geometry on Hot Gas Ingestion into the Upstream Cavity of a 1.5 Stage Turbine. ASME Paper GT2006-90453.

[55] Daily, J. W., Ernst, W. D. and Asbedian, V. V. (1964). Enclosed Rotating Discs with Superposed Throughflow. MIT Department of Civil Engineering, Hydrodynamics Laboratory Report No. 64.

[56] Dadkhah, S. (1989). Ingestion and Sealing Performance of Rim Seals in Rotor-Stator Wheelspaces. D. Phil. Thesis, University of Sussex, UK.

[57] Micio, M. (2010). Gas Turbine Secondary Air System: Experimental Analysis and Design Tools Developing. Scuola Di Dottorato In Ingegneria Industriale, Firenze.

[58] Owen, J. M. and Rogers, R. H. (1989). Flow and Heat Transfer in Rotating-Disc Systems. Research Studies Press, John Wiley, N. Y., UK.

[59] Sangan, C. M. (2011). Measurement of Ingress through Gas Turbine Rim Seals. Ph. D. Thesis, University of Bath, UK.

[60] Vaughan, C. M. (1986). A Numerical Investigation into the Effect of an External Flow Field on the Sealing of a Rotor-Stator Cavity. D. Phil. Thesis, University of Sussex, UK.

[61] Chew, J. W. and Vaughan, C. M. (1988). Numerical Predictions for the Flow Induced by an Enclosed Rotating Disc. ASME Paper 88-GT-127.

APPENDIX A – SWIRL RATIO CONTOURS

The figures presented in this appendix are the swirl ratio contours on the axial-radial plane for all of the rim-seal geometries considered in this research, each seal shows five different sealing flow rates (in increasing order from left to right), which correspond to the λ_T cases presented for the individual swirl plots of each seal.

- Axial-clearance seal (section 6.3):

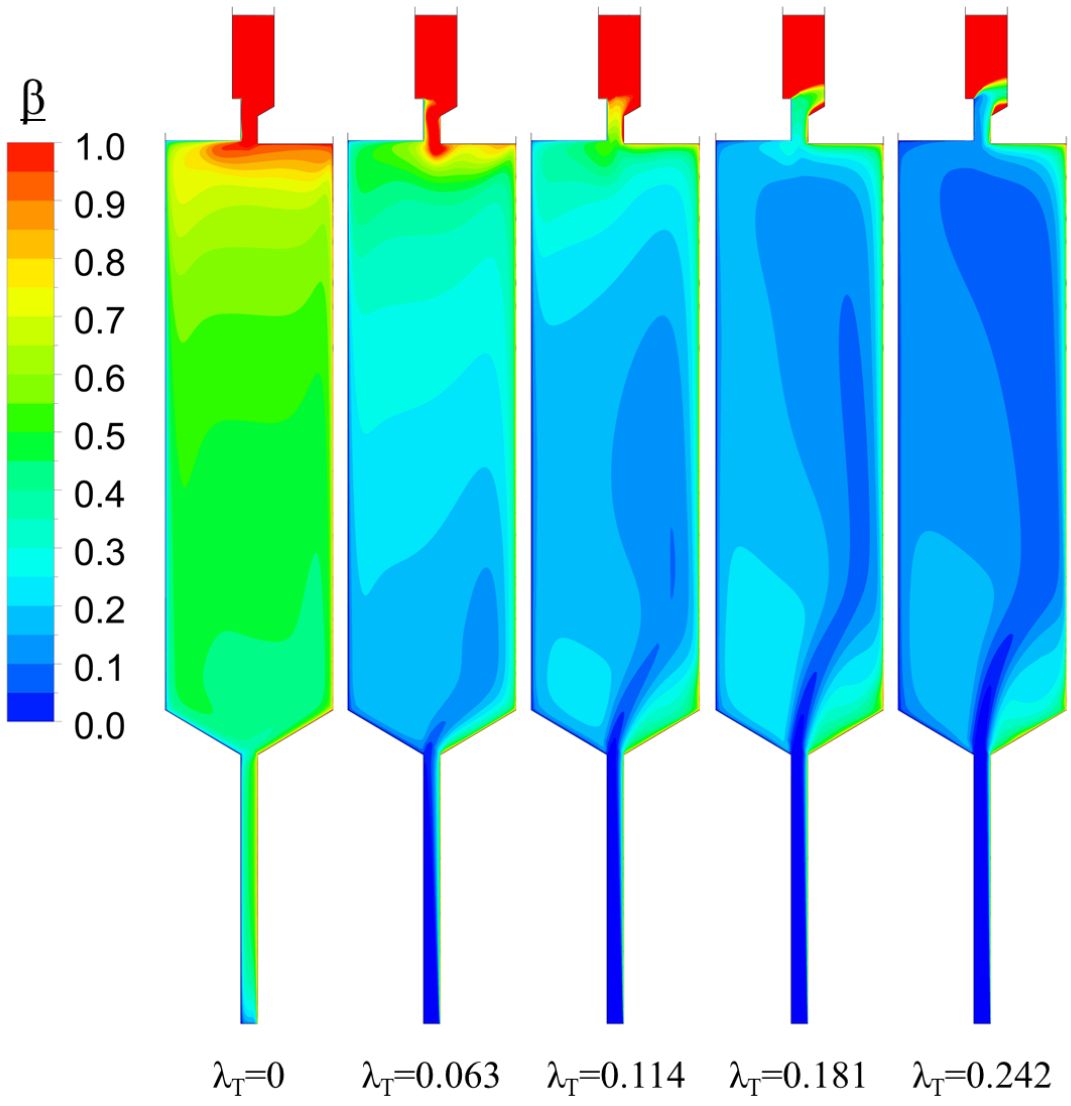

Figure A - 1 Wheel-space swirl contours (axial-radial plane) for axial-clearance seal at periodic surface for various sealing flow rates

- Radial-clearance seal (section 7.1):

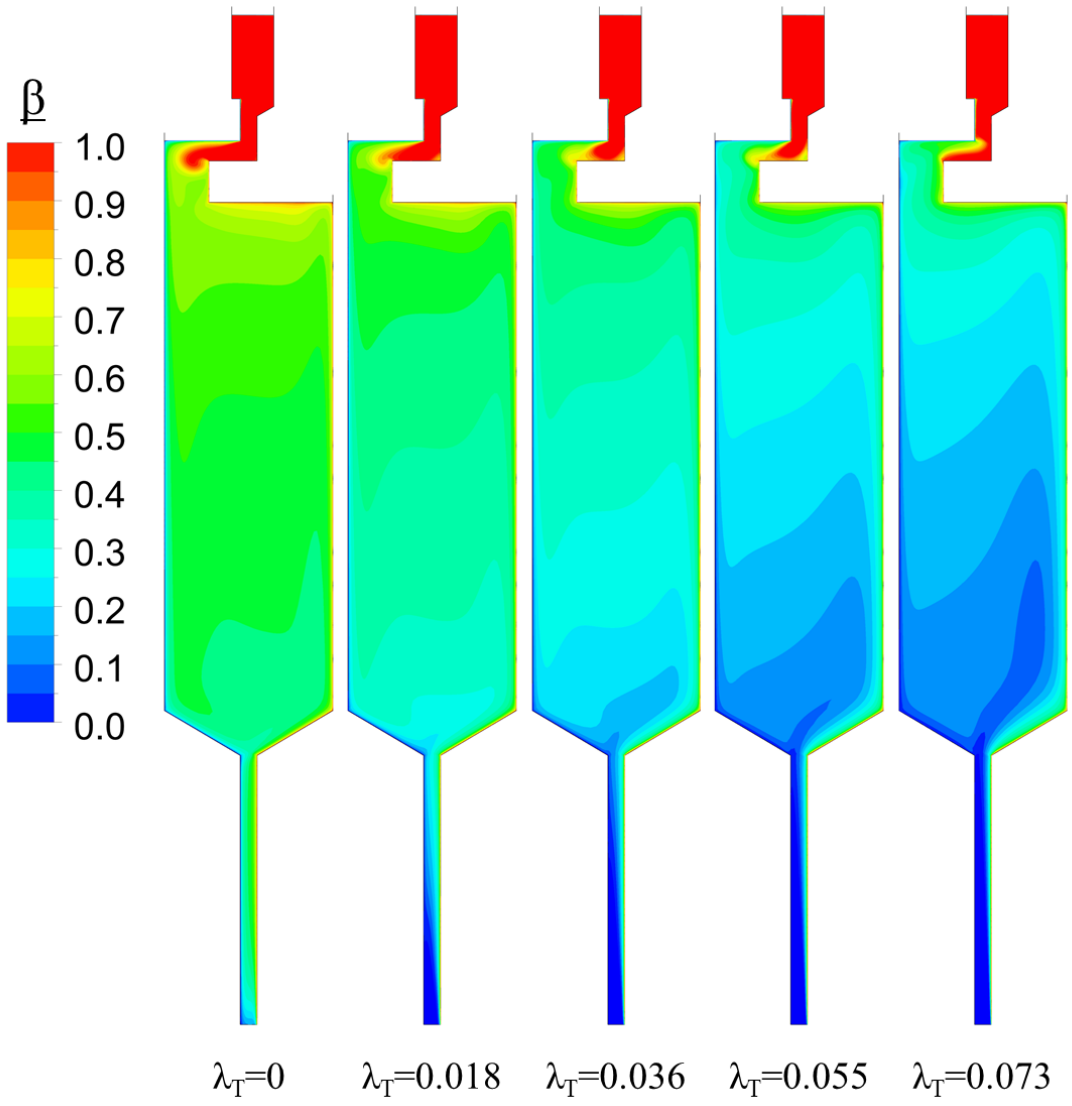

Figure A - 2 Wheel-space swirl contours (axial-radial plane) for radial-clearance seal at periodic surface for various sealing flow rates

- Double-axial-clearance seal (section 7.2):

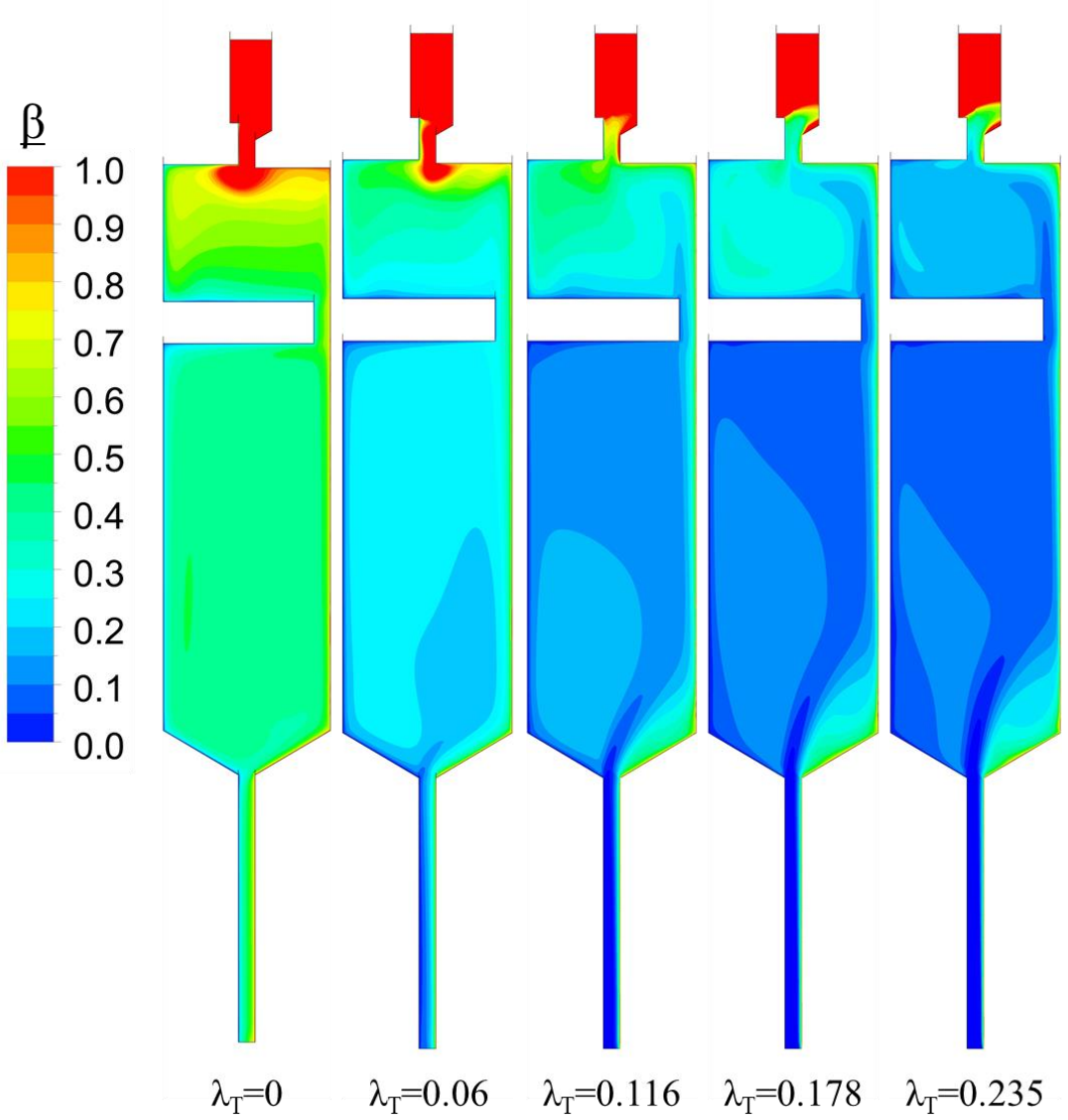

Figure A - 3 Wheel-space swirl contours (axial-radial plane) for double-axial-clearance seal at periodic surface for various sealing flow rates

- Radial-axial-clearance seal (section 7.3):

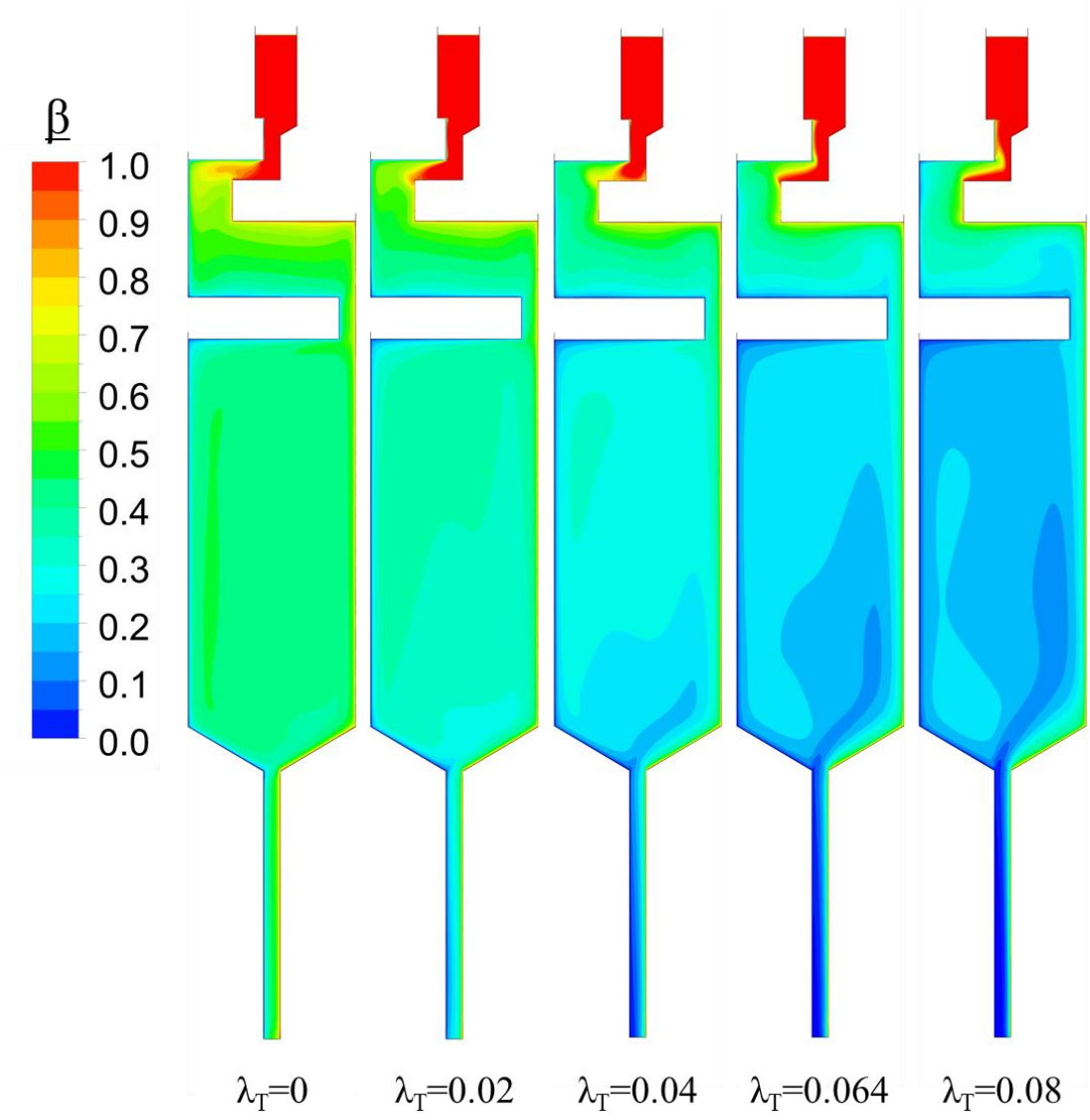

Figure A - 4 Wheel-space swirl contours (axial-radial plane) for radial-axial-clearance seal at periodic surface for various sealing flow rates

- Tighter radial-clearance seal (section 7.4):

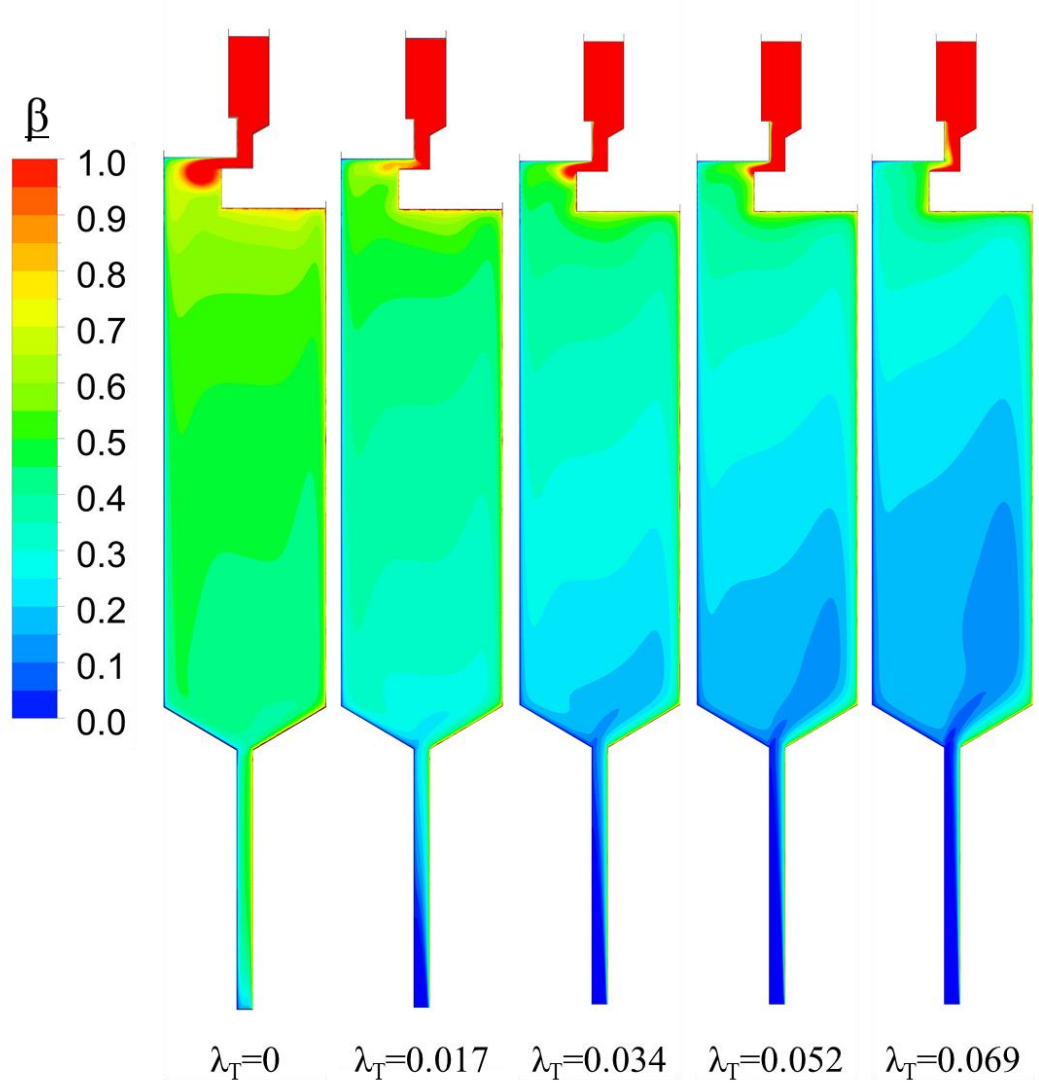

Figure A - 5 Wheel-space swirl contours (axial-radial plane) for tighter radial-clearance seal at periodic surface for various sealing flow rates

- Double-radial-clearance seal (section 7.5):

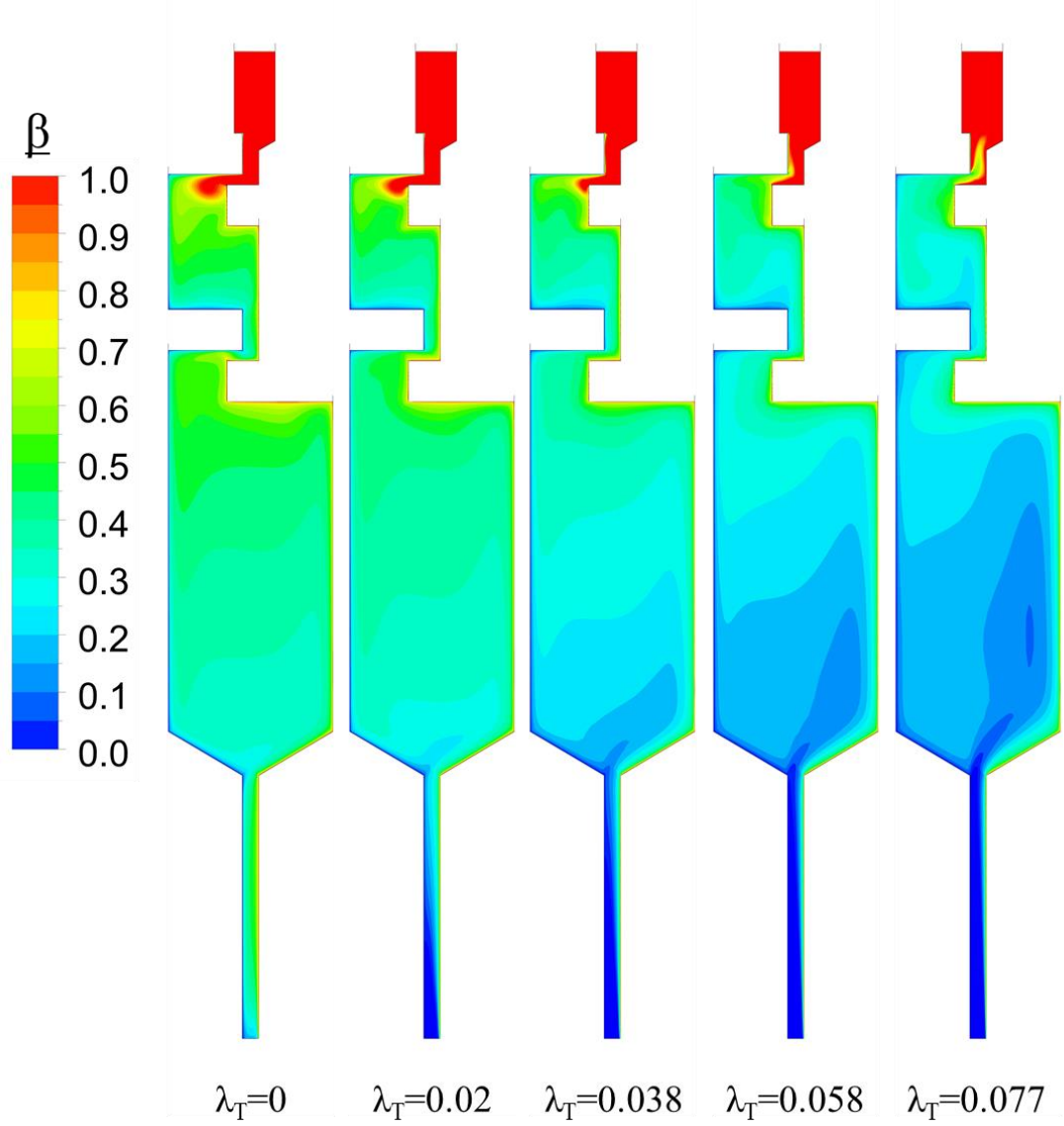

Figure A - 6 Wheel-space swirl contours (axial-radial plane) for double-radial-clearance seal at periodic surface for various sealing flow rates

APPENDIX B – SEALING EFFECTIVENESS CONTOURS

The figures presented in this appendix are the sealing effectiveness contours on the axial-radial plane for all of the rim-seal geometries considered in this research, each seal shows five different sealing flow rates (in increasing order from left to right), corresponding to the same sealing flow cases shown in the above appendix (equivalent λ_T case as the swirl ratio contours).

- Axial-clearance seal (section 6.3):

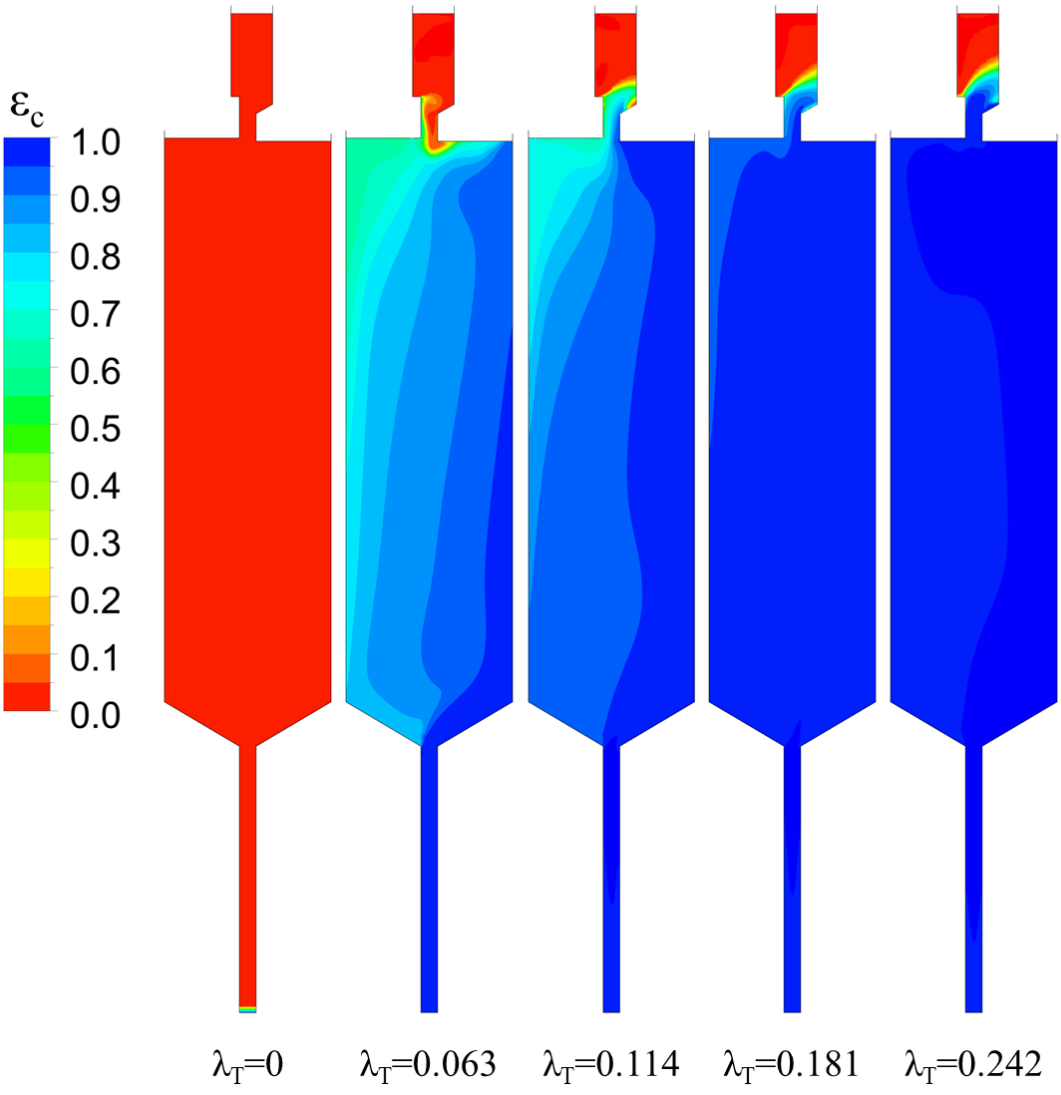

Figure B - 1 Wheel-space effectiveness contours (axial-radial plane) for axial-clearance seal at periodic surface for various sealing flow rates

- Radial-clearance seal (section 7.1):

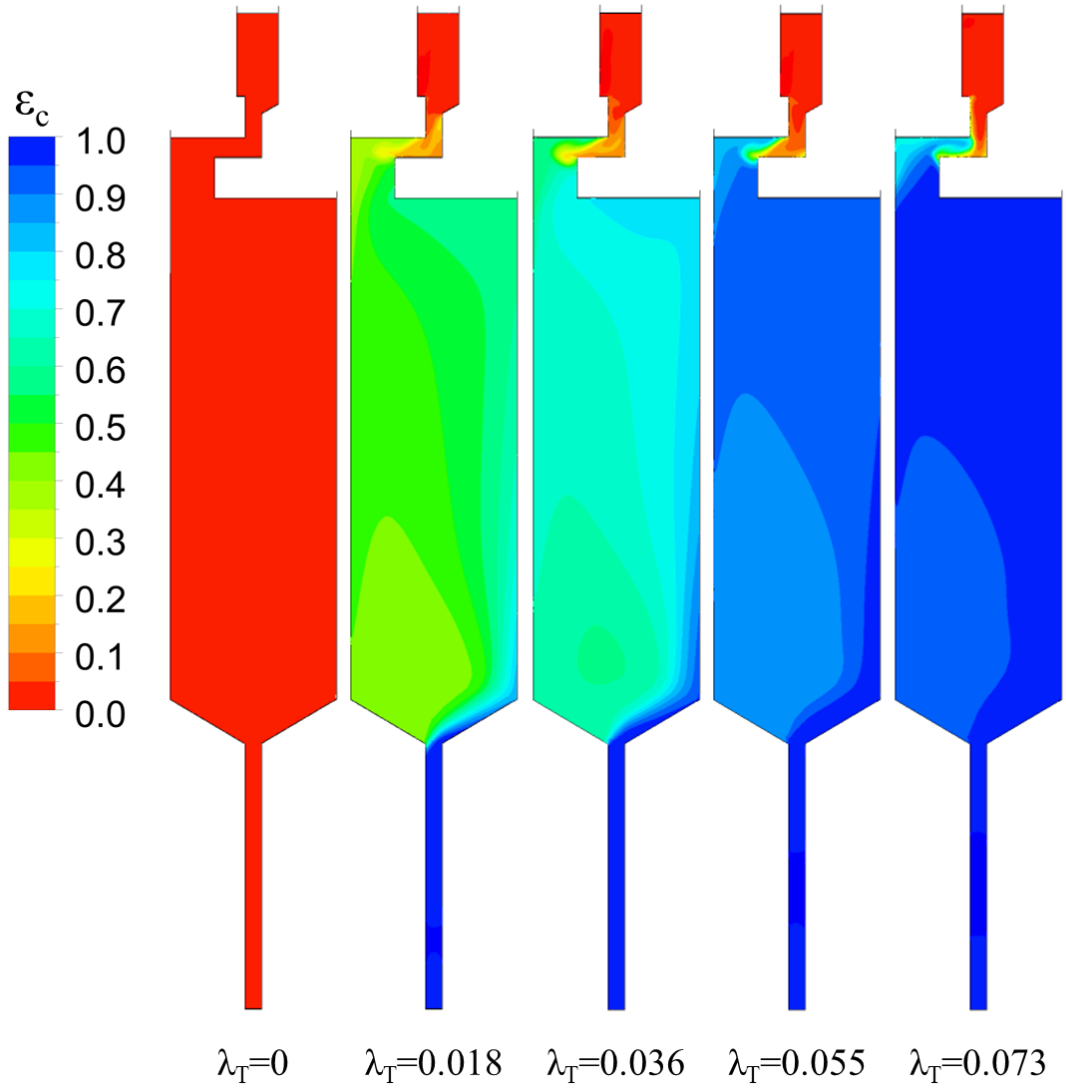

Figure B - 2 Wheel-space effectiveness contours (axial-radial plane) for radial-clearance seal at periodic surface for various sealing flow rates

- Double-axial-clearance seal (section 7.2):

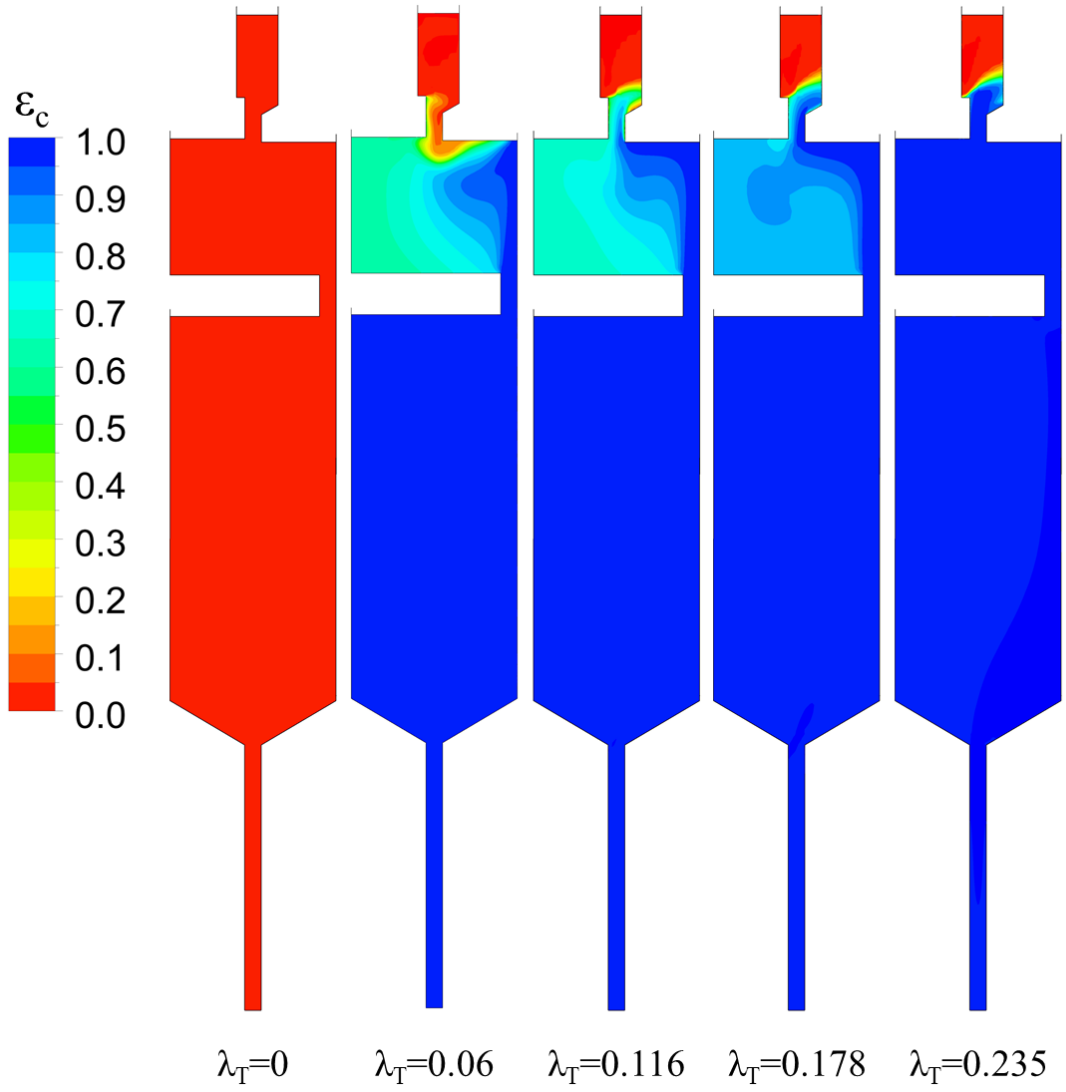

Figure B - 3 Wheel-space effectiveness contours (axial-radial plane) for double-axial-clearance seal at periodic surface for various sealing flow rates

- Radial-axial-clearance seal (section 7.3):

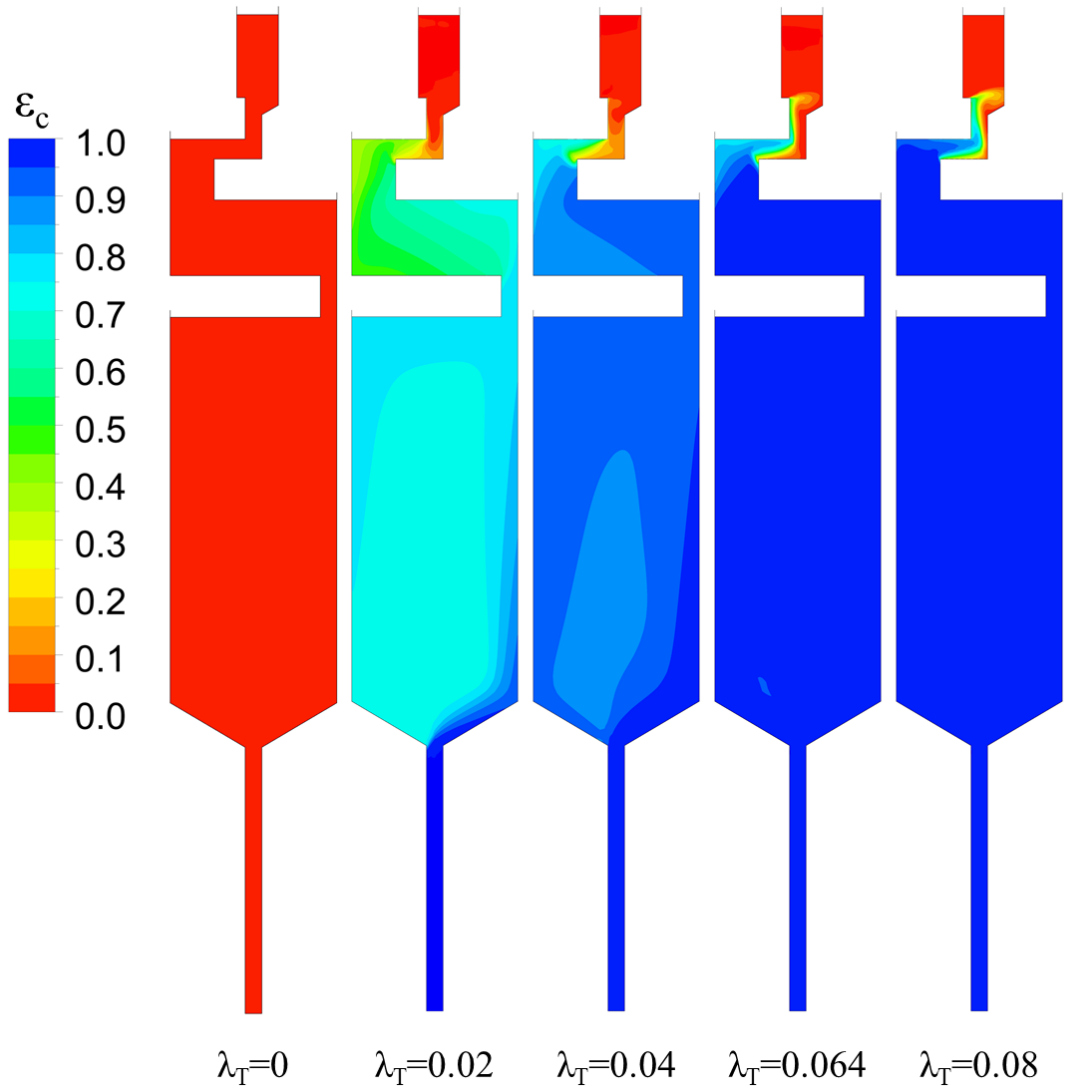

Figure B - 4 Wheel-space effectiveness contours (axial-radial plane) for radial-axial-clearance seal at periodic surface for various sealing flow rates

- Tighter radial-clearance seal (section 7.4):

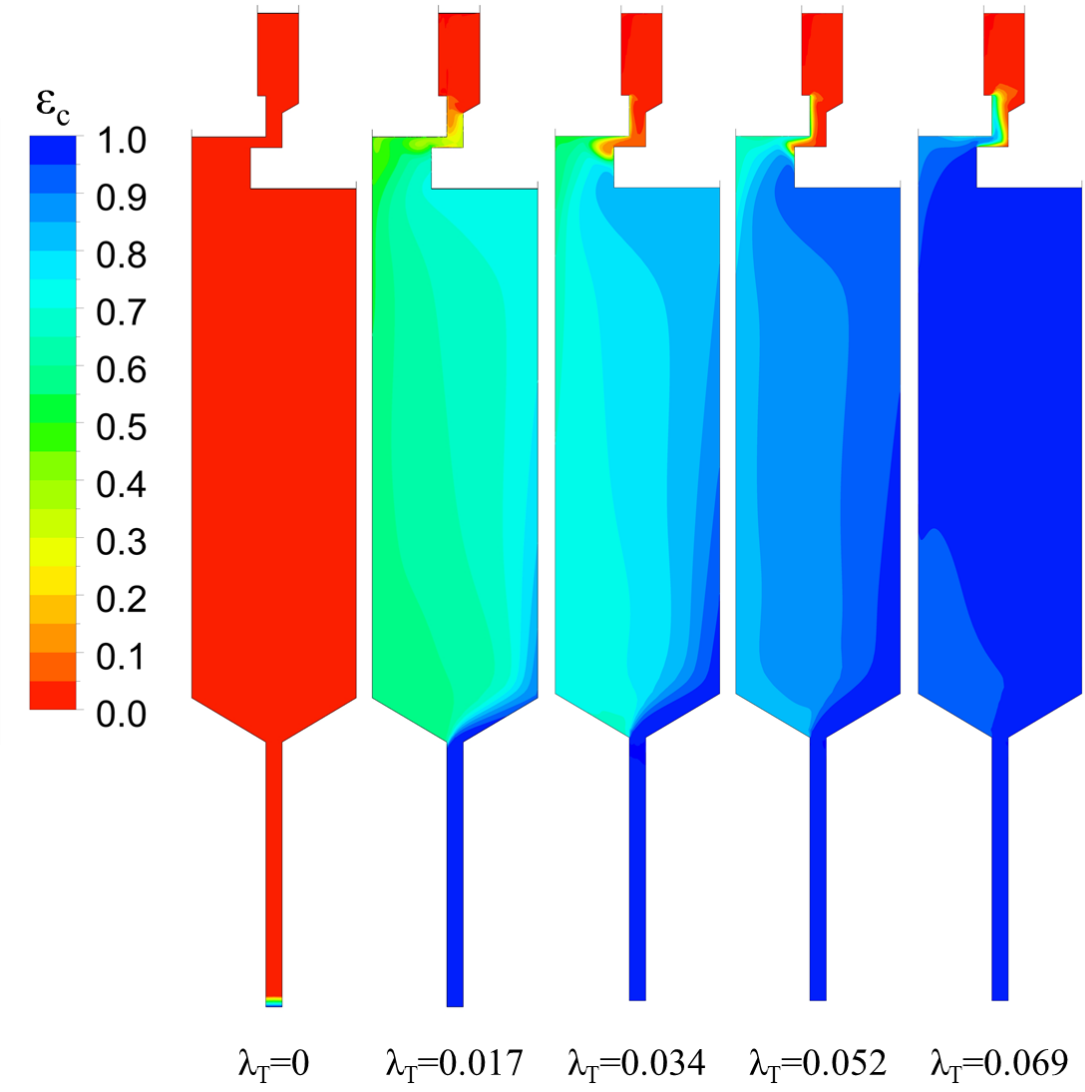

Figure B - 5 Wheel-space effectiveness contours (axial-radial plane) for tighter radial-clearance seal at periodic surface for various sealing flow rates

- Double-radial-clearance seal (section 7.5):

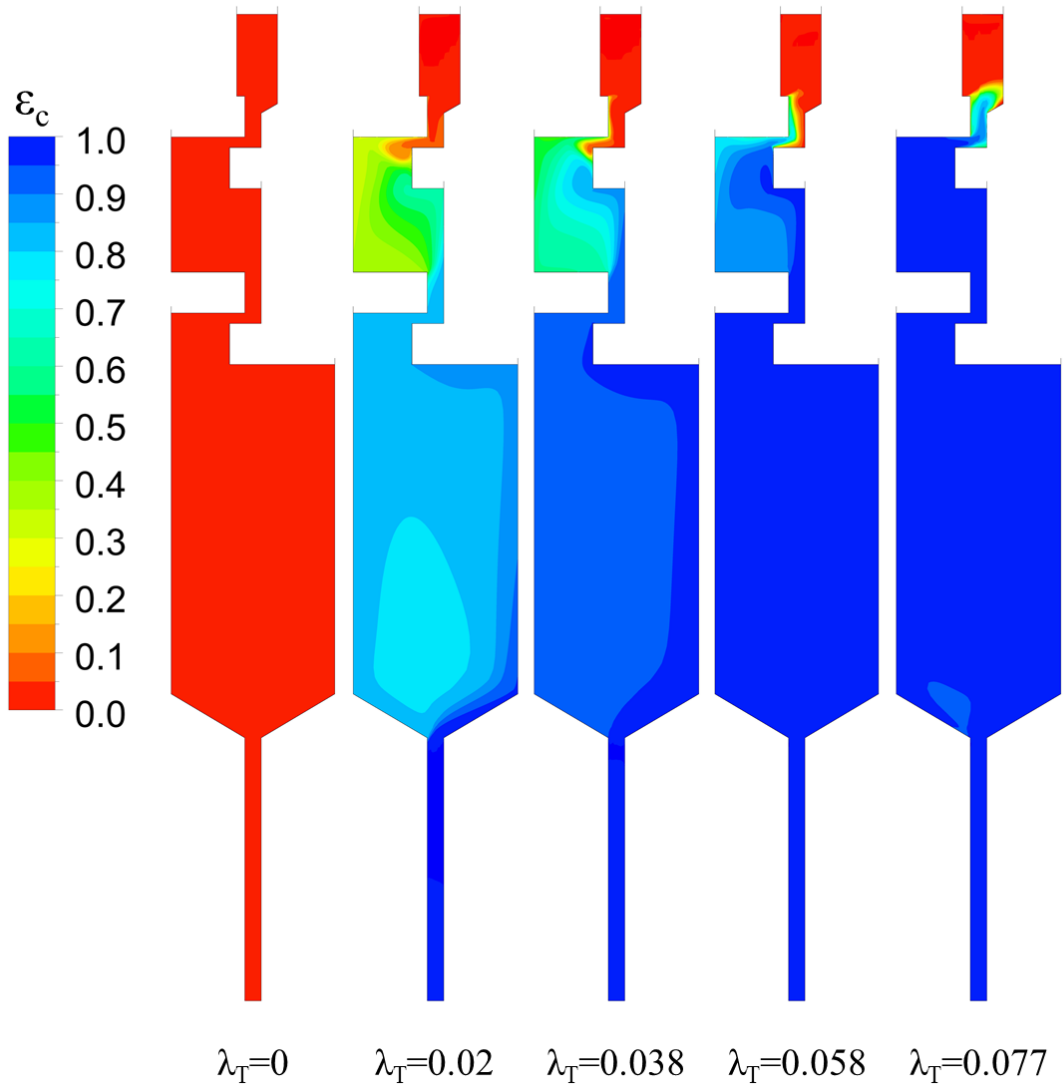

Figure B - 6 Wheel-space effectiveness contours (axial-radial plane) for double-radial-clearance seal at periodic surface for various sealing flow rates

APPENDIX C

PROCEEDINGS OF ASME TURBO EXPO 2013: POWER FOR LAND, SEA AND AIR, ASME PAPER GT2013-94148

Experimental Measurements of Ingestion through Turbine Rim Seals. Part 5: Fluid Dynamics of Wheel-Space

* Accepted for publication in the Proceedings of the IMechE, Part A: Journal of Power and Energy.

Proceedings of ASME Turbo Expo 2013: Power for Land, Sea and Air
June 3-7, 2013, San Antonio, Texas, USA

GT2013-94148

EXPERIMENTAL MEASUREMENTS OF INGESTION THROUGH TURBINE RIM SEALS. PART 5: FLUID DYNAMICS OF WHEEL-SPACE

Carl M Sangan Yogesh Lalwani J Michael Owen Gary D Lock

Dept. of Mechanical Engineering
University of Bath
Bath, BA2 7AY
United Kingdom

ABSTRACT

This paper discusses the flow structure in typical rotor-stator systems with ingress and egress. Measurements of concentration, velocity and pressure were made using a rotating-disc rig which experimentally simulated hot gas ingestion into the wheel-space of an axial turbine stage. Externally-induced ingress through rim seals was generated from the non-axisymmetric pressures produced by the flow over the vanes and blades in the external annulus. Measurements were conducted using several single- and double-seal geometries and for a range of sealing flow rates and rotational speeds. The concentration measurements showed that the amount of ingress, which increased with decreasing sealing flow rate, depended on the seal geometry. The swirl velocity in the fluid core increased with decreasing sealing-flow rate but, outside the outer region in the wheel-space, it was largely unaffected by the seal geometry or by the amount of ingress. The radial distribution of static pressure, calculated from the measured swirl velocity in the core, was in good agreement with the pressures measured on the stator. The data for the double seals demonstrated that the ingested gas was predominately confined to the region between the seals near the periphery of the wheel-space; in the inner wheel-space, the effectiveness is shown to be significantly higher.

NOMENCLATURE

b	radius of seal
c	concentration
$C_{d,e}$ $C_{d,i}$	discharge coefficients for egress, ingress
C_F	flow coefficient [= Re_w / Re_ϕ]
C_w	non-dimensional flow rate [= $\dot{m}$ / μb]
$C_{w,i}$	value of C_w for ingress
$C_{w,o}$	non-dimensional sealing flow rate
$C_{w,min}$	minimum value of $C_{w,o}$ to prevent ingress
G_c	seal-clearance ratio [= s_c / b]
h_{buffer}	depth of buffer cavity
$\dot{m}$	mass flow rate
M	Mach number of flow in annulus
p	absolute static pressure
p_T	total pressure
r	radius
Re_ϕ	rotational Reynolds number [= $\rho\Omega b^2 / \mu$]
Re_w	axial Reynolds number in annulus [$\rho Wb/\mu$]
S	axial clearance between rotor and stator
s_c	seal clearance
$s_{overlap}$	axial overlap of radial clearance seal
V_ϕ	tangential component of velocity
x	non-dimensional radius [= r / b]
z	axial co-ordinate
β	swirl ratio [= $V_\phi / \Omega r$]
Γ_c	ratio of discharge coefficients [= $C_{d,i} / C_{d,e}$]
ε	sealing effectiveness
ε_c	concentration effectiveness [= $(c_s - c_a) / (c_o - c_a)$]
Φ	non-dimensional sealing parameter [= $C_w / 2\pi G_c Re_\Phi$]
Φ_i	value of Φ when $C_w = C_{w,i}$
Φ_{min}	value of Φ when $C_w = C_{w,min}$
Φ_0	value of Φ when $C_w = C_{w,0}$
λ_T	turbulent flow parameter [= $C_{w,o} Re_\phi^{-0.8}$]
$\lambda_{T,min}$	value of λ_T when $\Phi_o = \Phi_{min}$
μ	dynamic viscosity
ρ	density
θ	circumferential angle
Ω	angular velocity of rotating disc

Subscripts

a	annulus, radius of inlet seal
b	radius of seal
EI	externally-induced ingress
fd	free disc
o	superposed flow

RI	rotationally-induced ingress
s	stator
∞	core

1. INTRODUCTION

Figure 1 illustrates a typical high-pressure gas-turbine stage where cooling of the turbine components allows the mainstream gas temperature to exceed the material's melting point without affecting the blade and vane integrity. This simplified view of the stage shows the rim seal and the wheel-space between the stator and the rotating turbine disc. It is important to prevent the ingestion of hot mainstream gas into the wheel-space; this is achieved by supplying the required quantity of cooling and sealing air, which flows outwards over the disc faces. The flow is usually controlled by an inner seal (not shown in Fig. 1) and is expelled from the wheel-space into the mainstream through the rim seal.

The flow past the stationary vanes and rotating blades in the turbine annulus creates an unsteady 3D variation of pressure radially outward of the rim seal. Ingress and egress occur through those parts of the seal clearance where the external pressure is higher and lower, respectively, than that in the wheel-space; this non-axisymmetric type of ingestion is referred to here as externally-induced (EI) ingress. Although the sealing air can reduce ingress, superfluous use reduces the engine efficiency and insufficient flow can cause serious overheating, resulting in damage to the turbine rim and blade roots.

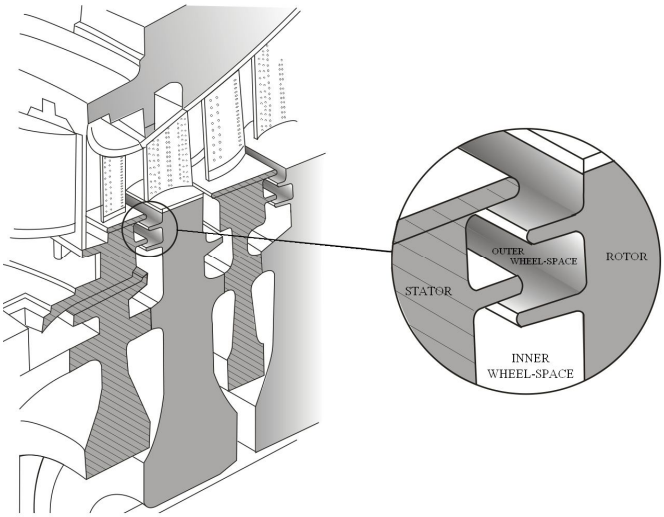

Fig. 1: Generic rotor-stator turbine stage and typical rim-seal (inset)

Rotating fluid in the wheel-space creates a radial gradient of pressure, so that the pressure inside the wheel-space can drop below that outside. So, even when there is no circumferential variation of external pressure, ingress can still occur. The so-called *disc-pumping effect* causes a radial outflow of fluid, or egress, near the rotating disc, and the low pressure in the wheel-space causes ingress of external fluid through the rim seal into the wheel-space. This type of ingestion is referred to here as rotationally-induced (RI) ingress. The term combined ingress is used here for the case where the EI ingress is the same order-of-magnitude as the RI ingress.

In gas turbines, EI ingress is usually the dominant type of ingestion. However, in double rim seals (like that shown in Fig. 1) the circumferential variation in pressure is attenuated in the annular space between the two seals. If this annular space is large enough to damp out the pressure asymmetry, EI ingress dominates for the outer seal and combined ingress for the inner one.

The engine designer needs to know: 1) how much sealing air is required to prevent ingress; 2) when ingress occurs, how much ingested fluid enters the wheel-space; 3) what is the effect of ingress on the flow and heat transfer in the wheel-space. Most research, including that of the authors, has concentrated on the first two points, and little attention has been paid to the latter.

In most experiments, the flow rate of the sealing air is controlled and the radial distribution of pressure and swirl in the wheel-space develops consequentially. In an engine, the converse is the case: the pressure difference between the compressor and the turbine annulus is fixed and the flow rate of sealing air 'comes out in the wash'. For the designer to calculate the flow rate of sealing air, the radial distribution of pressure (which depends principally on the swirl velocity) must be calculated. In addition, the heat transfer from the turbine disc to the cooling flow depends on the flow structure, particularly the swirl ratio. Consequently, measurements of the effect of ingress on the swirl are required to validate theoretical and computational models which assess flow and heat transfer.

This paper follows on from a previously-published three-part paper [1-3] which presented results from a research facility that experimentally models ingress (both RI and EI) into the wheel-space of an axial turbine stage. In Part 5, the fluid dynamics is explored in terms of the radial variation of concentration effectiveness on the stator and the internal distribution of swirl. A brief review of references 1-3 is given in Section 2. Section 3 discusses simplified, axisymmetric diagrams of ingress and egress in typical rotating-disc systems. Section 4 describes the experimental rig, associated instrumentation and seal geometries tested. Section 5 presents the experimental results and discusses the effect of different rim-seal configurations. Section 6 summarises the principal conclusions. The orifice equations relevant to this paper are summarised in the appendix.

2. OVERVIEW OF INGRESS RESEARCH

Ingress has been reviewed extensively in previous parts of this paper, and an overview of references 1-3 is given here. To the authors' best knowledge, there are no publications presenting velocity measurements in a wheel-space featuring ingested flow. The definitions of variables not defined below can be found in the Nomenclature.

2.1 Rotationally-induced ingress

In Part 2, Sangan *et al.* [2] presented an experimental study of RI ingress in the rotating-disc rig described in Section 4. There was no external flow in the annulus and the outlet was open to the atmosphere. Rotating fluid in the wheel-space created a radial gradient of pressure, so that the

pressure inside the cavity was sub-atmospheric. The pumping action of the rotating disc caused a radial outflow of fluid, or egress, in the disc boundary layer, and the low pressure in the wheel-space caused ingress of external fluid through the rim seal into the cavity. Sealing air, seeded with CO_2, was introduced into the wheel-space at a low radius through an inlet seal. Increasing this superposed radial flow rate increased the relative pressure inside the wheel-space and consequently reduced the amount of ingested air. At sufficiently high superposed flow rates, concentration measurements showed that ingress did not occur.

The variation of concentration effectiveness (ε_c) with sealing flow rate was compared with theoretical curves for RI ingress obtained from a theoretical model [4]. Instead of separate correlations for the effects of $C_{w,o}$, G_c and Re_ϕ, a non-dimensional sealing parameter, Φ_0, was used to collapse the data onto a single curve. Data for a simple axial-clearance seal (denoted S1 – see section 4) is shown in Fig. 2 and discussed further below. The theoretical variation of effectiveness with Φ_0 was in very good agreement with the data for a wide range of flow rates and rotational speeds.

2.2 Externally-induced ingress

In Parts 1 and 3 of this series, Sangan *et al.* [1, 3] presented an experimental study of EI ingress in the rotating-disc rig described in Section 4. Measurements of CO_2 gas concentration inside the cavity were used to assess the performance of single and double seals in terms of the variation of concentration effectiveness with sealing flow rate.

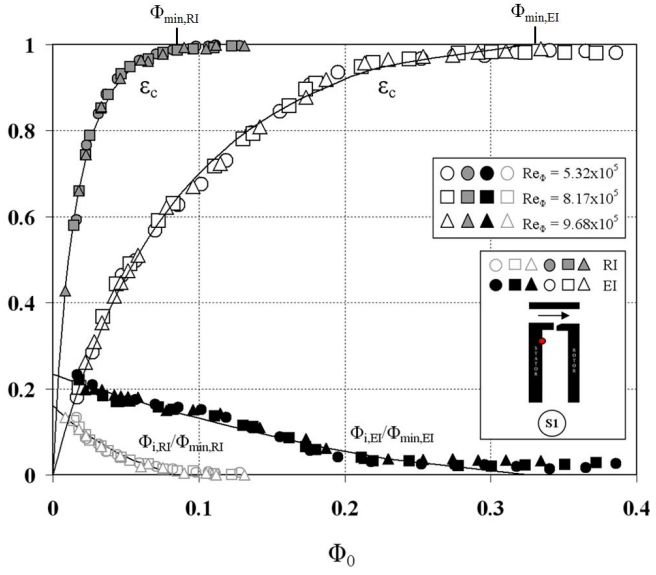

Fig. 2 Comparison between theoretical effectiveness And experimental data for axial-clearance seal [3] (Symbols denote data; lines are theoretical curves)

Figure 2 shows the variation of ε_c for the single axial seal plotted *versus* Φ_o for both EI and RI ingress, based on the concentration measured on the stator at a non-dimensional radius r/b = 0.958. All rim seals were shown to be characterised by a single value of $\Phi_{min,EI}$ or $\Phi_{min,RI}$, the minimum non-dimensional sealing flow rate to prevent EI and RI ingress respectively, which was independent of Re_ϕ . The sealing effectiveness for the RI case is significantly greater than that for the EI case: for the same sealing flow rates, EI ingress causes much more ingestion. Similar curves were produced for a variety of single- and double-clearance seals. Also shown in Fig. 2 are comparisons between the experimental data and theoretical predictions from a theoretical model [4].

The effectiveness is a convenient parameter but the engine designer wants to know how much hot gas enters the wheel-space when $\Phi_o < \Phi_{min}$. In Fig. 2 this ingested flow rate is presented as the ratios $\Phi_{i,EI} / \Phi_{min,EI}$ or $\Phi_{i,RI} / \Phi_{min,RI}$; these quantities are discussed in section 3.4 below.

The values of $\Phi_{min,EI}$ for all seals used in this paper are discussed and summarised in section 4.5 below. As only experiments conducted under conditions of EI ingress will be discussed, $\Phi_{min,EI}$ will be simply denoted Φ_{min}.

3. FLOW STRUCTURE IN ROTOR-STATOR SYSTEMS

The flow structure in rotor-stator systems without ingress is well documented [5,6]. This section describes simplified flow structures for such systems experiencing ingress. It begins by revisiting the fluid dynamics associated with isolated rotating and stationary discs.

3.1 Flow near a rotating disc

Consider a flat disc of radius b which rotates about an axis perpendicular to its plane with a uniform angular velocity, Ω, in a fluid otherwise stationary (Fig 3a). A boundary layer will develop over the disc in which fluid is accelerated by friction and ejected centrifugally. To satisfy the conservation of mass, external fluid will become entrained axially (V_z) into the disc boundary layer. The tangential velocity will decrease from a maximum at the disc surface ($V_\phi = \Omega r$) to zero in the free-stream outside the boundary layer. The radial velocity component (V_r) will be zero at the disc surface and in the free-stream. This phenomenon is often referred to as *free-disc pumping*.

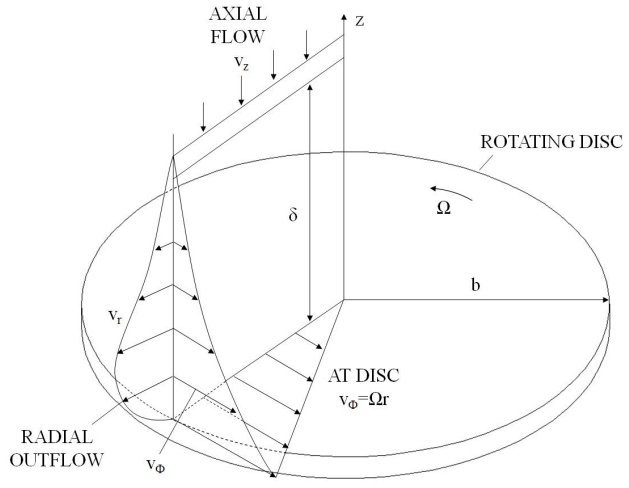

Fig. 3a: Local velocity profiles associated with a rotating disc in free-air (adapted from [6])

Rotating flow near a stationary disc

When placed adjacent to a stationary disc (*stator*), the rotating disc (*rotor*) causes an inviscid *core* of air to rotate between them at a fraction, β, of the disc speed. If the gap between the discs is sufficiently large, separate boundary layers are formed on the internal surfaces. The flow rotating outside the boundary layer is in equilibrium under the influence of the centrifugal force which is balanced by a radial-pressure gradient. The tangential velocity near the wall decreases, with a consequential reduction in the local centrifugal force. The radial pressure gradient is independent of *z*, the distance from the disc; as illustrated in Fig. 3b, this causes the flow near the wall to flow radially inwards, and for reasons of continuity that motion must be compensated by an axial flow (V_z) away from the surface.

3.2 Models of flow structure in rotor-stator systems

Fig. 4a shows the simplified flow structure for a rotor-stator system *without ingress*. The gap ratio is large enough to ensure separate boundary layers on the two discs, both of which start at $r = a$. There is a clearance between the discs at both the inlet and at the shroud as well as a superposed radial flow, with swirl, at $r = a$. Fluid moves radially outward in the boundary layer on the rotor and inward in the boundary layer on the stator. The net flow rate in the two boundary layers must equal the superposed flow rate. Fluid also moves axially across the rotating inviscid core from the boundary layer on the stator to that on the rotor. (Note: the entrainment by the boundary layer on the rotor decreases as the swirl ratio in the core increases. It should also be noted that there can be no axial gradients of the tangential and axial components of velocity in the core and that the radial component must be zero; *all radial flow is confined to the boundary layers on the rotor and stator*.)

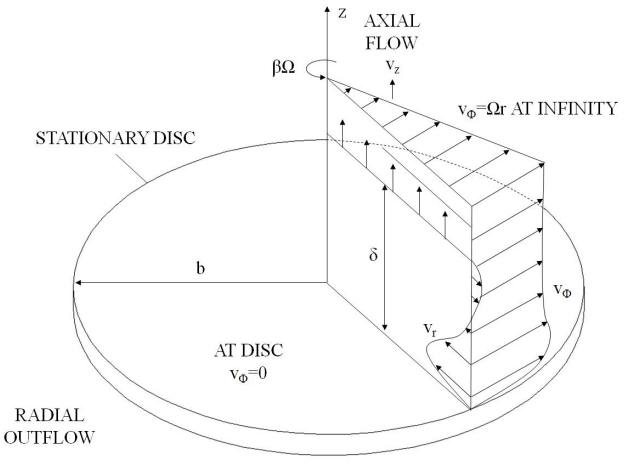

Fig. 3b: Local velocity profiles associated with a stationary disc in a rotating fluid (adapted from [6])

The superposed flow enters the system through an *inner region* which extends to $r = r_{in}$, where all the available flow has been entrained by the boundary layer on the rotor. In the *outer region* for $r_{out} < r < b$ fluid, with a flow rate equal to that of the superposed flow, leaves the system through the rim seal; the additional fluid entrained by the boundary layer on the rotor flows axially across the outer region to be entrained by the boundary layer on the stator. The inner and outer regions are the sources for the flow in the boundary layers on the rotor and stator respectively.

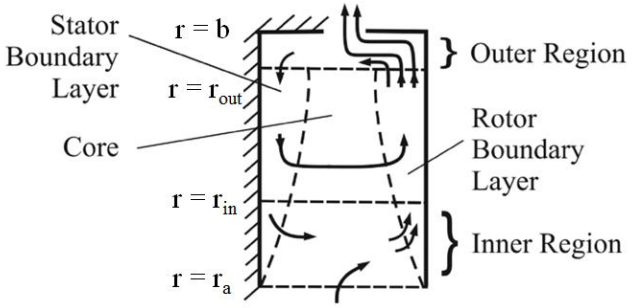

Fig. 4a: Simplified flow structure for a rotor-stator system with superposed sealing flow and no ingress

Fig. 4b, which shows the flow structure for the case where there is *ingress but no superposed sealing flow*, has similarities with Fig. 4a though there is no inner region. The main difference is in the outer region, where the ingress and egress (which have equal flow rates) mix; conservation of mass, angular momentum and energy will determine the resultant swirl, concentration and temperature of the fluid in the outer region. This region is the source of the flow in the boundary layer on the stator; outside the outer region, there will be equal flow rates in the boundary layers on the rotor and stator.

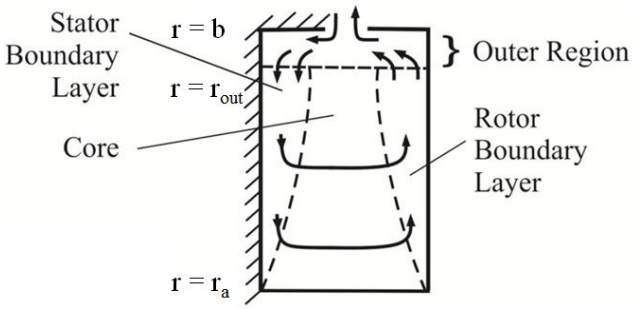

Fig. 4b: Simplified flow structure for a rotor-stator system with ingress and no superposed sealing flow

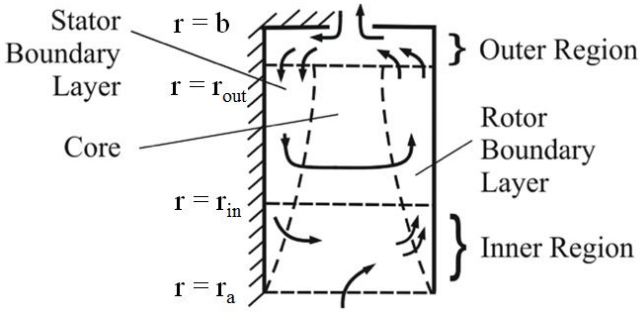

Fig. 4c: Simplified flow structure for a rotor-stator system with superposed sealing flow and ingress

Fig. 4c shows the flow structure for the case where there is a *superposed radial flow, with swirl, together with ingress through the rim seal.* The structure is a combination of those shown in Figs 4a and 4b, and, outside the inner and outer regions, fluid leaves the boundary layer on the stator to be entrained by that on the rotor. *Consequently, if the fluid is fully mixed in the outer region, the concentration (and, for an adiabatic stator, the temperature) of the fluid in the boundary layer on the stator, and that in the adjacent core, will be invariant with radius.*

3.4 Some relevant parameters

The ingestion of fluid through the rim seal is an inviscid phenomenon, whereas the flow inside the wheel-space is controlled by the boundary-layers on the rotor and stator. Some of the important parameters that are relevant to this paper are defined below.

Ingress parameters

The ingress into the wheel-space is characterised by the ratio Φ_0/Φ_{min}. The sealing flow parameter, Φ_0, combines the effects of $C_{w,o}$, G_c and Re_ϕ into a single variable:

$$\Phi_o = \frac{C_{w,o}}{2\pi G_c\, Re_\phi} \tag{3.1}$$

As Re_ϕ and $C_{w,0}$ include viscous terms which cancel in the above equation, this definition disguises the fact that Φ_o is an *inviscid* parameter. It is more appropriate to use an alternative definition, which is equivalent to eq (3.2):

$$\Phi_o = \frac{U}{\Omega b} \tag{3.2}$$

where U is the bulk mean radial velocity of sealing air through the seal clearance, so that

$$U = \frac{\dot{m}_o}{2\pi\rho b s_c} \tag{3.3}$$

The system is sealed if the sealing flow rate increases to Φ_{min}, the value of Φ_0 required to prevent ingress.

The amount of ingested fluid entering the wheel-space is characterised by, Φ_i, where

$$\Phi_i = \frac{C_{w,i}}{2\pi G_c\, Re_\phi} \tag{3.4}$$

It can be shown (see appendix) that

$$\frac{\Phi_i}{\Phi_o} = \varepsilon^{-1} - 1 \tag{3.5}$$

and the ratio Φ_i/Φ_o determines the concentration and temperature of the fluid inside the outer region of the wheel-space.

Wheel-space parameters

The swirl ratio of the fluid in the inviscid core between the boundary layers in the wheel-space is defined as

$$\beta = \frac{V_\varphi}{\Omega r} \tag{3.6}$$

Where V_ϕ is the tangential component of velocity in the core. As stated above, in a rotating inviscid fluid the radial component of velocity must be zero and the axial gradients of the axial and tangential components of velocity must also be zero. All radial flow occurs inside the boundary layers, and the value of β adjusts to satisfy the continuity of the flow rate in the boundary layers.

The swirl ratio also controls the radial distribution of static pressure p in the wheel-space, and the pressure coefficient is defined as

$$C_p = \frac{p - p_{ref}}{\frac{1}{2}\rho\Omega^2 b^2} \tag{3.7}$$

where p_{ref} is a convenient reference pressure.

The structure of the flow in the wheel-space is determined by the turbulent flow parameter, which is defined as

$$\lambda_T = C_{w,0}\, Re_\varphi^{-0.8} \tag{3.8}$$

For the free disc, where there is no stator, the entrained flow rate is characterised by $\lambda_{T,fd} \approx 0.22$. In a wheel-space, values of $\lambda_T > \lambda_{T,fd}$ are expected to suppress the core rotation.

It follows from eqs (3.1) and (3.8) that

$$\lambda_T = 2\pi G_c\, Re_\phi^{0.2}\, \Phi_o \tag{3.9}$$

4. EXPERIMENTAL FACILITY

The research facility, which experimentally simulates hot gas ingestion into the wheel-space of an axial turbine stage, is described extensively in Part 1 [1].

4.1 Test rig

The test section of the facility, shown in Fig. 5, features a turbine stage with 32 vanes and 41 blades which were formed from nylon by rapid-prototyping. The rotor disc could be rotated by an electric motor, and (to avoid the necessity of a dynamometer to remove the unwanted power) the blades were symmetric NACA 0018 aerofoils. The diameter of the rotor was 380 mm and the radial height of the annulus was 10 mm.

The vanes and blades were secured to aluminium platforms which form the periphery of the stator and rotor respectively. Both the stationary and rotating discs (highlighted in red and blue, respectively, in Fig. 5) were manufactured from transparent polycarbonate; this allowed optical access to the wheel-space for measurements of effectiveness on the rotor using thermochromic liquid crystal, as discussed by Pountney *et al.* [7].

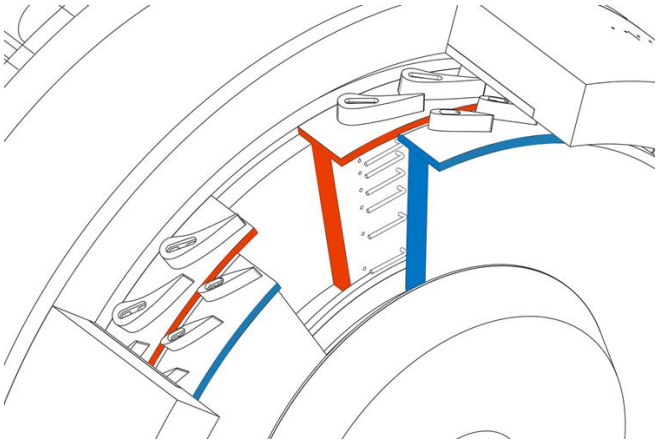

Fig. 5: Rig test section highlighting pressure instrumentation (red, stationary; blue, rotating)

Sealing air was introduced into the wheel-space at a low radius through an inlet seal. In order to measure the degree of ingestion, the sealing flow was seeded to a 1% level with a carbon dioxide tracer gas. The concentration of CO_2 was monitored at the entrance to the wheel-space, c_0, and in the unseeded upstream flow through the annulus, c_a. The variation of concentration c_s with radius ($0.55 < r/b < 0.993$) along the stator in the wheel-space was determined by sampling through 15 tubes of diameter 1.6 mm. The gas was extracted by a pump, which delivered the samples to a dual channel infra-red gas analyser. The concentration measurements were made within a combined uncertainty of +/- 1.5% of the measured value.

The concentration taps were also used to determine the static pressure, p, on the stator. Seven complementary Pitot tubes in the wheel-space, aligned with the tangential direction, were used to measure the total pressure, p_T, at $z/S = 0.25$ in the fluid core. The tangential component of velocity in the core at each of the seven radial locations was calculated from Bernouilli's equation:

$$V_\varphi = \left[\frac{2(p_T - p)}{\rho}\right]^{1/2} \qquad (4.1)$$

The estimated uncertainty in the measured values of V_ϕ were +/- 3%.

The disc could be rotated up to speeds of 4000 rpm, providing a maximum rotational Reynolds numbers, Re_ϕ (based on disc radius) up to 1.1×10^6. This value is typically an order-of-magnitude less than that found in gas turbines. However, for rotating flow the turbulent flow structure in the boundary layers is principally governed by the turbulent flow parameter, λ_T, and depends only weakly on Re_ϕ [5]. Hence the flow structure in the rig is considered to be representative of that found in the cooling systems of engines.

The vanes and blades in the annulus also produced a flow structure representative of those found in engines, albeit at lower Reynolds and Mach numbers. All data for EI ingress presented in this paper are for the *design condition*, with similar annulus velocity triangles at the two operating points listed in Table 1. At the design condition, the flow coefficient was $C_F = 0.538$ and the swirl ratio in the annulus was $\beta_a = 1.8$.

Parameter	Disc Speed (RPM)	
	2000	3000
$Re_ø$	5.32×10^5	8.17×10^5
Re_w	2.86×10^5	4.40×10^5
C_F	0.538	0.538
M	0.225	0.339

Table 1: Parameters for EI experiments

4.3 Definition of sealing effectiveness

Concentration measurements can be used to determine the *concentration effectiveness* ε_c. This is defined as

$$\varepsilon_c = \frac{c_s - c_a}{c_o - c_a} \qquad (4.2)$$

where the subscripts a, o and s respectively denote the air in the annulus, the sealing air at inlet, and at the surface of the stator. For the experiments conducted here, c_a and c_o were constants (approximately 1% and 0% respectively) and c_s varied with radius on the stator. In particular, $\varepsilon_c = 1$ when $c_s = c_o$ (zero ingress) and $\varepsilon_c = 0$ when $c_s = c_a$ (zero sealing flow).

4.4 Details of rim-seal configurations

Two single seal configurations and two double-clearance configurations were investigated. The notation is consistent with that used in Part 3 [3]: an axial-clearance seal (S1), three different single radial-clearance seals (S2a-c), a radial-axial double seal (D1) and a double-radial seal (D2). Schematics of these geometries are shown as Fig. 6 and static dimensions are given in Table 2. The rotor attachments bolt onto the underside the platform and a modular design allows for a range of seals to be tested.

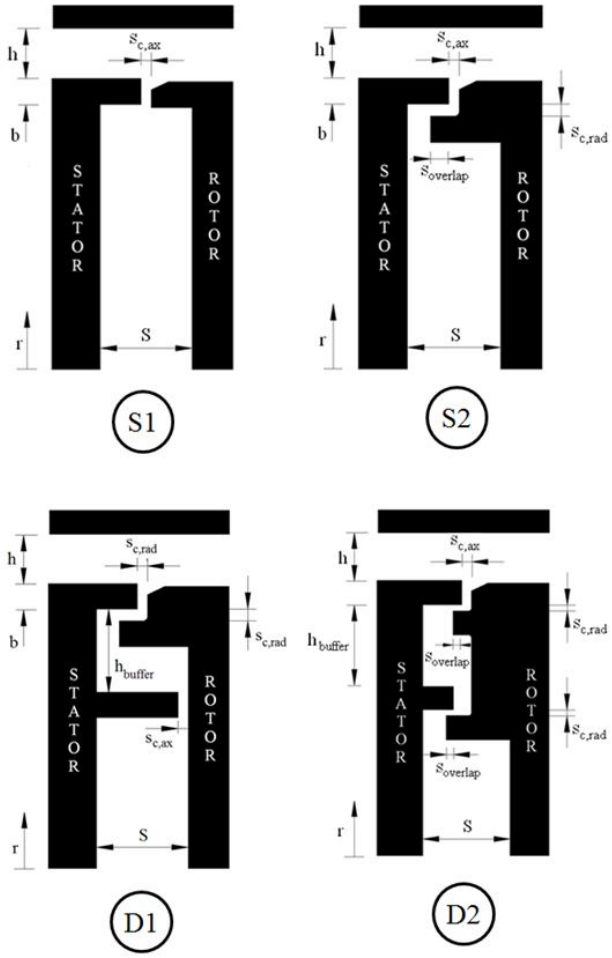

Fig. 6: Rim-seal configurations

The simple axial-clearance seal (S1) is formed between the vane and blade platforms at the wheel-space periphery. The radial-clearance seals (note only S2a is shown in Fig. 6) feature an identical geometry at the wheel-space periphery, with an axial-overlap from a radial lip at lower radius on the rotor. The three variations of the radial-clearance seal tested were designed to investigate the effect of axial overlap and radial seal-clearance.

Geometric Symbol	Seal Configuration					
	S1	S2a	S2b	S2c	D1	D2
h	10.0					
b	190					
S	20.0					
$s_{c,ax}$	2.00					
$s_{c,rad}$	-	2.40	2.40	1.28	2.40	1.28
$s_{overlap}$	-	3.70	1.86	1.86	3.70	1.86
h_{buffer}	-	-	-	-	16.5	16.5

Table 2: Geometric properties for all seal configurations (dimensions in mm under static conditions)

Double-clearance seals were created by installing a second seal at lower radius; an *outer* wheel-space is formed between the seal attachments, the *inner* wheel-space was located radially inward of both seals. A secondary inner axial-clearance seal was added to seal configuration, S2a, to form double seal, D1. A secondary radial-clearance seal was added to configuration, S2c, to form the double seal D2.

The seal-clearance ratio, $G_c = s_{c,ax} / b = 0.0105$ used in Eqs. (3.2) and (3.5) for all seal geometries, was based on the axial clearance $s_{c,ax} = 2.0$ mm.

4.5 Sealing performance of rim-seal configurations

Figure 7 shows a bar chart ranking all seals relevant to this paper in order of the magnitudes of Φ_{min}. For double seals, Φ_{min} is based on sampling points in both the inner wheel-space at $r/b = 0.85$ (denoted *inner*) and the outer wheel-space at $r/b = 0.958$ (denoted *outer*). It can be seen that double seal D2 is the most, and single seal S1 the least, effective seal. All further references to Φ_{min} are based on the outer sampling point.

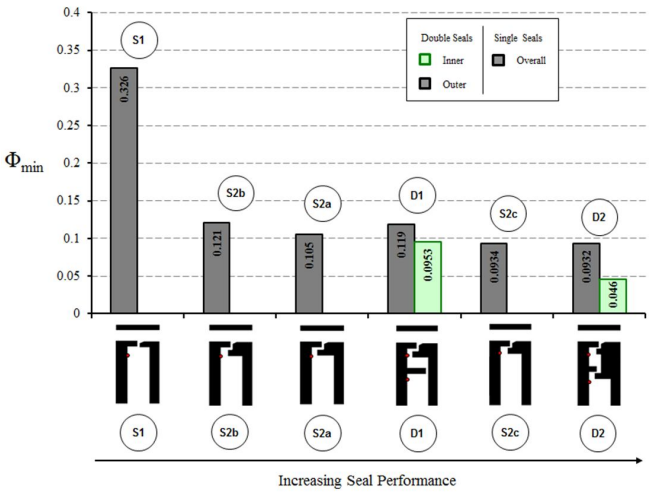

Fig. 7: Performance of all seal configurations, adapted from [3]

5. EXPERIMENTAL MEASUREMENTS

This section describes experiments conducted using both single and double seals. Principally, the data reveals that (i) the concentration in the stator boundary layer is determined by the ratio Φ_i/Φ_0 and the inlet conditions fixed by the flow in the *outer region*; and (ii) that the flow structure is controlled by the boundary layers on the rotor and stator, which themselves are principally governed by λ_T. The data for the double seals demonstrates that the ingested gas is predominately confined to the outer wheel-space; in the inner wheel-space, the effectiveness is shown to be significantly higher. As with the single-clearance seals, the flow structure in the inner wheel-space is governed by λ_T.

5.1 Effectiveness

Figure 8 compares the radial variation of concentration sealing effectiveness ε_c on the stator surface for the axial-clearance seal (S1) and the three radial-clearance seals S2a/b/c, all with $\lambda_T \approx 0.05$. The values of Φ_0/Φ_{min} and Φ_i/Φ_0 are also labelled. Note, for no superposed flow, $\Phi_i/\Phi_0 \rightarrow \infty$ and for the axial clearance seal $\Phi_i/\Phi_{min} \rightarrow 0.23$ (see Fig. 2). As shown in Fig. 7, there are significant differences between the values of Φ_{min} for the four seals; consequently at the same value of λ_T (hence the same Φ_0) there are significant differences in the ingress through these seals into the wheel-space.

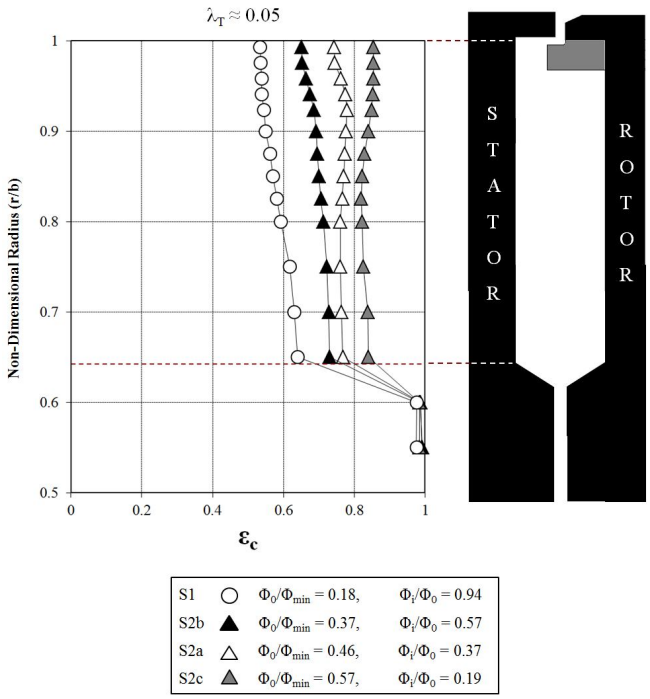

Fig. 8: Radial variation of effectiveness for all single-clearance seals (S1, S2a-c) for a consistent λ_T.

The addition of a radial-clearance component improves the performance of the simple axial-clearance seal. As expected, seal S2b with the smaller axial overlap ($s_{overlap}$ = 1.86 mm) and larger radial-clearance ($s_{c,rad}$ = 2.4 mm) provides the least improvement in sealing performance. With reference to this seal, the increase in the axial overlap to 3.7 mm for Seal S2a improves the performance; however a greater improvement is gained by reducing the radial-clearance to 1.28 mm for Seal S2c. Though it was not tested, a seal with both the larger axial overlap and smaller radial-

clearance would be expected to produce an even better performance.

As illustrated by flow-structure depicted in Fig. 4c, the concentration in the stator boundary layer is determined by the ratio Φ_i/Φ_0 and the inlet conditions fixed by the flow in the outer region: here, near the seal clearance, the ingress and egress fluids are mixed; the mixed fluid enters the boundary layer on the stator and flows radially inward. Though fluid is progressively entrained across the core into the rotor boundary layer, away from the outer region no fluid enters the boundary layer on the stator.

Fig. 8 illustrates that for all seals the effectiveness is broadly invariant with radius for $r/b > 0.65$, suggesting that near-complete mixing has occurred in a region very close to the rim seal. *Note that if the flow is not fully mixed then there will be concentration gradients in the stator boundary layer and consequently a radial variation.* The rapid increase in ε_c at the smaller radii is caused by the presence of the *inlet* seal, which prevents, or strongly reduces, the ingestion of fluid into the region where the sealing flow is introduced.

5.2 Swirl

Figure 9 illustrates the variation of swirl ratio with non-dimensional radius for the axial-clearance seal (S1). The measurement points for total pressure in the wheel-space (at $z/S = 0.25$) are shown on the right of the figure. The tests were conducted at $Re_\phi = 8.2 \times 10^5$ for several values of λ_T hence Φ_0 ; in all cases ingress occurred with $\beta_a = 1.8$. The values of Φ_0/Φ_{min} and Φ_i/Φ_0 are also labelled.

Consider first the data for $\lambda_T = 0$, where the flow structure in the wheel-space should be similar to that depicted in Fig 4b. There is no superposed flow and the core rotation $\beta = \beta^* \approx 0.44$ for $r/b < 0.8$. The swirl ratio at larger radii increases radially outward to $\beta \approx 0.9$ at the wheel-space periphery with the influence of highly-swirling ingress. The case $\lambda_T = 0$ has the maximum ingress and the concentration effectiveness everywhere in the wheel-space is zero.

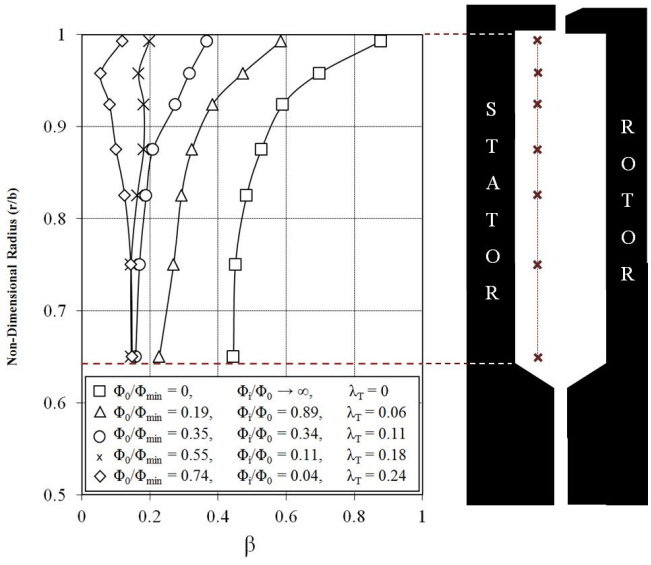

Fig. 9: Variation of swirl ratio with radius for axial-clearance seal (S1) for different λ_T at $Re_\phi = 8.2 \times 10^5$

Increasing the sealing flow to 19% of Φ_{min} (corresponding to $\lambda_T = 0.06$) caused a reduction in the core rotation. The level of swirl at the wheel-space periphery also diminished, as the pressurised wheel-space reduced the ingress from the annulus. A further increase in sealing flow amplifies these effects. At small values of λ_T the flow structure might be expected to be similar to that illustrated by Fig 4c, though the extent of the *outer region* is difficult to quantify.

Figure 10 compares the variation of swirl ratio for the axial-clearance seal (S1) and the three radial-clearance seals. The measurements were made at $Re_\phi = 8.2 \times 10^5$ with $\lambda_T = 0$ and 0.06. As shown in Fig. 8, there are significant differences in the ingress into the wheel-space for the four seals. Despite this, differences in the measured swirl only appear near the outer periphery and the flow structure is governed principally by λ_T.

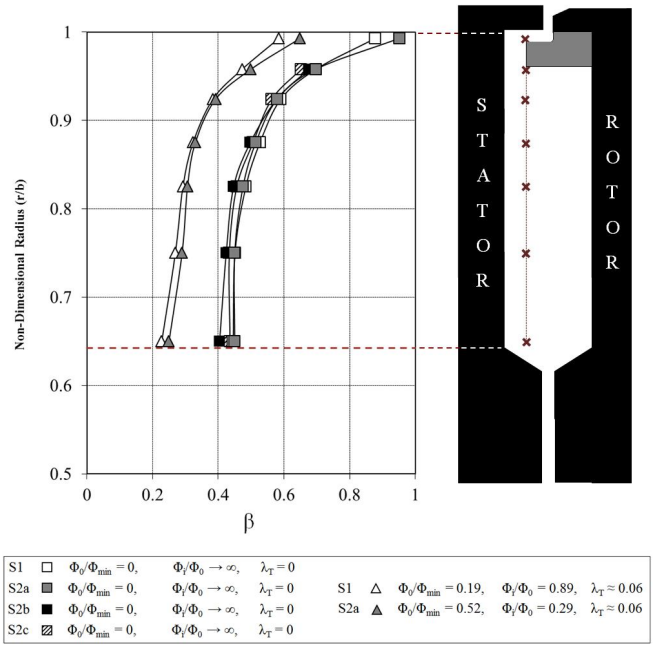

Fig. 10: Variation of swirl ratio with radius for all single-clearance seals (S1, S2a-c) at $Re_\phi = 8.2 \times 10^5$

At first sight, it might be surprising that ingress has so little effect on the velocity distribution in the core. As explained in Section 3.3, ingress will change the swirl in the outer region, which is the source of the flow in the boundary layer on the stator. This will affect the flow in that boundary layer, which in turn will affect the flow in the boundary layer on the rotor and the swirl in the core. However, boundary layers are relatively insensitive to initial conditions, which decay with distance from the start of the flow. Consequently, the changes to the swirl in the outer region have only a small effect outside this region. (For laminar flow, Dijkstra and van Heijst [8] made measurements in sealed rotor-stator systems with rotating and stationary outer shrouds; their results showed that the effects of the shroud on the core rotational speed were confined to the outer part of the wheel-space.)

5.3 Pressure

For a rotating inviscid core, the radial momentum equation reduces to a balance between the pressure force and the centripetal acceleration so that

$$\frac{1}{\rho}\frac{dp}{dr} = \frac{V_\varphi^{\,2}}{r} \qquad (5.1)$$

Using the definitions of C_p and β in Section 3.4, eq (5.1) can be integrated to give

$$C_p = \frac{p - p_{ref}}{0.5\rho\Omega^2 b^2} = 2\int_{x_{ref}}^{x} x\beta^2 dx \qquad (5.2)$$

where p_{ref} is the pressure at $x = r/b = x_{ref}$; for the results presented here, x_{ref} = 0.6. The numerical integration was carried out using Simpson's rule, with values of β obtained from a least-squares cubic spline fitted to the experimental data.

Figs 11a/b show comparisons between the distributions of C_p calculated from eq (5.2) and the values obtained from the measured static pressures. In both cases, there is very good agreement between the calculated and measured distributions of C_p. In view of the similarity between the distributions of β for the two seals, it is not surprising that the distributions of C_p are also similar. This shows two important things: (i) the radial distribution of the swirl ratio determines the radial distribution of pressure in the wheel-space; (ii) the distributions of swirl and pressure are controlled by λ_T and there is very little effect of ingress on these distributions.

Fig. 12 shows the circumferential distribution (across one vane pitch) of $C_{p,a}$ measured on the vane platform in the annulus at the design condition, i.e., C_F = 0.538 and swirl ratio β_a = 1.8. This distribution is independent of Re_ϕ for incompressible flow. Here, p_{ref} was taken as the mean pressure.

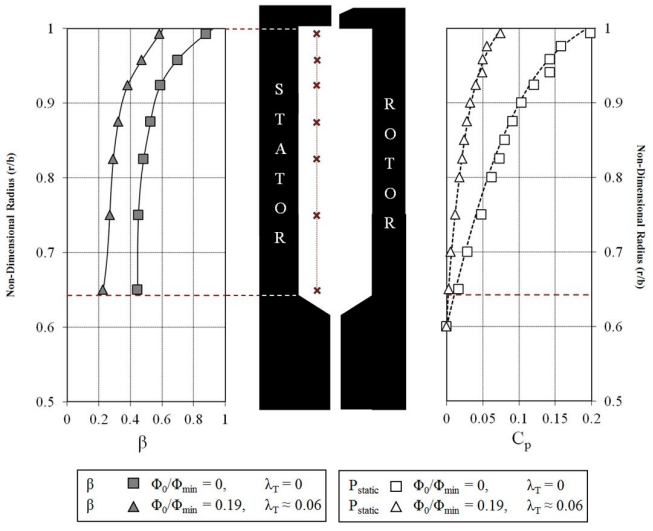

Fig.11a: Effect of λ_T on radial distribution of swirl ratio and pressure coefficient (static) for axial-clearance seal (S1). Symbols denote measured values; lines denote fitted distribution for β and calculated distribution for C_p.

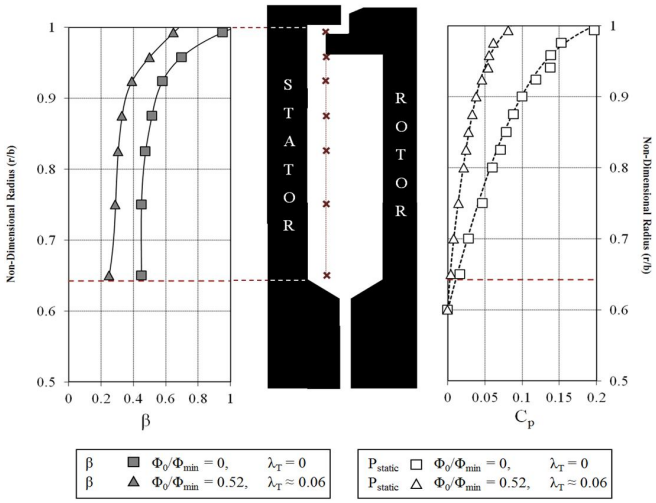

Fig.11b: Effect of λ_T on radial distribution of swirl ratio and pressure coefficient (static) for radial-clearance seal (S2a). Symbols denote measured values; lines denote fitted distribution for β and calculated distribution for C_p.

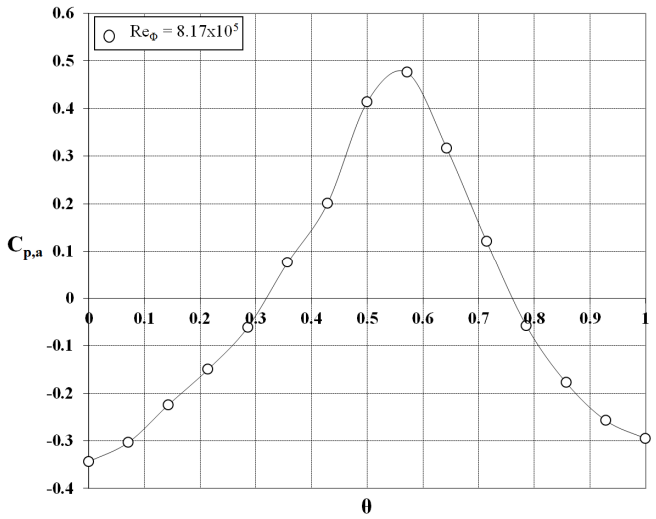

Figure. 12: Circumferential distribution of $C_{p,a}$ over non-dimensional vane pitch at design condition: C_F = 0.538

As shown by eq (A2), EI ingress is controlled by the peak-to-trough pressure difference near the rim seal; ingress cannot occur if the pressure in the wheel-space, radially inward of the seal, is greater than the maximum pressure in the annulus. The pressure criterion, which has been used successfully by experimenters to determine the minimum flow rate to prevent ingress, is usually based on a pressure at the outer part of the wheel-space.

In an engine, the pressure at the *inlet* to the wheel-space is fixed by the outlet pressure of the compressor and by the flow rate of the sealing air. For given conditions, the distribution of swirl and pressure in the wheel-space is also fixed by the flow rate, and - as shown above - this determines the pressure near the *outlet* of the wheel-space. In principle, therefore, if the variation of the swirl ratio with

flow rate were known, the sealing effectiveness could be calculated. This link, which is of practical significance to the engine designer, is beyond the scope of this paper.

5.4 Swirl and effectiveness: double-clearance seals

Figure 13a shows the variation of swirl ratio with radius for the radial-clearance (S2a) and double-clearance (D1) seals. The seal geometry and measurement locations are shown in the schematic on the right. The data for both the single-radial and the double seal are shown for pairs of common superposed flow rates (λ_T = 0, 0.04 and 0.07) at Re_ϕ = 8.2 x 10^5. The data for the single-radial seal has been discussed above but is shown here for the purposes of comparison.

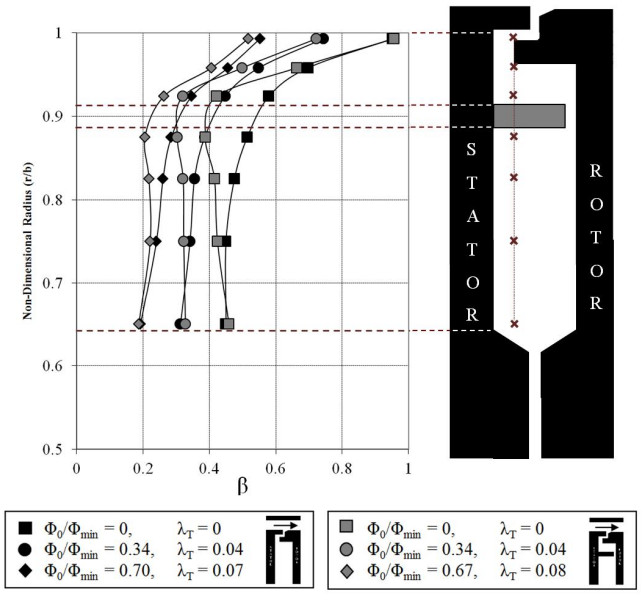

Fig. 13a: Radial distribution of swirl for radial-clearance seal (S2a) and double clearance seal (D1) for different λ_T at Re_ϕ = 8.2 x 10^5

Consider the data for the double seal, first at λ_T = 0. In the *inner wheel-space* (r/b < 0.88) the swirl ratio 0.4 < β < 0.44 is almost invariant with radius; the swirl ratio in the *outer wheel-space* (r/b > 0.924) is seen to increase rapidly from $\beta \approx 0.44$ to $\beta \approx 0.96$ under the influence of highly-swirling ingested flow. The inner seal is seen to constrain the ingress predominantly within the outer wheel-space.

Increasing the sealing flow (*i.e.* increasing λ_T) caused a reduction in the core rotation in the inner wheel-space. The level of swirl at the wheel-space periphery also diminished, as the pressurised wheel-space reduced the ingress from the annulus.

For the single seal, there is a progressive rise in β with increasing radius for r/b > 0.8. For the double seal, the swirl in the inner wheel-space is virtually invariant with radius due to the protection of the inner seal. As discussed below with reference to Fig 13b, at common values of λ_T there are significant differences in the amount of ingress with the single and double-seal. Despite this, the swirl ratios in the inner wheel-space for the two cases are similar, illustrating that β is governed principally by λ_T.

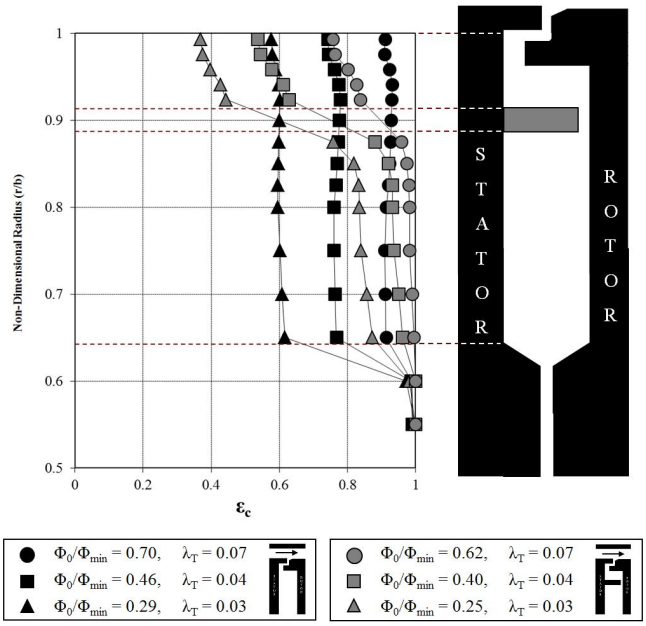

Fig. 13b: Effect of λ_T on radial variation of effectiveness for radial-clearance seal (S2a) and radial-axial double clearance seal (D1)

In Fig. 13b the sealing performance of the radial-clearance (S2a) double-clearance (D1) seals is presented in terms of the radial variation of effectiveness measured on the stator. The data complement Fig 13a and were conducted at Re_ϕ = 5.3 x 10^5 with λ_T = 0.03, 0.04 and 0.07. Consider first the data from the single seal. As expected, ε_c increases as Φ_0/Φ_{min} (hence λ_T) increases. The effectiveness is virtually invariant with radius for r/b > 0.65, which suggests that complete mixing has occurred in a region very close to the rim seal. The rapid increase in ε_c at r/b < 0.65 is caused by the presence of the wheel-space inlet seal, which strongly reduces (but does not eliminate) the ingestion of fluid into the region where the sealing flow is introduced.

Consider now the results for the double seal, where data has been collected at the same values of λ_T used for the single seal. In the inner wheel-space, radially inward of the inner seal, the effectiveness of the double seal is significantly higher than that for the single seal using the same sealing flow rates. For all λ_T, the effectiveness is essentially constant for 0.65 < r/b < 0.85 with a decrease near the inner seal-clearance, possibly indicating a mixing region just inboard of the seal.

In the outer wheel-space (r/b > 0.913) there is a significant reduction in effectiveness when the ingress is contained between the two seals. The effectiveness decreases with increasing radius, suggesting the flow here has not mixed fully.

In the practical situation of an engine, the stator wall in the inner wheel-space could operate at an acceptably low metal temperature with the hot, ingested gas confined to the outer wheel-space protected by a more robust alloy.

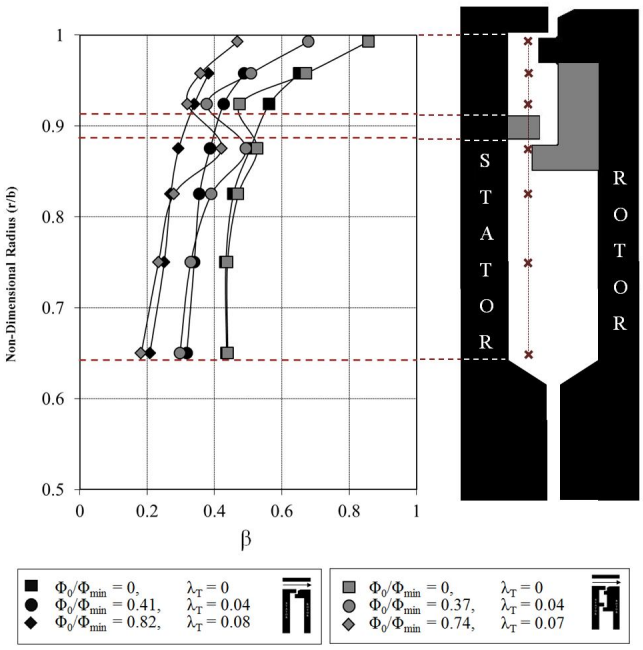

Fig. 14a: Radial distribution of swirl for radial-clearance seal (S2c) and double clearance seal (D2) for different λ_T at $Re_\phi = 8.2 \times 10^5$

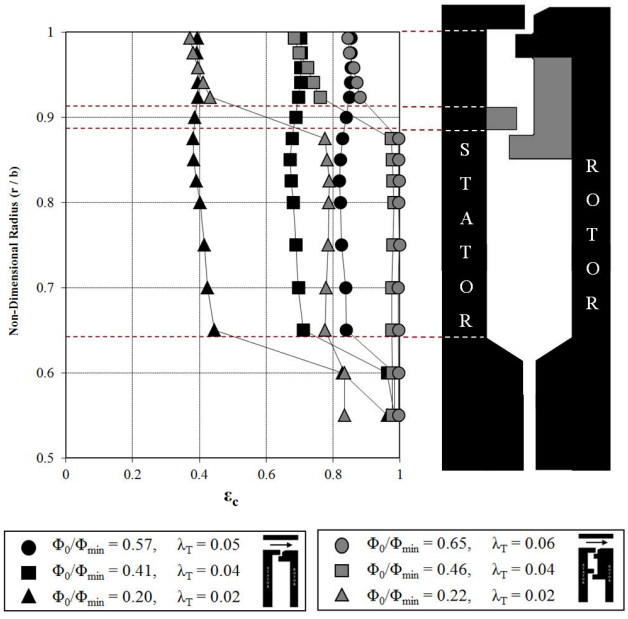

Fig. 14b: Effect of λ_T on radial variation of effectiveness for radial-clearance seal (S2c) and radial-axial double clearance seal (D2)

Swirl and concentration data for the double-radial seal (D2) is shown in Figs. 14a/b respectively. The above discussion related to Seal D1 also applies to this seal. However, some differences are noted. The swirl at r/b = 0.875 is shown to be influenced by the lower portion of the rotating radial seal (absent in the case of the single seal). In the outer wheel-space (r/b > 0.913) the effectiveness for the single and double seals is virtually the same at common λ_T. Despite the high swirl, the concentration is invariant with radius, suggesting better mixing than in the case of seal D1. Relative to D1, D2 has a superior performance across both the inner and outer seal clearances. This is probably due to the larger area of rotating surface in the outer wheel-space which helps to damp out pressure asymmetry.

6. CONCLUSIONS

To understand the effect of ingress on the distribution of velocity and pressure in the wheel-space of a gas turbine, it is necessary to understand the flow structure in simple rotor-stator systems. In these systems, the flow is dominated by the boundary layers on the rotor and stator between which is a core of inviscid rotating fluid. There is no radial velocity in the core, and all radial flow occurs inside the boundary layers. In addition, there are inner and outer regions, which act as the respective sources for the radial flow in the boundary layers on the rotor and stator. Ingress, which passes from the external annulus through the rim seal into the wheel-space, will affect the swirl, concentration and temperature in the outer region.

The rotor-stator rig in the experiments had an inner-to-outer radius ratio of 0.6, and externally-induced ingress through the rim seals was created from the circumferential distribution of pressure produced by the flow over the vanes and blades in the external annulus. For a given seal, the ratio of ingress to sealing flow rate was varied over a wide range (including the case where the sealing flow was zero). Radial distributions of concentration, swirl ratio and pressure were made for a range of rotational speeds and sealing flow rates for several single and double rim seals. As expected for the axial-clearance and radial-clearance single seals, the swirl ratios increased with increasing radius and decreased with increasing sealing flow rate. However, and perhaps surprisingly, ingress had no significant effect on the radial distribution of velocity and pressure beyond the outer region. For a given sealing flow rate, there was little difference between the radial distribution of swirl ratio for the different seals, despite the fact that the ingress for the axial-clearance seal was much greater than for the radial-clearance ones. The radial distribution of pressure, which was calculated from the measured swirl ratios, agreed with the pressures measured on the stator; again, there was little difference between the results for the different seals. In principle, knowing the relationship between the sealing flow rate and the pressure increase in the wheel-space, it should be possible to determine the sealing effectiveness in terms of the pressure at *inlet* to the wheel-space. This should be of interest to the designers of internal air systems.

The experiments using the double seals demonstrated that the ingested gas was predominately confined to the region between the seals near the periphery of the wheel-space; in the inner wheel-space, the effectiveness is shown to be significantly higher.

ACKNOWLEDGEMENTS

The research described here is part of a programme jointly funded by the UK Engineering and Physical Sciences Research Council, Siemens Fossil Power Generation and Siemens Oil & Gas.

REFERENCES

1. Sangan, C. M., Pountney, O. J., Zhou, K., Wilson, M.,Owen, J. M., and Lock, G. D., 2011, "Experimental Measurements of Ingestion through Turbine Rim Seals. Part 1: Externally-Induced Ingress," ASME Paper GT2011-45310. To appear in ASME J. Turbomach.
2. Sangan, C. M., Pountney, O. J., Zhou, K., Wilson, M., Owen, J. M., and Lock, G. D., 2011, "Experimental Measurements of Ingestion through Turbine Rim Seals. Part 2: Rotationally-Induced Ingress," ASME Paper GT2011-45313. To appear in ASME J. Turbomach.
3. Sangan, C. M., Pountney, O. J., Scobie, J. A., Wilson, M, Owen, J.M., and Lock, G.D., 2012 "Experimental Measurements of Ingestion through Turbine Rim Seals. Part 3: Single and Double Seals," ASME Paper GT2012-68493. To appear in ASME J. Turbomach.
4. Zhou, K., Wood, S. N., and Owen, J. M., "Statistical and Theoretical Models of Ingestion through Turbine Rim Seals," 2011 ASME Paper GT2011-45139. To appear in ASME J. Turbomach.
5. Owen, J. M., and Rogers, R. H., 1989, "Flow and Heat Transfer in Rotating-Disc Systems, Volume 1 - Rotor Stator Systems." Research Studies Press Ltd, Taunton, UK.
6. Childs, P.R.N., 2010, "Rotating Flow," Butterworth-Heinemann, Oxford.
7. Pountney, O.J., Sangan, C. M., Owen, J. M., and Lock, G. D., 2012, "Effect of Ingestion on Heat Transfer to Turbine Discs," ASME Paper GT2012-68496. To appear in ASME J. Turbomach.
8. Dijkstra, D. and Van Heist, G.J.F., 1983, "The Flow Between Two Finite Rotating Discs Enclosed by a Cylinder," J. Fluid Mechanics., 128, pp 123-154
9. Scobie, J.A., Sangan, C.M., Teuber, R., Pountney, O.J., Owen, J.M., Wilson, M., and Lock, G.D., 2013, "Experimental Measurements of Ingestion Through Turbine Rim Seals. Part 4: Off-Design Conditions," AMSE Paper No. GT2013-94147
10. Owen, J.M., 2011, "Prediction of Ingestion Through Turbine Rim Seals---Part I: Rotationally Induced Ingress"; ASME J. Turbomach., Vol. 133, 031005-1 to 9.
11. Owen, J.M., 2011, "Prediction of Ingestion Through Turbine Rim Seals---Part II: Externally Induced and Combined Ingress"; ASME J. Turbomach., Vol. 133, 031006-1 to 9.

Appendix: Equations for externally-induced (EI) ingress

Theoretical *orifice models* [10,11] have been developed at the University of Bath. The models treat the seal clearance as an orifice and use variations of Bernoulli's equation, including swirl terms, to relate the sealing flow rate to the pressure drop across the seal. Although the equations are derived for inviscid incompressible flow, discharge coefficients, analogous to those used for the standard orifice equations, are introduced to account for losses.

The EI effectiveness equation when $\Phi_0 \le \Phi_{min,EI}$ is,

$$\frac{\Phi_0}{\Phi_{\mathrm{min,EI}}} = \frac{\varepsilon}{[1+\Gamma_c^{-2/3}(1-\varepsilon)^{2/3}]^{3/2}} \qquad \text{(A1)}$$

where Γ_c is the ratio of the discharge coefficients for ingress and egress, and

$$\Phi_{\mathrm{min,EI}} = \frac{2}{3} C_{\mathrm{d,e}} \, \Delta C_{\mathrm{p}}^{1/2} \qquad \text{(A2)}$$

where

$$\Delta C_{\mathrm{p}} = \frac{\Delta p}{\tfrac{1}{2}\rho \Omega^2 b^2} \qquad \text{(A3)}$$

Δp is the peak-to-trough circumferential pressure difference in the annulus, and $C_{d,e}$ is the discharge coefficient for egress through the rim seal. When $\Phi_0 > \Phi_{min,EI}$, $\varepsilon = 1$.

The ratio of ingress to the sealing flow rate can found from

$$\frac{\Phi_{\mathrm{i,EI}}}{\Phi_{\mathrm{o}}} = \varepsilon^{-1} - 1 \qquad \text{(A4)}$$

and it follows from eq (A1) that

$$\frac{\Phi_{\mathrm{i,EI}}}{\Phi_{\mathrm{min,EI}}} = \frac{1-\varepsilon}{[1+\Gamma_c^{-2/3}(1-\varepsilon)^{2/3}]^{3/2}} \qquad \text{(A5)}$$